Membrane and Shell Formulations for Biological Materials such as Arteries and Lung Tissue

Membran- und Schalenformulierungen für biologische Materialien wie Arterien und Lungengewebe

Von der Fakultät für Maschinenwesen der
Rheinisch-Westfälischen Technischen Hochschule Aachen
zur Erlangung des akademischen Grades eines Doktors
der Ingenieurwissenschaften genehmigte Dissertation

vorgelegt von

Farshad Roohbakhshan

Berichter: Univ.-Prof. Roger Andrew Sauer, Ph.D.
apl.-Prof. Dr.-Ing. Marcus Stoffel

Tag der mündlichen Prüfung: 07. November 2017

Abstract

This work introduces different membrane and shell formulations for the computational modeling of biological materials, in particular soft tissues. Soft tissues are usually considered as being incompressible or nearly incompressible. Moreover, they can easily undergo large deformations and therefore they show highly nonlinear behavior. Many living tissues, such as cardiovascular, lung and skin tissues, are constructed from an isotropic ground substance and an anisotropic network of collagen fibers. Thus, the presented computational models of soft tissues take the geometrical and material nonlinearities as well as the anisotropic response into account .

In addition to the membrane formulation, three different constitutive approaches are introduced to model *thin rotation-free shells* based on the Kirchhoff–Love hypothesis. One approach is based on numerical integration through the shell thickness while the other two approaches do not need any numerical integration and therefore are computationally more efficient. The formulations are examined for different isotropic and anisotropic material models, which are commonly used to model soft biological materials, including arteries and lung tissues. The formulations are further extended to *laminated composite shells* that can be used to model arteries. The finite element method, based on isogeometric analysis (IGA), is employed to solve the governing equations. Accordingly, the surfaces of shells and membranes are represented by Non-Uniform Rational B-Splines (NURBS), which can provide high smoothness and continuity in interpolation of field variables and discretization of the weak form.

Several numerical examples, including linear and nonlinear benchmark tests, are performed to demonstrate the robustness and accuracy of the proposed formulations. Furthermore, the capabilities of the presented models to analyze soft tissues are examined by means of different numerical examples, among which are contact simulations during indentation test and balloon angioplasty.

Zusammenfassung

Die vorliegende Arbeit thematisiert verschiedene Membran- und Schalenformulierungen zur numerischen Modellierung der biologischer Materialien, insbesondere von weichen Geweben. Weichgewebe werden für gewöhnlich als inkompressibel oder nahezu inkompressibel betrachtet. Zudem sind sie häufig großen Verformungen ausgesetzt und zeigen deshalb ein stark nichtlineares Verhalten. Viele biologische Gewebe wie Kardiovaskulär-, Lungen- und Hautgewebe bestehen aus einer isotropen Grundsubstanz und einem anisotropen Netz aus Kollagenfasern. Aus diesem Grund berücksichtigen die vorgestellten numerischen Gewebemodelle sowohl geometrische und materialspezifische Nichtlinearitäten als auch anisotropes Verhalten.

Zusätzlich zur Membranformulierung werden drei verschiedene konstitutive Modelle vorgestellt, um dünne, rotationsfreie Schalen auf Grundlage der Kirchhoff–Love-Hypothese zu modellieren. Der erste Ansatz basiert auf numerischer Integration über die Schalendicke, wohingegen die beiden anderen Ansätze keine numerische Integration benötigen und daher rechnerisch effizienter sind. Die Formulierungen werden für verschiedene isotrope und anisotrope Materialmodelle untersucht, die üblicherweise zur Modellierung weicher, biologischer Materialien einschließlich Arterien und Lungengewebe verwendet werden. Im Anschluss werden die Formulierungen auf laminierte Verbundschalen erweitert, die zur Modellierung von Arterien verwendet werden können. Zu diesem Zweck wird die Finite-Elemente-Methode in Kombination mit isogeometrischer Analyse (IGA) eingesetzt, um die entsprechenden Modellgleichungen zu lösen. Somit werden die Oberflächen von Schalen und Membranen durch nicht-uniforme rationale B-Splines (NURBS) dargestellt, die eine hohe Glattheit und Stetigkeit bei der Interpolation der Feldvariablen und der Diskretisierung der schwachen Form liefern können.

Mehrere numerische Beispiele, einschließlich linearer und nichtlinearer Benchmark-Tests, werden durchgeführt, um die Robustheit und Genauigkeit der vorgeschlagenen Formulierungen zu demonstrieren. Darüber hinaus werden die Eigenschaften und Vorteile der vorgestellten Modelle zur Analyse von Weichgewebe anhand verschiedener numerischer Beispiele untersucht, die unter anderem Kontaktsimulationen von Eindrücktests oder Ballonangioplastie enthalten.

Dedicated to Mitra

> “. . . And her dreams in the bright day
> Makes the suns evaporate . . . ”
> — Paul Eluard

To my father

> “. . . Do not go gentle into that good night.
> Rage, rage against the dying of the light.”
> — Dylan Thomas

Acknowledgements

I would like to express my deepest gratitude to my advisor Prof. Roger A. Sauer for his great support and continuous guidance through the entire work. I have been always privileged to benefit from his extensive knowledge and inspiring hints. Further, I would like to thank Prof. Marcus Stoffel for kindly accepting to review this dissertation. I really appreciate Prof. Georg May for chairing the session of my doctoral examination.

I also thank all my colleagues in Aachen Institute for Advanced Study in Computational Engineering Science (AICES) and particularly my group members. My special thanks go to the administration, IT and service teams of AICES who helped me to pursue my academic and research career in the past couple of years. In particular, I am grateful to my colleague Reza Ghaffari for carefully reading the manuscript and for his helpful suggestions and comments. I am also thankful to Dr. Thang X. Duong for his helps and his collaboration in writing two papers. This project is done in the research group for “Computational Contact and Adhesion Mechanics” in AICES Graduate School with the financial support of the German Research Foundation (DFG) through grant GSC 111, which is acknowledged.

Furthermore, I would like to especially thank my family for their continuous support and encouragement throughout my life. Last and foremost, I am grateful to my friend, my comrade and my wife, Mitra Yousefimashhour, who has been a real support in the last years. Definitely, it would have been impossible to accomplish this dissertation without her love, patience and helps.

Note on the prior publications

This dissertation contains material from seven (see below) papers by the author, namely

1) *Roohbakhshan, F.*, Duong, T. X., and Sauer, R. A. (2016). A projection method to extract biological membrane models from 3D material models. *J. Mech. Behav. Biomed. Mater.*, 58:90–104.
2) *Roohbakhshan, F.* and Sauer, R. A. (2016). Isogeometric nonlinear shell elements for thin laminated composites based on analytical thickness integration. *J. Micromech. Molec. Phys.*, 01(03 & 04):1640010(1–24).
3) Duong, T. X., *Roohbakhshan, F.*, and Sauer, R. A. (2017). A new rotation-free isogeometric thin shell formulation and a corresponding C^1-constraint for patch boundaries. *Comp. Meth. Appl. Mech. Engrg.*, 316:43–83.
4) *Roohbakhshan, F.* and Sauer, R. A. (2017). Efficient isogeometric thin shell formulations for soft biological materials. *Biomech. Model. Mechanobiol.*, 16:1569–1597.
5) *Roohbakhshan, F.*, Duong, T. X., and Sauer, R. A. (2017). Isogeometric Kirchhoff–Love shells: Numerics, constitution and biomechanical applications. *Proc. 11th Int. Conf. SSTA*, 4.
6) *Roohbakhshan, F.* and Sauer, R. A. (2018a). A finite membrane element formulation for surfactants. Preprint available online, arXiv: 1807.08693.
7) *Roohbakhshan, F.* and Sauer, R. A. (2018b). Simulation of angioplasty using isogoemetric laminated composite shell elements. *Proc. Appl. Math. Mech.*, To be published.

In particular, Chap. 3 summarizes the shell theory of Duong et al. (2017). Chaps. 4 and 6 use materials from Roohbakhshan and Sauer (2017). Further, Chap. 5 is based on Duong et al. (2017) and Chap. 7 is a summary of Roohbakhshan and Sauer (2018a). Finally, in Chap. 9, examples from the above mentioned references are presented, which are cited separately. Within the text, the interpolated sections are marked by footnotes.

Contents

List of Figures

List of Tables

Chapter 1

Introduction

In this chapter, the motivation of this research, a concise review of the state of the art for the computational modeling of biological membranes and shells, the scope and the outline of the presented work are discussed.

1.1 Motivation

Soft tissues – such as cardiovascular, lung and skin tissues – are biological materials that usually have incompressible or nearly incompressible behavior (Fung, 1993). Furthermore, they can easily undergo large deformations and exhibit highly nonlinear behavior. Besides, many of soft tissues are anisotropic, which means that they respond differently depending on the direction of the exerted load. The anisotropic behavior of soft tissues roots in their structure, which is often constructed from a ground substance of elastin reinforced by a network of collagen fibers. For such tissues, it is assumed that the ground matrix is isotropic and the anisotropic behavior is due to the distribution of collagen fibers (Holzapfel et al., 2000). Hence, any computational model for the analysis of soft biological tissues should take the geometrical and material nonlinearities as well as the anisotropic response into account. In particular interest of this work are those biological structures that are geometrically thin; thus, they can be mathematically modeled as membranes and shells (see Fig. 1.1).

Remark 1.1. Here, membranes and shells are distinguished as two thin structures with different mechanical characteristics. Membranes can only bear in-plane stresses but shells bear bending moments as well. In literature, the term "(bio)membrane" has been used interchangeably for both structures. (cf. Tepole et al., 2015).

Since many soft tissues do not bear bending and transverse shear deformation, they can be described within the framework of membrane theory. Among different examples in the human body, one can mention cell membranes, aneurysms, the meninges covering the brain and spinal chord, the pericardia around the heart, the visceral pleura supporting the lungs, skin, blood vessels, fetal membranes and the urinary bladder as examples of biological membranes (Humphrey, 1998). On the other hand, if the bending effects are not negligible and a tissue resists against bending, as arteries and heart valves do, a shell formulation is required. For thin structures, where the transverse shear strain and stress are negligible, rotation-free formulations based on the Kirchhoff–Love hypothesis are not only computationally feasible but also mathematically accurate. Therefore, it is of great importance to develop nonlinear membrane and shell formulations that are computationally efficient and are able to handle the challenges of biological thin-walled structures, shortly discussed above.

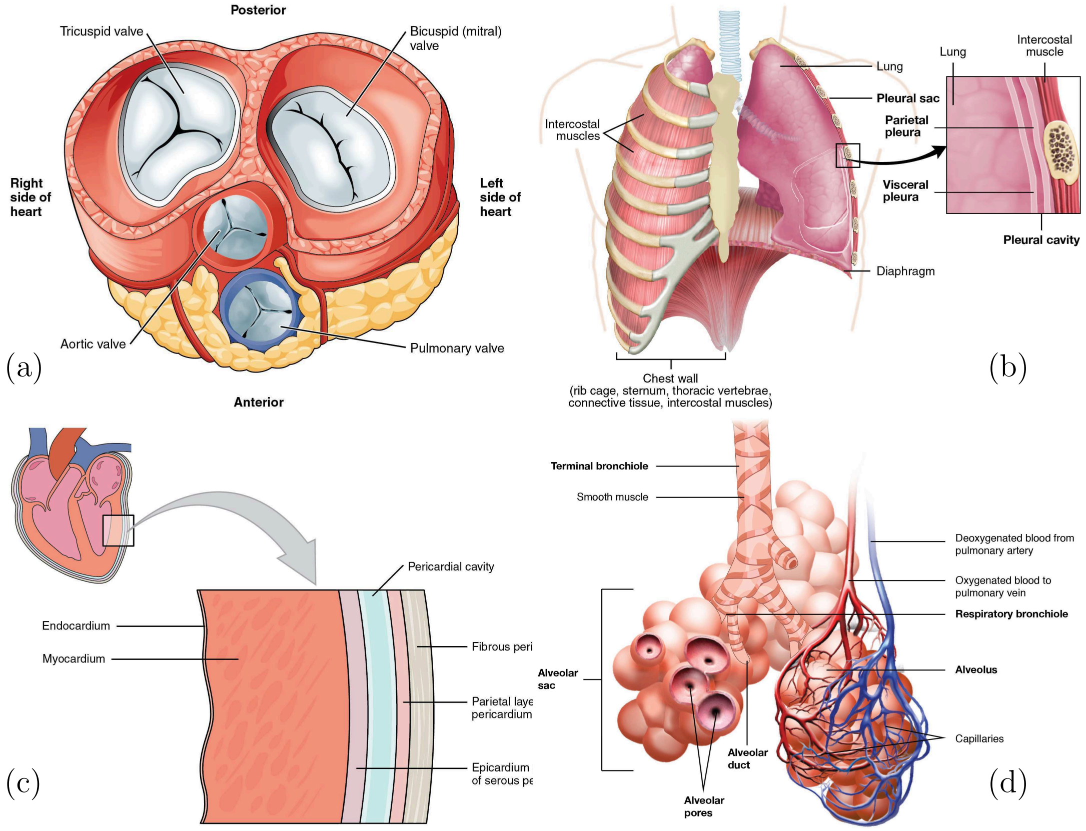

FIGURE 1.1: Membrane and shell-like structures in human body: (a) Heart leaflets, (b) visceral pleura around the lung, (c) pericardia around the heart and (d) alveoli (Illustrations are adopted under CC BY 3.0 license from OpenStax, 2014).

1.2 State of the art

Having discussed the motivation of this research, the rest of this chapter is devoted to briefly reviewing the existing literature on biological membranes and shells as well as the recent advances in isogeometric formulation of rotation-free shells.

1.2.1 Biological membranes

There are plenty of nonlinear membrane formulations introduced for the computational modeling of rubber-like materials that allow for the material incompressibility (e.g. Oden and Sato, 1967; Haughton and Ogden, 1978; Fried, 1982; Wriggers and Taylor, 1990; Ibrahimbegovic and Gruttmann, 1993 and Bonet et al., 2000). They can be employed to model soft tissues if the tissue is considered to be isotropic. However, in most of the soft tissues, networks of collagen fibers are present, which are anisotrpoic in general. Thus, one of the main distinctions between soft tissues and the typical (isotropic) rubber-like materials is the anisotropic behavior (Ogden, 2003). Despite membrane theory, anisotropic hyperelasticity and material incompressibility are the subjects that have been separately studied by different scholars within the framework of continuum mechanics, there are few studies that brings them together to investigate nonlinear biological membranes, which are membranes with incompressible anisotropic nonlinear material behavior. For example, Kyriacou et al. (1996) propose a finite element model for nonlinear orthotropic hyperelastic membranes, which is derived from a two-dimensional constitutive law. Of great interest, is the theoretical framework presented by Humphrey et al. (1992) and Humphrey (1998), which can be used to study nonlinear biological membranes. Holzapfel et al. (1996a) develop an isotropic membrane model that can include material anisotropy for the axially symmetric membranes. The orthotropic model of Reese et al. (2001), to describe the behavior of pneumatic membranes reinforced with fibers, may also be employed for the modeling of anisotropic biological membranes. Further, Kazakevičiūtė-Makovska (2001) explore different nonlinear response functions for transversely isotropic elastic membranes considering the incompressibility and plane stress conditions. Massabò and Gambarotta (2006) investigate the wrinkling of biological membranes although their approach is restricted to isotropic materials. Prot et al. (2007) employ the anisotropic material model proposed by Holzapfel et al. (2000) to develop a transversely isotropic membrane for the analysis of mitral valve. Kroon and Holzapfel (2009) examine elastic properties of anisotropic vascular membranes by using an inverse finite element approach. A fibrous membrane based on the statistical distribution of the activation stretch of the collagen fibers is analyzed by Borri-Brunetto et al. (2009). Abdessalem et al. (2011) also propose a finite element formulation for orthotropic and transversely isotropic incompressible hyperelastic membranes. Planar soft tissues are studied by Flynn et al. (1998), Sun and Sacks (2005), Holzapfel and Ogden (2009), Jacobs et al. (2013) and Fan and Sacks (2014). The growth of thin biological membranes is studied by Rausch and Kuhl (2014). Balzani et al. (2007) and Rausch and Kuhl (2013) investigate the effect of residual stresses in biological membranes. Recently, Roohbakhshan et al. (2016) propose a projection method to extract biological membrane models from the existing 3D material models.

1.2.2 Biological shells

As reviewed in Sec. 1.2.1, most of the developed computational models to study thin soft tissues allow only for membrane stresses, many of which are even limited to planar tissues. In contrast, there are few examples that consider the bending moments and model soft tissues by shell formulations. For instance, Balzani et al. (2008) and Balzani et al. (2010) analyze anisotropic polyconvex energy densities for shells. Tepole et al. (2015) introduce the first isogeometric Kirchhoff–Love shell, particularly formulated for soft tissues, based on numerical integration through the shell thickness. Furthermore, Kiendl et al. (2015b) and Duong et al. (2017) suggest two different isogeometric formulations for the modeling of the rotation-free thin shells with arbitrary nonlinear hyperelastic materials. Both approaches can be used for the modeling of biological shells. Recently, Roohbakhshan and Sauer (2017) present different efficient isogeometric thin shell formulations for soft biological materials, which are explained and used in this work.

1.2.3 Isogeometric shells

As the objective of this dissertation is to investigate membranes and rotation-free thin shells, based on the Kirchhoff–Love hypothesis, here we shortly review the existing literature on the modeling of shells. In particular, the survey is focused on the formulations that use isogeoemtric analysis, which is used here. Among the existing shell theories, the rotation-free Kirchhoff–Love shell theory has this advantage that it only requires displacement degrees of freedom in order to describe the shell behavior. However, its disadvantage is that the shell surface should be described and discretized as a smooth surface with at least C^1-continuity. This a big challenge for the classical Lagrange elements, which require computationnally complex and expensive formulations to impose C^1-continuity on the shared boundaries of elements (see e.g. Oñate and Zárate (2000), Brunet and Sabourin (2006), Stolarski et al. (2013) and Munglani et al. (2015) and references therein). Alternatively, shell formulations derived from Reissner–Mindlin theory, which require only C^0-continuity, can be used (e.g. Simo and Fox, 1989; Simo et al., 1990; Bischoff and Ramm, 1997; Yang et al., 2000; Bischoff et al., 2004 and Wriggers, 2008) although they need additional rotational degrees of freedom. It should be noted that there are some other formulations, like extended rotation-free shells including transverse shear effects (Zárate and Oñate, 2012), rotation-free thin shells with subdivision finite elements (Cirak et al., 2000;

Cirak and Ortiz, 2001; Green and Turkiyyah, 2005 and Cirak and Long, 2010), meshfree Kirchhoff–Love shells (Ivannikov et al., 2014) and discontinuous Galerkin method for Kirchhoff–Love shells (Noels and Radovitzky, 2008 and Becker et al., 2011).

After being introduced by Hughes et al. (2005), Isogeometric analysis (IGA) has become a helpful tool for the computational modeling of shells. Initially, Hughes et al. (2005) modeled thin shells by solid elements based on non-uniform rational B-splines (NURBS) without any shell assumption. Although Hughes et al. (2005) assume no shell theory, the results are satisfying compared to the classical shell theory when one or two quadratic NURBS are used through the thickness. Later, Cottrell et al. (2006) use the formulation of Hughes et al. (2005) for the structural vibration analysis of different problems including plates. Since then, many isogeoemtric formulations are introduced that are based on different shell theories. In the following, we briefly review the existing isogeoemtric formulations, which are successfully used for the analysis of shells, based on the solid-shell, Reissner–Mindlin, blended and in particular Kirchhoff–Love theories.

Solid-shell elements, which form an intermediated class of finite element models between thin shell and conventional 3D solid elements, have the same nodes and degrees of freedom as solid elements but they account for the specific behavior through the thickness of the shell. As the shell becomes thin, finite solid elements suffer from shear, membrane and thickness locking, which are classically treated e.g. by the Assumed Natural Strain (ANS) method (Stanley and Park, 1986). However, the locking effects can be alleviated by using higher order NURBS-based finite elements. For instance, Bouclier et al. (2013a,b) propose a NURBS-based solid-shell element with mixed formulation and B-bar-method. Hosseini et al. (2013) introduce an isogeometric solid-like shell formulation that uses B-spline basis functions to construct the mid-surface of the shell and a linear Lagrange shape function in the thickness direction. Later, in contrast to the standard continuum shell (solid-like shell) formulation of Hosseini et al. (2013), Hosseini et al. (2014) suggest an isogeometric continuum shell element for nonlinear analysis, where through-the-thickness behavior is interpolated using a higher-order B-spline. Caseiro et al. (2014) extended the ANS method, initially proposed for the Lagrangian formulations to reduce locking behaviors, to the NURBS-based solid-shell elements. However, their formulation is restricted to linear elasticity. Bouclier et al. (2015) extend the mixed method of Bouclier et al. (2013a,b) to deal with locking in the context of large rotations and large displacements. Caseiro et al. (2015) extend their earlier work (Caseiro et al., 2014) to nonlinear deformations and elasto-plastic regimes. Recently, Ambati and De Lorenzis (2016) study the fracture in shells with a phase-field modeling approach. Their shell model is based on solid-shell kinematics with small rotations and displacements and is discretized using quadratic NURBS basis functions. In their model, membrane and shear locking is reduced through the ANS approach.

Many isogeoemtric formulations are proposed based on the Reissner–Mindlin shell theory, which allows shells to have out-of-plane shear deformations. For instance, Uhm and Youn (2009) propose a Reissner–Mindlin shell formulation described by T-splines. The first isogeometric Reissner–Mindlin shell formulation is proposed by Benson et al. (2010), which is based on a degenerated solid implemented for NURBS-based finite elements. It is examined for both linear elastic and nonlinear elasto-plastic benchmark examples successfully. Dornisch et al. (2013) introduce an isogeometric Reissner–Mindlin shell with exactly calculated director vectors, which requires six degrees of freedom per each control point. Later, Dornisch and Klinkel (2014) extend the formulation of Dornisch et al. (2013) to multi-patch geometries. They investigate two methods for the interpolation of the current director vector and the other relevant quantities. The variation of the director vector is expressed as a function of the variation of nodal rotations. The formulation of Adam et al. (2015) has an improved numerical integration for locking treatment in isogeometric Reissner–Mindlin shells and plates. A locking-free model for Reissner–Mindlin plates is developed by Beirão Da Veiga et al. (2015), where classical Reissner–Mindlin plate theory is reformulated so that rotational variables are eliminated in favor of transverse shear strains. They discretize the shell surface by both NURBS and triangular (non-uniform rational Powell–Sabin B-splines (NURPS). Dornisch et al. (2015) applz the mortar method for patch coupling to the NURBS-based Reissner–Mindlin shells. Du et al. (2015) use Nitsche's method for isogeometric analysis of Reissner–Mindlin plates with non-conforming multi-patches. Kang and Youn (2015) propose an isogeometric approach for the analysis of topologically complex shell structures with trimmed surfaces. Kiendl et al. (2015a) introduce isogeometric collocation methods for Reissner–Mindlin plate problems using both locking-free primal and mixed formulations. Lei et al. (2015a) use the Serendipity basis to express the fiber rotation in an isogeometric Reissner–Mindlin shell. They also propose a modified reduced quadrature scheme to improve the efficiency. The Reissner–Mindlin shell formulation of Dornisch et al. (2016) is able to handle finite rotations and large deformations. It is more efficient than their earlier works (Dornisch et al., 2013 and Dornisch and Klinkel, 2014) as the continuous rotation of the director vector is modeled by a multiplicative update scheme. Dornisch et al. (2017) investigate different concepts for dual basis functions for B-splines and NURBS and propose approximate dual basis functions for NURBS. Their method is shown to be applicable for the nonlinear Reissner–Mindlin shell formulations. Kang and Youn (2016a,b) extend the formulation of Kang and Youn (2015) for topology optimization. Oesterle et al. (2016) present a rotation-free shear-deformable shell formulation following the Reissner–Mindlin theory. Their formulation exclusively uses displacement degrees of freedom but it is restricted to geometrically linear shells. The total displacement is subdivided into a part representing the membrane and bending deformation and a part representing transverse shear deformation. An isogeoemtric Reissner–Mindlin shell formulation is used by Sobota et al. (2016) for implicit dynamic calculations.

Benson et al. (2013) suggest a shell formulation that blends both Kirchhoff–Love and Reissner–Mindlin theories. Echter et al. (2013) and Echter (2013) propose a hierarchic family of isogeometric shell elements including Kirchhoff–Love (3-parameter), Reissner–Mindlin (5-parameter) and 3D (7-parameter) shell models. However, their formulations are restricted to linear elastic problems.

The first step towards isogeometric analysis of Kirchhoff–Love shells is taken by Kiendl et al. (2009). However, their formulation is limited to linear material model (i.e. St. Venant–Kirchhoff solid) and single-patch NURBS-based meshes. Later, Kiendl et al. (2010) extend the earlier work of Kiendl et al. (2009) to multi-patch meshes. They use the bending strip method to impose the C^1-continuity of the Kirchhoff–Love shell structures comprised of multiple patches. Benson et al. (2011) propose a rotation-free shell where the Kirchhoff–Love assumptions are satisfied only at discrete points. Different choices for defining the shell normal vector are examined. The rotation-free shell formulation of Nguyen-Thanh et al. (2011) is based on the polynomial splines over hierarchical T-meshes (PHT-splines). Their method exploits the flexibility of T-meshes for local refinement. Bazilevs et al. (2012) use a cubic T-spline-based discretization of a rotation-free Kirchhoff–Love shell to study the fluid–structure interaction of wind turbine rotors. Chen et al. (2014) use an explicit time integration scheme to compute the transient response of membrane structures and the Kirchhoff–Love shells to time-domain excitations, where a dynamic relaxation method is employed to obtain steady-state solutions. Zhang et al. (2014) present an isogeometric-meshfree coupled strategy for the static and free vibration analysis of the Kirchhoff plates. Breitenberger et al. (2015) introduce an approach for nonlinear isogeometric B-Rep analysis of the Kirchhoff–Love shell structures. Boundary representation (B-Rep) models consist of trimmed NURBS surfaces and they are usually used in industrial applications, especially for the modeling of free-form geometries. Isogeoemtric analysis is also used for laminated composite shells (see Chap. 5). For instance, Deng et al. (2015) model a composite rotation-free shell formulation equipped with a inter-laminar damage model. Kiendl et al. (2015b) extend the formulation of Kiendl et al. (2009) from linear to nonlinear material models. Their formulation uses numerical integration over the shell thickness and allows for arbitrary nonlinear material models. Further, through-the-thickness cracks in thin shell structures based on Kirchhoff–Love theory is analyzed by the extended isogeometric element formulation of Nguyen-Thanh et al. (2015). Reali and Gomez (2015) employ an isogeometric collocation approach for Euler–Bernoulli beams and Kirchhoff plates as an alternative for isogeometric Galerkin approaches. Kiendl et al. (2016) investigate an approach for the phase-field modeling of fracture in thin structures like plates and shells, where brittle fracture is considered based on the Kirchhoff–Love shell model. Tepole et al. (2015) develop the first isogeoemtric formulation to study thin biological shells. They also use numerical integration through the thickness of shell to derive the stress and bending moment resultants. An efficient model reduction method is proposed by Luo et al. (2016) for the Kirchhoff–Love thin shell buckling analysis, where a simple reduced order model is obtained by using perturbation technique. They embed different strategies for nonlinear buckling analyses into the procedure. Nguyen-Thanh et al. (2016) extend the earlier work of Nguyen-Thanh et al. (2011), which is for the shells modeled by RTH splines, to the cases with large deformations and multiple patches. They couple patches based on Nitsche's method, which allows also coupling of a shell to a solid model. In the formulation of Riffnaller-Schiefer et al. (2016), the Kirchhoff–Love thin shells are discretized based on NURBS compatible subdivision surfaces. Casquero et al. (2017) use arbitrary-degree T-splines for isogeometric analysis of fully nonlinear Kirchhoff–Love shells. In their approach, trimmed NURBS-based surfaces are converted to untrimmed T-spline representations for isogeometric analysis.

1.3 Scope

In the presented work, different constitutive approaches are introduced to model membranes and thin rotation-free shells based on the Kirchhoff–Love hypothesis. In particular for the shells, two approaches are proposed that do not need any numerical integration; therefore, they are computationally more efficient. Further, an approach based on numerical integration through the shell thickness is also presented. The formulation is designed for large deformations and allows for geometrical and material nonlinearities as well as anisotropic behavior, which are of great importance for the modeling of soft tissues. The formulations is also applied to laminated composite shells that can be used for example to model arteries. Furthermore, different isotropic and anisotropic material models, which are commonly used to model soft biological materials, are examined for the proposed constitutive projection approaches. In particular, the formulation is employed for the modeling of the artery and alveolar tissues. Following an isogeometric approach, NURBS-based finite elements are used for the discretization of the shell surface. Several numerical examples are investigated to demonstrate the capabilities of the formulation.

1.4 Outline

The remaining part of this dissertation is organized as follows: Chap. 2 reviews the fundamentals of nonlinear continuum mechanics, which includes the differential geometry of surfaces and bodies in 3D space; the basics of continuum mechanics – namely, the kinematics, strains, stresses and balance laws – and a short introduction to contact mechanics. In Chap. 3, the theories of membranes and thin rotation free shells are summarized. In Chap. 4, different constitutive projection approaches are presented to project the constitutive laws of 3D continua onto the surface of a thin-walled structure, i.e. a rotation-free shell or a membrane. Next, the proposed shell formulations are adopted to model thin composite shells and membranes in Chap. 5. Then, the corresponding membrane and shell formulations are derived for various isotropic and anisotropic constitutive in Chap. 6. The interfacial mechanics, in particular a dynamic surface tension model for the pulmonary surfactants lining the alveolar tissue, is investigated in Chap. 7. Chap. 8 discusses the finite element solution in the framework of isogeometric analysis (IGA). Several numerical experiments are performed in Chap. 9 to demonstrate the capabilities of the presented models, in particular for the simulation of artery and alveolar tissue. Finally, Chap. 10 concludes the dissertation.

Chapter 2

Nonlinear Continuum Mechanics

This chapter presents the fundamentals of nonlinear continuum mechanics to establish the main theoretical framework of this thesis. Sec. 2.1 is devoted to differential geometry of surfaces and bodies in 3D space. This helps to describe geometrically nonlinear deformations of deformable surfaces. This approach allows us to efficiently model thin structures such as membranes and shells, which can be both solid and liquid. Then the basics of continuum mechanics is reviewed in Sec. 2.2, which includes the kinematics of deformation, strains, stresses and balance laws.

2.1 Differential geometry of surfaces and bodies

In this section, first the kinetics of a deformable 2D surface in 3D space is described using differential geometry of surfaces. Then, the description is generalized to deformable 3D solids, which is used in Chap. 4 to describe 2D shells and membranes from the perspective of a 3D continuum. Here, a familiarity with tensor analysis and curvilinear coordinate systems is assumed. Useful introductions with more details on tensor analysis and differential geometry can be found, respectively, in Itskov (2009) and Sokolnikoff (1964), Kreyszig (1991), Doolin and Martin (2013), Willmore (2013) and Nguyen-Schäfer and Schmidt (2014).

2.1.1 Two-dimensional surfaces in 3D space

As discussed by Sauer and Duong (2017), any point $\boldsymbol{x} \in \mathbb{R}^3$ on a surface $\mathcal{S}$ can be described in terms of a convective coordinate system that maps a parametric domain $\mathcal{P}$ with components ξ^α to

$$\boldsymbol{x} = \boldsymbol{x}\left(\xi^{\alpha}\right) \ , \tag{2.1}$$

where $\xi^\alpha \in [-1,1]$ and $\alpha = 1,2$.

Note 2.1. Here, the Greek indices take values in $\{1,2\}$. Repeated indices are implicitly summed over assuming the Einstein summation convention.

At any point of the parameterized surface, a co-variant basis vector, which is tangent to $\mathcal{S}$, is defined as

$$\boldsymbol{a}_\alpha := \boldsymbol{x}_{,\alpha} = \frac{\partial \boldsymbol{x}}{\partial \xi^\alpha} \ . \tag{2.2}$$

Note 2.2. Henceforth, $(\bullet)_{,\alpha} := \dfrac{\partial(\bullet)}{\partial \xi^\alpha}$ denotes partial derivative w.r.t. the convective coordinate ξ^α.

The co-variant basis vectors $\boldsymbol{a}_\alpha$ give

$$a_{\alpha\beta} = \boldsymbol{a}_\alpha \cdot \boldsymbol{a}_\beta \ , \tag{2.3}$$

which are the co-variant components of the *first fundamental form* of surface or as it is called the *metric tensor*. The contra-variant components of the metric tensor are $[a^{\alpha\beta}] = [a_{\alpha\beta}]^{-1}$. The contra-variant basis vector $\boldsymbol{a}^\alpha$, which is the dual vector of $\boldsymbol{a}_\alpha$, is defined as

$$\boldsymbol{a}^\alpha \cdot \boldsymbol{a}_\beta = \delta^\alpha_\beta \ , \tag{2.4}$$

where δ^α_β is the Kronecker delta. Eq. (2.4) simply implies that $\boldsymbol{a}_1$ and $\boldsymbol{a}_2$ are perpendicular to $\boldsymbol{a}^2$ and $\boldsymbol{a}^1$, respectively. From Eqs. (2.3) and (2.4), the dual vectors are related via the metric tensor as

$$\begin{aligned} \boldsymbol{a}^\alpha &= a^{\alpha\beta}\, \boldsymbol{a}_\beta \ , \\ \boldsymbol{a}_\alpha &= a_{\alpha\beta}\, \boldsymbol{a}^\beta \ . \end{aligned} \tag{2.5}$$

Having the surface tangent vectors $\boldsymbol{a}_\alpha$, one can find the surface normal as

$$\boldsymbol{n} = \frac{\boldsymbol{a}_1 \times \boldsymbol{a}_2}{\|\boldsymbol{a}_1 \times \boldsymbol{a}_2\|} \ . \tag{2.6}$$

A surface element on $\mathcal{S}$ is related to a corresponding area element $\mathrm{d}\square := \mathrm{d}\xi^1\,\mathrm{d}\xi^2$ on the parameter domain $\mathcal{P}$ by $\mathrm{d}a = J_a\,\mathrm{d}\square$, where $J_a = \sqrt{\det a_{\alpha\beta}} = \|\boldsymbol{a}_1 \times \boldsymbol{a}_2\|$ is the Jacobian determinant.

The convective bases $\{\boldsymbol{a}_1,\ \boldsymbol{a}_2,\ \boldsymbol{n}\}$ and $\{\boldsymbol{a}^1,\ \boldsymbol{a}^2,\ \boldsymbol{n}\}$ can then be used to decompose any vector or tensor on $\mathcal{S}$ into in-plane and out-of-plane components. For instance, on $\mathcal{S}$, an arbitrary vector $\boldsymbol{v}$ is decomposed as

$$\boldsymbol{v} = v^\alpha\, \boldsymbol{a}_\alpha + v_n\, \boldsymbol{n} = v_\alpha\, \boldsymbol{a}^\alpha + v_n\, \boldsymbol{n} \ , \tag{2.7}$$

where

$$\begin{aligned} v^{\alpha} &:= \boldsymbol{v} \cdot \boldsymbol{a}^{\alpha} \ , \\ v_{\alpha} &:= \boldsymbol{v} \cdot \boldsymbol{a}_{\alpha} \ , \\ v_{n} &:= \boldsymbol{v} \cdot \boldsymbol{n} \ . \end{aligned} \tag{2.8}$$

The metric tensors $a_{\alpha\beta}$ and $a^{\alpha\beta}$ can be used to raise and lower the indices of the components of a vector or a tensor. For instance, the contra- and co-variant components of the vector $\boldsymbol{v}$ are interrelated as

$$v^{\alpha} = a^{\alpha\beta}\, v_{\beta} \ , \quad v_{\alpha} = a_{\alpha\beta}\, v^{\beta} \ . \tag{2.9}$$

Considering a second order tensor $\boldsymbol{t}$ on $\mathcal{S}$ as

$$\boldsymbol{t} = t^{\alpha\beta}\, \boldsymbol{a}_{\alpha} \otimes \boldsymbol{a}_{\beta} = t_{\alpha\beta}\, \boldsymbol{a}^{\alpha} \otimes \boldsymbol{a}^{\beta} = t^{\beta}_{\alpha}\, \boldsymbol{a}^{\alpha} \otimes \boldsymbol{a}_{\beta} \tag{2.10}$$

where

$$\begin{aligned} t^{\alpha\beta} &= \boldsymbol{a}^{\alpha} \cdot (\boldsymbol{t}\, \boldsymbol{a}^{\beta}) \ , \\ t_{\alpha\beta} &= \boldsymbol{a}_{\alpha} \cdot (\boldsymbol{t}\, \boldsymbol{a}_{\beta}) \ , \\ t^{\alpha}_{\beta} &= \boldsymbol{a}^{\alpha} \cdot (\boldsymbol{t}\, \boldsymbol{a}_{\beta}) \ , \end{aligned} \tag{2.11}$$

the indices of components are lowered as

$$\begin{aligned} t^{\alpha}_{\beta} &= t^{\alpha\gamma}\, a_{\beta\gamma} \ , \\ t_{\alpha\beta} &= t^{\alpha}_{\gamma}\, a_{\beta\gamma} = t^{\gamma\delta}\, a_{\alpha\gamma}\, a_{\beta\delta} \ . \end{aligned} \tag{2.12}$$

Remark 2.3. From Eqs. (2.7) and (2.8),

$$\begin{aligned} \boldsymbol{v} &= v^{\alpha}\, \boldsymbol{a}_{\alpha} + v_{n}\, \boldsymbol{n} \\ &= (\boldsymbol{v} \cdot \boldsymbol{a}^{\alpha})\, \boldsymbol{a}_{\alpha} + (\boldsymbol{v} \cdot \boldsymbol{n})\, \boldsymbol{n} \\ &= a^{\alpha\beta}\, (\boldsymbol{v} \cdot \boldsymbol{a}_{\beta})\, \boldsymbol{a}_{\alpha} + (\boldsymbol{n} \otimes \boldsymbol{n})\, \boldsymbol{v} \\ &= \big(a^{\alpha\beta}\, \boldsymbol{a}_{\alpha} \otimes \boldsymbol{a}_{\beta} + \boldsymbol{n} \otimes \boldsymbol{n}\big)\, \boldsymbol{v} \\ &= \mathbf{1}\, \boldsymbol{v} \ . \end{aligned} \tag{2.13}$$

Thus, the full identity tensor $\mathbf{1} \in \mathbb{R}^3$ can be decomposed as

$$\mathbf{1} = \boldsymbol{i} + \boldsymbol{n} \otimes \boldsymbol{n} \tag{2.14}$$

on $\mathcal{S}$, where

$$\boldsymbol{i} = a^{\alpha\beta}\, \boldsymbol{a}_{\alpha} \otimes \boldsymbol{a}_{\beta} = a_{\alpha\beta}\, \boldsymbol{a}^{\alpha} \otimes \boldsymbol{a}^{\beta} = \delta^{\alpha}_{\beta}\, \boldsymbol{a}_{\alpha} \otimes \boldsymbol{a}^{\beta} = \boldsymbol{a}_{\alpha} \otimes \boldsymbol{a}^{\alpha} = \boldsymbol{a}^{\alpha} \otimes \boldsymbol{a}_{\alpha} \tag{2.15}$$

is the surface identity tensor on $\mathcal{S}$.

The other important tensor-like objects associated to surface $\mathcal{S}$ are *Christoffel symbols* of the first and second kind given, respectively, by

$$\begin{aligned} \Gamma_{\gamma\alpha\beta} &= \boldsymbol{a}_{\gamma} \cdot \boldsymbol{a}_{\alpha,\beta} \ , \\ \Gamma^{\gamma}_{\alpha\beta} &= \boldsymbol{a}^{\gamma} \cdot \boldsymbol{a}_{\alpha,\beta} \ . \end{aligned} \tag{2.16}$$

The Christoffel symbols of the first and second kind are related as

$$\Gamma_{\gamma\alpha\beta} = a_{\gamma\mu}\, \Gamma^{\mu}_{\alpha\beta} \ . \tag{2.17}$$

Following Note 2.2, a comma denotes the parametric derivative $\boldsymbol{a}_{\alpha,\beta} = \partial \boldsymbol{a}_{\alpha} / \partial \xi^{\beta}$. With the definition of the Christoffel symbol (2.16), the so-called co-variant derivative is defined as

$$\boldsymbol{a}_{\alpha;\beta} := \boldsymbol{a}_{\alpha,\beta} - \Gamma^{\gamma}_{\alpha\beta}\, \boldsymbol{a}_{\gamma} = (\boldsymbol{n} \otimes \boldsymbol{n})\, \boldsymbol{a}_{\alpha,\beta} \ . \tag{2.18}$$

The covariant derivatives of the basis vectors $\boldsymbol{a}_{\beta}$ and the surface normal $\boldsymbol{n}$ are given by the Gauss–Weingarten equations

$$\begin{aligned} \boldsymbol{a}_{\alpha,\beta} &= b_{\alpha\beta}\, \boldsymbol{n} \ , \\ \boldsymbol{n}_{,\alpha} &= -b^{\epsilon}_{\alpha}\, \boldsymbol{a}_{\epsilon} \ , \end{aligned} \tag{2.19}$$

where $b_{\alpha\beta}$ and b^{α}_{β} are the co-variant and mixed components of the *curvature tensor*, or as it is called the *second fundamental form* of the surface manifold,

$$\boldsymbol{b} = b_{\alpha\beta}\, \boldsymbol{a}^{\alpha} \otimes \boldsymbol{a}^{\beta} = b^{\alpha\beta}\, \boldsymbol{a}_{\alpha} \otimes \boldsymbol{a}_{\beta} = b^{\alpha}_{\beta}\, \boldsymbol{a}_{\alpha} \otimes \boldsymbol{a}^{\beta} \ . \tag{2.20}$$

Considering Eqs. (2.18) and (2.19.1), the co-variant components of $\boldsymbol{b}$ are

$$b_{\alpha\beta} := \boldsymbol{n} \cdot \boldsymbol{a}_{\alpha,\beta} = \boldsymbol{n} \cdot \boldsymbol{a}_{\alpha;\beta} \tag{2.21}$$

or alternatively, from Eqs. (2.12) and (2.19.2),

$$b_{\alpha\beta} := -\boldsymbol{n}_{,\beta} \cdot \boldsymbol{a}_{\alpha} \ . \tag{2.22}$$

The contra-variant and mixed components of $\boldsymbol{b}$ can be obtained similar to Eq. (2.12) as $b^{\alpha}_{\beta} = b_{\alpha\gamma}\, a^{\beta\gamma}$ and $b^{\alpha\beta} = a^{\alpha\gamma}\, b_{\gamma\delta}\, a^{\beta\delta}$.

The mean and Gaussian curvature of $\mathcal{S}$ can be computed from the first and second invariants of the curvature tensor $\boldsymbol{b}$, respectively, as

$$H := \frac{1}{2} \mathrm{tr}\, \boldsymbol{b} = \frac{1}{2}\, b^{\alpha}_{\alpha} = \frac{1}{2}\, a^{\alpha\beta}\, b_{\alpha\beta} \tag{2.23}$$

and

$$K := \det \boldsymbol{b} = \frac{b}{a} \ , \tag{2.24}$$

where

$$a := \det[a_{\alpha\beta}] \ , \quad b := \det[b_{\alpha\beta}] \tag{2.25}$$

are determinants defined on the surface.

The principle curvatures κ_1 and κ_2 are the eigenvalues of the curvature tensor, which can be written based on the Gaussian curvature $K = \kappa_1\,\kappa_2$ and the mean curvature $H = \frac{1}{2}(\kappa_1 + \kappa_2)$ as

$$\kappa_{1/2} = H \pm \sqrt{H^2 - K} \ . \tag{2.26}$$

The variation of the introduced surface objects can be found in Sauer and Duong (2017), a summary of which is appended as Appendix A.1.

2.1.2 Three-dimensional bodies

Similar to a surface, a deformable 3D body can be described in terms of a convective coordinate system, which is defined by a mapping from a 3D parametric domain with components $\xi^i \in [-1, 1]$ as

$$\tilde{\boldsymbol{x}} \ = \tilde{\boldsymbol{x}}\,(\xi^i) \ , \quad i = 1, 2, 3 \ . \tag{2.27}$$

Note 2.4. Henceforth, a tilde is used to identify quantities corresponding to 3D continua. This notation is useful to distinguish the 2D and 3D kinematics of shells discussed in Sec. 4.1.1.

Note 2.5. The italic roman indices take values in $\{1, 2, 3\}$ if they refer to the basis vectors or the components of a general 3D vector or a 3D second-order tensor. If so, the Einstein summation convention is implied on the repeated indices.

Likewise to Sec. 2.1.1, it is assumed that $\tilde{\boldsymbol{x}}$ is sufficiently differentiable; therefore, we can define convective bases, which are tangent to the curvilinear coordinates, as

$$\boldsymbol{g}_i := \tilde{\boldsymbol{x}}_{,i} = \frac{\partial \tilde{\boldsymbol{x}}}{\partial \xi^i} \ , \quad i = 1, 2, 3 \ . \tag{2.28}$$

Note 2.6. Likewise to a surface, $(\bullet)_{,i} := \dfrac{\partial(\bullet)}{\partial \xi^i}$ denotes partial derivative w.r.t. the convective coordinate ξ^i.

The basis dual to $\boldsymbol{g}_i$ is given by

$$\boldsymbol{g}^i \cdot \boldsymbol{g}_j = \delta^i_j \ , \quad i, j = 1, 2, 3 \ , \tag{2.29}$$

which implies that $\boldsymbol{g}_1$ is perpendicular to $\boldsymbol{g}^2$ and $\boldsymbol{g}^3$ and so forth. The contra- and co-variant components of 3D metric tensor, also called metric coefficients, are

$$\begin{aligned} g^{ij} &= \boldsymbol{g}^i \cdot \boldsymbol{g}^j \ , \\ g_{ij} &= \boldsymbol{g}_i \cdot \boldsymbol{g}_j \ , \end{aligned} \tag{2.30}$$

which are related through $[g^{ij}] = [g_{ij}]^{-1}$. The contra- and co-variant tangent vectors are related via metric coefficients as

$$\begin{aligned} \boldsymbol{g}^i &= g^{ij}\, \boldsymbol{g}_j \ , \\ \boldsymbol{g}_i &= g_{ij}\, \boldsymbol{g}^j \ . \end{aligned} \tag{2.31}$$

They can also be used to represent vectors and tensors. Considering a general vector $\boldsymbol{v}$, we have

$$\boldsymbol{v} = v^i\, \boldsymbol{g}_i \ , \quad \boldsymbol{v} = v_i\, \boldsymbol{g}^i \ , \tag{2.32}$$

with contra- and co-variant components

$$v^i = \boldsymbol{v} \cdot \boldsymbol{g}^i \ , \quad v_i = \boldsymbol{v} \cdot \boldsymbol{g}_i \ . \tag{2.33}$$

A general 3D tensor $\tilde{\boldsymbol{t}}$ can be expressed as

$$\tilde{\boldsymbol{t}} = \tilde{t}^{ij}\, \boldsymbol{g}_i \otimes \boldsymbol{g}_j = \tilde{t}_{ij}\, \boldsymbol{g}^i \otimes \boldsymbol{g}^j = \tilde{t}^j_i\, \boldsymbol{g}^i \otimes \boldsymbol{g}_j \ , \tag{2.34}$$

where

$$\begin{aligned} \tilde{t}^{ij} &= \boldsymbol{g}^i \cdot (\tilde{\boldsymbol{t}}\, \boldsymbol{g}^j) \ , \\ \tilde{t}_{ij} &= \boldsymbol{g}_i \cdot (\tilde{\boldsymbol{t}}\, \boldsymbol{g}_j) \ , \\ \tilde{t}^i_j &= \boldsymbol{g}^i \cdot (\tilde{\boldsymbol{t}}\, \boldsymbol{g}_j) \ . \end{aligned} \tag{2.35}$$

The metric tensor may be used to to lower and raise the indices on vectors and tensors. For instance,

$$v^i = g^{ij}\, v_j \ , \quad v_i = g_{ij}\, v^j \ . \tag{2.36}$$

Remark 2.7. From Eqs. (2.32) and (2.33),

$$\begin{aligned} \boldsymbol{v} &= v^i\, \boldsymbol{g}_i \\ &= (\boldsymbol{v} \cdot \boldsymbol{g}^i)\, \boldsymbol{g}_i \\ &= \boldsymbol{g}^{ij} \left(\boldsymbol{v} \cdot \boldsymbol{g}_j\right) \boldsymbol{g}_i \\ &= \boldsymbol{g}^{ij} \left(\boldsymbol{g}_j \otimes \boldsymbol{g}_i\right) \boldsymbol{v} \\ &= \boldsymbol{1}\, \boldsymbol{v} \ . \end{aligned} \tag{2.37}$$

Thus, one can easily show that the components of the full identity tensor $\boldsymbol{1} \in \mathbb{R}^3$ are the metric coefficients, i.e.

$$\boldsymbol{1} = g^{ij}\, \boldsymbol{g}_i \otimes \boldsymbol{g}_j = g_{ij}\, \boldsymbol{g}^i \otimes \boldsymbol{g}^j = \delta^i_j\, \boldsymbol{g}_i \otimes \boldsymbol{g}^j = \boldsymbol{g}_i \otimes \boldsymbol{g}^i = \boldsymbol{g}^i \otimes \boldsymbol{g}_i \ , \tag{2.38}$$

Remark 2.8. The 3D convective curvilinear coordinate system, briefly reviewed in Sec. 2.1.2, can be reduced to the surface description of Sec. 2.1.1 as a special case. This, corresponds to a dimensional reduction or a projection procedure, which is the core idea of the projected membrane and shell formulations presented in Chap. 4.

2.2 Basics of continuum mechanics

This section discusses the basics of continuum mechanics in curvilinear coordinates. More details can be found e.g. in Bonet and Wood (1997), Holzapfel (2000) and Wriggers (2008). In continuum mechanics, a deformable body $\mathcal{B}$ can be described as a set of material points, i.e. $\mathcal{B} = \{P\}$. The location of any material point P is defined by a (Cartesian) coordinate system. The deformable body can occupy different configurations at any time $t \in \mathbb{R}^+$. In finite strain theory, the continuum can undergo large deformations. Thus, it is crucial to distinguish between the reference (or initial) configuration at $t = 0$, which is denoted by $\mathcal{B}_0$, and the current (or deformed) configuration at $t > 0$ denoted by $\mathcal{B}$. Accordingly, the very same material point P has the positions $\tilde{\boldsymbol{x}}$ and $\tilde{\boldsymbol{X}}$ in the current and reference configurations, respectively.

Note 2.9. Henceforth, small letters are used to distinguish the quantities in the current configuration and the same quantities in the reference configuration are denoted by capital letters.

Similar to a body, the surface reference and current configurations are denoted by $\mathcal{S}_0$ and $\mathcal{S}$, respectively. Correspondingly, surface points on $\mathcal{S}_0$ and $\mathcal{S}$ are distinguished by $\boldsymbol{x}$ and $\boldsymbol{X}$, respectively.

2.2.1 Deformation

A deformation is defined by the mapping $\tilde{\boldsymbol{\psi}} : \mathcal{B}_0 \mapsto \mathcal{B}$ from the reference to the current configuration of a deformable 3D body as

$$\tilde{\boldsymbol{x}} = \tilde{\boldsymbol{\psi}}(\tilde{\boldsymbol{X}}) \tag{2.39}$$

or by the mapping $\boldsymbol{\psi} : \mathcal{S}_0 \mapsto \mathcal{S}$ from the reference to the current configuration of a deformable 2D surface as

$$\boldsymbol{x} = \boldsymbol{\psi}(\boldsymbol{X}) \ . \tag{2.40}$$

The deformation gradients corresponding to the mappings (2.39) and (2.40) are, respectively

$$\tilde{\boldsymbol{F}} := \nabla_{\tilde{\boldsymbol{X}}} \tilde{\boldsymbol{x}} = \frac{\partial \tilde{\boldsymbol{x}}}{\partial \tilde{\boldsymbol{X}}} \tag{2.41}$$

and

$$\boldsymbol{F} := \nabla_{\boldsymbol{X}} \boldsymbol{x} = \frac{\partial \boldsymbol{x}}{\partial \boldsymbol{X}} \ . \tag{2.42}$$

For line elements on a 3D body, we have

$$\mathrm{d}\tilde{\boldsymbol{X}} = \tilde{\boldsymbol{X}}_{,i}\,\mathrm{d}\xi^i = \boldsymbol{G}_i\,\mathrm{d}\xi^i \ , \quad \mathrm{d}\tilde{\boldsymbol{x}} = \tilde{\boldsymbol{x}}_{,i}\,\mathrm{d}\xi^i = \boldsymbol{g}_i\,\mathrm{d}\xi^i \ , \quad (i = 1, 2, 3) \tag{2.43}$$

and for line elements on a 2D surface

$$\mathrm{d}\boldsymbol{X} = \boldsymbol{X}_{,\alpha}\,\mathrm{d}\xi^\alpha = \boldsymbol{A}_\alpha\,\mathrm{d}\xi^\alpha \ , \quad \mathrm{d}\boldsymbol{x} = \boldsymbol{x}_{,\alpha}\,\mathrm{d}\xi^\alpha = \boldsymbol{a}_\alpha\,\mathrm{d}\xi^\alpha \ , \quad (\alpha = 1, 2) \ , \tag{2.44}$$

which give

$$\mathrm{d}\tilde{\boldsymbol{x}} = \left(\boldsymbol{g}_i \otimes \boldsymbol{G}^i\right) \mathrm{d}\tilde{\boldsymbol{X}} \ , \quad (i = 1, 2, 3) \tag{2.45}$$

and

$$\mathrm{d}\boldsymbol{x} = \left(\boldsymbol{a}_\alpha \otimes \boldsymbol{A}^\alpha\right) \mathrm{d}\boldsymbol{X} \ , \quad (\alpha = 1, 2) \ . \tag{2.46}$$

From Eqs. (2.41) and (2.45), the 3D deformation gradient is then

$$\tilde{\boldsymbol{F}} = \boldsymbol{g}_i \otimes \boldsymbol{G}^i \ , \quad (i = 1, 2, 3) \ , \tag{2.47}$$

and from Eqs. (2.42) and (2.46),

$$\boldsymbol{F} = \boldsymbol{a}_\alpha \otimes \boldsymbol{A}^\alpha \ , \quad (\alpha = 1, 2) \ , \tag{2.48}$$

is the surface deformation gradient. As $\tilde{\boldsymbol{\psi}}\big(\tilde{\boldsymbol{X}}\big)$ and $\boldsymbol{\psi}\big(\boldsymbol{X}\big)$ are assumed to be continuous, deformation gradient has the inverse. The inverse and transpose of deformation gradient tensor are

$$\begin{aligned} \tilde{\boldsymbol{F}}^{-1} &= \boldsymbol{G}_i \otimes \boldsymbol{g}^i \ , & \tilde{\boldsymbol{F}}^{\mathrm{T}} &= \boldsymbol{G}^i \otimes \boldsymbol{g}_i \ , & \tilde{\boldsymbol{F}}^{-\mathrm{T}} &= \boldsymbol{g}^i \otimes \boldsymbol{G}_i \ , \\ \boldsymbol{F}^{-1} &= \boldsymbol{A}_i \otimes \boldsymbol{a}^i \ , & \boldsymbol{F}^{\mathrm{T}} &= \boldsymbol{A}^i \otimes \boldsymbol{a}_i \ , & \boldsymbol{F}^{-\mathrm{T}} &= \boldsymbol{a}^i \otimes \boldsymbol{A}_i \ . \end{aligned} \tag{2.49}$$

Considering that $\boldsymbol{g}_i = \bar{g}_{ij}\,\boldsymbol{G}^j$ and $\boldsymbol{a}_\alpha = \bar{a}_{\alpha\beta}\,\boldsymbol{A}^\beta$, where

$$\begin{aligned} \bar{g}_{ij} &:= \boldsymbol{g}_i \cdot \boldsymbol{G}_j \ , & &(i, j = 1, 2, 3), \\ \bar{a}_{\alpha\beta} &:= \boldsymbol{a}_\alpha \cdot \boldsymbol{A}_\beta \ , & &(\alpha, \beta = 1, 2) \ , \end{aligned} \tag{2.50}$$

the deformation gradient tensors can be represented as

$$\tilde{\boldsymbol{F}} = \bar{g}_{ij}\,\boldsymbol{G}^j \otimes \boldsymbol{G}^i \ , \qquad (i, j = 1, 2, 3) \ , \tag{2.51}$$

and

$$\boldsymbol{F} = \bar{a}_{\alpha\beta}\,\boldsymbol{A}^\beta \otimes \boldsymbol{A}^\alpha \ , \qquad (\alpha, \beta = 1, 2) \ . \tag{2.52}$$

The Jacobian determinants of the deformation, or as it is simply called Jacobians, are[1]

$$\begin{aligned} \tilde{J} &:= \det \tilde{\boldsymbol{F}} \ , \\ J &:= \det \boldsymbol{F} \ . \end{aligned} \tag{2.53}$$

For a 3D body, $\tilde{J}$ measures how the volume of an infinitesimal 3D element has changed with the deformation, i.e.

$$\mathrm{d}v = \tilde{J}\,\mathrm{d}V \tag{2.54}$$

and, for a 2D surface, J measures the surface change, i.e.

$$\mathrm{d}a = J\,\mathrm{d}A \ , \tag{2.55}$$

where

$$J := \det \boldsymbol{F} = \frac{J_a}{J_A} \ . \tag{2.56}$$

Similar to J_a, described in Sec. 2.1.1, $\mathrm{d}A = J_A\,\mathrm{d}\square$, where $J_A = \sqrt{\det A_{\alpha\beta}} = \|\boldsymbol{A}_1 \times \boldsymbol{A}_2\|$ is the Jacobian determinant on the reference surface.

Based on physical grounds, volumes and areas cannot be negative. Besides, as $\tilde{\boldsymbol{F}}$ and $\boldsymbol{F}$ are invertible, they should be nonsingular. Therefore, $\tilde{J},\ J > 0$.

Remark 2.10. In continuum mechanics, push forward and pull back operations are used to map vectors and tensors from the reference to the current configurations and vice versa, respectively. For the convective bases, we have

$$\begin{aligned} \boldsymbol{g}_i &= \tilde{\boldsymbol{F}}\,\boldsymbol{G}_i \ , \quad \boldsymbol{g}^i = \tilde{\boldsymbol{F}}^{-\mathrm{T}}\,\boldsymbol{G}^i \ , \quad \boldsymbol{G}_i = \tilde{\boldsymbol{F}}^{-1}\,\boldsymbol{g}_i \ , \quad \boldsymbol{G}^i = \tilde{\boldsymbol{F}}^{\mathrm{T}}\,\boldsymbol{g}^i \ , \\ \boldsymbol{a}_\alpha &= \boldsymbol{F}\,\boldsymbol{A}_\alpha \ , \quad \boldsymbol{a}^\alpha = \boldsymbol{F}^{-\mathrm{T}}\,\boldsymbol{A}^\alpha \ , \quad \boldsymbol{A}_\alpha = \boldsymbol{F}^{-1}\,\boldsymbol{a}_\alpha \ , \quad \boldsymbol{A}^\alpha = \boldsymbol{F}^{\mathrm{T}}\,\boldsymbol{a}^\alpha \ . \end{aligned} \tag{2.57}$$

Similar operators will be defined for strain and stress tensors in the next sections.

2.2.2 Strain measures

The deformation gradient does not capture rigid-body displacements of surfaces and bodies in space as $\nabla_{\boldsymbol{X}}(\boldsymbol{x} + \boldsymbol{c}) = \nabla_{\boldsymbol{X}}\boldsymbol{x}$ and $\nabla_{\tilde{\boldsymbol{X}}}(\tilde{\boldsymbol{x}} + \boldsymbol{c}) = \nabla_{\tilde{\boldsymbol{X}}}\tilde{\boldsymbol{x}}$, where $\boldsymbol{c}$ is the vector that describes the rigid-body displacement. Thus, for a rigid-body translation, $\tilde{\boldsymbol{F}} = \boldsymbol{1}$ and $\boldsymbol{F} = \boldsymbol{I}$ as there is no motion. Here,

$$\begin{aligned} \boldsymbol{1} &= G^{ij}\,\boldsymbol{G}_i \otimes \boldsymbol{G}_j = G_{ij}\,\boldsymbol{G}^i \otimes \boldsymbol{G}^j \\ &= \delta^i_j\,\boldsymbol{G}_i \otimes \boldsymbol{G}^j = \boldsymbol{G}_i \otimes \boldsymbol{G}^i = \boldsymbol{G}^i \otimes \boldsymbol{G}_i \end{aligned} \ , \qquad (i, j = 1, 2, 3) \ , \tag{2.58}$$

---

[1] It should be noted that $\det \boldsymbol{F}$ is strictly defined in the tangent space as it would be zero otherwise.

is the usual identity tensor on $\mathcal{B}_0$ and

$$\begin{aligned} \boldsymbol{I} &= A^{\alpha\beta}\,\boldsymbol{A}_\alpha \otimes \boldsymbol{A}_\beta = A_{\alpha\beta}\,\boldsymbol{A}^\alpha \otimes \boldsymbol{A}^\beta \\ &= \delta^\alpha_\beta\,\boldsymbol{A}_\alpha \otimes \boldsymbol{A}^\beta = \boldsymbol{A}_\alpha \otimes \boldsymbol{A}^\alpha = \boldsymbol{A}^\alpha \otimes \boldsymbol{A}_\alpha \end{aligned} \quad , \qquad (\alpha,\beta = 1,2) \; , \tag{2.59}$$

is the surface identity tensor on $\mathcal{S}_0$, which can define the full identity tensor $\mathbf{1} \in \mathbb{R}^3$ as

$$\mathbf{1} = \boldsymbol{I} + \boldsymbol{N} \otimes \boldsymbol{N} \; . \tag{2.60}$$

To overcome the mentioned deficiency of the deformation gradient tensor, strain measures, which give more information about the deformation, are usually used in continuum mechanics. Specifically, the left and right Cauchy–Green strain tensors not only measure the changes in the lengths of line elements but also the variation of angles between them. By definition, the right Cauchy–Green strain tensors are

$$\tilde{\boldsymbol{C}} := \tilde{\boldsymbol{F}}^{\mathrm{T}}\,\tilde{\boldsymbol{F}} = g_{ij}\,\boldsymbol{G}^i \otimes \boldsymbol{G}^j \; , \qquad (i,j = 1,2,3) \; , \tag{2.61}$$

and

$$\boldsymbol{C} := \boldsymbol{F}^{\mathrm{T}}\,\boldsymbol{F} = a_{\alpha\beta}\,\boldsymbol{A}^\alpha \otimes \boldsymbol{A}^\beta \; , \qquad (\alpha,\beta = 1,2) \; , \tag{2.62}$$

on $\mathcal{B}_0$ and $\mathcal{S}_0$, respectively. The left Cauchy–Green strain tensors are defined on $\mathcal{B}$ and $\mathcal{S}$, respectively, as

$$\tilde{\boldsymbol{b}} := \tilde{\boldsymbol{F}}\,\tilde{\boldsymbol{F}}^{\mathrm{T}} = G^{ij}\,\boldsymbol{g}_i \otimes \boldsymbol{g}_j \; , \qquad (i,j = 1,2,3) \; , \tag{2.63}$$

and[2]

$$\boldsymbol{b} := \boldsymbol{F}\,\boldsymbol{F}^{\mathrm{T}} = A^{\alpha\beta}\,\boldsymbol{a}_\alpha \otimes \boldsymbol{a}_\beta \; , \qquad (\alpha,\beta = 1,2) \; . \tag{2.64}$$

To describe large deformations, it is more convenient to use the Green–Lagrange strain tensor, which measures the difference between $\tilde{\boldsymbol{C}}$ and $\mathbf{1}$ or between $\boldsymbol{C}$ and $\boldsymbol{I}$. Therefore, it can distinguish rigid-body displacements. On $\mathcal{B}_0$,

$$\tilde{\boldsymbol{E}} := \frac{1}{2}\big(\tilde{\boldsymbol{C}} - \mathbf{1}\big) = E_{ij}\,\boldsymbol{G}^i \otimes \boldsymbol{G}^j \; , \qquad (i,j = 1,2,3) \; , \tag{2.65}$$

and on $\mathcal{S}_0$,

$$\boldsymbol{E} := \frac{1}{2}\big(\boldsymbol{C} - \boldsymbol{I}\big) = E_{\alpha\beta}\,\boldsymbol{A}^\alpha \otimes \boldsymbol{A}^\beta \; , \qquad (\alpha,\beta = 1,2) \; , \tag{2.66}$$

where

$$\tilde{E}_{ij} = \frac{1}{2}\big(g_{ij} - G_{ij}\big) \; , \qquad (i,j = 1,2,3) \; , \tag{2.67}$$

and

$$E_{\alpha\beta} = \frac{1}{2}\big(a_{\alpha\beta} - A_{\alpha\beta}\big) \; , \qquad (\alpha,\beta = 1,2) \; . \tag{2.68}$$

---

[2] The left Cauchy–Green strain tensor of the surface should not be confused with the curvature tensor of the surface defined by Eq. (2.20).

Furthermore, for the Kirchhoff–Love shells, discussed in Chap. 3, it is useful to introduce the *bending strain* as

$$\boldsymbol{K} := K_{\alpha\beta}\, \boldsymbol{A}^{\alpha} \otimes \boldsymbol{A}^{\beta} \ , \tag{2.69}$$

where

$$K_{\alpha\beta} = b_{\alpha\beta} - B_{\alpha\beta} \tag{2.70}$$

measures the changes of curvature.

2.2.3 Displacements

In solid mechanics, it is convenient to describe the motion and deformation in terms of the displacement. Here, we are interested in the Lagrangian (or material) description of displacement, i.e.

$$\tilde{\boldsymbol{u}} = \tilde{\boldsymbol{u}}\big(\tilde{\boldsymbol{X}}, t\big) = \tilde{\boldsymbol{\psi}}\big(\tilde{\boldsymbol{X}}, t\big) - \tilde{\boldsymbol{X}} = \tilde{\boldsymbol{x}} - \tilde{\boldsymbol{X}} \tag{2.71}$$

and

$$\boldsymbol{u} = \boldsymbol{u}\big(\boldsymbol{X}, t\big) = \boldsymbol{\psi}\big(\boldsymbol{X}, t\big) - \boldsymbol{X} = \boldsymbol{x} - \boldsymbol{X} \ . \tag{2.72}$$

Remark 2.11. The Eulerian (or spatial) description of displacement, i.e.

$$\tilde{\boldsymbol{u}} = \tilde{\boldsymbol{u}}\big(\tilde{\boldsymbol{x}}, t\big) = \tilde{\boldsymbol{x}} - \tilde{\boldsymbol{\psi}}^{-1}\big(\tilde{\boldsymbol{x}}, t\big) = \tilde{\boldsymbol{x}} - \tilde{\boldsymbol{X}} \tag{2.73}$$

and

$$\boldsymbol{u} = \boldsymbol{u}\big(\boldsymbol{x}, t\big) = \boldsymbol{x} - \boldsymbol{\psi}^{-1}\big(\boldsymbol{x}, t\big) = \boldsymbol{x} - \boldsymbol{X} \tag{2.74}$$

results also in the same displacement values but with different independent variables.

From Eqs. (2.71) and (2.72),

$$\begin{aligned} \nabla_{\tilde{\boldsymbol{X}}} \tilde{\boldsymbol{u}} &= \tilde{\boldsymbol{F}} - \mathbf{1} \ , \\ \nabla_{\boldsymbol{X}} \boldsymbol{u} &= \boldsymbol{F} - \boldsymbol{I} \ . \end{aligned} \tag{2.75}$$

Plugging Eq. (2.75) into Eqs. (2.65) and (2.66), the Green–Lagrange strain tensor can be written in terms of the displacement gradients as

$$\begin{aligned} \tilde{\boldsymbol{E}} &= \frac{1}{2}\Big[\nabla_{\tilde{\boldsymbol{X}}} \tilde{\boldsymbol{u}} + \big(\nabla_{\tilde{\boldsymbol{X}}} \tilde{\boldsymbol{u}}\big)^{\mathrm{T}} + \big(\nabla_{\tilde{\boldsymbol{X}}} \tilde{\boldsymbol{u}}\big)^{\mathrm{T}} \nabla_{\tilde{\boldsymbol{X}}} \tilde{\boldsymbol{u}}\Big] \ , \\ \boldsymbol{E} &= \frac{1}{2}\Big[\nabla_{\boldsymbol{X}} \boldsymbol{u} + \big(\nabla_{\boldsymbol{X}} \boldsymbol{u}\big)^{\mathrm{T}} + \big(\nabla_{\boldsymbol{X}} \boldsymbol{u}\big)^{\mathrm{T}} \nabla_{\boldsymbol{X}} \boldsymbol{u}\Big] \ . \end{aligned} \tag{2.76}$$

Remark 2.12. In infinitesimal strain theory, where the strains and displacement gradients are small, the quadratic rear terms in Eq. (2.76) are neglected. Considering only the linear terms, the geometrically linearized Green–Lagrange strain tensor is

$$\begin{aligned} \tilde{\boldsymbol{E}}_{\mathrm{lin}} &= \frac{1}{2}\left[\nabla_{\tilde{\boldsymbol{X}}}\tilde{\boldsymbol{u}} + \left(\nabla_{\tilde{\boldsymbol{X}}}\tilde{\boldsymbol{u}}\right)^{\mathrm{T}}\right] = \frac{1}{2}\left(\tilde{\boldsymbol{F}} + \tilde{\boldsymbol{F}}^{\mathrm{T}}\right) - \boldsymbol{1} = \tilde{E}^{\mathrm{lin}}_{ij}\,\boldsymbol{G}^i \otimes \boldsymbol{G}^j \ , \\ \boldsymbol{E}_{\mathrm{lin}} &= \frac{1}{2}\left[\nabla_{\boldsymbol{X}}\boldsymbol{u} + \left(\nabla_{\boldsymbol{X}}\boldsymbol{u}\right)^{\mathrm{T}}\right] = \frac{1}{2}\left(\boldsymbol{F} + \boldsymbol{F}^{\mathrm{T}}\right) - \boldsymbol{I} = E^{\mathrm{lin}}_{\alpha\beta}\,\boldsymbol{A}^\alpha \otimes \boldsymbol{A}^\beta \ , \end{aligned} \tag{2.77}$$

where

$$\begin{aligned} \tilde{E}^{\mathrm{lin}}_{ij} &= \frac{1}{2}\left(\bar{g}_{ij} + \bar{g}_{ji}\right) - G_{ij} \ , \qquad (i,j = 1,2,3) \ , \\ E^{\mathrm{lin}}_{\alpha\beta} &= \frac{1}{2}\left(\bar{a}_{\alpha\beta} + \bar{a}_{\beta\alpha}\right) - A_{\alpha\beta} \ , \quad (\alpha,\beta = 1,2) \ . \end{aligned} \tag{2.78}$$

2.2.4 Stress measures

In continuum mechanics, there are different measures of the internal forces of a continuous material. Some can be physically interpreted and measured and some are defined conceptually and do not correspond to a physical quantity. Considering an imaginary surface cut on $\mathcal{B}$, whose normal is $\boldsymbol{n}$, the surface traction $\boldsymbol{t}$ along $\boldsymbol{n}$ is given by Cauchy's theorem as

$$\boldsymbol{t} = \tilde{\boldsymbol{\sigma}}^{\mathrm{T}}\,\boldsymbol{n} \ , \tag{2.79}$$

where

$$\tilde{\boldsymbol{\sigma}} = \tilde{\sigma}^{ij}\,\boldsymbol{g}_i \otimes \boldsymbol{g}_j \tag{2.80}$$

is called the Cauchy stress tensor. Similarly, on an elastic surface $\mathcal{S}$, the surface Cauchy stress tensor is

$$\boldsymbol{\sigma} = \sigma^{\alpha\beta}\,\boldsymbol{a}_\alpha \otimes \boldsymbol{a}_\beta \ . \tag{2.81}$$

The Cauchy stress (or true stress) basically determines the force acting on an infinitesimal vector area of the deformed configuration. In computational approaches and variational formulations, it is more convenient to introduce the Kirchhoff stress tensors,

$$\begin{aligned} \tilde{\boldsymbol{\tau}} &:= \tilde{J}\,\tilde{\boldsymbol{\sigma}} = \tilde{\tau}^{ij}\,\boldsymbol{g}_i \otimes \boldsymbol{g}_j \ , \\ \boldsymbol{\tau} &:= J\,\boldsymbol{\sigma} = \tau^{\alpha\beta}\,\boldsymbol{a}_\alpha \otimes \boldsymbol{a}_\beta \ , \end{aligned} \tag{2.82}$$

with

$$\begin{aligned} \tilde{\tau}^{ij} &= \tilde{J}\,\tilde{\sigma}^{ij} \ , \qquad (i,j = 1,2,3) \ , \\ \tau^{\alpha\beta} &= J\,\sigma^{\alpha\beta} \ , \quad (\alpha,\beta = 1,2) \ . \end{aligned} \tag{2.83}$$

The definition of the Kirchhoff stress tensor helps to integrate over the reference configuration rather than the current configuration since $\tilde{\boldsymbol{\sigma}}\,\mathrm{d}v = \tilde{\boldsymbol{\tau}}\,\mathrm{d}V$ and $\boldsymbol{\sigma}\,\mathrm{d}a = \boldsymbol{\tau}\,\mathrm{d}A$.

The first Piola–Kirchhoff stress tensors (also called nominal stress) relates a force vector in the current configuration to a corresponding infinitesimal vector area in the reference configuration. It is defined with basis vectors both in the current and in the reference configuration as

$$\begin{aligned} \tilde{\boldsymbol{P}} &:= \tilde{J}\,\tilde{\boldsymbol{\sigma}}\,\tilde{\boldsymbol{F}}^{-\mathrm{T}} &&= \tilde{\boldsymbol{\tau}}\,\tilde{\boldsymbol{F}}^{-\mathrm{T}} &&= \tilde{P}^{ij}\,\boldsymbol{g}_i \otimes \boldsymbol{G}_j \;, \\ \boldsymbol{P} &:= J\,\boldsymbol{\sigma}\,\boldsymbol{F}^{-\mathrm{T}} &&= \boldsymbol{\tau}\,\boldsymbol{F}^{-\mathrm{T}} &&= P^{\alpha\beta}\,\boldsymbol{a}_\alpha \otimes \boldsymbol{A}_\beta \;, \end{aligned} \tag{2.84}$$

where

$$\begin{aligned} \tilde{P}^{ij} &= \tilde{J}\,\tilde{\sigma}^{ij} &&= \tilde{\tau}^{ij} \;, \qquad (i,j=1,2,3) \;, \\ P^{\alpha\beta} &= J\,\sigma^{\alpha\beta} &&= \tau^{\alpha\beta} \;, \qquad (\alpha,\beta=1,2) \;. \end{aligned} \tag{2.85}$$

The first Piola–Kirchhoff stress tensor is a a two-field tensor (like the deformation tensor) and it is non-symmetric (in contrast to the Cauchy and Kirchhoff stress tensors, which are symmetric).

The second Piola–Kirchhoff stress tensor relates a force vector to an infinitesimal vector area, both in the reference configuration, as

$$\begin{aligned} \tilde{\boldsymbol{S}} &:= \tilde{\boldsymbol{F}}^{-1}\,\tilde{\boldsymbol{P}} &&= \tilde{\boldsymbol{F}}^{-1}\,\tilde{\boldsymbol{\tau}}\,\tilde{\boldsymbol{F}}^{-\mathrm{T}} &&= \tilde{S}^{ij}\,\boldsymbol{G}_i \otimes \boldsymbol{G}_j \;, \\ \boldsymbol{S} &:= \boldsymbol{F}^{-1}\,\boldsymbol{P} &&= \boldsymbol{F}^{-1}\,\boldsymbol{\tau}\,\boldsymbol{F}^{-\mathrm{T}} &&= S^{\alpha\beta}\,\boldsymbol{A}_\alpha \otimes \boldsymbol{A}_\beta \;, \end{aligned} \tag{2.86}$$

where

$$\begin{aligned} \tilde{S}^{ij} &= \tilde{J}\,\tilde{\sigma}^{ij} &&= \tilde{\tau}^{ij} \;, \qquad (i,j=1,2,3) \;, \\ S^{\alpha\beta} &= J\,\sigma^{\alpha\beta} &&= \tau^{\alpha\beta} \;, \qquad (\alpha,\beta=1,2) \;. \end{aligned} \tag{2.87}$$

Like the Cauchy and Kirchhoff stress tensors, the second Piola–Kirchhoff stress tensor is also symmetric.

Remark 2.13. By definition (2.86), the Kirchhoff and the second Piola–Kirchhoff stress tensors are mapped to each other by means of the push-forward and pull-back operations as

$$\begin{aligned} \tilde{\boldsymbol{S}} &= \tilde{\boldsymbol{F}}^{-1}\,\tilde{\boldsymbol{\tau}}\,\tilde{\boldsymbol{F}}^{-\mathrm{T}} \;, \qquad & \tilde{\boldsymbol{\tau}} &= \tilde{\boldsymbol{F}}\,\tilde{\boldsymbol{S}}\,\tilde{\boldsymbol{F}}^{\mathrm{T}} \;, \qquad & (i,j=1,2,3) \;, \\ \boldsymbol{S} &= \boldsymbol{F}^{-1}\,\boldsymbol{\tau}\,\boldsymbol{F}^{-\mathrm{T}} \;, \qquad & \boldsymbol{\tau} &= \boldsymbol{F}\,\boldsymbol{S}\,\boldsymbol{F}^{\mathrm{T}} \;, \qquad & (\alpha,\beta=1,2) \;. \end{aligned} \tag{2.88}$$

As shown in Eq. (2.87), the components of the Kirchhoff and the second Piola–Kirchhoff stress tensors are identical while only the bases are different.

2.2.5 Balance equations

The fundamental relations of continuum mechanics are given by balance equations, i.e. balance of mass, balance of linear and angular momentum, and the balance of mechanical power, which are shortly reviewed here. More details can be found e.g. in Malvern (1969), Marsden and Hughes (1994), Truesdell and Noll (2004), Holzapfel (2000) and Wriggers (2008).

2.2.5.1 Balance of mass

An infinitesimal mass element can be related to the volume element through the (volumetric mass) densities $\tilde{\rho}_0$ and $\tilde{\rho}$, in the reference and current configurations of a 3D body, as

$$\mathrm{d}m = \tilde{\rho}_0 \, \mathrm{d}V = \tilde{\rho} \, \mathrm{d}v \ . \tag{2.89}$$

For a surface, the mass element can be defined in terms of densities ρ_0 and ρ per initial and current surface, respectively, as

$$\mathrm{d}m = \rho_0 \, \mathrm{d}A = \rho \, \mathrm{d}a \ . \tag{2.90}$$

Thus, the conservation of mass or continuity equation can be expressed as

$$\begin{aligned} \tilde{\rho}_0 &= \tilde{J} \, \tilde{\rho} \ , \\ \rho_0 &= J \, \rho \ . \end{aligned} \tag{2.91}$$

2.2.5.2 Balance of linear and angular momentum

From Eq. (2.89), the linear momentum in the current and reference configuration is

$$\tilde{\boldsymbol{L}} := \int_{\mathcal{B}} \tilde{\rho} \, \dot{\tilde{\boldsymbol{x}}} \, \mathrm{d}v = \int_{\mathcal{B}_0} \tilde{\rho}_0 \, \dot{\tilde{\boldsymbol{x}}} \, \mathrm{d}V \ , \tag{2.92}$$

where $\dot{\tilde{\boldsymbol{x}}}$ is the material velocity. The balance of linear momentum implies that the change of linear momentum in time is equal to the sum of external forces, i.e.

$$\dot{\tilde{\boldsymbol{L}}} = \int_{\mathcal{B}} \tilde{\rho} \, \ddot{\tilde{\boldsymbol{x}}} \, \mathrm{d}v = \int_{\mathcal{B}} \tilde{\rho} \, \tilde{\boldsymbol{b}} \, \mathrm{d}v + \int_{\partial\mathcal{B}} \boldsymbol{t} \, \mathrm{d}a \ , \tag{2.93}$$

where $\ddot{\tilde{\boldsymbol{x}}}$ is the material acceleration and $\tilde{\boldsymbol{b}}$ is the body force (e.g. gravitational force) and $\boldsymbol{t}$ is the traction on the surface of $\mathcal{B}$ given by Eq. (2.79). As shown by Bonet et al. (2000) and Wriggers (2008), considering the Cauchy's theorem (see Sec. 2.2.4) and the divergence theorem, the balance of linear momentum reads

$$\nabla_{\tilde{\boldsymbol{x}}} \cdot \tilde{\boldsymbol{\sigma}} + \tilde{\rho} \, \tilde{\boldsymbol{b}} = \tilde{\rho} \, \ddot{\tilde{\boldsymbol{x}}} \ , \qquad \forall \, \tilde{\boldsymbol{x}} \in \mathcal{B} \ . \tag{2.94}$$

The balance of angular momentum simply demands the symmetry of the Cauchy stress tensor (Wriggers, 2008), i.e. $\tilde{\boldsymbol{\sigma}} = \tilde{\boldsymbol{\sigma}}^{\mathrm{T}}$. The balance equation (2.94) together with the boundary conditions

$$\begin{aligned} \tilde{\boldsymbol{u}} &= \bar{\boldsymbol{u}} \quad \text{on} \quad \partial_u\mathcal{B} \ , \\ \boldsymbol{t} &= \bar{\boldsymbol{t}} \quad \text{on} \quad \partial_t\mathcal{B} \end{aligned} \tag{2.95}$$

give the strong from of the boundary value problem (BVP), which describes the deformation of $\mathcal{B}$ due to given boundary conditions. Here, $\bar{\boldsymbol{u}}$ is a prescribed displacement on the Dirichlet boundary $\partial_u\mathcal{B}$ and $\bar{\boldsymbol{t}}$, given by Eq. (2.79), is a traction on the Neumann boundary $\partial_t\mathcal{B}$. In Sec. (3.1.1), an alternative formulation of Eq. (2.94) is introduced for thin shells and membranes.

2.2.5.3 Balance of mechanical power

Balance of mechanical power, which is motivated from the first law of thermodynamics, can be written as

$$\dot{K} + W = P, \tag{2.96}$$

where K, W and P are the kinetic energy, stress power and power of external forces. The kinetic energy is

$$K = \frac{1}{2}\int_{\mathcal{B}} \dot{\tilde{\boldsymbol{x}}} \cdot \dot{\tilde{\boldsymbol{x}}}\, \tilde{\rho}\, \mathrm{d}v \ . \tag{2.97}$$

The stress power is

$$W = \frac{1}{2}\int_{\mathcal{B}} \tilde{\boldsymbol{\sigma}} : \tilde{\boldsymbol{d}}\, \mathrm{d}v \ , \tag{2.98}$$

where

$$\tilde{\boldsymbol{d}} := \frac{1}{2}\left(\tilde{\boldsymbol{l}} + \tilde{\boldsymbol{l}}^{\mathrm{T}}\right) = \frac{1}{2}\dot{g}_{ij}\, \boldsymbol{g}^i \otimes \boldsymbol{g}^j \ , \quad (i,j = 1,2,3) \tag{2.99}$$

is called the rate of deformation tensor and

$$\tilde{\boldsymbol{l}} := \nabla_{\tilde{\boldsymbol{x}}}\dot{\tilde{\boldsymbol{x}}} = \frac{\partial \dot{\tilde{\boldsymbol{x}}}}{\partial \tilde{\boldsymbol{x}}} = \dot{\boldsymbol{g}}_i \otimes \boldsymbol{g}^i = \dot{\tilde{\boldsymbol{x}}}_{,i} \otimes \boldsymbol{g}^i \ , \quad (i = 1,2,3) \tag{2.100}$$

is the spacial velocity gradient. The power of external forces is

$$P = \int_{\mathcal{B}} \dot{\tilde{\boldsymbol{x}}} \cdot \tilde{\boldsymbol{b}}\, \mathrm{d}v + \int_{\partial\mathcal{B}} \dot{\tilde{\boldsymbol{x}}} \cdot \boldsymbol{t}\, \mathrm{d}a \ . \tag{2.101}$$

2.3 Contact mechanics

The presented membrane and shell formulations can be easily used to model contact problems. The investigation of contact formulations is beyond the scope of this work. Nonetheless, the applicability of this framework to model contact between deformable bodies and a deformable and a rigid body is demonstrated by two examples in Chap. 9. Thus, for the sake of self-containedness, a brief introduction to the employed frictionless normal contact formulation is given here. For more details on the theory, implementation and alternative approaches, readers are recommended to refer to Wriggers (2006), Sauer (2013), Sauer and De Lorenzis (2013) and Sauer and De Lorenzis (2015).

Contact between two bodies $\mathcal{B}_1$ and $\mathcal{B}_2$ is characterized by the impenetrability constraint (Sauer et al., 2014)

$$g_{\mathrm{n}} := \big(\boldsymbol{x} - \boldsymbol{x}_{\mathrm{p}}\big) \cdot \boldsymbol{n}_{\mathrm{p}} \geq 0 \ , \tag{2.102}$$

where defines the normal gap between a point $\boldsymbol{x}$ on the contact surface of one of the bodies, e.g. $\partial_c\mathcal{B}_1$ and a corresponding projected point $\boldsymbol{x}_{\mathrm{p}}$ on the contact surface of the other body, i.e. $\partial_c\mathcal{B}_2$. The projected point $\boldsymbol{x}_{\mathrm{p}}$ is obtained by solving the minimum distance problem

$$\boldsymbol{x}_{\mathrm{p}} = \boldsymbol{x}_{\mathrm{p}}(\boldsymbol{x}) = \big\{\boldsymbol{y}\big| \min_{\forall \boldsymbol{y} \in \partial_c\mathcal{B}_2} \|\boldsymbol{x} - \boldsymbol{y}\|, \ \forall \boldsymbol{x} \in \partial_c\mathcal{B}_1\big\} \tag{2.103}$$

and $\boldsymbol{n}_{\mathrm{p}}$ is the surface normal at $\boldsymbol{x}_{\mathrm{p}}$.

Having the normal gap, the contact constraint (2.102) can be enforced using the penalty method, the Lagrange multiplier method, the augmented Lagrange multiplier method (Wriggers, 2006). Following the penalty approach, the contact traction can be defined as

$$\boldsymbol{f}_{\mathrm{c}} = \begin{cases} -\epsilon_{\mathrm{n}}\, g_{\mathrm{n}}\, \boldsymbol{n}\mathrm{p} & , \quad g_{\mathrm{n}} < 0 \ , \\ \boldsymbol{0} & , \quad g_{\mathrm{n}} \geq 0 \ , \end{cases} \tag{2.104}$$

where ϵ_{n} is the penalty parameter. In Chap. 3, the contribution of the contact traction $\boldsymbol{f}_{\mathrm{c}}$ to the weak form of shells and membranes will be shown.

Chapter 3

Theory of Thin Shells and Membranes[3]

The current section presents the kinematics and governing equations of thin membranes and rotation-free shells. First, the mathematical and theoretical foundations of thin shells are reviewed, which follows the formulation of Sauer and Duong (2017). The shell theory is based on the Kirchhoff–Love hypothesis and is described in terms of the first and second fundamental forms of the surface. Then, following Sauer et al. (2014), the membrane theory is introduced. In Sec. 3.2, it is discussed how a membrane formulation can be extracted from a Kirchhoff–Love shell theory as a special case. Upon this theoretical foundation, the projection of 3D material models onto the membrane and shell surfaces is investigated in Chap. 4.

3.1 Thin shell theory

This section summarizes the nonlinear theory of rotation-free thin shells based on the Kirchhoff–Love hypothesis. Further details can be found e.g. in Naghdi (1982), Steigmann (1999) and Sauer and Duong (2017). The geometrical description, kinematics and deformation of a deformable surface is discussed in detail in Secs. 2.1.1 and 2.2 and they are not repeated here. Those kinematics can also be derived from 3D kinematics rather than being formulated directly on the shell mid-surface. Later, in Sec. 4.1.1, which is devoted to the projection approaches, the kinematics of thin shells is formulated from a 3D perspective. Here, first the strong form of the equilibrium equation of a thin shell is introduced. This is followed by a brief discussion of the weak form of the governing equation. Last, the weak form is linearized in order to be solved by the Newton–Raphson method.

---

[3] This chapter is based on Duong et al. (2017).

3.1.1 Strong form

The equilibrium of a thin shell is governed by the field equation (Steigmann, 1999)

$$\boldsymbol{T}^{\alpha}_{;\alpha} + \boldsymbol{f} = \rho\,\ddot{\boldsymbol{x}}\;, \qquad \forall\,\boldsymbol{x} \in \mathcal{S}\;, \tag{3.1}$$

which is obtained by the balance of linear momentum and the conservation of mass (Sauer and Duong, 2017). In Eq. (3.1), ρ is the mass density per the current surface area, $\ddot{\boldsymbol{x}}$ is the surface material acceleration and $\boldsymbol{f}$ is a distributed surface force on $\mathcal{S}$, which can be decomposed as

$$\boldsymbol{f} = f_{\alpha}\,\boldsymbol{a}^{\alpha} + p_{\mathrm{ext}}\,\boldsymbol{n} = f^{\alpha}\,\boldsymbol{a}_{\alpha} + p_{\mathrm{ext}}\,\boldsymbol{n}\;, \tag{3.2}$$

where $f_{\alpha} = \boldsymbol{f}\cdot\boldsymbol{a}_{\alpha}$ and $f^{\alpha} = \boldsymbol{f}\cdot\boldsymbol{a}^{\alpha}$ are the co-variant and contra-variant of $\boldsymbol{f}$ and p_{ext} is the out-of-plane external pressure acting on $\mathcal{S}$. The traction vector

$$\boldsymbol{T}^{\alpha} = N^{\alpha\beta}\,\boldsymbol{a}_{\beta} + S^{\alpha}\,\boldsymbol{n}\;, \tag{3.3}$$

acting on the surface normal to $\boldsymbol{a}^{\alpha}$, can be related to the Cauchy stress tensor

$$\tilde{\boldsymbol{\sigma}} := N^{\alpha\beta}\,\boldsymbol{a}_{\alpha}\otimes\boldsymbol{a}_{\beta} + S^{\alpha}\,\boldsymbol{a}_{\alpha}\otimes\boldsymbol{n} + \sigma^{33}\,\boldsymbol{n}\otimes\boldsymbol{n}\;, \tag{3.4}$$

according to Cauchy's theorem (see Sec. 2.2.4) as $\boldsymbol{T}^{\alpha} = \tilde{\boldsymbol{\sigma}}^{\mathrm{T}}\,\boldsymbol{a}^{\alpha}$. For a general in-plane vector $\boldsymbol{\nu} = \nu_{\alpha}\,\boldsymbol{a}^{\alpha}$, we get $\boldsymbol{T} = \tilde{\boldsymbol{\sigma}}^{\mathrm{T}}\,\boldsymbol{\nu} = T^{\alpha}\,\nu_{\alpha}$. For thin shells, it is usually assumed that the *plane-stress* assumption holds, which implies $\sigma^{33} = 0$. This issue is further investigated in Chap. 4, where the 3D constitution of hyperelastic membrane and shells are discussed. Here, (Sauer and Duong, 2017)

$$N^{\alpha\beta} = \sigma^{\alpha\beta} + b^{\beta}_{\gamma}\,M^{\gamma\alpha} \tag{3.5}$$

is the distributed in-plane sectional force and $M^{\alpha\beta}$ is the distributed bending moment. The balance of angular momentum implies that $\sigma^{\alpha\beta}$ is symmetric and the distributed out-of-plane sectional force is

$$S^{\alpha} = -M^{\beta\alpha}_{\;\;;\beta}\;. \tag{3.6}$$

Further, $M^{\alpha\beta}$ is also symmetric but $N^{\alpha\beta}$ is not symmetric necessarily as it is influenced by bending. Similar to Eq. (3.4), the distributed moments are collected in moment tensor

$$\boldsymbol{\mu} = -M^{\alpha\beta}\,\boldsymbol{a}_{\alpha}\otimes\boldsymbol{a}_{\beta}\;, \tag{3.7}$$

which gives the distributed moment vector on the surface normal to $\boldsymbol{\nu}$ as

$$\boldsymbol{M} := \boldsymbol{\mu}^{\mathrm{T}}\,\boldsymbol{\nu} = \boldsymbol{M}^{\alpha}\,\nu_{\alpha}\;, \tag{3.8}$$

with

$$\boldsymbol{M}^{\alpha} := \boldsymbol{\mu}^{\mathrm{T}}\,\boldsymbol{a}^{\alpha} = -M^{\alpha\beta}\,\boldsymbol{a}_{\beta}\ . \tag{3.9}$$

The equilibrium equation (3.1) is closed by appropriate boundary conditions on the surface boundary $\partial\mathcal{S} = \partial_u\mathcal{S} \cup \partial_n\mathcal{S} \cup \partial_t\mathcal{S} \cup \partial_m\mathcal{S}$ as

$$\begin{aligned} \boldsymbol{u} &= \bar{\boldsymbol{u}} && \text{on } \partial_u\mathcal{S}\ , \\ \boldsymbol{n} &= \bar{\boldsymbol{n}} && \text{on } \partial_n\mathcal{S}\ , \\ \boldsymbol{t} &= \bar{\boldsymbol{t}} && \text{on } \partial_t\mathcal{S}\ , \\ m_{\tau} &= \bar{m}_{\tau} && \text{on } \partial_m\mathcal{S}\ , \end{aligned} \tag{3.10}$$

where $\bar{\boldsymbol{u}}$ is a prescribed displacement, $\bar{\boldsymbol{n}}$ is a prescribed rotation, $\bar{\boldsymbol{t}} := \bar{t}^{\alpha}\,\boldsymbol{a}_{\alpha} + \bar{t}\,\boldsymbol{n}$ is a prescribed effective boundary traction and $\bar{m}_{\tau}$ is a prescribed distributed bending moment parallel to the boundary $\partial_m\mathcal{S}$. On the boundary of shell, the distributed moment vector can be decomposed as

$$\boldsymbol{M} = m_{\tau}\,\boldsymbol{\nu} - m_{\nu}\,\boldsymbol{\tau}\ , \tag{3.11}$$

where $\boldsymbol{\tau}$ is the unit tangent along the boundary $\partial_m\mathcal{S}$ and $\boldsymbol{\nu} = \boldsymbol{\tau}\times\boldsymbol{n}$ is the unit normal to the boundary $\partial_m\mathcal{S}$. As discussed by Sauer and Duong (2017), on the boundary, the effective traction $\boldsymbol{t}$, which is introduced in Eq. (3.10), includes the bending moments as

$$\boldsymbol{t} := \boldsymbol{T} - (\bar{m}_{\nu}\,\boldsymbol{n})'\ , \tag{3.12}$$

where $\bar{m}_{\nu}$ is a prescribed bending moment perpendicular to the boundary $\partial_m\mathcal{S}$. If the problem involves contact, as described in Sec. 2.3, the contact traction $\boldsymbol{f}_{\mathrm{c}}$, which is a distributed force per surface, is also considered as an external force.

As shown by Sauer and Duong (2017), the stress and bending moment components $\sigma^{\alpha\beta}$ and $M^{\alpha\beta}$ are obtained from the shell constitution. In Chap. 4, it will be demonstrated that, for the shell formulations projected from 3D constitution, $\sigma^{\alpha\beta}$ and $M^{\alpha\beta}$ correspond to the *resultant stress tensor* and the *resultant moment tensor*, respectively.

3.1.2 Constitution

For thin shells, $\tau^{\alpha\beta}$ and $\delta a_{\alpha\beta}$ as well as $M_0^{\alpha\beta}$ and $\delta b_{\alpha\beta}$ are work conjugate to one another with respect to the initial configuration (Sauer and Duong, 2017). Thus, considering a hyperelastic constitution given by $W(a_{\alpha\beta}, b_{\alpha\beta})$, which is a stored energy density per reference surface,

$$\int_{\mathcal{S}_0} \delta W\,\mathrm{d}A = \int_{\mathcal{S}_0} \tau^{\alpha\beta}\,\frac{1}{2}\delta a_{\alpha\beta}\,\mathrm{d}A + \int_{\mathcal{S}_0} M_0^{\alpha\beta}\,\delta b_{\alpha\beta}\,\mathrm{d}A\ , \tag{3.13}$$

where

$$\begin{aligned} \tau^{\alpha\beta} &:= 2\,\frac{\partial W}{\partial a_{\alpha\beta}}\ , \\ M_0^{\alpha\beta} &:= \frac{\partial W}{\partial b_{\alpha\beta}} \end{aligned} \tag{3.14}$$

are the surface Kirchhoff stress tensor and the moment tensor on the reference surface, respectively. From Eq. (3.14), the surface Cauchy stress tensor and the moment tensor on the current surface are, respectively,

$$\begin{aligned} \sigma^{\alpha\beta} &:= \frac{1}{J}\,\tau^{\alpha\beta}\ , \\ M^{\alpha\beta} &:= \frac{1}{J}\,M_0^{\alpha\beta}\ . \end{aligned} \tag{3.15}$$

The variational form (3.13) is obtained assuming that a 2D stored energy $W(a_{\alpha\beta}, b_{\alpha\beta})$ is directly formulated on a 2D manifold. The examples of such stain energy density functions, which are not in the focus of this thesis, are the Canham model or the Koiter shell model (Sauer and Duong, 2017). The bending model of Canham, initially proposed for red blood cells (Canham, 1970), can be expresses as

$$W(a_{\alpha\beta}, b_{\alpha\beta}) = c\,J\,(2\,H^2 - K) \tag{3.16}$$

where c is a material constant. The stored energy of a Koiter shell model (Ciarlet, 2005), which is based on a linear elastic material model, is

$$W(a_{\alpha\beta}, b_{\alpha\beta}) = \frac{1}{2}\,c^{\alpha\beta\gamma\delta}\,E_{\alpha\beta}\,E_{\gamma\delta} + \frac{1}{2}\,f^{\alpha\beta\gamma\delta}\,K_{\alpha\beta}\,K_{\gamma\delta}\ , \tag{3.17}$$

where, for a *plane-strain* condition,

$$\begin{aligned} c^{\alpha\beta\gamma\delta} &= \Lambda\,A^{\alpha\beta}\,A^{\gamma\delta} + \mu\,\left(A^{\alpha\gamma}\,A^{\beta\delta} + A^{\alpha\delta}\,A^{\beta\gamma}\right)\ , \\ f^{\alpha\beta\gamma\delta} &= \frac{T^2}{12}\,c^{\alpha\beta\gamma\delta}\ . \end{aligned} \tag{3.18}$$

Here, $\Lambda = T\,\tilde{\Lambda}$ and $\mu = T\,\tilde{\mu}$ are the 2D counterparts of the lamé's first and second parameters of a 3D continuum, denoted by $\tilde{\Lambda}$ and $\tilde{\mu}$, respectively. From Eqs. (3.17) and (3.18), the stress and moment tensors of the Koiter shell model are

$$\begin{aligned} \tau^{\alpha\beta} &= \Lambda\,\mathrm{tr}\,\boldsymbol{E}\,A^{\alpha\beta} + 2\,\mu\,E^{\alpha\beta}\ , \\ M_0^{\alpha\beta} &= \frac{T^2}{12}\left(\Lambda\,\mathrm{tr}\,\boldsymbol{K}\,A^{\alpha\beta} + 2\,\mu\,K^{\alpha\beta}\right)\ . \end{aligned} \tag{3.19}$$

Later, in Secs. 4.2-4.4, it is shown in detail how to project the available 3D constitutive laws onto the surface of shells and membranes.

3.1.3 Weak form

Eqs. (3.1) and (3.13), together with the boundary conditions (3.10), make the strong form of the boundary value problem (BVP) for thin shells. As the BVP cannot be solved exactly, finite element method, which approximates values of the unknowns at discrete number of points over the domain, is used in this thesis. The FEM does not fulfill the governing equation point-wise (i.e. $\forall \boldsymbol{x} \in \mathcal{S}$). Instead, it fulfills the field equation as an integral over the whole domain. Thus, one need to use the principle of virtual work to construct the weak form of BVP (Bonet and Wood, 1997).

Consider a kinematically admissible variation of the surface denoted by $\delta\boldsymbol{x} \in \mathcal{V}$, the weak form of Eq. (3.1) can be obtained by contracting the equilibrium equation (3.1) with $\delta\boldsymbol{x} \in \mathcal{V}$ and integrating over $\mathcal{S}$ as (Sauer and Duong, 2017)

$$\int_{\mathcal{S}} \delta\boldsymbol{x} \cdot \big(\boldsymbol{T}^{\alpha}_{;\alpha} + \boldsymbol{f} - \rho\,\ddot{\boldsymbol{x}}\big)\,\mathrm{d}a = 0\ . \tag{3.20}$$

The first term in Eq. (3.20), can be written as

$$\int_{\mathcal{S}} \delta\boldsymbol{x} \cdot \boldsymbol{T}^{\alpha}_{;\alpha}\,\mathrm{d}a = \int_{\partial_t\mathcal{S}} \delta\boldsymbol{x} \cdot \boldsymbol{T}\,\mathrm{d}s - \int_{\mathcal{S}} \delta\boldsymbol{a}_{\alpha} \cdot \boldsymbol{T}^{\alpha}\,\mathrm{d}a\ , \tag{3.21}$$

where $\boldsymbol{T} = \boldsymbol{T}^{\alpha}\,\nu_{\alpha}$. The rear term of Eq. (3.21) is (Sauer and Duong, 2017)

$$\int_{\mathcal{S}} \delta\boldsymbol{a}_{\alpha} \cdot \boldsymbol{T}^{\alpha}\,\mathrm{d}a = \int_{\mathcal{S}} \sigma^{\alpha\beta}\,\frac{1}{2}\delta a_{\alpha\beta}\,\mathrm{d}a + \int_{\mathcal{S}} M^{\alpha\beta}\,\delta b_{\alpha\beta}\,\mathrm{d}a + \int_{\partial\mathcal{S}} \delta\boldsymbol{n} \cdot \boldsymbol{M}\,\mathrm{d}s\ . \tag{3.22}$$

Thus, the weak form is formulated in terms of the inertial, internal and external virtual work contributions as

$$G_{\mathrm{in}} + G_{\mathrm{int}} - G_{\mathrm{ext}} = 0\ , \qquad \forall\,\delta\boldsymbol{x} \in \mathcal{V}\ . \tag{3.23}$$

The inertial virtual work is

$$G_{\mathrm{in}} = \int_{\mathcal{S}} \delta\boldsymbol{x} \cdot \rho\,\ddot{\boldsymbol{x}}\,\mathrm{d}a = \int_{\mathcal{S}_0} \delta\boldsymbol{x} \cdot \rho_0\,\ddot{\boldsymbol{x}}\,\mathrm{d}A\ . \tag{3.24}$$

Following Eq. (3.13), the internal virtual work can be written as (Sauer and Duong, 2017)

$$\begin{aligned} G_{\mathrm{int}} &= \int_{\mathcal{S}_0} \frac{1}{2}\,\delta a_{\alpha\beta}\,\tau^{\alpha\beta}\,\mathrm{d}A + \int_{\mathcal{S}_0} \delta b_{\alpha\beta}\,M_0^{\alpha\beta}\,\mathrm{d}A \\ &= \int_{\mathcal{S}} \frac{1}{2}\,\delta a_{\alpha\beta}\,\sigma^{\alpha\beta}\,\mathrm{d}a + \int_{\mathcal{S}} \delta b_{\alpha\beta}\,M^{\alpha\beta}\,\mathrm{d}a\ . \end{aligned} \tag{3.25}$$

The external virtual work is (Sauer et al., 2014 and Sauer and Duong, 2017)

$$G_{\mathrm{ext}} = G_{\mathrm{ext}f} + G_{\mathrm{ext}p} + G_{\mathrm{ext}t} + G_{\mathrm{ext}m} + G_{\mathrm{extc}} \ , \tag{3.26}$$

where

$$G_{\mathrm{ext}f} = \int_{\mathcal{S}} \delta\boldsymbol{x} \cdot f_\alpha \, \boldsymbol{a}^\alpha \, \mathrm{d}a \ , \tag{3.27}$$

$$G_{\mathrm{ext}p} = \int_{\mathcal{S}} \delta\boldsymbol{x} \cdot \boldsymbol{n} \, \mathrm{d}a \ , \tag{3.28}$$

$$G_{\mathrm{ext}t} = \int_{\partial_t\mathcal{S}} \delta\boldsymbol{x} \cdot \boldsymbol{t} \, \mathrm{d}s \tag{3.29}$$

and

$$G_{\mathrm{ext}m} = \int_{\partial_m\mathcal{S}} \delta\boldsymbol{n} \cdot m_\tau \, \boldsymbol{\nu} \, \mathrm{d}s + [\delta\boldsymbol{x} \cdot m_\nu \, \boldsymbol{n}] \ . \tag{3.30}$$

Here, G_{extc} is the contribution of contact forces to the balance of virtual work (3.23) as

$$G_{\mathrm{extc}} = \int_{\mathcal{S}} \delta\boldsymbol{x} \cdot \boldsymbol{f}_{\mathrm{c}} \, \mathrm{d}a \ , \tag{3.31}$$

where $\boldsymbol{f}_{\mathrm{c}}$ is the traction force, given by Eq. (2.104), and it is assumed that all the shell surface $\mathcal{S}$ can be involved in contact.

3.1.4 Linearization of the weak form

As the weak form (3.23) is nonlinear, it needs to be linearized in order to be solved by the Newton–Raphson method. The linearized inertial virtual work is

$$\Delta G_{\mathrm{in}} = \int_{\mathcal{S}_0} \delta\boldsymbol{x} \cdot \rho_0 \, \Delta\ddot{\boldsymbol{x}} \, \mathrm{d}A \ , \tag{3.32}$$

where $\Delta\ddot{\boldsymbol{x}}$ follows from a time integration scheme.

3.1.4.1 Internal virtual work

The linearized internal virtual work contribution is (Sauer and Duong, 2017 and Duong et al., 2017)

$$\Delta G_{\mathrm{int}} = \Delta G_{\mathrm{intm}} + \Delta G_{\mathrm{intg}} \ . \tag{3.33}$$

The material contribution is

$$\begin{aligned} \Delta G_{\mathrm{intm}} = & \int_{\mathcal{S}_0} \frac{1}{2}\delta a_{\alpha\beta} \left(c^{\alpha\beta\gamma\delta} \, \frac{1}{2}\Delta a_{\gamma\delta} + d^{\alpha\beta\gamma\delta} \, \Delta b_{\gamma\delta} \right) \mathrm{d}A \\ & + \int_{\mathcal{S}_0} \delta b_{\alpha\beta} \left(e^{\alpha\beta\gamma\delta} \, \frac{1}{2}\Delta a_{\gamma\delta} + f^{\alpha\beta\gamma\delta} \, \Delta b_{\gamma\delta} \right) \mathrm{d}A \ , \end{aligned} \tag{3.34}$$

where

$$\begin{aligned} c^{\alpha\beta\gamma\delta} &:= 2\,\frac{\partial\tau^{\alpha\beta}}{\partial a_{\gamma\delta}}\ , \qquad & d^{\alpha\beta\gamma\delta} &:= \frac{\partial\tau^{\alpha\beta}}{\partial b_{\gamma\delta}}\ , \\ e^{\alpha\beta\gamma\delta} &:= 2\,\frac{\partial M_0^{\alpha\beta}}{\partial a_{\gamma\delta}}\ , \qquad & f^{\alpha\beta\gamma\delta} &:= \frac{\partial M_0^{\alpha\beta}}{\partial b_{\gamma\delta}} \end{aligned} \tag{3.35}$$

are the material tangent tensors, and the geometrical contribution is

$$\Delta G_{\mathrm{intg}} \int_{\mathcal{S}_0} = \Big(\tau^{\alpha\beta}\,\frac{1}{2}\Delta\delta a_{\alpha\beta} + M_0^{\alpha\beta}\,\Delta\delta b_{\alpha\beta}\Big)\,\mathrm{d}A\ . \tag{3.36}$$

3.1.4.2 External virtual work

Considering a dead loading of $\boldsymbol{f}$, the linearized external virtual work contribution is (Sauer and Duong, 2017)

$$\Delta G_{\mathrm{ext}} = \Delta G_{\mathrm{ext}p} + \Delta G_{\mathrm{ext}t} + \Delta G_{\mathrm{ext}m} + \Delta G_{\mathrm{extc}}\ , \tag{3.37}$$

where (Sauer et al., 2014)

$$\Delta G_{\mathrm{ext}p} = \int_{\mathcal{S}} p\,\delta\boldsymbol{x}\cdot(\boldsymbol{n}\otimes\boldsymbol{a}^{\alpha} - \boldsymbol{a}^{\alpha}\otimes\boldsymbol{n})\,\Delta\boldsymbol{a}_{\alpha}\,\mathrm{d}a\ . \tag{3.38}$$

Denoting the convective coordinate along the curve $\partial_m\mathcal{S}$ as ξ^{ϵ}, where $\epsilon = 1$ or $\epsilon = 2$, the co-variant base vector at $\boldsymbol{x}\in\partial_m\mathcal{S}$ is $\boldsymbol{a}_{\epsilon} := \partial\boldsymbol{x}/\partial\xi^{\epsilon}$. The corresponding contra-variant base vector is then $\boldsymbol{a}^{\epsilon} := a^{\epsilon\alpha}\boldsymbol{a}_{\alpha}$ $(\alpha = 1,2)$. This gives (Duong et al., 2017)

$$\begin{aligned} \Delta G_{\mathrm{ext}m} &= \int_{\partial_m\mathcal{S}} \delta\boldsymbol{a}_{\alpha}\cdot\big(\nu^{\beta}\,\boldsymbol{n}\otimes\boldsymbol{a}^{\alpha} + \nu^{\alpha}\,\boldsymbol{a}^{\beta}\otimes\boldsymbol{n}\big)\,\Delta\boldsymbol{a}_{\beta}\,\mathrm{d}s \\ &\quad - \int_{\partial_m\mathcal{S}} \frac{1}{\|\boldsymbol{a}_{\epsilon}\|^2}\,m_{\tau}\,\nu^{\alpha}\,\delta\boldsymbol{a}_{\alpha}\cdot\big(\boldsymbol{n}\otimes\boldsymbol{a}^{\epsilon}\big)\,\Delta\boldsymbol{a}_{\epsilon}\,\mathrm{d}s\ , \end{aligned} \tag{3.39}$$

where $\|\boldsymbol{a}_{\epsilon}\| = \sqrt{\boldsymbol{a}_{\epsilon}\cdot\boldsymbol{a}_{\epsilon}}$. For a dead loading of $\boldsymbol{M}$, $m_{\tau}\,\mathrm{d}s = \mathrm{const}$, thus the second part of Eq. (3.39) will vanish. Further,

$$\Delta G_{\mathrm{ext}t} = \int_{\partial_t\mathcal{S}} \delta\boldsymbol{x}\cdot\Delta\boldsymbol{t}\,\mathrm{d}s + \int_{\partial_t\mathcal{S}} \frac{1}{\|\boldsymbol{a}_{\epsilon}\|^2}\,\delta\boldsymbol{x}\cdot\big(\boldsymbol{t}\otimes\boldsymbol{a}^{\epsilon}\big)\,\Delta\boldsymbol{a}_{\epsilon}\,\mathrm{d}s\ . \tag{3.40}$$

If the traction $\boldsymbol{t}$ is not a displacement follower load, $\Delta_x\boldsymbol{t} = \boldsymbol{0}$. Linearization of Eq. (3.31) yields

$$\Delta G_{\mathrm{extc}} = \int_{\mathcal{S}} \delta\boldsymbol{x}\cdot\Delta\boldsymbol{f}_{\mathrm{c}}\,\mathrm{d}a + \int_{\mathcal{S}_0} \delta\boldsymbol{x}\cdot\boldsymbol{f}_{\mathrm{c}}\,J\,\boldsymbol{a}^{\alpha}\,\Delta\boldsymbol{a}_{\alpha}\,\mathrm{d}A\ , \tag{3.41}$$

where $\Delta \boldsymbol{f}_{\mathrm{c}}$ can be found in Sauer and De Lorenzis (e.g. 2015) for normal contact. The discretized weak form, which gives the FE force vectors and the FE tangent matrices, is given in Chap. 8.

3.2 Membrane theory

In general, there are three approaches to formulate a finite strain theory of membranes: (1) It can be derived from nonlinear shell theories by neglecting the stresses associated with bending and transverse shear deformations (e.g. Kraus, 1967; Libai, 1988; Green, 1992 and Oden, 2006). (2) It can also be derived from 3D nonlinear elasticity (e.g. Steigmann, 2009). (3) It can be directly formulated on a 2D manifold based on in-plane membrane strains and stresses (e.g. Sauer et al., 2014). In this research, we employ a combined approach: First, we adopt the membrane formulation of Sauer et al. (2014), which is formulated in the framework of curvilinear coordinates following Steigmann (1999). Then, in Chap. 4, we project the 3D constitutions of nonlinear elasticity on to the membrane surface. The kinematics of membranes is similar to the kinematics of thin rotation-free shells and can be found in Secs. 2.1.1 and 2.2.

3.2.1 Strong form

The equilibrium equation of a membrane is also given by Eq. (3.1) considering that

$$\boldsymbol{T}^{\alpha} = N^{\alpha\beta}\, \boldsymbol{a}_{\beta} = \sigma^{\alpha\beta}\, \boldsymbol{a}_{\beta} \ . \tag{3.42}$$

For the membranes, the Cauchy stress (3.4) is reduced to

$$\tilde{\boldsymbol{\sigma}} := N^{\alpha\beta}\, \boldsymbol{a}_{\alpha} \otimes \boldsymbol{a}_{\beta} + \sigma^{33}\, \boldsymbol{n} \otimes \boldsymbol{n} \tag{3.43}$$

as $S^{\alpha} = 0$; and therefore, $N^{\alpha\beta} = \sigma^{\alpha\beta}$. Like the thin shells, for membranes $\sigma^{33} = 0$ following a *plane-stress* condition. The governing equation of the membrane is closed by the Neumann and/or Dirichlet boundary conditions on the surface boundary $\partial\mathcal{S} = \partial_u\mathcal{S} \cup \partial_t\mathcal{S}$ as

$$\begin{aligned} \boldsymbol{u} &= \bar{\boldsymbol{u}} \quad \text{on } \partial_u\mathcal{S} \ , \\ \boldsymbol{t} &= \bar{\boldsymbol{t}} \quad \text{on } \partial_t\mathcal{S} \ . \end{aligned} \tag{3.44}$$

Here, the effective traction is $\boldsymbol{t} = \boldsymbol{T}$ as membranes bear no bending moment.

3.2.2 Constitution

For the membranes, $\tau^{\alpha\beta}$ and $\delta a_{\alpha\beta}$ are work conjugate to one another with respect to the initial configuration (Sauer et al., 2014). If a hyperelastic constitution is dircely given on 2D surface of a membrane by $W(a_{\alpha\beta})$, then

$$\int_{\mathcal{S}_0} \delta W \,\mathrm{d}A = \int_{\mathcal{S}_0} \tau^{\alpha\beta}\, \frac{1}{2} \delta a_{\alpha\beta} \,\mathrm{d}A \;, \tag{3.45}$$

where

$$\tau^{\alpha\beta} := 2\, \frac{\partial W}{\partial a_{\alpha\beta}} \;, \tag{3.46}$$

is the surface Kirchhoff stress. This membrane formulation allows for both solid and liquid materials. In Chap. 4, the constitutive projection of 3D nonlinear hyperelastic solids is investigated. In Chap. 7, the same formulation is applied to liquid membranes.

3.2.3 Weak form

Resorting to the principle of virtual displacements, the weak form of the membrane equilibrium equation is obtained from contributions of the inertial, internal and external virtual works according to Eq. (3.23). The inertial virtual work is also given by (3.24). From Eq. (3.45), the internal virtual work is (Sauer et al., 2014)

$$G_{\mathrm{int}} = \int_{\mathcal{S}_0} \frac{1}{2}\, \delta a_{\alpha\beta}\, \tau^{\alpha\beta} \,\mathrm{d}A = \int_{\mathcal{S}} \frac{1}{2}\, \delta a_{\alpha\beta}\, \sigma^{\alpha\beta} \,\mathrm{d}a \;. \tag{3.47}$$

The external virtual work is (Sauer et al., 2014)

$$G_{\mathrm{ext}} = G_{\mathrm{ext}f} + G_{\mathrm{ext}p} + G_{\mathrm{ext}t} + G_{\mathrm{extc}} \;, \tag{3.48}$$

where $G_{\mathrm{ext}f}$, $G_{\mathrm{ext}p}$, $G_{\mathrm{ext}t}$ and G_{extc} are given by Eqs. (3.28-3.29) and (3.31), respectively.

3.2.4 Linearization of the weak form

The linearization of the weak form is done as explained in Sec. 3.1.4. The linearized inertial virtual work is given by Eq. (3.32). By the linearization of the internal virtual work, one gets Eq. (3.33), where the material contribution is

$$\Delta G_{\mathrm{intm}} = \int_{\mathcal{S}_0} \frac{1}{2} \delta a_{\alpha\beta}\, c^{\alpha\beta\gamma\delta}\, \frac{1}{2} \Delta a_{\gamma\delta} \tag{3.49}$$

and

$$c^{\alpha\beta\gamma\delta} := 2\,\frac{\partial \tau^{\alpha\beta}}{\partial a_{\gamma\delta}} \tag{3.50}$$

is the surface elasticity tensor. The geometrical contribution is then

$$\Delta G_{\mathrm{intg}} \int_{\mathcal{S}_0} = \tau^{\alpha\beta}\,\frac{1}{2}\Delta\delta a_{\alpha\beta}\,\mathrm{d}A\ . \tag{3.51}$$

Similar to a shell formulation, the linearized components of the external virtual work, i.e. $\Delta G_{\mathrm{ext}p}$, $\Delta G_{\mathrm{ext}t}$ and ΔG_{extc}, are given by Eqs. (3.38), (3.40) and (3.41), respectively.

Chapter 4

Constitutive Projection[4]

In this chapter, different constitutive projection approaches are used to project the constitutive laws of 3D continua onto the surface of a thin-walled structure, i.e. a rotation-free shell or a membrane. The objective of the projection procedure is to extract 2D stored energy functions per unit reference surface of shells and membranes from common 3D hyperelastic models. Having a projected 2D surface material model, several structural models can be derived as discussed in the next sessions. Here, first the projection procedure is presented and then various structural models resulting from different kinematical assumptions are introduced.

4.1 Projection procedure

The projection approaches has been widely used to derive membrane and shell formulations (Hughes and Carnoy, 1983; De Borst, 1991; Dvorkin et al., 1995; Klinkel and Govindjee, 2002 and Kiendl et al., 2015b). Here, a general framework is presented that can be reduced to several different structural models. Our projection procedure includes two step: First, the 3D kinematics, which is based on the Kirchhoff–Love hypothesis, is defined. It can be considered as a special case of the kinematics introduced in Sec. 2.1.2. Then, 3D material models can be reduced to the corresponding 2D ones following appropriate kinematical assumptions.

---

[4] This chapter is based on Roohbakhshan et al. (2016) and Roohbakhshan and Sauer (2017).

4.1.1 Three-dimensional kinematics

As shown in Fig. 4.1, a material point P within the thickness of a thin-walled structure can be described w.r.t. the mid-surface as (Wriggers, 2008)

$$\tilde{\boldsymbol{X}}(\xi^\alpha, \xi) = \boldsymbol{X}(\xi^\alpha) + \xi\, \boldsymbol{D}(\xi^\alpha) \;, \quad (\alpha = 1, 2) \;, \tag{4.1}$$

in the reference configuration and

$$\tilde{\boldsymbol{x}}(\xi^\alpha,\, \xi) = \boldsymbol{x}(\xi^\alpha) + \xi\, \boldsymbol{d}(\xi^\alpha) \;, \quad (\alpha = 1, 2) \;, \tag{4.2}$$

in the current configuration. Here, $\xi \in [-T/2,\, T/2]$ is the through-the-thickness coordinate. The director vectors $\boldsymbol{D}$ and $\boldsymbol{d}$, which have three unknown components in general, describe the rotation of the cross section relative to the mid-surface. According to the Kirchhoff–Love hypothesis, which is considered here, the cross sections remain (1) straight, (2) unstretched and (3) perpendicular to the mid-surface during the deformation; therefore, $\boldsymbol{D} := \boldsymbol{N}$ and $\boldsymbol{d} := \boldsymbol{n}$.

Note 4.1. To simplify the notation, henceforth we denote the thickness coordinate ξ^3 by ξ. Further, $\xi := \xi^3$ is directly defined over the thickness, whose interval is different from the parametric domain of Sec. 2.1.2.

Remark 4.2. Following the Kirchhoff–Love hypothesis, in Eq. (4.2), it is assumed that the shell thickness does not change. Such assumption is justified for thin shells. One can take into account the thickness variations by modifying Eq. (4.2) as

$$\tilde{\boldsymbol{x}}(\xi^\alpha,\, \xi) = \boldsymbol{x}(\xi^\alpha) + \lambda_3(\xi^\alpha)\, \xi\, \boldsymbol{d}(\xi^\alpha) \;, \tag{4.3}$$

where $\lambda_3 := t/T$ is the thickness stretch and t is the current thickness of the shell. This assumption results in a different kinematics, which is investigated in Sec. 4.4.

Considering a layer-wise description, likewise to $\mathcal{S}$, a (shell) layer $\overset{*}{\mathcal{S}}$ is defined at ξ (see Fig. 4.1). The corresponding layer in the reference configuration is denoted by $\overset{*}{\mathcal{S}}_0$. As described in Sec. 2.1.2, the tangent vectors on $\overset{*}{\mathcal{S}}_0$ and $\overset{*}{\mathcal{S}}$ are, respectively,

$$\begin{aligned} \boldsymbol{G}_\alpha &:= \tilde{\boldsymbol{X}}_{,\alpha} &= \boldsymbol{A}_\alpha - \xi\, B^\gamma_\alpha\, \boldsymbol{A}_\gamma \;, \\ \boldsymbol{G}_3 &:= \tilde{\boldsymbol{X}}_{,3} &= \boldsymbol{D} = \boldsymbol{N} = \boldsymbol{G}^3 \end{aligned} \tag{4.4}$$

and

$$\begin{aligned} \boldsymbol{g}_\alpha &:= \tilde{\boldsymbol{x}}_{,\alpha} &= \boldsymbol{a}_\alpha - \xi\, b^\gamma_\alpha\, \boldsymbol{a}_\gamma \;, \\ \boldsymbol{g}_3 &:= \tilde{\boldsymbol{x}}_{,3} &= \boldsymbol{d} = \boldsymbol{n} = \boldsymbol{g}^3 \;. \end{aligned} \tag{4.5}$$

Such a layer-wise description of the structure relates the bases and metric tensor on $\overset{*}{\mathcal{S}}$ to the bases and metric tensor on the mid-surface.

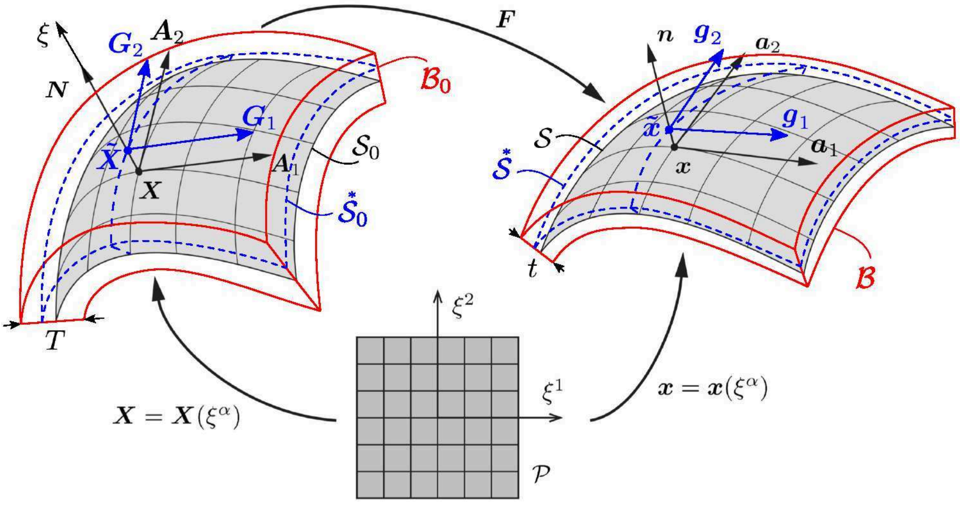

FIGURE 4.1: Mapping between parameter domain, reference and current configurations of a thin-walled structure. The physical boundaries are shown by solid red lines. A layer through the thickness is denoted by blue color (Figure adopted from Duong et al., 2017).

Note 4.3. Henceforth, the variables of a shell layer $\overset{*}{\mathcal{S}}$, located at ξ within the shell thickness, are distinguished by an asterisk. The variables of the shell mid-surface $\mathcal{S}$, located at $\xi = 0$, have no mark. A hat is used to denote the quantities calculated at $\xi = 0$, i.e. $\hat{\bullet} = (\overset{*}{\bullet})_{\xi=0}$. In general, such quantities can be defined for each shell layer. In particular, they can be dimensionally linked to a counterpart in the membrane theory (e.g. $a_{\alpha\beta} = \hat{g}_{\alpha\beta}$ and $\tau^{\alpha\beta} = T\,\hat{\tau}^{\alpha\beta}$) or there might be no corresponding quantity in the membrane theory (e.g. for $\hat{\tau}^{\alpha\beta}_{,3}$ introduced in Sec. 4.3.2.2).

Plugging Eqs. (4.5) and (4.4) into Eq. (2.30), we obtain

$$\begin{aligned} g_{\alpha\beta} &:= \boldsymbol{g}_\alpha \cdot \boldsymbol{g}_\beta = a_{\alpha\beta} - 2\,\xi\, b_{\alpha\beta} + \xi^2\,(2\,H\, b_{\alpha\beta} - K\, a_{\alpha\beta})\ , \\ G_{\alpha\beta} &:= \boldsymbol{G}_\alpha \cdot \boldsymbol{G}_\beta = A_{\alpha\beta} - 2\,\xi\, B_{\alpha\beta} + \xi^2\,(2\,H_0\, B_{\alpha\beta} - K_0\, A_{\alpha\beta})\ , \end{aligned} \tag{4.6}$$

$$\begin{aligned} g_{\alpha 3} &:= \boldsymbol{g}_\alpha \cdot \boldsymbol{g}_3 = 0\ , \\ G_{\alpha 3} &:= \boldsymbol{G}_\alpha \cdot \boldsymbol{G}_3 = 0 \end{aligned} \tag{4.7}$$

and

$$\begin{aligned} g_{33} &:= \boldsymbol{g}_3 \cdot \boldsymbol{g}_3 = \boldsymbol{n} \cdot \boldsymbol{n} = 1\ , \\ G_{33} &:= \boldsymbol{G}_3 \cdot \boldsymbol{G}_3 = \boldsymbol{N} \cdot \boldsymbol{N} = 1\ . \end{aligned} \tag{4.8}$$

Here, H and K are the mean and Gaussian curvature of $\mathcal{S}$, given by Eqs. (2.23) and (2.24), respectively. Similarly, we have defined on $\mathcal{S}_0$

$$H_0 := \frac{1}{2}\mathrm{tr}\,\boldsymbol{B} = \frac{1}{2}\,B^{\alpha}_{\alpha} = \frac{1}{2}\,A^{\alpha\beta}\,B_{\alpha\beta} \tag{4.9}$$

and

$$K_0 := \det\boldsymbol{B} = \frac{B}{A}\ , \tag{4.10}$$

where

$$A = \det[A_{\alpha\beta}]\ , \quad B = \det[B_{\alpha\beta}]\ . \tag{4.11}$$

The contra-variant components of the metric tensor on $\overset{*}{\mathcal{S}}$ and $\overset{*}{\mathcal{S}}_0$ are, respectively,

$$\begin{aligned} [g^{\alpha\beta}] &= [g_{\alpha\beta}]^{-1}\ , \\ [G^{\alpha\beta}] &= [G_{\alpha\beta}]^{-1}\ , \end{aligned} \tag{4.12}$$

which give

$$\begin{aligned} \boldsymbol{g}^{\alpha} &= g^{\alpha\beta}\,\boldsymbol{g}_{\beta}\ , \\ \boldsymbol{G}^{\alpha} &= G^{\alpha\beta}\,\boldsymbol{G}_{\beta}\ . \end{aligned} \tag{4.13}$$

Furthermore, one can define a a two-point tensor $\boldsymbol{\mu}$[5], called “shifter” or “translator” tensor, that transforms the in-plane bases from the mid-surface $\mathcal{S}$ to the layer $\overset{*}{\mathcal{S}}$ and vice versa (Ericksen, 1960; Basar and Ding, 1996; Arciniega and Reddy, 2005; Schlebusch and Zastrau, 2005 and Arciniega and Reddy, 2007). It is formulated for the reference and current configurations, respectively, as

$$\begin{aligned} \boldsymbol{\mu}_0 &:= \boldsymbol{G}_{\alpha}\otimes\boldsymbol{A}^{\alpha} = {\mu_0}^{\beta}_{\alpha}\,\boldsymbol{A}_{\beta}\otimes\boldsymbol{A}^{\alpha}\ , \\ \boldsymbol{\mu} &:= \ \boldsymbol{g}_{\alpha}\otimes\boldsymbol{a}^{\alpha} \ = \mu^{\beta}_{\alpha}\,\boldsymbol{a}_{\beta}\otimes\boldsymbol{a}^{\alpha}\ , \end{aligned} \tag{4.14}$$

where the shifter tensor components of the continuum are derived from Eqs. (4.4.1) and (4.5.1) as

$$\begin{aligned} \boldsymbol{G}_{\alpha} &= {\mu_0}^{\beta}_{\alpha}\,\boldsymbol{A}_{\beta}\ , \\ \boldsymbol{g}_{\alpha} &= \mu^{\beta}_{\alpha}\,\boldsymbol{a}_{\beta}\ , \end{aligned} \tag{4.15}$$

with

$$\mu^{\beta}_{\alpha} = \delta^{\beta}_{\alpha} - \xi\,b^{\beta}_{\alpha}\ . \tag{4.16}$$

Alternatively, from Eqs. (4.14) and (4.16),

$$\begin{aligned} \boldsymbol{\mu}_0 &= \boldsymbol{I} - \xi\,\boldsymbol{B}\ , \\ \boldsymbol{\mu} &= \boldsymbol{i} - \xi\,\boldsymbol{b}\ . \end{aligned} \tag{4.17}$$

---

[5] Shifter tensor $\boldsymbol{\mu}$ should not be confused with the moment tensor defined by Eq. (3.7)

The metric tensors can also be related through the shifter tensors as

$$\begin{aligned} G_{\alpha\beta} &= {\mu_0}^{\epsilon}_{\alpha}\, {\mu_0}^{\nu}_{\beta}\, A_{\epsilon\nu} \ , \\ g_{\alpha\beta} &= \mu^{\epsilon}_{\alpha}\, \mu^{\nu}_{\beta}\, a_{\epsilon\nu} \ . \end{aligned} \tag{4.18}$$

The determinants of the shifting tensors, called *shifters*, are

$$\begin{aligned} \mu \ &:= \ \det \boldsymbol{\mu} \ = \ \sqrt{g/a} \ = 1 - 2\,H\,\xi + K\,\xi^2 \ , \\ \mu_0 \ &:= \ \det \boldsymbol{\mu}_0 \ = \ \sqrt{G/A} \ = 1 - 2\,H_0\,\xi + K_0\,\xi^2 \ , \end{aligned} \tag{4.19}$$

where we have defined

$$G := \det[G_{\alpha\beta}] \ , \qquad g := \det[g_{\alpha\beta}] \ . \tag{4.20}$$

As schematically depicted in Fig. 4.2, the shifter μ relates an infinitesimal surface element $\mathrm{d}g$ on $\overset{*}{\mathcal{S}}$ to a corresponding surface element $\mathrm{d}a$ on $\mathcal{S}$, and likewise for μ_0, as

$$\mathrm{d}g = \sqrt{g}\,\mathrm{d}\xi^1\,\mathrm{d}\xi^2 = \mu\,\mathrm{d}a \ , \qquad \mathrm{d}G = \sqrt{G}\,\mathrm{d}\xi^1\,\mathrm{d}\xi^2 = \mu_0\,\mathrm{d}A \ . \tag{4.21}$$

due to Eq. (4.19) and

$$\mathrm{d}a = \sqrt{a}\,\mathrm{d}\xi^1\,\mathrm{d}\xi^2 \ , \qquad \mathrm{d}A = \sqrt{A}\,\mathrm{d}\xi^1\,\mathrm{d}\xi^2 \ . \tag{4.22}$$

Therefore, the volume elements in $\mathcal{B}$ and $\mathcal{B}_0$ can be expressed, respectively, as

$$\mathrm{d}v = \mathrm{d}\xi\,\mathrm{d}g = \mu\,\mathrm{d}\xi\,\mathrm{d}a \ , \qquad \mathrm{d}V = \mathrm{d}\xi\,\mathrm{d}G = \mu_0\,\mathrm{d}\xi\,\mathrm{d}A \ . \tag{4.23}$$

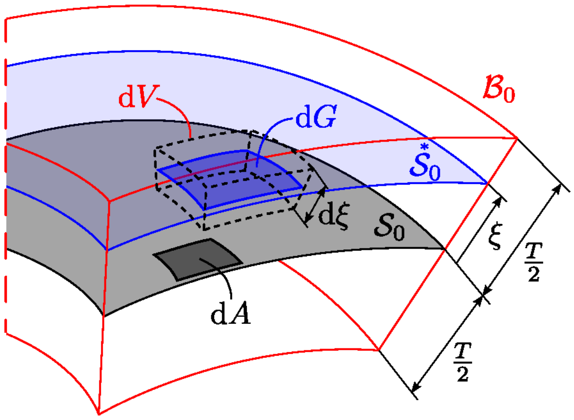

FIGURE 4.2: Schematic illustration of $\mathrm{d}A$, $\mathrm{d}G$ and $\mathrm{d}V$ on $\mathcal{S}_0$, $\overset{*}{\mathcal{S}}_0$ and $\mathcal{B}_0$, respectively

4.1.2 Projection of 3D constitutive models

Considering a 3D hyperelastic material model given by $\tilde{W}(\tilde{E}_{ij}) = \tilde{W}(g_{ij})$, it can be expressed as $\tilde{W}(g_{\alpha\beta}, g_{33})$, following the 3D kinematics described in Sec. 4.1.1. The objective of the projection is to obtain a 2D stored energy per reference surface, e.g. $W(a_{\alpha\beta}, b_{\alpha\beta})$ from the given 3D stored energy per reference volume, i.e. $\tilde{W}(g_{\alpha\beta}, g_{33})$ defined on $\overset{*}{\mathcal{S}}$.

The total energy stored in a shell or membrane is

$$\begin{aligned} \int_{\mathcal{B}_0} \tilde{W}(g_{ij})\,\mathrm{d}V &= \int_{\mathcal{B}_0} \tilde{W}(g_{\alpha\beta}, g_{33})\,\mathrm{d}V \\ &= \int_{\mathcal{S}_0} \int_{-\frac{T}{2}}^{\frac{T}{2}} \tilde{W}(g_{\alpha\beta}, g_{33})\,\mu_0\,\mathrm{d}\xi\,\mathrm{d}A \\ &= \int_{\mathcal{S}_0} W(a_{\alpha\beta}, b_{\alpha\beta}, \lambda_3)\,\mathrm{d}A\ , \end{aligned} \tag{4.24}$$

which gives the projected strain energy density function per reference surface as

$$W(a_{\alpha\beta}, b_{\alpha\beta}, \lambda_3) = \int_{-\frac{T}{2}}^{\frac{T}{2}} \tilde{W}(g_{\alpha\beta}, g_{33})\,\mu_0\,\mathrm{d}\xi\ . \tag{4.25}$$

Remark 4.4. According to the Kirchhoff–Love hypothesis, cross sections remain unstretched as the shell deforms, which implies that $G_{33} = g_{33} = 1$. This corresponds to a plain-strain condition considering that the out-of-plane shear strains are always assumed to be zero, i.e. $G_{\alpha 3} = g_{\alpha 3} = 0$. However, for thin membranes and shells, a plain-stress condition is usually more preferred, which requires g_{33} to be derived from a plane-stress assumption at the constitutive level. Henceforth, it is assumed that g_{33} is not necessarily equal to one and may vary through the thickness although the thickness is kept fixed in Eq. (4.2). Such contradiction is observed (Bischoff et al., 2004) both in Kirchhoff–Love formulations derived from a 3D continuum (e.g. Kiendl et al., 2015b) and also classical plate and shell theory.

As illustrated in Tab. 4.1, depending on the considered strain distribution through the thickness of a thin-walled structure, defined by Eq. (4.6), different structural models can be obtained, namely membranes, classical Kirchhoff–Love shells and modified Kirchhoff–Love shells. In the next sections, each structural model is investigated particularly. A quadratic in-plane strain distribution results in a complicated shell formulation (see e.g. Duong et al., 2017), which is not studied here. In practice, the assumption of a linear in-plane strain variation across the shell thickness considerably simplifies the formulation (cf. Duong et al., 2017) yet it is accurate for thin shells.

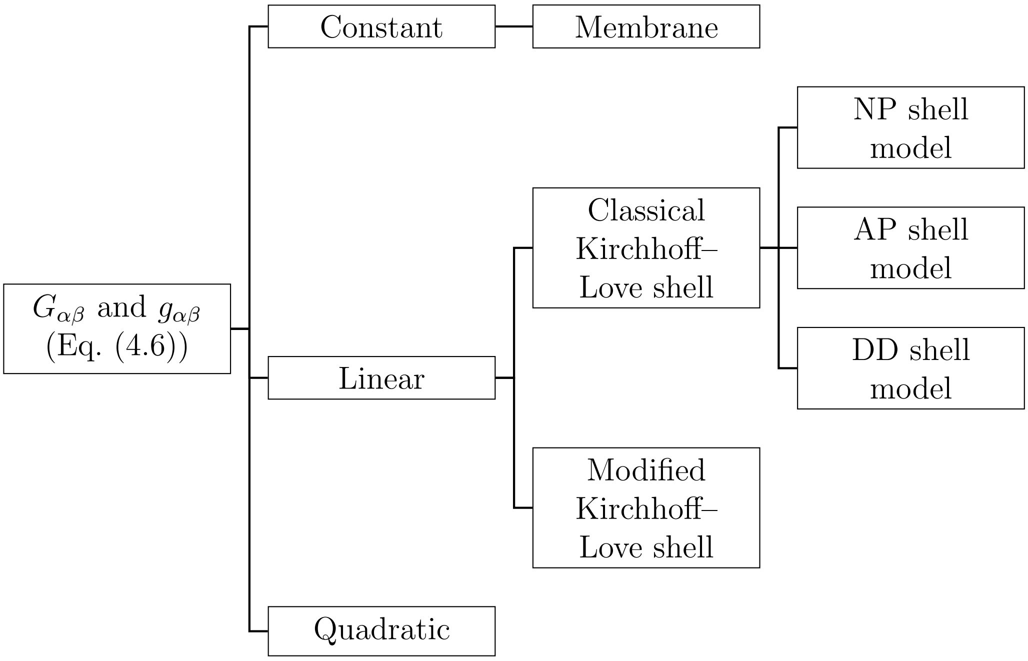

Table 4.1: Projection approaches for a thin-walled structure according to the strain distribution through the thickness

4.2 Membranes

For membranes, where the thickness is much smaller than the other dimensions, it can be assumed that the strains are constant through the thickness. Thus, the resistance of membranes to bending is negligible. Further, as out-of-plane shear deformations are neglected and the thickness stretch is considered constant across the surface, the in-plane stresses of membrane are constant over the thickness. Therefore stresses can be directly derived from the strain energy density function of a two-dimensional manifold (Roohbakhshan et al., 2016).

4.2.1 Kinematics of membranes

Neglecting linear and quadratic terms in Eq. (4.6), we have

$$\begin{aligned} g_{\alpha\beta} &= a_{\alpha\beta}\ , \\ G_{\alpha\beta} &= A_{\alpha\beta}\ . \end{aligned} \tag{4.26}$$

Besides, it is assumed that the normal stretch is also constant through the membrane thickness, i.e. $g_{33} = \lambda_3^2$, where $\lambda_3 := t/T$ is the thickness stretch introduced in Remark 4.2. Accordingly, keeping the constant term in Eq. (4.19.2), $\mu_0 = 1$. The deformation gradient can be expressed as

$$\tilde{\boldsymbol{F}} := \boldsymbol{F} + \lambda_3\, \boldsymbol{n} \otimes \boldsymbol{N} \ , \tag{4.27}$$

where $\boldsymbol{F}$ is given by Eq. (2.48). Following the decomposition of deformation into in-plane and out-of-plane components, the determinant of deformation gradient is

$$\tilde{J} := \det \tilde{\boldsymbol{F}} = J\, \lambda_3 \ , \tag{4.28}$$

where the surface changes are determined by

$$J := \det \boldsymbol{F} = \sqrt{a/A} \ . \tag{4.29}$$

The 3D right Cauchy-Green deformation tensor (2.61) becomes

$$\tilde{\boldsymbol{C}} = \boldsymbol{C} + \lambda_3^2\, \boldsymbol{N} \otimes \boldsymbol{N} \ , \tag{4.30}$$

where $\boldsymbol{C}$ is the surface right Cauchy-Green deformation tensor, given by Eq. (2.62). The first invariant of $\tilde{\boldsymbol{C}}$ is

$$\tilde{I}_1 = \tilde{\boldsymbol{C}} : \boldsymbol{1} = I_1 + \lambda_3^2 \ , \tag{4.31}$$

where

$$I_1 = \boldsymbol{C} : \boldsymbol{I} = A^{\alpha\beta}\, a_{\alpha\beta} \ , \tag{4.32}$$

is the first invariant of the surface right Cauchy-Green deformation tensor. Here, $\boldsymbol{1}$ and $\boldsymbol{I}$ are the full and the reference in-plane identity tensors, respectively, which are related by Eqs. (2.59) and (2.60). The second and third invariants of the right Cauchy-Green deformation tensor are then

$$\tilde{I}_2 := \frac{1}{2}\left[\left(\operatorname{tr}\tilde{\boldsymbol{C}}\right)^2 - \operatorname{tr}\tilde{\boldsymbol{C}}^2\right] = \lambda_3^2\, I_1 + J^2 \tag{4.33}$$

and

$$\tilde{I}_3 := \det \tilde{\boldsymbol{C}} = \tilde{J}^2 = \lambda_3^2\, J^2 \ . \tag{4.34}$$

The Green–Lagrange strain tensor is then

$$\tilde{\boldsymbol{E}} := \frac{1}{2}\left(\tilde{\boldsymbol{C}} - \boldsymbol{1}\right) = \boldsymbol{E} + E_{33}\, \boldsymbol{N} \otimes \boldsymbol{N} \ , \tag{4.35}$$

where the surface Green–Lagrange strain tensor, $\boldsymbol{E}$, is given by Eqs. (2.66) and (2.68). The out-of-plane component of $\tilde{\boldsymbol{E}}$ is then

$$E_{33} = \frac{1}{2}\left(\lambda_3^2 - 1\right) \ . \tag{4.36}$$

4.2.2 Constitution

As the strains are constant over the thickness, i.e. $g_{\alpha\beta} = a_{\alpha\beta}$ and $g_{33} = \lambda_3^2$, and $\mu_0 = 1$, a 3D material model can be reduced to a 2D constitution according to Eq. (4.25) as

$$W_\mathrm{M} = W_\mathrm{M}(a_{\alpha\beta}, \lambda_3) = \int_{-\frac{T}{2}}^{\frac{T}{2}} \tilde{W}(g_{\alpha\beta}, g_{33})\,\mathrm{d}\xi = T\,\hat{W}(a_{\alpha\beta}, \lambda_3)\ , \tag{4.37}$$

where

$$\hat{W}(a_{\alpha\beta}, \lambda_3) := \Big[\tilde{W}(g_{\alpha\beta}, g_{33})\Big]_{\xi=0} \tag{4.38}$$

is the 3D strain energy density function in terms of the mid-surface metric tensor $a_{\alpha\beta}$ and normal stretch λ_3. From Eq. (4.37), we have

$$\begin{aligned} \delta W_\mathrm{M} &= \tau^{\alpha\beta}\,\delta E_{\alpha\beta} \ + \tau^{33}\,\delta E_{33} \\ &= \tau^{\alpha\beta}\,\frac{1}{2}\,\delta a_{\alpha\beta} \ + \tau^{33}\,\lambda_3\,\delta\lambda_3\ , \end{aligned} \tag{4.39}$$

where we have defined

$$\begin{aligned} \tau^{\alpha\beta} &:= \frac{\partial W_\mathrm{M}}{\partial E_{\alpha\beta}} = 2\,\frac{\partial W_\mathrm{M}}{\partial a_{\alpha\beta}} = 2\,T\,\frac{\partial \hat{W}}{\partial a_{\alpha\beta}}\ , \\ \tau^{33} &:= \frac{\partial W_\mathrm{M}}{\partial E_{33}} = \frac{1}{\lambda_3}\,\frac{\partial W_\mathrm{M}}{\partial \lambda_3} = \frac{T}{\lambda_3}\,\frac{\partial \hat{W}}{\partial \lambda_3}\ . \end{aligned} \tag{4.40}$$

Remark 4.5. For a membrane, the normal stretch λ_3 can be determined from either the *plane-stress* or the *plane-strain* condition. If the plane-stress condition is assumed, $\tau^{33} = 0$. If the plane-strain condition is considered, $\lambda_3 = 1$; therefore, $\delta\lambda_3 = 0$. Hence, both approaches imply that the rear term in Eq. (4.39.2) would vanish.

From Eq. (3.50), it follows that and

$$c^{\alpha\beta\gamma\delta} := 2\,\frac{\partial \tau^{\alpha\beta}}{\partial a_{\gamma\delta}} = 4\,T\,\frac{\partial^2 \hat{W}}{\partial a_{\alpha\beta}\,\partial a_{\gamma\delta}} \tag{4.41}$$

are the components of the membrane elasticity tensor.

4.3 Classical Kirchhoff–Love shells

In the classical Kirchhoff–Love shell theory, it is common to consider a linear strain distribution through the thickness (see e.g. Kiendl et al., 2009; Echter et al., 2013 and Kiendl et al., 2015b). This assumption is suitable for thin shells, which have a curvature radius larger than the thickness ($R/t \geq 20$). The presented work is mainly focused on this type of thin shells, which is computationally feasible and robust for many applications. An alternative formulation, which has a slightly different kinematics, is introduced in Sec. 4.4.

4.3.1 Kinematics of Kirchhoff–Love shells

Neglecting quadratic terms in Eqs. (4.6) and (4.19), we get

$$\begin{aligned} g_{\alpha\beta} &= a_{\alpha\beta} - 2\,\xi\, b_{\alpha\beta}\ , \\ G_{\alpha\beta} &= A_{\alpha\beta} - 2\,\xi\, B_{\alpha\beta} \end{aligned} \tag{4.42}$$

and

$$\mu_0 = 1 - 2\,H_0\,\xi\ . \tag{4.43}$$

Remark 4.6. For thin shells, it is also common to use $\mu_0 \approx 1$. For initially-flat shells, where $H_0 = 0$, Eq. (4.43) reduces to $\mu_0 = 1$ without any approximation. For initially-curved shells, this approximation introduces error if the shell is not considerably thin.

On $\overset{*}{\mathcal{S}}$, the deformation gradient can be decomposed to in-plane and out-of-plane components as

$$\tilde{\boldsymbol{F}} := \overset{*}{\boldsymbol{F}} + \overset{*}{\lambda}_3\, \boldsymbol{n} \otimes \boldsymbol{N}\ , \tag{4.44}$$

where $\overset{*}{\boldsymbol{F}} = \boldsymbol{g}_\alpha \otimes \boldsymbol{G}^\alpha$ is the layer deformation gradient and $\overset{*}{\lambda}_3$ is the normal stretch so that

$$g_{33} = \overset{*}{\lambda}{}_3^2\ . \tag{4.45}$$

Remark 4.7. It should be noted that $\lambda_3 = \overset{*}{\lambda}_3$ only for a membrane formulation. In general, λ_3 is the average of $\overset{*}{\lambda}_3$ over the shell thickness as

$$\lambda_3 = \frac{1}{T}\int_{-\frac{T}{2}}^{\frac{T}{2}} \overset{*}{\lambda}_3\, \mathrm{d}\xi\ . \tag{4.46}$$

From Eq. (4.44), we get

$$\tilde{J} := \det \tilde{\boldsymbol{F}} = \overset{*}{J}\,\overset{*}{\lambda}_3\ , \tag{4.47}$$

where

$$\overset{*}{J} := \det \overset{*}{\boldsymbol{F}} = \sqrt{g/G}\ . \tag{4.48}$$

The 3D right Cauchy–Green deformation tensor (2.61) is split as

$$\tilde{\boldsymbol{C}} = \overset{*}{\boldsymbol{C}} + \overset{*}{\lambda}{}_3^2\, \boldsymbol{N} \otimes \boldsymbol{N}\ , \tag{4.49}$$

where

$$\overset{*}{\boldsymbol{C}} := \overset{*}{\boldsymbol{F}}{}^{\mathrm{T}}\overset{*}{\boldsymbol{F}} = g_{\alpha\beta}\,\boldsymbol{G}^{\alpha} \otimes \boldsymbol{G}^{\beta} \tag{4.50}$$

is the right Cauchy–Green deformation tensor on $\overset{*}{\mathcal{S}}$. The first invariant of $\tilde{\boldsymbol{C}}$ is

$$\tilde{I}_1 = \tilde{\boldsymbol{C}} : \boldsymbol{1} = \overset{*}{I}_1 + \overset{*}{\lambda}{}_3^2 \ , \tag{4.51}$$

where

$$\overset{*}{I}_1 = \overset{*}{\boldsymbol{C}} : \overset{*}{\boldsymbol{I}} = G^{\alpha\beta}\,g_{\alpha\beta} \ , \tag{4.52}$$

is the first invariant of $\overset{*}{\boldsymbol{C}}$. Here, $\boldsymbol{1}$ is the usual identity tensor in $\mathbb{R}^3$ and $\overset{*}{\boldsymbol{I}}$ is the in-plane identity tensor on $\overset{*}{\mathcal{S}}$ given by

$$\overset{*}{\boldsymbol{I}} = G_{\alpha\beta}\,\boldsymbol{G}^{\alpha} \otimes \boldsymbol{G}^{\beta} = G^{\alpha\beta}\,\boldsymbol{G}_{\alpha} \otimes \boldsymbol{G}_{\beta} \ . \tag{4.53}$$

The second and third invariants of $\tilde{\boldsymbol{C}}$ are then

$$\tilde{I}_2 := \frac{1}{2}\left[\left(\mathrm{tr}\,\tilde{\boldsymbol{C}}\right)^2 - \mathrm{tr}\,\tilde{\boldsymbol{C}}^2\right] = \overset{*}{\lambda}{}_3^2\,\overset{*}{I}_1 + \overset{*}{J}{}^2 \tag{4.54}$$

and

$$\tilde{I}_3 := \det\tilde{\boldsymbol{C}} = \tilde{J}^2 = \overset{*}{\lambda}{}_3^2\,\overset{*}{J}{}^2 \ . \tag{4.55}$$

Likewise, the Green–Lagrange strain tensor is split into in-plane and out-of-plane components as

$$\tilde{\boldsymbol{E}} := \frac{1}{2}\left(\tilde{\boldsymbol{C}} - \boldsymbol{1}\right) = \overset{*}{\boldsymbol{E}} + \overset{*}{E}_{33}\,\boldsymbol{N} \otimes \boldsymbol{N} \ . \tag{4.56}$$

Here, the surface Green–Lagrange strain tensor is

$$\overset{*}{\boldsymbol{E}} := \frac{1}{2}\left(\overset{*}{\boldsymbol{C}} - \overset{*}{\boldsymbol{I}}\right) = \overset{*}{E}_{\alpha\beta}\,\boldsymbol{G}^{\alpha} \otimes \boldsymbol{G}^{\beta} \ , \tag{4.57}$$

where

$$\overset{*}{E}_{\alpha\beta} = \frac{1}{2}\left(g_{\alpha\beta} - G_{\alpha\beta}\right) \ . \tag{4.58}$$

The out-of-plane component of $\tilde{\boldsymbol{E}}$ becomes

$$\overset{*}{E}_{33} = \frac{1}{2}\left(g_{33} - G_{33}\right) = \frac{1}{2}\left(\overset{*}{\lambda}{}_3^2 - 1\right) \ . \tag{4.59}$$

Remark 4.8. Eqs. (4.42) and (4.58) imply that the distribution of the in-plane strain across the shell thickness is linear, i.e.

$$\overset{*}{E}_{\alpha\beta} = E_{\alpha\beta} - \xi\,K_{\alpha\beta} \ , \tag{4.60}$$

where $E_{\alpha\beta}$ and $K_{\alpha\beta}$ are given by Eqs. (2.68) and (2.70), respectively.

4.3.2 Constitution: Three modeling approaches

In general, there are two different approaches for structural modeling in shell theory (Bischoff et al., 2004). In the *projection approach*, a shell constitution is derived from a 3D continuum. This approach requires through-the-thickness integration, which is performed rarely analytically and mostly numerically (e.g. Duong et al., 2017). In the *direct surface approach*, a shell is considered as a 2D manifold, physically defined on the mid-surface of the shell continuum. Thus, the stresses are directly derived from a 2D strain energy density function per reference surface (e.g. Sauer and Duong, 2017). Alternatively, the *degenerated solid approach* can also be used, which is a method to reduce the dimension of 3D solid finite elements and is not based on a shell theory (Bischoff et al., 2004).

<table>
<tr><th></th><th colspan="2">*Projection approach*</th><th>*Direct surface approach*</th></tr>
<tr><td>Model</td><td>Numerically-projected (NP)</td><td>Analytically-projected (AP)</td><td>Directly-decoupled (DD)</td></tr>
<tr><td>Geometry</td><td>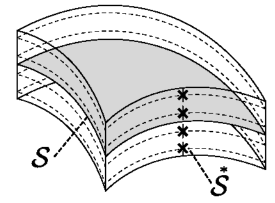
</td><td>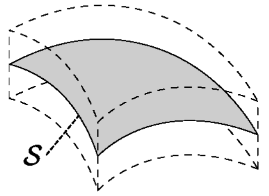
</td><td>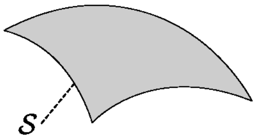
</td></tr>
<tr><td>Strain</td><td>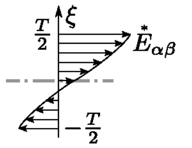
</td><td>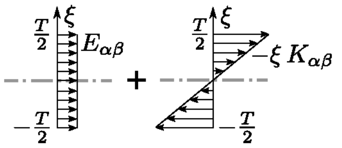
</td><td>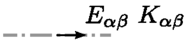
</td></tr>
<tr><td>Stress</td><td>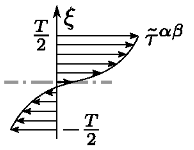
</td><td>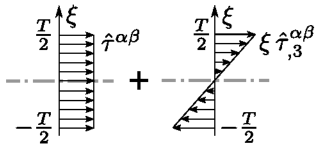
</td><td>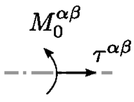
</td></tr>
<tr><td>Variables</td><td>$\tilde{\tau}^{\alpha\beta}$ (4.62)
$\tilde{c}^{\alpha\beta\gamma\delta}$ (4.67)</td><td>$\hat{\tau}^{\alpha\beta}$ (4.71.1)
$\hat{\tau}^{\alpha\beta}_{,3}$ (4.71.2)
$\hat{c}^{\alpha\beta\gamma\delta}$, $\hat{d}^{\alpha\beta\gamma\delta}$ (4.74.1)
$\hat{c}^{\alpha\beta\gamma\delta}_{,3}$, $\hat{d}^{\alpha\beta\gamma\delta}_{,3}$ (4.74.2)</td><td>$\tau^{\alpha\beta}$ (4.40)
$c^{\alpha\beta\gamma\delta}$ (4.41)
$c_0^{\alpha\beta\gamma\delta}$ (4.97)
$f^{\alpha\beta\gamma\delta}$ (4.101)</td></tr>
<tr><td colspan="4">Efficiency
Accuracy
</td></tr>
</table>

TABLE 4.2: Three constitutive modeling approaches for thin shells

As shown in Tab. 4.2, here, three different constitutive modeling strategies for thin shells are introduced: The *numerically-projected* (NP) shell model, which is a classical projection approach (Bischoff et al., 2004) based on numerical integration through the shell thickness. The *directly-decoupled* (DD) shell model, which is a direct surface approach, is a systematic extension of the combined Koiter/Neo-Hooke shell formulation of Duong et al. (2017). Further, the *analytically-projected* (AP) shell model is presented, which combines elements of both approaches and provides an algorithm to analytically evaluate the integration through the shell thickness.

4.3.2.1 Numerically-projected (NP) shell model

Considering $\tilde{W} = \tilde{W}(g_{\alpha\beta}, g_{33})$ to be the 3D strain energy density function defined on a shell layer $\overset{*}{\mathcal{S}}$ at $\xi \in [-T/2, T/2]$,

$$\delta\tilde{W} = \frac{1}{2}\,\tilde{\tau}^{\alpha\beta}\,\delta g_{\alpha\beta} + \frac{1}{2}\,\tilde{\tau}^{33}\,\overset{*}{\lambda}_3\,\delta\overset{*}{\lambda}_3 \;, \tag{4.61}$$

where we have defined

$$\begin{aligned}\tilde{\tau}^{\alpha\beta} &:= \frac{\partial\tilde{W}}{\partial\overset{*}{E}_{\alpha\beta}} = 2\,\frac{\partial\tilde{W}}{\partial g_{\alpha\beta}} \;, \\ \tilde{\tau}^{33} &:= \frac{\partial\tilde{W}}{\partial\overset{*}{E}_{33}} = 2\,\frac{\partial\tilde{W}}{\partial g_{33}} = \frac{1}{\overset{*}{\lambda}_3}\,\frac{\partial\tilde{W}}{\partial\overset{*}{\lambda}_3}\end{aligned} \tag{4.62}$$

as the Kirchhoff stress components on $\overset{*}{\mathcal{S}}$.

Remark 4.9. Likewise to the membranes, the contribution of normal strains and stresses to the total internal energy of a shell can be omitted by assuming either a *plane-strain* condition, i.e. $\delta\overset{*}{\lambda}_3 = 0$, or a *plane-stress* condition, i.e. $\tilde{\tau}^{33} = 0$.

Remark 4.10. In general, the Kirchhoff–Love shell theory seems to be restrictive as assuming $\overset{*}{E}_{33} = \overset{*}{E}_{3\alpha} = 0$ implies a *plane-strain* condition while $\tilde{\tau}^{33} = \tilde{\tau}^{3\alpha} = 0$ corresponds to a *plane-stress* condition. In linear elasticity, both cases can simultaneously happen only in special cases, e.g. if the Poisson's ratio is zero. Nevertheless, the assumption of zero shearing strains (i.e. $\overset{*}{E}_{3\alpha} = 0$) and zero shearing stresses (i.e. $\tilde{\tau}^{3\alpha} = 0$) is consistent in both conditions. However, if thin shells undergo large strains, as biological membranes and shells do, the assumption of zero through-the-thickness strain (i.e. $\overset{*}{E}_{33} = 0$) is not valid anymore. For thin structures, it is physically more consistent to assume that the normal stress is zero. Thus, the material law is modified by assuming $\tilde{\tau}^{33} = 0$ to eliminate $\overset{*}{E}_{33}$ by static condensation (Bischoff et al., 2004; Echter, 2013; Kiendl et al., 2015b; Duong et al., 2017) and the assumption of $\overset{*}{E}_{33} = 0$ is dropped.

Thus, Eq. (4.61) is reduced to

$$\delta\tilde{W} = \frac{1}{2}\,\tilde{\tau}^{\alpha\beta}\,\delta g_{\alpha\beta}\ , \tag{4.63}$$

where $\overset{*}{\lambda}_3$ is found from a plane-stress condition and is statically condensed into $\tilde{\tau}^{\alpha\beta}$. Plugging Eqs. (4.63) and (A.10) into Eq. (4.25), we get

$$\delta W = \frac{1}{2}\int_{-\frac{T}{2}}^{\frac{T}{2}} \tilde{\tau}^{\alpha\beta}\,\mu_0\,\mathrm{d}\xi\,\delta a_{\alpha\beta} + \int_{-\frac{T}{2}}^{\frac{T}{2}} \xi\,\tilde{\tau}^{\alpha\beta}\,\mu_0\,\mathrm{d}\xi\,\delta b_{\alpha\beta}\ . \tag{4.64}$$

Thus, the resultant stress and moment tensors are

$$\begin{aligned} \tau^{\alpha\beta} &:= 2\,\frac{\partial W}{\partial a_{\alpha\beta}} &&= \int_{-\frac{T}{2}}^{\frac{T}{2}} \tilde{\tau}^{\alpha\beta}\,\mu_0\,\mathrm{d}\xi\ , \\ M_0^{\alpha\beta} &:= \frac{\partial W}{\partial b_{\alpha\beta}} &&= -\int_{-\frac{T}{2}}^{\frac{T}{2}} \xi\,\tilde{\tau}^{\alpha\beta}\,\mu_0\,\mathrm{d}\xi\ . \end{aligned} \tag{4.65}$$

To derive the material tangent tensors, one needs to linearize Eq. (4.65) w.r.t. $a_{\alpha\beta}$ and $b_{\alpha\beta}$. Therefore, from Eq. (A.10) we have

$$\begin{aligned} \Delta\tau^{\alpha\beta} &= \frac{1}{2}\int_{-\frac{T}{2}}^{\frac{T}{2}} \tilde{c}^{\alpha\beta\gamma\delta}\,\Delta g_{\gamma\delta}\,\mu_0\,\mathrm{d}\xi \\ &= \frac{1}{2}\int_{-\frac{T}{2}}^{\frac{T}{2}} \tilde{c}^{\alpha\beta\gamma\delta}\,\mu_0\,\mathrm{d}\xi\,\Delta a_{\gamma\delta} - \int_{-\frac{T}{2}}^{\frac{T}{2}} \xi\,\tilde{c}^{\alpha\beta\gamma\delta}\,\mu_0\,\mathrm{d}\xi\,\Delta b_{\gamma\delta}\ , \end{aligned} \tag{4.66}$$

where we have introduced the elasticity tensor

$$\tilde{c}^{\alpha\beta\gamma\delta} := 2\,\frac{\partial\tilde{\tau}^{\alpha\beta}}{\partial g_{\gamma\delta}} \tag{4.67}$$

on $\overset{*}{\mathcal{S}}$. In Chap. 6, $\tilde{c}^{\alpha\beta\gamma\delta}$ is derived specifically for each material model. Similarly, for $M_0^{\alpha\beta}$, one can obtain

$$\begin{aligned} \Delta M_0^{\alpha\beta} &= -\frac{1}{2}\int_{-\frac{T}{2}}^{\frac{T}{2}} \xi\,\tilde{c}^{\alpha\beta\gamma\delta}\,\Delta g_{\gamma\delta}\,\mu_0\,\mathrm{d}\xi \\ &= -\frac{1}{2}\int_{-\frac{T}{2}}^{\frac{T}{2}} \xi\,\tilde{c}^{\alpha\beta\gamma\delta}\,\mu_0\,\mathrm{d}\xi\,\Delta a_{\gamma\delta} + \int_{-\frac{T}{2}}^{\frac{T}{2}} \xi^2\,\tilde{c}^{\alpha\beta\gamma\delta}\,\mu_0\,\mathrm{d}\xi\,\Delta b_{\gamma\delta}\ . \end{aligned} \tag{4.68}$$

From Eqs. (3.35) (4.66), and (4.68), the material tangents are then

$$\begin{aligned} c^{\alpha\beta\gamma\delta} &= \int_{-\frac{T}{2}}^{\frac{T}{2}} \tilde{c}^{\alpha\beta\gamma\delta}\,\mu_0\,\mathrm{d}\xi\ , \\ d^{\alpha\beta\gamma\delta} &= e^{\alpha\beta\gamma\delta} = -\int_{-\frac{T}{2}}^{\frac{T}{2}} \xi\,\tilde{c}^{\alpha\beta\gamma\delta}\,\mu_0\,\mathrm{d}\xi\ , \\ f^{\alpha\beta\gamma\delta} &= \int_{-\frac{T}{2}}^{\frac{T}{2}} \xi^2\,\tilde{c}^{\alpha\beta\gamma\delta}\,\mu_0\,\mathrm{d}\xi\ . \end{aligned} \tag{4.69}$$

In general, the thickness integration in Eqs. (4.65) and (4.69) is performed *numerically* due to the constitutive nonlinearities. Hence, the shell model derived from this approach is called *numerically-projected* here. As already mentioned in Remark 4.6, one can use $\mu_0 \approx 1$ to simplify Eqs. (4.65) and (4.69) further.

4.3.2.2 Analytically-projected (AP) shell model

If the shell thickness is considerably smaller than its in-plane dimensions and its radii of curvature, a first-order Taylor expansion can be used to analytically evaluate the integrals in Eqs. (4.65) and (4.69). This procedure requires all the kinematical objects, stress and moment tensors to be linearized w.r.t. the out-of-plane coordinate ξ. The linearization of the kinematical parameters are given in Appendix A.3. Here, the resultant stress and moment tensors and their corresponding material tangents are derived. As schematically shown in Fig. 4.3, two scenarios are possible for the stress distribution over the cross section of a shell: (1) The cross section of the shell is fully stressed as the whole thickness of the shell contributes to the strain energy density function. (2) The cross section of the shell is partially stressed, i.e. only a portion of the shell thickness, e.g. $[T_1\ T_2] \subset [-T/2\ T/2]$, is contributing due to the constitutive constraints. The former scenario is the typical condition of thin shells while the latter happens for instance if the material bears only compression (e.g. concrete) or only tension (e.g. collagen fibers).

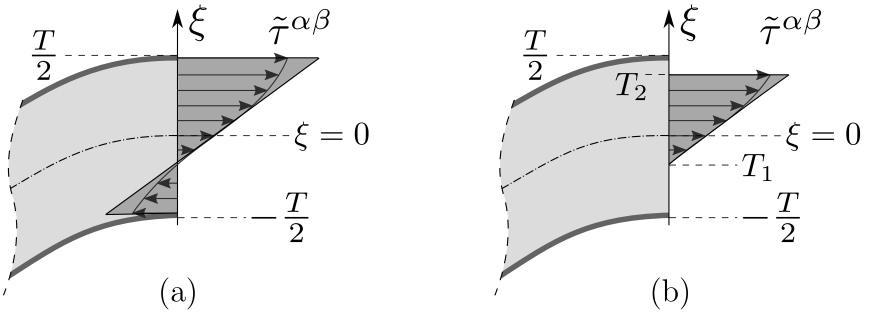

FIGURE 4.3: Stress distribution over the cross section of a shell: (a) Fully-stressed cross-section and (b) Partially-stressed cross-section. The physical stress distribution is denoted by the arrows and the approximated stress is shown by the gray color.

Using a Taylor expansion of $\tilde{\tau}^{\alpha\beta}$ about $\xi = 0$, we have

$$\tilde{\tau}^{\alpha\beta} = \hat{\tau}^{\alpha\beta} + \xi\, \hat{\tau}^{\alpha\beta}_{,3} + O(\xi^2)\ , \tag{4.70}$$

where we have defined

$$\hat{\tau}^{\alpha\beta} := \Big(\tilde{\tau}^{\alpha\beta}\Big)_{\xi=0}\ , \qquad \hat{\tau}^{\alpha\beta}_{,3} := \Big(\frac{\partial \tilde{\tau}^{\alpha\beta}}{\partial \xi}\Big)_{\xi=0}\ . \tag{4.71}$$

4.3.2.2.1 Fully-stressed cross-section

Plugging Eq. (4.70) into Eq. (4.65) and integrating analytically, the resultant stresses and bending moments are

$$\begin{aligned} \tau^{\alpha\beta} &= T\,\hat{\tau}^{\alpha\beta} - H_0\,\frac{T^3}{6}\,\hat{\tau}^{\alpha\beta}_{,3}\ , \\ M_0^{\alpha\beta} &= H_0\,\frac{T^3}{6}\,\hat{\tau}^{\alpha\beta} - \frac{T^3}{12}\,\hat{\tau}^{\alpha\beta}_{,3}\ . \end{aligned} \tag{4.72}$$

The tangent matrices are derived from Eq. (4.72) as

$$\begin{aligned} c^{\alpha\beta\gamma\delta} &:= 2\,\frac{\partial \tau^{\alpha\beta}}{\partial a_{\gamma\delta}} = T\,\hat{c}^{\alpha\beta\gamma\delta} - H_0\,\frac{T^3}{6}\,\hat{c}^{\alpha\beta\gamma\delta}_{,3}\ , \\ d^{\alpha\beta\gamma\delta} &:= \frac{\partial \tau^{\alpha\beta}}{\partial b_{\gamma\delta}} = T\,\hat{d}^{\alpha\beta\gamma\delta} - H_0\,\frac{T^3}{6}\,\hat{d}^{\alpha\beta\gamma\delta}_{,3}\ , \\ e^{\alpha\beta\gamma\delta} &:= 2\,\frac{\partial M_0^{\alpha\beta}}{\partial a_{\gamma\delta}} = H_0\,\frac{T^3}{6}\,\hat{c}^{\alpha\beta\gamma\delta} - \frac{T^3}{12}\,\hat{c}^{\alpha\beta\gamma\delta}_{,3}\ , \\ f^{\alpha\beta\gamma\delta} &:= \frac{\partial M_0^{\alpha\beta}}{\partial b_{\gamma\delta}} = H_0\,\frac{T^3}{6}\,\hat{d}^{\alpha\beta\gamma\delta} - \frac{T^3}{12}\,\hat{d}^{\alpha\beta\gamma\delta}_{,3}\ , \end{aligned} \tag{4.73}$$

where we have defined

$$\begin{aligned} \hat{c}^{\alpha\beta\gamma\delta} &= 2\,\frac{\partial \hat{\tau}^{\alpha\beta}}{\partial a_{\gamma\delta}}\ , \qquad & \hat{d}^{\alpha\beta\gamma\delta} &= \frac{\partial \hat{\tau}^{\alpha\beta}}{\partial b_{\gamma\delta}}\ , \\ \hat{c}^{\alpha\beta\gamma\delta}_{,3} &= 2\,\frac{\partial \hat{\tau}^{\alpha\beta}_{,3}}{\partial a_{\gamma\delta}}\ , \qquad & \hat{d}^{\alpha\beta\gamma\delta}_{,3} &= \frac{\partial \hat{\tau}^{\alpha\beta}_{,3}}{\partial b_{\gamma\delta}}\ . \end{aligned} \tag{4.74}$$

If $\mu_0 \approx 1$, Eq. (4.72) is reduced to

$$\begin{aligned} \tau^{\alpha\beta} &= T\,\hat{\tau}^{\alpha\beta}\ , \\ M_0^{\alpha\beta} &= -\frac{T^3}{12}\,\hat{\tau}^{\alpha\beta}_{,3} \end{aligned} \tag{4.75}$$

and the tangent matrices are then

$$\begin{aligned} c^{\alpha\beta\gamma\delta} &= T\,\hat{c}^{\alpha\beta\gamma\delta}\ , \qquad & d^{\alpha\beta\gamma\delta} &= T\,\hat{d}^{\alpha\beta\gamma\delta}\ , \\ e^{\alpha\beta\gamma\delta} &= -\frac{T^3}{12}\,\hat{c}^{\alpha\beta\gamma\delta}_{,3}\ , \qquad & f^{\alpha\beta\gamma\delta} &= -\frac{T^3}{12}\,\hat{d}^{\alpha\beta\gamma\delta}_{,3}\ . \end{aligned} \tag{4.76}$$

4.3.2.2.2 Partially-stressed cross-section

As already mentioned, in many applications, the strain energy density function and accordingly the in-plane stresses are nonzero only in a portion of the shell thickness, i.e.

$$\begin{aligned} \tau^{\alpha\beta} &= \int_{T_1}^{T_2} \tilde{\tau}^{\alpha\beta}\,\mathrm{d}\xi\ , \\ M_0^{\alpha\beta} &= -\int_{T_1}^{T_2} \xi\,\tilde{\tau}^{\alpha\beta}\,\mathrm{d}\xi\ . \end{aligned} \tag{4.77}$$

Plugging Eq. (4.70) into Eq. (4.77), one can analytically calculate the stress and the bending moment resultants as

$$\begin{aligned} \tau^{\alpha\beta} &= \big(T_2 - T_1\big)\,\hat{\tau}^{\alpha\beta} + \frac{1}{2}\big(T_2^2 - T_1^2\big)\,\hat{\tau}^{\alpha\beta}_{,3} \\ &\quad - H_0\left[\big(T_2^2 - T_1^2\big)\,\hat{\tau}^{\alpha\beta} + \frac{2}{3}\big(T_2^3 - T_1^3\big)\,\hat{\tau}^{\alpha\beta}_{,3}\right]\ , \\ M_0^{\alpha\beta} &= \frac{1}{2}\big(T_1^2 - T_2^2\big)\,\hat{\tau}^{\alpha\beta} + \frac{1}{3}\big(T_1^3 - T_2^3\big)\,\hat{\tau}^{\alpha\beta}_{,3} \\ &\quad + H_0\left[\frac{2}{3}\big(T_2^3 - T_1^3\big)\,\hat{\tau}^{\alpha\beta} + \frac{1}{2}\big(T_2^4 - T_1^4\big)\,\hat{\tau}^{\alpha\beta}_{,3}\right]\ . \end{aligned} \tag{4.78}$$

However, the derivation of the material tangents is not so simple since T_1 and T_2 are not considered to be generally fixed and they may vary with $\boldsymbol{x}$, i.e.

$$\begin{aligned} T_1 &= T_1(\boldsymbol{x}) = T_1(a_{\alpha\beta}, b_{\alpha\beta}) \ , \\ T_2 &= T_2(\boldsymbol{x}) = T_2(a_{\alpha\beta}, b_{\alpha\beta}) \end{aligned} \tag{4.79}$$

and they are defined based on the constitution and application. Thus, introducing

$$\begin{aligned} U_1^{\alpha\beta} &:= \frac{\partial T_1}{\partial a_{\alpha\beta}} \ , \qquad U_2^{\alpha\beta} := \frac{\partial T_2}{\partial a_{\alpha\beta}} \ , \\ V_1^{\alpha\beta} &:= \frac{\partial T_1}{\partial b_{\alpha\beta}} \ , \qquad V_2^{\alpha\beta} := \frac{\partial T_2}{\partial b_{\alpha\beta}} \ , \end{aligned} \tag{4.80}$$

the material tangents are derived as

$$\begin{aligned} c^{\alpha\beta\gamma\delta} &= \big(T_2 - T_1\big)\, \hat{c}^{\alpha\beta\gamma\delta} + \frac{1}{2}\big(T_2^2 - T_1^2\big)\, \hat{c}^{\alpha\beta\gamma\delta}_{,3} \\ &\quad - H_0 \Big[\big(T_2^2 - T_1^2\big)\, \hat{c}^{\alpha\beta\gamma\delta} + \frac{2}{3}\big(T_2^3 - T_1^3\big)\, \hat{c}^{\alpha\beta\gamma\delta}_{,3}\Big] \\ &\quad + 2\,\tilde{\tau}_2^{\alpha\beta}\, U_2^{\gamma\delta}\,(1 - 2\,H_0\,T_2) - 2\,\tilde{\tau}_1^{\alpha\beta}\, U_1^{\gamma\delta}\,(1 - 2\,H_0\,T_1) \ , \end{aligned} \tag{4.81}$$

$$\begin{aligned} d^{\alpha\beta\gamma\delta} &= \big(T_2 - T_1\big)\, \hat{d}^{\alpha\beta\gamma\delta} + \frac{1}{2}\big(T_2^2 - T_1^2\big)\, \hat{d}^{\alpha\beta\gamma\delta}_{,3} \\ &\quad - H_0 \Big[\big(T_2^2 - T_1^2\big)\, \hat{d}^{\alpha\beta\gamma\delta} + \frac{2}{3}\big(T_2^3 - T_1^3\big)\, \hat{d}^{\alpha\beta\gamma\delta}_{,3}\Big] \\ &\quad + \tilde{\tau}_2^{\alpha\beta}\, V_2^{\gamma\delta}\,(1 - 2\,H_0\,T_2) - \tilde{\tau}_1^{\alpha\beta}\, V_1^{\gamma\delta}\,(1 - 2\,H_0\,T_1) \ , \end{aligned} \tag{4.82}$$

$$\begin{aligned} e^{\alpha\beta\gamma\delta} &= \frac{1}{2}\big(T_1^2 - T_2^2\big)\, \hat{c}^{\alpha\beta\gamma\delta} + \frac{1}{3}\big(T_1^3 - T_2^3\big)\, \hat{c}^{\alpha\beta\gamma\delta}_{,3} \\ &\quad + H_0 \Big[\frac{2}{3}\big(T_2^3 - T_1^3\big)\, \hat{c}^{\alpha\beta\gamma\delta} + \frac{1}{2}\big(T_2^4 - T_1^4\big)\, \hat{c}^{\alpha\beta\gamma\delta}_{,3}\Big] \\ &\quad + 2\,T_2\,\tilde{\tau}_2^{\alpha\beta}\, U_2^{\gamma\delta}\,(2\,H_0\,T_2 - 1) - 2\,T_1\,\tilde{\tau}_1^{\alpha\beta}\, U_1^{\gamma\delta}\,(2\,H_0\,T_1 - 1) \end{aligned} \tag{4.83}$$

and

$$\begin{aligned} f^{\alpha\beta\gamma\delta} &= \frac{1}{2}\big(T_1^2 - T_2^2\big)\, \hat{d}^{\alpha\beta\gamma\delta} + \frac{1}{3}\big(T_1^3 - T_2^3\big)\, \hat{d}^{\alpha\beta\gamma\delta}_{,3} \\ &\quad + H_0 \Big[\frac{2}{3}\big(T_2^3 - T_1^3\big)\, \hat{d}^{\alpha\beta\gamma\delta} + \frac{1}{2}\big(T_2^4 - T_1^4\big)\, \hat{d}^{\alpha\beta\gamma\delta}_{,3}\Big] \\ &\quad + T_2\,\tilde{\tau}_2^{\alpha\beta}\, V_2^{\gamma\delta}\,(2\,H_0\,T_2 - 1) - T_1\,\tilde{\tau}_1^{\alpha\beta}\, V_1^{\gamma\delta}\,(2\,H_0\,T_1 - 1) \ . \end{aligned} \tag{4.84}$$

Here, $\tilde{\tau}_1^{\alpha\beta}$ and $\tilde{\tau}_2^{\alpha\beta}$ are the stresses corresponding to the lower and upper limits, respectively, which are defined as

$$\begin{aligned} \tilde{\tau}_1^{\alpha\beta} &:= \big(\tilde{\tau}^{\alpha\beta}\big)_{\xi=T_1} = \hat{\tau}^{\alpha\beta} + T_1\, \hat{\tau}^{\alpha\beta}_{,3} \ , \\ \tilde{\tau}_2^{\alpha\beta} &:= \big(\tilde{\tau}^{\alpha\beta}\big)_{\xi=T_2} = \hat{\tau}^{\alpha\beta} + T_2\, \hat{\tau}^{\alpha\beta}_{,3} \ . \end{aligned} \tag{4.85}$$

If $\mu_0 \approx 1$, Eq. (4.78) and Eqs. (4.81)-(4.84) are reduced, respectively, to

$$\begin{aligned} \tau^{\alpha\beta} &= \big(T_2 - T_1\big)\,\hat{\tau}^{\alpha\beta} + \frac{1}{2}\big(T_2^2 - T_1^2\big)\,\hat{\tau}^{\alpha\beta}_{,3}\,, \\ M_0^{\alpha\beta} &= \frac{1}{2}\big(T_1^2 - T_2^2\big)\,\hat{\tau}^{\alpha\beta} + \frac{1}{3}\big(T_1^3 - T_2^3\big)\,\hat{\tau}^{\alpha\beta}_{,3} \end{aligned} \tag{4.86}$$

and

$$\begin{aligned} c^{\alpha\beta\gamma\delta} &= \big(T_2 - T_1\big)\,\hat{c}^{\alpha\beta\gamma\delta} + \frac{1}{2}\big(T_2^2 - T_1^2\big)\,\hat{c}^{\alpha\beta\gamma\delta}_{,3} + 2\,\tilde{\tau}_2^{\alpha\beta}\,U_2^{\gamma\delta} - 2\,\tilde{\tau}_1^{\alpha\beta}\,U_1^{\gamma\delta}\,, \\ d^{\alpha\beta\gamma\delta} &= \big(T_2 - T_1\big)\,\hat{d}^{\alpha\beta\gamma\delta} + \frac{1}{2}\big(T_2^2 - T_1^2\big)\,\hat{d}^{\alpha\beta\gamma\delta}_{,3} + \tilde{\tau}_2^{\alpha\beta}\,V_2^{\gamma\delta} - \tilde{\tau}_1^{\alpha\beta}\,V_1^{\gamma\delta}\,, \\ e^{\alpha\beta\gamma\delta} &= \frac{1}{2}\big(T_1^2 - T_2^2\big)\,\hat{c}^{\alpha\beta\gamma\delta} + \frac{1}{3}\big(T_1^3 - T_2^3\big)\,\hat{c}^{\alpha\beta\gamma\delta}_{,3} + 2\,T_1\,\tilde{\tau}_1^{\alpha\beta}\,U_1^{\gamma\delta} - 2\,T_2\,\tilde{\tau}_2^{\alpha\beta}\,U_2^{\gamma\delta}\,, \\ f^{\alpha\beta\gamma\delta} &= \frac{1}{2}\big(T_1^2 - T_2^2\big)\,\hat{d}^{\alpha\beta\gamma\delta} + \frac{1}{3}\big(T_1^3 - T_2^3\big)\,\hat{d}^{\alpha\beta\gamma\delta}_{,3} + T_1\,\tilde{\tau}_1^{\alpha\beta}\,V_1^{\gamma\delta} - T_2\,\tilde{\tau}_2^{\alpha\beta}\,V_2^{\gamma\delta}\,. \end{aligned} \tag{4.87}$$

Remark 4.11. It should be noted that the tangent tensors $d^{\alpha\beta\gamma\delta}$ and $e^{\alpha\beta\gamma\delta}$ given by Eqs. (4.73), (4.76), (4.82) and (4.84) and (4.87) are not equal as the linearization and variation are treated differently.

Tab. 4.3 summarizes the procedure to derive a AP shell model from any given 3D material model.

4.3.2.3 Directly-decoupled (DD) shell model

In this approach, the stresses and moments are directly derived from a 2D strain energy density function. Thus, as an advantage, no numerical integration through the thickness of the shell is needed. The presented model completely decouples the membrane and bending forces of a thin shell. The stored stretching energy of the shell depends on the mid-surface metric tensor and the stored bending energy of the shell is only a function of the curvature tensor. A well-know example of this category of shell formulations is the classical Koiter shell model (Ciarlet, 2005 and Sauer and Duong, 2017) introduced in Sec. 3.1.2. The disadvantage of the Koiter shell model (3.17) is being limited to a linear constitutive law. In fact, it can be derived by the projection of a 3D St. Venant–Kirchhoff material model on the shell surface (Duong et al., 2017). A directly-decoupled shell model can be obtained alternatively by combining a membrane model and a bending model. For instance, Sauer and Duong (2017) have combined a Canham model (3.16) and a compressible Neo-Hookean membrane model. In particular, Duong et al. (2017) have proposed a mixed formulation that combines the stored bending energy of a Koiter shell, i.e. the rear term of Eq. (3.17), and the strain energy of a compressible Neo–Hookean membrane. Following this concept, a systematic approach is introduced here to find consistent 2D membrane and bending

1)	For any 3D constitution, with a given strain energy function $\tilde{W}$, derive $\tilde{\tau}^{\alpha\beta}$ according to Eq. (4.62).
2)	Determine $\hat{\tau}^{\alpha\beta}$ from Eqs. (4.71.1) and $\hat{c}^{\alpha\beta\gamma\delta}$ and $\hat{d}^{\alpha\beta\gamma\delta}$ from Eq. (4.74).
3)	Determine $\hat{\tau}^{\alpha\beta}_{,3}$ from Eq. (4.71.2) using the linearized kinematical variables (see Appendix A.3). Compute $\hat{c}^{\alpha\beta\gamma\delta}_{,3}$ and $\hat{d}^{\alpha\beta\gamma\delta}_{,3}$ from Eq. (4.74).
$\mu_0 = 1 - 2\,H_0\,\xi$	
4.a)	*Fully-stressed* shells: $\tau^{\alpha\beta}$ and $M_0^{\alpha\beta}$ and their corresponding tangents are found from Eq. (4.72) and (4.73).
4.b)	*Partially-stressed* shells: 4.b.1) Find the effective thickness $[T_1, T_2]$ and its corresponding tensors, given by Eq. (4.80), using Appendices A.3 and A.4. 4.b.2) Determine $\tau^{\alpha\beta}$ and $M_0^{\alpha\beta}$ and their corresponding tangents from Eq. (4.78) and Eqs. (4.81)-(4.84).
$\mu_0 = 1$	
4.c)	*Fully-stressed* shells: $\tau^{\alpha\beta}$ and $M_0^{\alpha\beta}$ and their corresponding tangents are found from Eq. (4.72) and (4.73).
4.d)	*Partially-stressed* shells: 4.d.1) See step 4.b.1. above. 4.d.2) Determine $\tau^{\alpha\beta}$ and $M_0^{\alpha\beta}$ and their corresponding tangents from Eqs. (4.86) and (4.87).

Table 4.3: Summary of the analytically-projected shell formulation

counterparts for any given 3D material model so that their combination results in a directly-decoupled shell model with a polyconvex 2D strain energy density function as

$$W = W(a_{\alpha\beta}, b_{\alpha\beta}) = W_{\mathrm{M}}(a_{\alpha\beta}) + W_{\mathrm{B}}(b_{\alpha\beta}) \ , \tag{4.88}$$

where W_{M} and W_{B} are the membrane and bending parts, respectively. The presented formulation has the following novelties:

i) It provides a a physically motivated link between the membrane and bending parts; thus, they are not chosen arbitrarily.
ii) It is not restricted to isotropic materials (cf. Duong et al., 2017). The DD shell model can capture anisotropic behavior very well, which is important for applications such as soft tissues.
iii) It is not restricted to Neo–Hookean or St. Venant–Kirchhoff solids and it allows for many material models with different polynomial and exponential forms of strain energy density function (see See Chap. 6).

Since many biological materials, such as soft tissues, can easily go through large deformations while being extremely stretched, the membrane formulation should allow for large material and geometrical nonlinearities (Roohbakhshan et al., 2016). This implies that, for the membrane part, a nonlinear stress-strain relationship is required. However, for the bending part, a linear stress-strain relationship is sufficient for most applications even if the shell exhibits large deformations.

For the membrane part, one can adopt the projection procedure introduced in Sec. 4.2 to get the 2D membrane strain energy density function $W_{\mathrm{M}}(a_{\alpha\beta}, \lambda_3)$ according to Eq. (4.37). Following Eq. (4.37), the membrane Kirchhoff stress, $\tau^{\alpha\beta}$, is given by Eq. (4.40) and the components of the membrane elasticity tensor, $c^{\alpha\beta\gamma\delta}$ are obtained from Eq. (4.41).

For the bending part, a physically well defined linear stress-strain relationship is needed. It can be derived from a linearized material model as

$$\tilde{W}_{\mathrm{lin}}(g_{\alpha\beta}) = \frac{1}{2}\,\tilde{c}_0^{\alpha\beta\gamma\delta}\,\overset{*}{E}_{\alpha\beta}\,\overset{*}{E}_{\gamma\delta}\ , \tag{4.89}$$

where

$$\tilde{c}_0^{\alpha\beta\gamma\delta} := \Big(\tilde{c}^{\alpha\beta\gamma\delta}\Big)_{\mathcal{S}_0} \tag{4.90}$$

is the elasticity tensor of 3D continuum before deformation, defined on $\mathcal{S}_0$. Following Eq. (4.60), one can express the 3D strain energy (4.89) as

$$\tilde{W}_{\mathrm{lin}} = \frac{1}{2}\,\tilde{c}_0^{\alpha\beta\gamma\delta}\,E_{\alpha\beta}\,E_{\gamma\delta} + \xi\,\tilde{c}_0^{\alpha\beta\gamma\delta}\,E_{\alpha\beta}\,K_{\gamma\delta} + \frac{1}{2}\,\xi^2\,\tilde{c}_0^{\alpha\beta\gamma\delta}\,K_{\alpha\beta}\,K_{\gamma\delta}\ . \tag{4.91}$$

Further, if the shell is thin, $\tilde{c}_0^{\alpha\beta\gamma\delta}$ can be expressed in terms of the mid-surface quantities using Taylor series as

$$\tilde{c}_0^{\alpha\beta\gamma\delta} \approx \hat{c}_0^{\alpha\beta\gamma\delta} + \xi\,\hat{c}_{0,3}^{\alpha\beta\gamma\delta} + O(\xi^2)\ , \tag{4.92}$$

where

$$\hat{c}_0^{\alpha\beta\gamma\delta} := \Big(\tilde{c}_0^{\alpha\beta\gamma\delta}\Big)_{\xi=0} \tag{4.93}$$

and

$$\hat{c}_{0,3}^{\alpha\beta\gamma\delta} := \left(\frac{\partial\tilde{c}_0^{\alpha\beta\gamma\delta}}{\partial\xi}\right)_{\xi=0} \tag{4.94}$$

are defined on the shell mid-surface $\mathcal{S}_0$. Neglecting the quadratic and higher order terms of Eq. (4.92), the corresponding 2D strain energy is obtained by analytically integrating the 3D strain energy over the thickness (4.91) as

$$\begin{aligned} W_{\mathrm{lin}} &= \int_{-\frac{T}{2}}^{\frac{T}{2}} \tilde{W}_{\mathrm{lin}} \mathrm{d}\xi \\ &= \frac{T}{2}\, \hat{c}_0^{\alpha\beta\gamma\delta}\, E_{\alpha\beta}\, E_{\gamma\delta} + \frac{T^3}{12}\, \hat{c}_{0,3}^{\alpha\beta\gamma\delta}\, E_{\alpha\beta}\, K_{\gamma\delta} + \frac{T^3}{24}\, \hat{c}_0^{\alpha\beta\gamma\delta}\, K_{\alpha\beta}\, K_{\gamma\delta}\ . \end{aligned} \tag{4.95}$$

Similar to this procedure, Steigmann (2013) has expressed the total energy of the shell by the expansion of the stored energy around the mid-surface of shell. If the shell sufficiently thin or the membranes strains are small, then $\hat{c}_{0,3}^{\alpha\beta\gamma\delta}\, E_{\alpha\beta} \ll \hat{c}_0^{\alpha\beta\gamma\delta}\, K_{\alpha\beta}$. Hence, the middle term in Eq. (4.95) can be neglected, which reduces the 2D stored energy to

$$W_{\mathrm{lin}} = \frac{T}{2}\, \hat{c}_0^{\alpha\beta\gamma\delta}\, E_{\alpha\beta}\, E_{\gamma\delta} + \frac{T^3}{24}\, \hat{c}_0^{\alpha\beta\gamma\delta}\, K_{\alpha\beta}\, K_{\gamma\delta}\ . \tag{4.96}$$

By definition, we have $\hat{c}_0^{\alpha\beta\gamma\delta} = \frac{1}{T}\, c_0^{\alpha\beta\gamma\delta}$, which is given by

$$c_0^{\alpha\beta\gamma\delta} := \left(c^{\alpha\beta\gamma\delta}\right)_{\mathcal{S}_0} \tag{4.97}$$

where $c^{\alpha\beta\gamma\delta}$ are the components of the membrane elasticity tensor defined by Eq. (4.41). This reduces Eq. (4.96) to

$$W_{\mathrm{lin}} = \frac{1}{2}\, c_0^{\alpha\beta\gamma\delta}\, E_{\alpha\beta}\, E_{\gamma\delta} + \frac{T^2}{24}\, c_0^{\alpha\beta\gamma\delta}\, K_{\alpha\beta}\, K_{\gamma\delta}\ . \tag{4.98}$$

The projection procedure from Eq. (4.91) to Eq. (4.98) allows us to completely decouple the stretching and bending strains and thus to split the strain energy function into two separated membrane and bending parts. Then, the rear part of Eq. (4.98) can be used for the 2D strain energy density function corresponding to the bending deformations as

$$W_{\mathrm{B}} = W_{\mathrm{B}}(b_{\alpha\beta}) = \frac{T^2}{24}\, c_0^{\alpha\beta\gamma\delta}\, K_{\alpha\beta}\, K_{\gamma\delta}\ . \tag{4.99}$$

From Eq. (4.99), the bending moments and their corresponding tangents are

$$M_0^{\alpha\beta} := \frac{\partial W_{\mathrm{B}}}{\partial b_{\alpha\beta}} = \frac{T^2}{12}\, c_0^{\alpha\beta\gamma\delta}\, K_{\gamma\delta}\ , \tag{4.100}$$

$$f^{\alpha\beta\gamma\delta} := \frac{\partial M_0^{\alpha\beta}}{\partial b_{\gamma\delta}} = \frac{T^2}{12}\, c_0^{\alpha\beta\gamma\delta}\ . \tag{4.101}$$

Remark 4.12. The presented decoupled membrane-bending equations are derived provided that (1) the material is symmetric w.r.t. the shell mid-surface, (2) shell is sufficiently thin and (3) the radii of curvature are much larger than the shell thickness (or ideally the shell is flat). If these three conditions are violated, the middle term of Eq. (4.95) does not vanish, which implies that mixed terms (i.e. strain gradients) are present in addition to the stretching and bending strains; therefore, the membrane and bending parts cannot be easily decoupled.

Remark 4.13. As the bending and membrane parts are decoupled, here $d^{\alpha\beta\gamma\delta} = e^{\alpha\beta\gamma\delta} = 0$, in contrast to the NP shell model (Sauer and Duong, 2017).

Tab. 4.4 summarizes the procedure to formulate a DD shell model for any given 3D material model.

1) For any 3D constitution, with a given strain energy function $\tilde{W}$, postulate a 2D counterpart as $W_{\mathrm{M}} + W_{\mathrm{B}}$.
2) For the membrane part W_{M}, compute
    2.1) the membrane stresses $\tau^{\alpha\beta}$ from Eqs. (4.37) and (4.40),
    2.1) the membrane elasticity tensor $c^{\alpha\beta\gamma\delta}$ from Eq. (4.41).
3) For the bending part W_{B}, compute
    3.1) $c_0^{\alpha\beta\gamma\delta}$ from Eq. (4.97),
    3.2) the bending moments $M_0^{\alpha\beta}$ from Eq. (4.100),
    3.3) $f^{\alpha\beta\gamma\delta}$ from Eq. (4.101).

Table 4.4: Summary of the directly-decoupled shell formulation

4.4 Modified Kirchhoff–Love shell

As already mentioned in Remark 4.2, one can consider the thickness stretch λ_3 directly in kinematics. Following Eq. (4.3), Eq. (4.5) should be modified as

$$\begin{aligned} \boldsymbol{g}_\alpha &:= \tilde{\boldsymbol{x}}_{,\alpha} = \boldsymbol{a}_\alpha - \lambda_3\, \xi\; b_\alpha^\gamma\, \boldsymbol{a}_\gamma + \lambda_{3,\alpha}\, \xi\, \boldsymbol{n} \ , \\ \boldsymbol{g}_3 &:= \tilde{\boldsymbol{x}}_{,3} = \lambda_3\, \boldsymbol{d} = \lambda_3\, \boldsymbol{n} = \boldsymbol{g}^3 \ . \end{aligned} \tag{4.102}$$

Neglecting the quadratic terms, we have

$$\begin{aligned} g_{\alpha\beta} &:= \boldsymbol{g}_\alpha \cdot \boldsymbol{g}_\beta = a_{\alpha\beta} - 2\,\lambda_3\, \xi\, b_{\alpha\beta} \ , \\ g_{\alpha 3} &:= \boldsymbol{g}_\alpha \cdot \boldsymbol{g}_3 = \lambda_{3,\alpha}\, \xi \ , \\ g_{33} &:= \boldsymbol{g}_3 \cdot \boldsymbol{g}_3 = \lambda_3^2\, \boldsymbol{n} \cdot \boldsymbol{n} = \lambda_3^2 \ . \end{aligned} \tag{4.103}$$

The spatial variation of the thickness stretch λ_3, i.e. $\lambda_{3,\alpha}\, \xi\, \boldsymbol{d} = \lambda_{3,\alpha}\, \xi\, \boldsymbol{n}$, corresponds to a non-zero out-of-plane shear deformation $g_{\alpha 3}$, which introduces an error of the same order as the Kirchhoff–Love assumption if being omitted (Cirak et al., 2005; Noels and Radovitzky, 2008 and Becker et al., 2011). Thus, we simply neglect the rear term in Eq. (4.102) to get $g_{\alpha 3} = 0$.

Compared to the metric tensor of a classical Kirchhoff–Love shell introduced in Sec. 4.3.1, Eq. (4.103) has tow main differences: (1) The thickness stretch λ_3 affects the curvature-dependent part of the in-plane strain and (2) the normal stretch is still constant but not equal to one anymore. The former issue would be reflected in the moment resultants and its tangents. The latter issue is treated as the classical Kirchhoff–Love shell formulation by assuming a *plain-stress* condition. Following Hughes and Carnoy (1983), the thickness parameter $\lambda_3 = \lambda_3(\xi^\alpha)$ is not included in the global degrees of freedom to avoid numerical ill-conditioning problems. Instead, it is determined locally through the constitutive relations assuming a *plain-stress* condition. Thus, likewise to Sec. 4.3.1, g_{33} is defined as Eq. (4.45) and λ_3 is averaged over the thickness according to Eq. (4.46). In practice, the stretch λ_3 is updated at the end of each Newton–Raphson iteration, after the force vector and tangent matrix are computed. Thus, the update of λ_3 lags other kinematical quantities (Hughes and Carnoy, 1983).

From Eqs. (4.65) and (4.69), the stress, moment and tangent tensors are

$$\begin{aligned} \tau^{\alpha\beta} &= \int_{-\frac{T}{2}}^{\frac{T}{2}} \tilde{\tau}^{\alpha\beta}\, \mu_0 \,\mathrm{d}\xi \ , \\ M_0^{\alpha\beta} &= -\lambda_3 \int_{-\frac{T}{2}}^{\frac{T}{2}} \xi\, \tilde{\tau}^{\alpha\beta}\, \mu_0 \,\mathrm{d}\xi \end{aligned} \tag{4.104}$$

and

$$\begin{aligned} c^{\alpha\beta\gamma\delta} &= \int_{-\frac{T}{2}}^{\frac{T}{2}} \tilde{c}^{\alpha\beta\gamma\delta}\, \mu_0 \,\mathrm{d}\xi \ , \\ d^{\alpha\beta\gamma\delta} &= e^{\alpha\beta\gamma\delta} = -\lambda_3 \int_{-\frac{T}{2}}^{\frac{T}{2}} \xi\, \tilde{c}^{\alpha\beta\gamma\delta}\, \mu_0 \,\mathrm{d}\xi \ , \\ f^{\alpha\beta\gamma\delta} &= \lambda_3^2 \int_{-\frac{T}{2}}^{\frac{T}{2}} \xi^2\, \tilde{c}^{\alpha\beta\gamma\delta}\, \mu_0 \,\mathrm{d}\xi \ , \end{aligned} \tag{4.105}$$

where $\tilde{\tau}^{\alpha\beta}$ and $\tilde{c}^{\alpha\beta\gamma\delta}$ are given by Eqs. (4.62) and (4.67), respectively.

Due to Eq. (4.46), λ_3 should be found by a numerical integration through the shell thickness. Therefore, for a modified Kirchhoff–Love shell kinematics, only a numerically-projected shell model is possible following Eqs. (4.104) and (4.105).

Chapter 5

Thin Laminated Composites[6]

In Chap. 4, different approaches to model membranes and thin shells are presented. There, it is assumed that a membrane or a shell consists of only one type of material. However, many biological materials are composites constructed from various constituents with different mechanical characteristics and material properties (Ramakrishna et al., 2001). Therefore, to describe the behavior of a composite shell or membrane, different homogenization approaches should be followed depending on the structural and material properties. In this Chapter, it is shown how composites, made of different layers through the thickness of a shell or a membrane, can be homogenized. In this sense, the approach of this chapter is *structural* homogenization. Later, in Sec. 6.3, it is shown how a single layer membrane or shell, made of different constituents such as the network of collagen fibers and matrix of elastins, can be homogenized into a single material model, which can be called a *constitutive* homogenization. For some applications such as arteries, examined in Sec. 9.4.2, a combination of both approaches is needed.

The laminated composite shells has been extensively investigated in the last years. Detailed surveys on the theoretical and numerical analysis of laminated composite shells can be found in Reddy and Robbins (1994), Yang et al. (2000), Carrera (2002), Carrera and Brischetto (2009), Zhang and Yang (2009), Qatu et al. (2010), Kreja (2011) and Qatu et al. (2012). Different theoretical and numerical approaches for the modeling and analysis of laminated composites are collected e.g. in Ochoa and Reddy (1992), Carrera (2002) and Reddy (2004). Recently, many isogeoemtric formulations are introduced for the modeling of thin laminated composite shells. For instance, Bazilevs et al. (2011) use the bending strip method of Kiendl et al. (2010) to model composite rotor blades following the equivalent single layer theory. However, they consider only a linear strain-stress relation, based on St. Venant–Kirchhoff material model. The formulation is later extended by Bazilevs et al. (2015) and Deng et al.

---

[6] Most of this chapter is taken from Roohbakhshan and Sauer (2016).

(2015) to predict damage in composites. The isogeometric formulation of Nagy et al. (2013) is used for the optimal design of composite Kirchhoff–Love shells that exhibit anisotropic behavior. Thai et al. (2013b) suggest a rotation-free isogeometric formulation for the analysis of composite sandwich thin plates. Kapoor and Kapania (2012), Thai et al. (2012), Casanova (2013), Thai et al. (2013a), Tran et al. (2013a), Tran et al. (2013b), Li et al. (2014), Thai et al. (2014), Thai et al. (2015), Yin et al. (2015), Yu et al. (2015) and Le-Manh et al. (2017) introduce isogeomrtric formulations for the analysis of composite plates based on first and higher order shear deformation theories. Furthermore, Thai et al. (2013a), Guo et al. (2014a), Guo et al. (2014b), Guo and Ruess (2015a) and Guo (2016) use layer-wise theories for the isogeometric analysis of laminated composites shells. Hosseini et al. (2014) and Hosseini et al. (2015) propose isogeometric 3D continuum shell formulations to model composite materials. In particular, laminated shell models are employed for the finite element analysis of soft and hard tissues. For instance, Horgan and Gilchrist (2003) use a composite shell element to model skull for simulating head impact biomechanics. Laminated shell models have been used for the finite element analysis of mitral leaflet tissue (e.g. Li et al., 2001 and Wenk et al., 2012). Further, aorta and other arteries are also studied as laminated composite shells (e.g. Guinovart-Sanjuán et al., 2016)

In this chapter, the shell formulations of Sec. 4.3 and the membrane formulation of Sec. 4.2 are adopted to model thin composite structure. First, the theory of composite shells is briefly reviewed and then the corresponding thin shell models are derived. The presented models are based on the equivalent single layer theory. The existing literature on isogeometric laminated shells based on ESL theory are mostly based on numerical integration through the shell thickness and are almost limited to linear constitutions. Here, it is shown that the presented formulation allows for any isotropic or anisotropic nonlinear constitution. Following Sec. 4.3, the analytically-projected and directly-decoupled shell models are adopted for laminated composite shells, which do not need any numerical integration through the shell thickness. Finally, the membrane/shell composites are introduced.

5.1 Theory of thin composite structures

In general, there are three different approaches to describe a composite laminate: (1) Equivalent single layer (ESL), (2) layer-wise (LW) and (3) continuum-based theories (Reddy, 1989). An equivalent single layer theory assumes a continuous strain distribution, which is usually considered to be linear, within the laminated layers of the shell. In contrast, a layer-wise theory considers piecewise continuous strain distributions for each layer. Following a continuum-based approach, a laminated shell is modeled as a 3D continuum with appropriate assumptions for the thickness. Equivalent single layer theories are the classical laminated plate theory (CLPT), the first order shear deformation theory (FSDT) and higher order shear deformation theory (HSDT) (Reddy, 2004). The ESL theory is suitable for thin shells, where the transverse shear forces are negligible. As the ESL theory do not account the inter-laminar stresses, they are not suitable for thick and moderately-thick shell. Here, we adopt the kinematics inherent to classical laminated plate theory, which is based on the Kirchhoff–Love hypothesis (see Sec. 4.1.1). Further it is assumed that (1) the layers are perfectly bonded together; (2) each layer is of uniform thickness; (3) the material can have any desired nonlinear isotropic or anisotropic constitution and (4) the strains and deformations can be arbitrary large.

As shown in Fig. 5.1, we describe the laminated layers of a composite shell for two cases. In the general setup, the laminated layers can have different thickness and mechanical properties and they are not necessarily symmetric w.r.t. the shell mid-surface. As a specific case, one can suppose that the geometrical and material properties of laminates are symmetric w.r.t. the shell mid-surface. For both the cases, the boundaries of each layer are defined by the distance T_i measured from the mid-surface. Accordingly, the i^{th} layer is located between T_{i-1} and T_i, where $i = 1, \ ..., \ n_{\text{l}}$. For the general case, n_{l} is the total number of layers, numbered from the bottom to the top surface of the shell so that $T_0 = -T/2$ and $T_{n_{\text{l}}} = T/2$ (see Fig. 5.1.a). For the symmetric case, the total number of layers is $2n_{\text{l}}$ and the layer numbers are mirrored w.r.t. the mid-surface implying $T_0 = 0$ and $T_{n_{\text{l}}} = T/2$ (see Fig. 5.1.b).

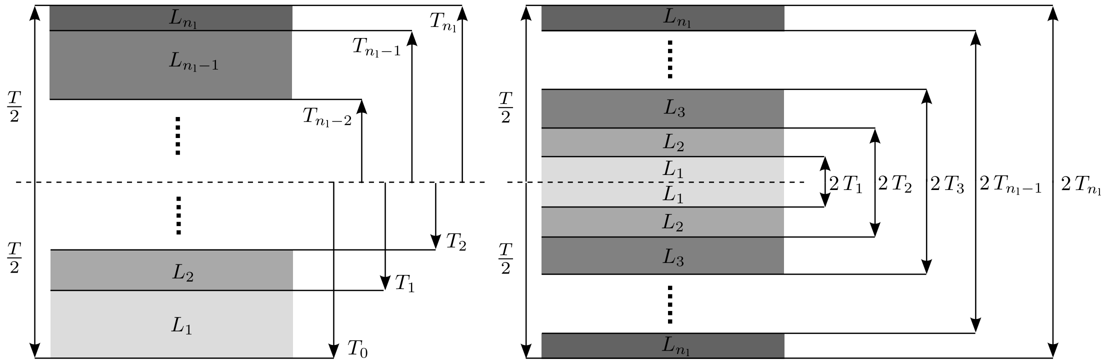

(a) (b)

FIGURE 5.1: Coordinate system and layer numbering of a laminated thin structure: (a) General and (b) symmetric configurations.

5.2 Thin composite shell and membrane models

In Sec. 4.3, three different approaches for the constitutive modeling of thin shells are introduced – namely the *numerically-projected* (NP), *analytically-projected* (AP) and *directly-decoupled* (DD) shell models. Following the classical laminated plate theory, those three shell models can be extended to laminated composite shells as it will be discussed in the following. Further, it is shown how composite membranes can be modeled and combined with shell structures.

5.2.1 Numerically-projected laminated shell model

The numerically-projected shell model is the most general formulation that can be used for both the asymmetric and symmetric composite shells; however, it generally requires numerical integration through the shell thickness. From Eq. (4.65), the stress and bending moment resultants are

$$\begin{aligned} \tau^{\alpha\beta} &= \sum_{i=1}^{n_l} \int_{T_{i-1}}^{T_i} \tilde{\tau}_i^{\alpha\beta} \, \mu_0 \, \mathrm{d}\xi \ , \\ M_0^{\alpha\beta} &= -\sum_{i=1}^{n_l} \int_{T_{i-1}}^{T_i} \xi \, \tilde{\tau}_i^{\alpha\beta} \, \mu_0 \, \mathrm{d}\xi \ . \end{aligned} \tag{5.1}$$

where

$$\tilde{\tau}_i^{\alpha\beta} := 2 \, \frac{\partial \tilde{W}_i(g_{\alpha\beta})}{\partial g_{\alpha\beta}} \tag{5.2}$$

is the in-plane Kirchhoff stress on a shell layer within the i^{th} laminate and $\tilde{W}_i(g_{\alpha\beta})$ is the strain energy density function of the same laminate layer. Following Eq. (4.69), the stiffness tangents are

$$\begin{aligned} c^{\alpha\beta\gamma\delta} &= \sum_{i=1}^{n_l} \int_{T_{i-1}}^{T_i} \tilde{c}_i^{\alpha\beta\gamma\delta} \, \mu_0 \, \mathrm{d}\xi \ , \\ d^{\alpha\beta\gamma\delta} &= e^{\alpha\beta\gamma\delta} = -\sum_{i=1}^{n_l} \int_{T_{i-1}}^{T_i} \xi \, \tilde{c}_i^{\alpha\beta\gamma\delta} \, \mu_0 \, \mathrm{d}\xi \ , \\ f^{\alpha\beta\gamma\delta} &= \sum_{i=1}^{n_l} \int_{T_{i-1}}^{T_i} \xi^2 \, \tilde{c}_i^{\alpha\beta\gamma\delta} \, \mu_0 \, \mathrm{d}\xi \ , \end{aligned} \tag{5.3}$$

where

$$\tilde{c}_i^{\alpha\beta\gamma\delta} := 2 \, \frac{\partial \tilde{\tau}_i^{\alpha\beta}}{\partial g_{\gamma\delta}} = 4 \, \frac{\partial^2 \tilde{W}_i(g_{\alpha\beta})}{\partial g_{\alpha\beta} \, \partial g_{\gamma\delta}} \ . \tag{5.4}$$

As mentioned in Remark 4.6, if the shell is initially flat or sufficiently thin, the shifter can be approximated as $\mu_0 \approx 1$.

5.2.2 Analytically-projected laminated shell model

For a laminate layer through the shell thickness, the stress is approximated similar to Eq. (4.70) as

$$\tilde{\tau}_i^{\alpha\beta} = \hat{\tau}_i^{\alpha\beta} + \xi\, \hat{\tau}_{i,3}^{\alpha\beta} \,, \tag{5.5}$$

where we have defined

$$\begin{aligned} \hat{\tau}_i^{\alpha\beta} &:= \left(\tilde{\tau}_i^{\alpha\beta}\right)_{\xi=0} \,, \\ \hat{\tau}_{i,3}^{\alpha\beta} &:= \left(\frac{\partial \tilde{\tau}_i^{\alpha\beta}}{\partial \xi}\right)_{\xi=0} \,. \end{aligned} \tag{5.6}$$

Here, $\tilde{\tau}_i^{\alpha\beta}$ is the Kirchhoff stress within the thickness of i^{th} laminate given by Eq. (5.1). Further, as shown in Fig. 5.1, one can consider two different arrangements of the laminates. For the analytically-projected shell models, it is of benefit to distinguish between the two arrangements as the symmetric setup has a simpler formulation.

5.2.2.1 General setup

Following the general setup (see Fig. 5.1.a), $-T/2 \leq T_{i-1} < T_i \leq T/2$, where $i = 1, \ldots, n_{\text{l}}$. Thus, plugging Eq. (5.5) into Eq. (5.1) and integrating analytically, we obtain

$$\begin{aligned} \tau^{\alpha\beta} = & \sum_{i=1}^{n_{\text{l}}} \left[\left(T_i - T_{i-1}\right) \hat{\tau}_i^{\alpha\beta} + \frac{1}{2}\left(T_i^2 - T_{i-1}^2\right) \hat{\tau}_{i,3}^{\alpha\beta} \right] \\ & - H_0 \sum_{i=1}^{n_{\text{l}}} \left[\left(T_i^2 - T_{i-1}^2\right) \hat{\tau}_i^{\alpha\beta} + \frac{2}{3}\left(T_i^3 - T_{i-1}^3\right) \hat{\tau}_{i,3}^{\alpha\beta} \right] \end{aligned} \tag{5.7}$$

and

$$\begin{aligned} M_0^{\alpha\beta} = & \sum_{i=1}^{n_{\text{l}}} \left[\frac{1}{2}\left(T_{i-1}^2 - T_i^2\right) \hat{\tau}_i^{\alpha\beta} + \frac{1}{3}\left(T_{i-1}^3 - T_i^3\right) \hat{\tau}_{i,3}^{\alpha\beta} \right] \\ & + H_0 \sum_{i=1}^{n_{\text{l}}} \left[\frac{2}{3}\left(T_i^3 - T_{i-1}^3\right) \hat{\tau}_i^{\alpha\beta} + \frac{1}{2}\left(T_i^4 - T_{i-1}^4\right) \hat{\tau}_{i,3}^{\alpha\beta} \right] . \end{aligned} \tag{5.8}$$

Similar to Eqs. (4.81)-(4.84), the corresponding stiffness tangents are

$$\begin{aligned} c^{\alpha\beta\gamma\delta} = & \sum_{i=1}^{n_{\text{l}}} \left[\left(T_i - T_{i-1}\right) \hat{c}_i^{\alpha\beta\gamma\delta} + \frac{1}{2}\left(T_i^2 - T_{i-1}^2\right) \hat{c}_{i,3}^{\alpha\beta\gamma\delta} \right] \\ & - H_0 \sum_{i=1}^{n_{\text{l}}} \left[\left(T_i^2 - T_{i-1}^2\right) \hat{c}_i^{\alpha\beta\gamma\delta} + \frac{2}{3}\left(T_i^3 - T_{i-1}^3\right) \hat{c}_{i,3}^{\alpha\beta\gamma\delta} \right] , \end{aligned} \tag{5.9}$$

$$\begin{aligned} d^{\alpha\beta\gamma\delta} = & \sum_{i=1}^{n_l} \left[\left(T_i - T_{i-1}\right) \hat{d}_i^{\alpha\beta\gamma\delta} + \frac{1}{2}\left(T_i^2 - T_{i-1}^2\right) \hat{d}_{i,3}^{\alpha\beta\gamma\delta} \right] \\ & - H_0 \sum_{i=1}^{n_l} \left[\left(T_i^2 - T_{i-1}^2\right) \hat{d}_i^{\alpha\beta\gamma\delta} + \frac{2}{3}\left(T_i^3 - T_{i-1}^3\right) \hat{d}_{i,3}^{\alpha\beta\gamma\delta} \right], \end{aligned} \tag{5.10}$$

$$\begin{aligned} e^{\alpha\beta\gamma\delta} = & \sum_{i=1}^{n_l} \left[\frac{1}{2}\left(T_{i-1}^2 - T_i^2\right) \hat{c}_i^{\alpha\beta\gamma\delta} + \frac{1}{3}\left(T_{i-1}^3 - T_i^3\right) \hat{c}_{i,3}^{\alpha\beta\gamma\delta} \right] \\ & + H_0 \sum_{i=1}^{n_l} \left[\frac{2}{3}\left(T_i^3 - T_{i-1}^3\right) \hat{c}_i^{\alpha\beta\gamma\delta} + \frac{1}{2}\left(T_i^4 - T_{i-1}^4\right) \hat{c}_{i,3}^{\alpha\beta\gamma\delta} \right] \end{aligned} \tag{5.11}$$

and

$$\begin{aligned} f^{\alpha\beta\gamma\delta} = & \sum_{i=1}^{n_l} \left[\frac{1}{2}\left(T_{i-1}^2 - T_i^2\right) \hat{d}_i^{\alpha\beta\gamma\delta} + \frac{1}{3}\left(T_{i-1}^3 - T_i^3\right) \hat{d}_{i,3}^{\alpha\beta\gamma\delta} \right] \\ & + H_0 \sum_{i=1}^{n_l} \left[\frac{2}{3}\left(T_i^3 - T_{i-1}^3\right) \hat{d}_i^{\alpha\beta\gamma\delta} + \frac{1}{2}\left(T_i^4 - T_{i-1}^4\right) \hat{d}_{i,3}^{\alpha\beta\gamma\delta} \right]. \end{aligned} \tag{5.12}$$

Here, we have introduced

$$\begin{aligned} \hat{c}_i^{\alpha\beta\gamma\delta} &= 2\,\frac{\partial \hat{\tau}_i^{\alpha\beta}}{\partial a_{\gamma\delta}}, \qquad & \hat{d}_i^{\alpha\beta\gamma\delta} &= \frac{\partial \hat{\tau}_i^{\alpha\beta}}{\partial b_{\gamma\delta}}, \\ \hat{c}_{i,3}^{\alpha\beta\gamma\delta} &= 2\,\frac{\partial \hat{\tau}_{i,3}^{\alpha\beta}}{\partial a_{\gamma\delta}}, \qquad & \hat{d}_{i,3}^{\alpha\beta\gamma\delta} &= \frac{\partial \hat{\tau}_{i,3}^{\alpha\beta}}{\partial b_{\gamma\delta}}. \end{aligned} \tag{5.13}$$

Considering $\mu_0 \approx 0$, Eqs. (5.7) and (5.8) would be reduced to

$$\begin{aligned} \tau^{\alpha\beta} &= \sum_{i=1}^{n_l} \left[\left(T_i - T_{i-1}\right) \hat{\tau}_i^{\alpha\beta} + \frac{1}{2}\left(T_i^2 - T_{i-1}^2\right) \hat{\tau}_{i,3}^{\alpha\beta} \right], \\ M_0^{\alpha\beta} &= \sum_{i=1}^{n_l} \left[\frac{1}{2}\left(T_{i-1}^2 - T_i^2\right) \hat{\tau}_i^{\alpha\beta} + \frac{1}{3}\left(T_{i-1}^3 - T_i^3\right) \hat{\tau}_{i,3}^{\alpha\beta} \right] \end{aligned} \tag{5.14}$$

and the tangents (5.9)-(5.12) can be written as

$$\begin{aligned} c^{\alpha\beta\gamma\delta} &= \sum_{i=1}^{n_l} \left[\left(T_i - T_{i-1}\right) \hat{c}_i^{\alpha\beta\gamma\delta} + \frac{1}{2}\left(T_i^2 - T_{i-1}^2\right) \hat{c}_{i,3}^{\alpha\beta\gamma\delta} \right], \\ d^{\alpha\beta\gamma\delta} &= \sum_{i=1}^{n_l} \left[\left(T_i - T_{i-1}\right) \hat{d}_i^{\alpha\beta\gamma\delta} + \frac{1}{2}\left(T_i^2 - T_{i-1}^2\right) \hat{d}_{i,3}^{\alpha\beta\gamma\delta} \right], \\ e^{\alpha\beta\gamma\delta} &= \sum_{i=1}^{n_l} \left[\frac{1}{2}\left(T_{i-1}^2 - T_i^2\right) \hat{c}_i^{\alpha\beta\gamma\delta} + \frac{1}{3}\left(T_{i-1}^3 - T_i^3\right) \hat{c}_{i,3}^{\alpha\beta\gamma\delta} \right], \\ f^{\alpha\beta\gamma\delta} &= \sum_{i=1}^{n_l} \left[\frac{1}{2}\left(T_{i-1}^2 - T_i^2\right) \hat{d}_i^{\alpha\beta\gamma\delta} + \frac{1}{3}\left(T_{i-1}^3 - T_i^3\right) \hat{d}_{i,3}^{\alpha\beta\gamma\delta} \right]. \end{aligned} \tag{5.15}$$

5.2.2.2 Symmetric setup

If the laminated layers are distributed symmetrically w.r.t. the shell mid-surface (see Fig. 5.1.b), $0 \leq T_{i-1} < T_i \leq T/2$, where $i = 1, \ ..., \ n_{\mathrm{l}}$. Thus, Eq. (5.14) can be reduced to

$$\begin{aligned} \tau^{\alpha\beta} &= 2 \sum_{i=1}^{n_{\mathrm{l}}} \left[\left(T_i - T_{i-1}\right) \hat{\tau}_i^{\alpha\beta} - \frac{2}{3} H_0 \left({T_i}^3 - T_{i-1}^3\right) \hat{\tau}_{i,3}^{\alpha\beta} \right] , \\ M_0^{\alpha\beta} &= \frac{2}{3} \sum_{i=1}^{n_{\mathrm{l}}} \left[2 H_0 \left({T_i}^3 - T_{i-1}^3\right) \hat{\tau}_i^{\alpha\beta} - \left({T_i}^3 - T_{i-1}^3\right) \hat{\tau}_{i,3}^{\alpha\beta} \right] . \end{aligned} \tag{5.16}$$

The tangent matrices are derived from Eq. (5.16) as

$$c^{\alpha\beta\gamma\delta} = 2 \sum_{i=1}^{n_{\mathrm{l}}} \left[\left(T_i - T_{i-1}\right) \hat{c}_i^{\alpha\beta\gamma\delta} - \frac{2}{3} H_0 \left({T_i}^3 - T_{i-1}^3\right) \hat{c}_{i,3}^{\alpha\beta\gamma\delta} \right] , \tag{5.17}$$

$$d^{\alpha\beta\gamma\delta} = 2 \sum_{i=1}^{n_{\mathrm{l}}} \left[\left(T_i - T_{i-1}\right) \hat{d}_i^{\alpha\beta\gamma\delta} - \frac{2}{3} H_0 \left({T_i}^3 - T_{i-1}^3\right) \hat{d}_{i,3}^{\alpha\beta\gamma\delta} \right] , \tag{5.18}$$

$$e^{\alpha\beta\gamma\delta} = \frac{2}{3} \sum_{i=1}^{n_{\mathrm{l}}} \left[2 H_0 \left(T_i^3 - T_{i-1}^3\right) \hat{c}_i^{\alpha\beta\gamma\delta} - \left({T_i}^3 - T_{i-1}^3\right) \hat{c}_{i,3}^{\alpha\beta\gamma\delta} \right] \tag{5.19}$$

and

$$f^{\alpha\beta\gamma\delta} = \frac{2}{3} \sum_{i=1}^{n_{\mathrm{l}}} \left[2 H_0 \left({T_i}^3 - T_{i-1}^3\right) \hat{d}_i^{\alpha\beta\gamma\delta} - \left({T_i}^3 - T_{i-1}^3\right) \hat{d}_{i,3}^{\alpha\beta\gamma\delta} \right] . \tag{5.20}$$

Considering $\mu_0 \approx 0$, Eq. (5.16) can be written as

$$\begin{aligned} \tau^{\alpha\beta} &= 2 \sum_{i=1}^{n_{\mathrm{l}}} \left(T_i - T_{i-1}\right) \hat{\tau}_i^{\alpha\beta} , \\ M_0^{\alpha\beta} &= -\frac{2}{3} \sum_{i=1}^{n_{\mathrm{l}}} \left(T_i^3 - T_{i-1}^3\right) \hat{\tau}_{i,3}^{\alpha\beta} , \end{aligned} \tag{5.21}$$

where the layers are numbered according to Fig. 5.1.b. From Eq. (5.21), the tangent tensors are then

$$
\begin{aligned}
c^{\alpha\beta\gamma\delta} &= 2\sum_{i=1}^{n_l} \left(T_i - T_{i-1}\right) \hat{c}_i^{\alpha\beta\gamma\delta} \ , \\
d^{\alpha\beta\gamma\delta} &= 2\sum_{i=1}^{n_l} \left(T_i - T_{i-1}\right) \hat{d}_i^{\alpha\beta\gamma\delta} \ , \\
e^{\alpha\beta\gamma\delta} &= -\frac{2}{3}\sum_{i=1}^{n_l} \left(T_i^3 - T_{i-1}^3\right) \hat{c}_{i,3}^{\alpha\beta\gamma\delta} \ , \\
f^{\alpha\beta\gamma\delta} &= -\frac{2}{3}\sum_{i=1}^{n_l} \left(T_i^3 - T_{i-1}^3\right) \hat{d}_{i,3}^{\alpha\beta\gamma\delta} \ .
\end{aligned}
\tag{5.22}
$$

Remark 5.1. In the formulations presented so far, it is assumed that the shell is *fully-stressed*, i.e. all the layers through the shell thickness contribute to the strain energy density function and the corresponding stress and bending moment resultants. However, as discussed in Sec. 4.3.2.2.2, depending on the constitution and application, the shell might only be *partially-stressed*. Hence, within each laminate layer, only a portion of shell thickness, e.g. $[T_{i1}, T_{i2}] \subset [T_{i-1}, T_i]$, might be active. This implies that

$$
\begin{aligned}
\tau^{\alpha\beta} &= \sum_{i=1}^{n_l} \int_{T_{i1}}^{T_{i2}} \tilde{\tau}_i^{\alpha\beta} \, \mathrm{d}\xi \ , \\
M_0^{\alpha\beta} &= -\sum_{i=1}^{n_l} \int_{T_{i1}}^{T_{i2}} \xi \, \tilde{\tau}_i^{\alpha\beta} \, \mathrm{d}\xi
\end{aligned}
\tag{5.23}
$$

for the numerically-projected laminated shell, where T_{i1} and T_{i2} need to be determined specifically for each problem. For the analytically-projected laminated shell, a general arrangement (see Fig. 5.1.b) should be followed as

$$
\begin{aligned}
\tau^{\alpha\beta} &= \sum_{i=1}^{n_l} \left[\left(T_{i2} - T_{i1}\right) \hat{\tau}_i^{\alpha\beta} + \frac{1}{2}\left(T_{i2}^2 - T_{i1}^2\right) \hat{\tau}_{i,3}^{\alpha\beta}\right] \ , \\
M_0^{\alpha\beta} &= \sum_{i=1}^{n_l} \left[\frac{1}{2}\left(T_{i1}^2 - T_{i2}^2\right) \hat{\tau}_i^{\alpha\beta} + \frac{1}{3}\left(T_{i1}^3 - T_{i2}^3\right) \hat{\tau}_{i,3}^{\alpha\beta}\right] \ .
\end{aligned}
\tag{5.24}
$$

5.2.3 Directly-decoupled laminated shell model

If a laminated shell is symmetric w.r.t. the mid-surface, one can use the directly-decoupled shell model of Sec. 4.3.2.3. The stored energy W of the shell can be decoupled into the membrane and bending parts according to Eq. (4.88). The membrane energy is

$$
W_{\mathrm{M}}(a_{\alpha\beta}) = \sum_{i=1}^{n_l} \left(T_i - T_{i-1}\right) \hat{W}_i(a_{\alpha\beta}) \ , \tag{5.25}
$$

where the constitutive law of the i^{th} laminate layer is

$$\hat{W}_i(a_{\alpha\beta}) := \left[\tilde{W}_i(g_{\alpha\beta})\right]_{\xi=0} , \tag{5.26}$$

which is formulated in terms of the mid-surface metric tensor $a_{\alpha\beta}$. The bending energy is then

$$W_{\mathrm{B}}(b_{\alpha\beta}) = \frac{1}{3}\sum_{i=1}^{n_{\mathrm{l}}}\left(T_i^3 - T_{i-1}^3\right)\hat{c}_{0i}^{\alpha\beta\gamma\delta}\,K_{\alpha\beta}\,K_{\gamma\delta} , \tag{5.27}$$

where

$$\hat{c}_{0i}^{\alpha\beta\gamma\delta} := \left(\hat{c}_i^{\alpha\beta\gamma\delta}\right)_{\mathcal{S}_0} \tag{5.28}$$

are the components of the membrane elasticity tensor prior to deformation and

$$\hat{c}_i^{\alpha\beta\gamma\delta} := 4\,\frac{\partial^2\hat{W}_i(a_{\alpha\beta})}{\partial a_{\alpha\beta}\,\partial a_{\gamma\delta}} . \tag{5.29}$$

Thus, the stress and bending moment resultants are

$$\begin{aligned} \tau^{\alpha\beta} &:= 2\,\frac{\partial W_{\mathrm{M}}(a_{\alpha\beta})}{\partial a_{\alpha\beta}} &&= 2\sum_{i=1}^{n_{\mathrm{l}}}\left(T_i - T_{i-1}\right)\hat{\tau}_i^{\alpha\beta} , \\ M_0^{\alpha\beta} &:= \frac{\partial W_{\mathrm{B}}(b_{\alpha\beta})}{\partial b_{\alpha\beta}} &&= \frac{2}{3}\sum_{i=1}^{n_{\mathrm{l}}}\left(T_i^3 - T_{i-1}^3\right)\hat{c}_{0i}^{\alpha\beta\gamma\delta}\,K_{\gamma\delta} , \end{aligned} \tag{5.30}$$

with

$$\hat{\tau}_i^{\alpha\beta} := 2\,\frac{\partial\hat{W}_i(a_{\alpha\beta})}{\partial a_{\alpha\beta}} . \tag{5.31}$$

The corresponding stiffness tangents are

$$\begin{aligned} c^{\alpha\beta\gamma\delta} &= 2\sum_{i=1}^{n_{\mathrm{l}}}\left(T_i - T_{i-1}\right)\hat{c}_i^{\alpha\beta\gamma\delta} , \\ f^{\alpha\beta\gamma\delta} &= \frac{2}{3}\sum_{i=1}^{n_{\mathrm{l}}}\left(T_i^3 - T_{i-1}^3\right)\hat{c}_{0i}^{\alpha\beta\gamma\delta} \end{aligned} \tag{5.32}$$

and $d^{\alpha\beta\gamma\delta} = e^{\alpha\beta\gamma\delta} = 0$, which illustrates the decoupling.

5.2.4 Composite membranes

As shown in Sec. 4.2, the stress distribution across the thickness of a physical membrane is constant and it bears no bending. Thus, if a thin structure is constructed of multiple layers of membranes or a combination of membranes and shells, the resultant stress tensor would be

$$\tau^{\alpha\beta} = \tau_{\mathrm{m}}^{\alpha\beta} + \tau_{\mathrm{s}}^{\alpha\beta} \ , \tag{5.33}$$

where $\tau_{\mathrm{m}}^{\alpha\beta}$ is the effective stress of all membrane layers given by

$$\tau^{\alpha\beta} = T \sum_{i=1}^{n_{\mathrm{l}}} \hat{\tau}_i^{\alpha\beta} \ . \tag{5.34}$$

Here, $\hat{\tau}_i^{\alpha\beta}$ corresponds to the contribution of the i^{th} membrane layer, given by Eq. (5.31). The resultant stress tensor of the shell layer(s), i.e. $\tau_{\mathrm{s}}^{\alpha\beta}$, is obtained by the formulations of Secs. 5.2.1-5.2.3 for laminated shells or following Sec. 4.3 for single layer shells.

Chapter 6

Material Models[7]

Having introduced the thin shell theory and three different approaches to model shells, various isotropic and anisotropic constitutive laws can be examined now. For each material model, the different constitutive projection approaches from Chap. 4 (i.e. the membrane model and the NP, AP and DD shell models), are derived. Most of the material models studied here are considered to be incompressible since most types of soft biological materials, in particular soft tissues, are regarded as incompressible (Holzapfel, 2001). Before introducing different material models, we discuss how material incompressibility is enforced in the presented work.

6.1 Incompressibility

In general, in continuum mechanics, there are two approaches, namely quasi-incompressibility and strict-incompressibility, to enforce the material incompressibility constraint

$$\tilde{g} := \tilde{J} - 1 = 0 \; , \tag{6.1}$$

where $\tilde{J} = \overset{*}{J}\,\overset{*}{\lambda}_3$ for a projected shell model and $\tilde{J} = J\,\lambda_3$ for a membrane model or a directly-decoupled shell model.

6.1.1 Quasi-incompressibility

When dealing with incompressible or nearly-incompressible material, it is beneficial to split the deformation gradient $\tilde{\boldsymbol{F}}$ into volumetric (or dilatational) part $\tilde{\boldsymbol{F}}_{\mathrm{vol}}$, which is

---

[7] This chapter is based on Roohbakhshan and Sauer (2017).

volume-changing, and an isochoric (or distortional) part $\bar{\tilde{\boldsymbol{F}}}$, which is volume-preserving as (Bonet and Wood, 1997 and Holzapfel, 2000)

$$\tilde{\boldsymbol{F}} := \tilde{\boldsymbol{F}}_{\mathrm{vol}}\,\bar{\tilde{\boldsymbol{F}}}\ , \tag{6.2}$$

where

$$\tilde{\boldsymbol{F}}_{\mathrm{vol}} := \tilde{J}^{1/3}\,\mathbf{1}\ , \qquad \bar{\tilde{\boldsymbol{F}}} := \tilde{J}^{-1/3}\,\tilde{\boldsymbol{F}}\ . \tag{6.3}$$

From Eq. (6.3), $\det \tilde{\boldsymbol{F}}_{\mathrm{vol}} = \tilde{J}$ and $\det \bar{\tilde{\boldsymbol{F}}} = 1$. Similar decompositions can be obtained for other strain measures such as the right Cauchy–Green tensor as $\tilde{\boldsymbol{C}} = \big(\tilde{J}^{2/3}\,\mathbf{1}\big)\,\bar{\tilde{\boldsymbol{C}}}$, where

$$\bar{\tilde{\boldsymbol{C}}} := \bar{\tilde{\boldsymbol{F}}}^{\mathrm{T}}\,\bar{\tilde{\boldsymbol{F}}} = \tilde{J}^{-2/3}\,\tilde{\boldsymbol{C}} \tag{6.4}$$

is called the *modified* right Cauchy–Green tensor.

In the quasi-incompressibility approach, the strain energy function is split into the deviatoric and volumetric parts following the multiplicative decomposition of the deformation gradient. Considering an incompressible hyperelastic solid with 3D strain energy function $\tilde{W}_{\mathrm{inc}}\big(\tilde{\boldsymbol{C}}\big)$, the decomposed strain energy would be

$$\tilde{W}\big(\tilde{\boldsymbol{C}},\tilde{J}\big) = \tilde{U}\big(\tilde{J}\big) + \tilde{W}_{\mathrm{inc}}\big(\bar{\tilde{\boldsymbol{C}}}\big)\ , \tag{6.5}$$

where $\tilde{W}_{\mathrm{inc}}\big(\bar{\tilde{\boldsymbol{C}}}\big)$ is the corresponding modified (distortional) strain energy function, expressed in terms of the modified right Cauchy–Green tensor, which leads to a purely deviatoric stress. An appropriate choice of the volume-preserving part can be

$$\tilde{U}\big(\tilde{J}\big) = \frac{\tilde{K}}{2}\,\tilde{g}^2\ , \tag{6.6}$$

where the bulk modulus $\tilde{K}$ acts as a penalty parameter for the incompressibility constraint. Other possible functions $U\big(\tilde{J}\big)$ suggested in the literature can be found in Doll and Schweizerhof (2000). To fulfill the constraint exactly, the bulk modulus should be set to infinity (corresponding to the Poisson's ratio $\nu = 0.5$) while, in practice, a finite large number is used to approximately enforce the incompressibility.

6.1.2 Strict-incompressibility

Alternatively, the incompressibility constraint can be enforced strictly through the Lagrange multiplier method as it is done in this thesis. In this approach, the incompressible strain energy is augmented by the contribution of a Lagrange multiplier as (Holzapfel, 2000)

$$\tilde{W}\big(\tilde{\boldsymbol{C}},\tilde{J}\big) = \tilde{W}_{\mathrm{inc}}\big(\tilde{\boldsymbol{C}}\big) + \tilde{p}\,\tilde{g} \tag{6.7}$$

or (Bonet and Wood, 1997)

$$\tilde{W}\big(\tilde{\boldsymbol{C}}, \tilde{J}\big) = \tilde{W}_{\mathrm{inc}}\big(\overline{\tilde{\boldsymbol{C}}}\big) + \tilde{p}\,\tilde{g}\ , \tag{6.8}$$

where the unknown Lagrange multiplier $\tilde{p}$ acts as a hydrostatic pressure. In particular for thin shells and membranes, it can be *analytically* determined from the plane-stress condition. In addition to the physical motivations, the plane-stress condition is favored for thin shells as it analytically eliminates the unknown Lagrange multiplier if the material is incompressible. For the NP shell model of Sec. 4.3.2.1, from Eq. (6.7), we get

$$\tilde{p} = \overset{*}{J}{}^{-1}\,\frac{\partial \tilde{W}_{\mathrm{inc}}\big(\tilde{\boldsymbol{C}}\big)}{\partial \overset{*}{\lambda}_3} \tag{6.9}$$

and from Eq. (6.8), we have

$$\tilde{p} = \overset{*}{J}{}^{-1}\,\frac{\partial \tilde{W}_{\mathrm{inc}}\big(\overline{\tilde{\boldsymbol{C}}}\big)}{\partial \overset{*}{\lambda}_3}\ . \tag{6.10}$$

Remark 6.1. For 3D solid elements, it is not possible to exactly fulfill the incompressibility at each point of the body due to volumetric locking, which introduces artificial stiffness to the system (Bonet and Wood, 1997). Thus, if the Lagrange multiplier approach is used, it is necessary to follow a mixed variational method including the Lagrange multiplier in global degrees of freedom. For instance, a three-field variational principle such as Hu–Washizu variational principle for incompressibility can be used (Wriggers, 2008). Finite elements derived form mixed methods have to fulfill the Babuška–Brezzi condition (Babuška, 1973 and Brezzi, 1974) to guarantee the stability of the formulation. This is the case for the thick shells modeled by solid elements (Elguedj et al., 2008) or solid-shell elements (Bouclier et al., 2013a; Bouclier et al., 2013b and Bouclier et al., 2015). Fortunately, for thin shells, the Lagrange multiplier is found locally at the constitutive level through the plane-stress condition.

For the membrane model of Sec. 4.2, the incompressibility constraint is added to the corresponding incompressible 2D stored energy $W_{\mathrm{inc}}(\tilde{\boldsymbol{C}})$ through the Lagrange multiplier method as

$$W_{\mathrm{M}}\big(\tilde{\boldsymbol{C}}, \tilde{J}\big) = W_{\mathrm{inc}}\big(\tilde{\boldsymbol{C}}\big) + p\,\tilde{g} \tag{6.11}$$

$$W_{\mathrm{M}}\big(\tilde{\boldsymbol{C}}, \tilde{J}\big) = W_{\mathrm{inc}}\big(\overline{\tilde{\boldsymbol{C}}}\big) + p\,\tilde{g}\ , \tag{6.12}$$

which are similar to the 3D formulations, cf. Eqs. (6.7) and (6.8). The unknown Lagrange multiplier $p = T\,\tilde{p}$ can also be *analytically* found from the plane-stress condition as

$$p = J^{-1}\,\frac{\partial W_{\mathrm{inc}}\big(\tilde{\boldsymbol{C}}\big)}{\partial \lambda_3} \tag{6.13}$$

and

$$p = J^{-1}\,\frac{\partial W_{\mathrm{inc}}\big(\bar{\tilde{\boldsymbol{C}}}\big)}{\partial \lambda_3}\;, \tag{6.14}$$

for Eqs. (6.11) and (6.12), respectively. In the DD shell model of Sec. 4.3.2.3, the incompressibility constraint is treated analogously for the membrane part. For the bending part, the effect of incompressibility constraint is condensed into $c_0^{\alpha\beta\gamma\delta}$.

Here, the approach of strict-incompressibility is used as (1) it exactly fulfills the incompressibility constraint, (2) its associated Lagrange multiplier can be eliminated analytically for thin shells and (3) its numerical implementation is more convenient.

Remark 6.2. Although the Lagrange multipliers derived from Eqs. (6.7) and (6.8) are different, both approaches give the same total in-plane Kirchhoff stress if the Lagrange multiplier is found from the plane-stress condition and then condensed into the stress tensor. Thus, for the numerically-projected shells, we use $\tilde{W}_{\mathrm{inc}}\big(\tilde{\boldsymbol{C}}\big)$ following Eq. (6.7) to enforce the incompressibility constraint. Similarly for a membrane model, $W_{\mathrm{inc}}\big(\tilde{\boldsymbol{C}}\big)$ is used following Eq. (6.11). Both approaches are compared for a Neo–Hookean membrane model in Sec. 6.2.2.1.

In Secs. 6.2 and 6.3, different isotropic and anisotropic material models are projected onto the surface of membrane and shell structures following the constitutive projection approaches of Chap. 4. Specifically for each material model, the following structural models are derived:

1) The membrane model, where $\tau^{\alpha\beta}$ and $c^{\alpha\beta\gamma\delta}$ should be derived according to Eqs. (4.40) and (4.41).
2) The NP shell model, where one needs to derive $\tilde{\tau}^{\alpha\beta}$ and $\tilde{c}^{\alpha\beta\gamma\delta}$ specifically for any given material model. Then, the stress and moment tensors and their corresponding tangents are determined by plugging the specific $\tilde{\tau}^{\alpha\beta}$ and $\tilde{c}^{\alpha\beta\gamma\delta}$ into Eqs. (4.65) and (4.69), respectively.
3) The AP shell model, where $\hat{\tau}^{\alpha\beta}$, $\hat{\tau}^{\alpha\beta}_{,3}$, $\hat{c}^{\alpha\beta\gamma\delta}$, $\hat{d}^{\alpha\beta\gamma\delta}$, $\hat{c}^{\alpha\beta\gamma\delta}_{,3}$ and $\hat{d}^{\alpha\beta\gamma\delta}_{,3}$ are needed. Then, the stress and moment tensors and their corresponding tangents follow from step 4 in Tab. 4.3.
4) The DD shell model, where $\tau^{\alpha\beta}$ and $c^{\alpha\beta\gamma\delta}$ are derived as for a membrane. Then, one can compute $c_0^{\alpha\beta\gamma\delta}$, $M_0^{\alpha\beta}$ and $f^{\alpha\beta\gamma\delta}$ from step 3 in Tab. 4.4.

6.2 Isotropic models

Soft biomaterials are commonly modeled with incompressible hyperelastic constitutive models that have been introduced for rubber-like materials. Although soft tissues are constructed from elastin and collagen fibres, the anisotropic part might be neglected and a purely isotropic model can be used. Examples are the modeling of liver, kidney, bladder and rectum, lungs, uterus, etc. (Chagnon et al., 2015). This section discusses a few isotropic constitutive models that are commonly used for biomaterials and soft tissues (Martins et al., 2006 and Wex et al., 2015). Both kinds of constitutive laws, i.e. material models with polynomial and exponential forms of strain energy functions, are included in the presented examples.

6.2.1 St. Venant–Kirchhoff

St. Venant–Kirchhoff material model is a generalization of the linear model for large displacements. It is based on a linear stress-strain relationship as

$$\tilde{W}(\tilde{\boldsymbol{E}}) = \frac{\tilde{\Lambda}}{2}\big(\operatorname{tr}\tilde{\boldsymbol{E}}\big)^2 + \tilde{\mu}\,\tilde{\boldsymbol{E}} : \tilde{\boldsymbol{E}} \ , \tag{6.15}$$

where $\tilde{\Lambda}$ and $\tilde{\mu}$ are the Lamé's first and second parameters. Therefore it is not suitable for soft tissues that usually exhibit large material nonlinearities. However, in the first attempts towards real-time simulation of surgery it was used for the modeling of soft tissues (Picinbono et al., 2001 and Delingette and Ayache, 2004). It has been also extended to anisotropic elasticity (Picinbono et al., 2003). Here, this material model is investigated to show how the classic 2D Koiter shell model can be derived from the perspective of 3D nonlinear elasticity.

6.2.1.1 Membrane model

From Eq. (4.35),

$$\operatorname{tr}\tilde{\boldsymbol{E}} = \operatorname{tr}\boldsymbol{E} + E_{33} \ , \tag{6.16}$$

where $\operatorname{tr}\boldsymbol{E} = A^{\alpha\beta}\,E_{\alpha\beta}$, and

$$\tilde{\boldsymbol{E}} : \tilde{\boldsymbol{E}} = \boldsymbol{E} : \boldsymbol{E} + E_{33}^2 \ , \tag{6.17}$$

where $\boldsymbol{E} : \boldsymbol{E} = E^{\alpha\beta}\,E_{\alpha\beta}$. The 2D membrane strain energy is

$$W_{\mathrm{M}}(\tilde{\boldsymbol{E}}) = \frac{\Lambda}{2}\big(\operatorname{tr}\tilde{\boldsymbol{E}}\big)^2 + \mu\,\tilde{\boldsymbol{E}} : \tilde{\boldsymbol{E}} \ , \tag{6.18}$$

where $\Lambda = T\,\tilde{\Lambda}$ and $\mu = T\,\tilde{\mu}$. Thus, the in-plane Kirchhoff stress is

$$\tau^{\alpha\beta} = \frac{\partial W_{\mathrm{M}}}{\partial E_{\alpha\beta}} = \Lambda\operatorname{tr}\tilde{\boldsymbol{E}}\,A^{\alpha\beta} + 2\,\mu\,E^{\alpha\beta} \ . \tag{6.19}$$

The normal stretch E_{33} can be determined through plane-strain or plane-stress conditions. Following the plane-strain approach, $E_{33} = 0$; therefore, $\operatorname{tr}\tilde{\boldsymbol{E}} = \operatorname{tr}\boldsymbol{E}$. Hence, Eq. (6.19) can be expressed as

$$\tau^{\alpha\beta} = \Lambda \operatorname{tr} \boldsymbol{E}\, A^{\alpha\beta} + 2\,\mu\, E^{\alpha\beta} \ . \tag{6.20}$$

As $E_{\alpha\beta}$ is symmetric,

$$\frac{\partial E_{\alpha\beta}}{\partial E_{\gamma\delta}} = \frac{1}{2}\left(\delta_\alpha^\gamma\, \delta_\beta^\delta + \delta_\alpha^\delta\, \delta_\beta^\gamma\right) \ , \tag{6.21}$$

where the right hand side is a fourth-order symmetric identity tensor. Following Eq. (2.12),

$$\delta E^{\alpha\beta} = \delta E_{\gamma\delta}\, A^{\alpha\gamma}\, A^{\beta\delta} \ . \tag{6.22}$$

Plugging Eq. (6.22) into Eq. (6.21), we get

$$\frac{\partial E^{\alpha\beta}}{\partial E_{\gamma\delta}} = \frac{1}{2}\left(A^{\alpha\gamma}\, A^{\beta\delta} + A^{\alpha\delta}\, A^{\beta\gamma}\right) \tag{6.23}$$

Thus, the elasticity tensor would be

$$c^{\alpha\beta\gamma\delta} = \frac{\partial \tau^{\alpha\beta}}{\partial E_{\alpha\beta}} = \Lambda\, A^{\alpha\beta}\, A^{\gamma\delta} + \mu\left(A^{\alpha\gamma}\, A^{\beta\delta} + A^{\alpha\delta}\, A^{\beta\gamma}\right) \tag{6.24}$$

Following the plane-stress approach,

$$\tau^{33} = \frac{\partial W_{\mathrm{M}}}{\partial E_{33}} = \Lambda\left(\operatorname{tr} \boldsymbol{E} + E_{33}\right) + 2\,\mu\, E_{33} = 0 \ , \tag{6.25}$$

which gives

$$E_{33} = -\frac{\Lambda \operatorname{tr} \boldsymbol{E}}{\Lambda + 2\,\mu} \ . \tag{6.26}$$

Plugging Eq. (6.26) into Eq. (6.19), we have

$$\tau^{\alpha\beta} = \frac{2\,\Lambda\,\mu}{\Lambda + 2\,\mu} \operatorname{tr} \boldsymbol{E}\, A^{\alpha\beta} + 2\,\mu\, E^{\alpha\beta} \ . \tag{6.27}$$

Similar to Eq. (6.24), the plane-stress elasticiy tensor is then

$$c^{\alpha\beta\gamma\delta} = \frac{\partial \tau^{\alpha\beta}}{\partial E_{\alpha\beta}} = \frac{2\,\Lambda\,\mu}{\Lambda + 2\,\mu} A^{\alpha\beta}\, A^{\gamma\delta} + \mu\left(A^{\alpha\gamma}\, A^{\beta\delta} + A^{\alpha\delta}\, A^{\beta\gamma}\right). \tag{6.28}$$

6.2.1.2 NP shell model

From Eq. (4.56),

$$\operatorname{tr} \tilde{\boldsymbol{E}} = \operatorname{tr} \overset{*}{\boldsymbol{E}} + \overset{*}{E}_{33} \ , \tag{6.29}$$

where

$$\operatorname{tr} \overset{*}{\boldsymbol{E}} = G^{\alpha\beta}\, \overset{*}{E}_{\alpha\beta} \tag{6.30}$$

and $\overset{*}{E}_{\alpha\beta}$ is given by Eq. (4.57). Further

$$\tilde{\boldsymbol{E}} : \tilde{\boldsymbol{E}} = \overset{*}{\boldsymbol{E}} : \overset{*}{\boldsymbol{E}} + \overset{*}{E}{}_{33}^{2} \ , \tag{6.31}$$

where $\overset{*}{\boldsymbol{E}} : \overset{*}{\boldsymbol{E}} = \overset{*}{E}{}^{\alpha\beta}\, \overset{*}{E}_{\alpha\beta}$. Similar to the membrane formulation,

$$\tilde{\tau}^{\alpha\beta} = \frac{\partial \tilde{W}}{\partial \overset{*}{E}_{\alpha\beta}} = \tilde{\Lambda} \operatorname{tr} \tilde{\boldsymbol{E}}\, G^{\alpha\beta} + 2\, \tilde{\mu}\, \overset{*}{E}{}^{\alpha\beta} \ , \tag{6.32}$$

where $\tilde{W}$ is given by Eq. (6.15) and

$$\overset{*}{E}{}^{\alpha\beta} = \overset{*}{E}_{\gamma\delta}\, G^{\alpha\gamma}\, G^{\beta\delta} \ . \tag{6.33}$$

Assuming the plane-strain condition,

$$\tilde{\tau}^{\alpha\beta} = \tilde{\Lambda} \operatorname{tr} \overset{*}{\boldsymbol{E}}\, G^{\alpha\beta} + 2\, \tilde{\mu}\, \overset{*}{E}{}^{\alpha\beta} \ , \tag{6.34}$$

with

$$\tilde{c}^{\alpha\beta\gamma\delta} = \frac{\partial \tilde{\tau}^{\alpha\beta}}{\partial \overset{*}{E}_{\alpha\beta}} = \tilde{\Lambda}\, G^{\alpha\beta}\, G^{\gamma\delta} + \tilde{\mu} \left(G^{\alpha\gamma}\, G^{\beta\delta} + G^{\alpha\delta}\, G^{\beta\gamma} \right) \ . \tag{6.35}$$

Considering a plane-stress condition,

$$\tilde{\tau}^{\alpha\beta} = \frac{2\, \tilde{\Lambda}\, \tilde{\mu}}{\tilde{\Lambda} + 2\, \tilde{\mu}} \operatorname{tr} \overset{*}{\boldsymbol{E}}\, G^{\alpha\beta} + 2\, \tilde{\mu}\, \overset{*}{E}{}^{\alpha\beta} \ , \tag{6.36}$$

with

$$\tilde{c}^{\alpha\beta\gamma\delta} = \frac{\partial \tilde{\tau}^{\alpha\beta}}{\partial \overset{*}{E}_{\alpha\beta}} = \frac{2\, \tilde{\Lambda}\, \tilde{\mu}}{\tilde{\Lambda} + 2\, \tilde{\mu}}\, G^{\alpha\beta}\, G^{\gamma\delta} + \tilde{\mu} \left(G^{\alpha\gamma}\, G^{\beta\delta} + G^{\alpha\delta}\, G^{\beta\gamma} \right). \tag{6.37}$$

6.2.1.3 AP shell model

First, we consider the plane-strain condition. Considering Eqs. (A.27) and (A.28) and plugging Eq. (6.34) into Eq. (4.71), we have

$$\hat{\tau}^{\alpha\beta} = \tilde{\Lambda} \operatorname{tr} \boldsymbol{E}\, A^{\alpha\beta} + 2\, \tilde{\mu}\, E^{\alpha\beta} \tag{6.38}$$

and

$$\begin{aligned}\hat{\tau}^{\alpha\beta}_{,3} &= 2\,\tilde{\Lambda}\,A^{\alpha\beta}\,B^{\gamma\delta}\,E_{\gamma\delta} + 4\,\tilde{\mu}\,E_{\gamma\delta}\left(B^{\alpha\gamma}\,A^{\beta\delta} + A^{\alpha\gamma}\,B^{\beta\delta}\right) \\ &- \tilde{\Lambda}\,\mathrm{tr}\,\boldsymbol{K}\,A^{\alpha\beta} - 2\,\tilde{\mu}\,K^{\alpha\beta}\ .\end{aligned} \tag{6.39}$$

If the shell is initially flat, i.e. $B^{\alpha\beta} = 0$ or if the shell is sufficiently thin to neglect the mixed terms, Eq. (6.39) can be written as

$$\hat{\tau}^{\alpha\beta}_{,3} = -\tilde{\Lambda}\,\mathrm{tr}\,\boldsymbol{K}\,A^{\alpha\beta} - 2\,\tilde{\mu}\,K^{\alpha\beta}\ . \tag{6.40}$$

If the shell is fully-stressed and $\mu_0 \approx 1$, the stress and bending moment tensors are obtained by plugging Eqs. (6.38) and (6.40) into Eq. (4.75) as

$$\begin{aligned}\tau^{\alpha\beta} &= \Lambda\,\mathrm{tr}\,\boldsymbol{E}\,A^{\alpha\beta} + 2\,\mu\,E^{\alpha\beta}\ , \\ M^{\alpha\beta}_{0} &= \frac{T^2}{12}\left(\Lambda\,\mathrm{tr}\,\boldsymbol{K}\,A^{\alpha\beta} + 2\,\mu\,K^{\alpha\beta}\right)\ ,\end{aligned} \tag{6.41}$$

which are the same as the stress and moment tensors of the Koiter shell model, cf. Eq. (3.19).

In the same fashion, if the plane-stress condition is assumed, the stress and moment tensors are then

$$\begin{aligned}\tau^{\alpha\beta} &= \frac{2\,\Lambda\,\mu}{\Lambda + 2\,\mu}\,\mathrm{tr}\,\boldsymbol{E}\,A^{\alpha\beta} + 2\,\mu\,E^{\alpha\beta}\ , \\ M^{\alpha\beta}_{0} &= \frac{T^2}{12}\left(\frac{2\,\Lambda\,\mu}{\Lambda + 2\,\mu}\,\mathrm{tr}\,\boldsymbol{K}\,A^{\alpha\beta} + 2\,\mu\,K^{\alpha\beta}\right)\ .\end{aligned} \tag{6.42}$$

6.2.1.4 DD shell model

From the elasticity tensors derived in Sec. 6.2.1.1, one can find the corresponding moment tangent $f^{\alpha\beta\gamma\delta}$ from Eqs. (4.97) and (4.101) as

$$f^{\alpha\beta\gamma\delta} = \frac{T^2}{12}\,c^{\alpha\beta\gamma\delta}_{0}\ . \tag{6.43}$$

For the plane-strain case, cf. Eq. (3.18),

$$c^{\alpha\beta\gamma\delta}_{0} = c^{\alpha\beta\gamma\delta} = \Lambda\,A^{\alpha\beta}\,A^{\gamma\delta} + \mu\left(A^{\alpha\gamma}\,A^{\beta\delta} + A^{\alpha\delta}\,A^{\beta\gamma}\right) \tag{6.44}$$

and for the plane-stress case,

$$c^{\alpha\beta\gamma\delta}_{0} = c^{\alpha\beta\gamma\delta} = \frac{2\,\Lambda\,\mu}{\Lambda + 2\,\mu}\,A^{\alpha\beta}\,A^{\gamma\delta} + \mu\left(A^{\alpha\gamma}\,A^{\beta\delta} + A^{\alpha\delta}\,A^{\beta\gamma}\right)\ . \tag{6.45}$$

With simple algebraic manipulation, the stress tensors of Eqs. (6.41) and (6.42) are obtained following

$$\tau^{\alpha\beta} = c^{\alpha\beta\gamma\delta}\, E_{\gamma\delta} \tag{6.46}$$

and the moment tensors of Eqs. (6.41) and (6.42) are found as

$$M_0^{\alpha\beta} = f^{\alpha\beta\gamma\delta}\, K_{\gamma\delta} \ . \tag{6.47}$$

Remark 6.3. If the plane-stress condition is assumed, the introduced formulations can also be used for an incompressible St. Venant–Kirchhoff solid. This is due to the fact that the first Lamé's parameter $\tilde{\Lambda}$ (or $\Lambda = T\,\tilde{\Lambda}$) shows up only in a combined expression (see e.g. the front term of Eq. (6.45)), which has a finite value in the incompressibility limit (Chapelle et al., 2004), i.e.

$$\lim_{\Lambda \to \infty} \left(\frac{2\,\Lambda\,\mu}{\Lambda + 2\,\mu} \right) = 2\,\mu \ . \tag{6.48}$$

For instance, under incompressibility, Eq. (6.45) would reduce to

$$c_0^{\alpha\beta\gamma\delta} = 2\,\mu\, A^{\alpha\beta}\, A^{\gamma\delta} + \mu \left(A^{\alpha\gamma}\, A^{\beta\delta} + A^{\alpha\delta}\, A^{\beta\gamma} \right) \ , \tag{6.49}$$

which is identical to the elasticity tensor of an incompressible Neo–Hookean solid before deformation, cf. Eq. (6.69).

6.2.2 Incompressible Neo–Hooke (NH)

The incompressible Neo–Hookean (NH) model is formulated based on the statistical thermodynamics of cross-linked polymer chains (Ogden, 1987). It is the most common hyperelastic constitution for rubber–like and soft biological materials. For instance, it is used to model the mechanical behavior of spleen (Davies et al., 2002), liver and kidney (Chui et al., 2004), breast (O'Hagan and Samani, 2008) and lung (Rausch et al., 2011) among others (Wex et al., 2015). The 3D strain-energy density function of an incompressible Neo-Hookean solid is

$$\tilde{W}_{\text{inc}}(\tilde{I}_1) = \frac{\tilde{c}_1}{2} \left(\tilde{I}_1 - 3 \right) \ , \tag{6.50}$$

where $\tilde{c}_1 = \tilde{\mu}$ is the infinitesimal 3D shear modulus to be set and $\tilde{I}_1$ is the first invariant of the right Cauchy–Green strain tensor $\tilde{\boldsymbol{C}}$.

6.2.2.1 Membrane model

Plugging Eq. (6.50) into Eqs. (4.37) and (4.38), the augmented 2D incompressible Neo–Hookean strain energy is

$$W_{\mathrm{M}}(\tilde{I}_1, \tilde{J}) = \frac{c_1}{2}\left(\tilde{I}_1 - 3\right) + p\,\tilde{g}\ , \tag{6.51}$$

where $c_1 = T\,\tilde{c}_1 = \mu$ is physically related to the 2D shear modulus μ as $\mu = T\,\tilde{\mu}$. From Eq. (4.40), the in-plane and out-of-plane Kirchhoff stress tensors are, respectively,

$$\begin{aligned} \tau^{\alpha\beta} &= 2\,\frac{\partial W_{\mathrm{M}}}{\partial a_{\alpha\beta}} &&= c_1\,A^{\alpha\beta} + p\,\tilde{J}\,a^{\alpha\beta}\ , \\ \tau^{33} &= \frac{1}{\lambda_3}\,\frac{\partial W_{\mathrm{M}}}{\partial \lambda_3} &&= c_1 + p\,\frac{J^2}{\tilde{J}}\ . \end{aligned} \tag{6.52}$$

Assuming the plane-stress condition $\tau^{33} = 0$, the Lagrange multiplier would be

$$p = -\frac{c_1}{J^2} \tag{6.53}$$

where is assumed that $\tilde{J} = 1$ following Eq. (6.1). Plugging Eq. (6.53) into Eq. (4.40.1), the in-plane stress components $\mathcal{S}$ are then

$$\tau^{\alpha\beta} = c_1\left(A^{\alpha\beta} - \frac{1}{J^2}\,a^{\alpha\beta}\right)\ . \tag{6.54}$$

According to Eq. (4.41), the components of the membrane elasticity tensor on $\mathcal{S}$ are

$$c^{\alpha\beta\gamma\delta} := 2\,\frac{\partial \tau^{\alpha\beta}}{\partial a_{\gamma\delta}} = \frac{2\,c_1}{J^2}\left(a^{\alpha\beta}\,a^{\gamma\delta} - a^{\alpha\beta\gamma\delta}\right)\ , \tag{6.55}$$

where $a^{\alpha\beta\gamma\delta}$ is given by Eq. (A.4).

As mentioned in Remark 6.2, the augmented strain energy function (6.51) can be represented by a modified (distortional) strain energy function as

$$W_{\mathrm{M}}(\tilde{I}_1, \tilde{J}) = \frac{c_1}{2}\left(\bar{\tilde{I}}_1 - 3\right) + p\,\tilde{g}\ , \tag{6.56}$$

where

$$\bar{\tilde{I}}_1 = \tilde{J}^{-2/3}\,\tilde{I}_1\ . \tag{6.57}$$

Thus, the Kirchoff stress tensors are now

$$\begin{aligned} \tau^{\alpha\beta} &= c_1\,\tilde{J}^{-2/3}\left(A^{\alpha\beta} - \frac{1}{3}\,\tilde{I}_1\,a^{\alpha\beta}\right) + p\,\tilde{J}\,a^{\alpha\beta}\ , \\ \tau^{33} &= c_1\,\tilde{J}^{-2/3}\left(1 - \frac{1}{3}\,\frac{J^2}{\tilde{J}^2}\,\tilde{I}_1\right) + p\,\frac{J^2}{\tilde{J}}\ . \end{aligned} \tag{6.58}$$

Assuming the incompressibility condition $\tilde{J} = 1$ and the plane-stress condition $\tau^{33} = 0$,

$$p = -c_1 \big(\frac{1}{J^2} - \frac{1}{3}\,\tilde{I}_1\big) \ , \tag{6.59}$$

which gives

$$\tau^{\alpha\beta} = c_1 \big(A^{\alpha\beta} - \frac{1}{J^2}\,a^{\alpha\beta}\big) \ . \tag{6.60}$$

As it can be seen from Eqs. (6.53) and (6.59), the two introduced approaches give different Lagrange multipliers although both leads to an identical total in-plane Kirchhoff stress (cf. Eqs. (6.54) and (6.60)).

6.2.2.2 NP shell model

Likewise to the membrane formulation, the strain energy function of a 3D incompressible Neo-Hookean solid (6.50) is modified by the contribution of the Lagrange multiplier as

$$\tilde{W}(\tilde{I}_1, \tilde{J}) = \frac{\tilde{c}_1}{2}\left(\tilde{I}_1 - 3\right) + \tilde{p}\,\tilde{g} \ . \tag{6.61}$$

From Eq. (4.62),

$$\begin{aligned} \tilde{\tau}^{\alpha\beta} \ &= \ 2\,\frac{\partial \tilde{W}}{\partial g_{\alpha\beta}} \ = \tilde{c}_1\,G^{\alpha\beta} + \tilde{p}\,\tilde{J}\,g^{\alpha\beta} \ , \\ \tilde{\tau}^{33} \ &= \ \frac{1}{\overset{*}{\lambda}_3}\,\frac{\partial \tilde{W}}{\partial \overset{*}{\lambda}_3} \ = \tilde{c}_1 + \tilde{p}\,\frac{\overset{*}{J}{}^2}{\tilde{J}} \ . \end{aligned} \tag{6.62}$$

Considering $\tilde{J} = 1$ and the plane-stress condition $\tilde{\tau}^{33} = 0$, the Lagrange multiplier is found as

$$\tilde{p} = -\frac{\tilde{c}_1}{\overset{*}{J}{}^2} \ . \tag{6.63}$$

Plugging Eq. (6.63) into Eq. (6.62.1), the in-plane stress components on $\overset{*}{\mathcal{S}}$ are then

$$\tilde{\tau}^{\alpha\beta} = \tilde{c}_1 \big(G^{\alpha\beta} - \frac{1}{\overset{*}{J}{}^2}\,g^{\alpha\beta}\big) \ . \tag{6.64}$$

Thus, the elasticity tensor on $\overset{*}{\mathcal{S}}$ is

$$\tilde{c}^{\alpha\beta\gamma\delta} := 2\,\frac{\partial \tilde{\tau}^{\alpha\beta}}{\partial g_{\gamma\delta}} = \frac{2\,\tilde{c}_1}{\overset{*}{J}{}^2}\,\big(g^{\alpha\beta}\,g^{\gamma\delta} - g^{\alpha\beta\gamma\delta}\big) \ , \tag{6.65}$$

following Eq. (4.67).

6.2.2.3 AP shell model

From Eqs. (4.71.1) and (6.64), we have

$$\hat{\tau}^{\alpha\beta} = \tilde{c}_1 \left(A^{\alpha\beta} - \frac{1}{J^2}\, a^{\alpha\beta} \right) . \tag{6.66}$$

Thus, from Eqs. (4.71.2) and (6.64), one can obtain

$$\hat{\tau}^{\alpha\beta}_{,3} = 2\,\tilde{c}_1 \left(B^{\alpha\beta} - \frac{1}{J^2} \left[b^{\alpha\beta} + 2\,(H - H_0)\, a^{\alpha\beta} \right] \right) . \tag{6.67}$$

The linearization of kinematic variables w.r.t. the through-the-thickness coordinate ξ can be found in Appendix A.3. The corresponding material tangents, defined in Sec. 4.3.2.2, are

$$\begin{aligned} \hat{c}^{\alpha\beta\gamma\delta} &= \frac{2\,\tilde{c}_1}{J^2} \left(a^{\alpha\beta}\, a^{\gamma\delta} - a^{\alpha\beta\gamma\delta} \right) , \\ \hat{d}^{\alpha\beta\gamma\delta} &= 0 , \\ \hat{c}^{\alpha\beta\gamma\delta}_{,3} &= \frac{4\,\tilde{c}_1}{J^2} \left(b^{\alpha\beta}\, a^{\gamma\delta} + a^{\alpha\beta}\, b^{\gamma\delta} \right) + 4\,(H - H_0)\, \hat{c}^{\alpha\beta\gamma\delta} , \\ \hat{d}^{\alpha\beta\gamma\delta}_{,3} &= -\hat{c}^{\alpha\beta\gamma\delta} . \end{aligned} \tag{6.68}$$

6.2.2.4 DD shell model

The membrane energy W_{M}, the membrane stress tensor $\tau^{\alpha\beta}$ and its corresponding tangent $c^{\alpha\beta\gamma\delta}$ are derived in Sec. 6.2.2.1. In the reference configuration, $J = 1$ and $a^{\alpha\beta} = A^{\alpha\beta}$. Thus, having the membrane elasticity tensor (4.41), we get

$$c_0^{\alpha\beta\gamma\delta} := 2\, c_1\, A^{\alpha\beta}\, A^{\gamma\delta} + c_1 \left(A^{\alpha\gamma}\, A^{\beta\delta} + A^{\alpha\delta}\, A^{\beta\gamma} \right) , \tag{6.69}$$

following Eq. (4.97).

Accordingly, the bending energy W_{B} can be found by plugging Eq. (6.69) into Eq. (4.99), which gives the bending moment

$$M_0^{\alpha\beta} = f^{\alpha\beta\gamma\delta}\, \left(b_{\gamma\delta} - B_{\gamma\delta} \right) , \tag{6.70}$$

where

$$f^{\alpha\beta\gamma\delta} := \frac{T^2}{12} \left[2\, c_1\, A^{\alpha\beta}\, A^{\gamma\delta} + c_1 \left(A^{\alpha\gamma}\, A^{\beta\delta} + A^{\alpha\delta}\, A^{\beta\gamma} \right) \right] . \tag{6.71}$$

Remark 6.4. The strain energy functions of the material models, introduced in this thesis, depend on the first invariant of the right Cauchy–Green deformation tensor. Thus, their corresponding stress, moment and tangent tensors include expressions similar to an incompressible Neo-Hookean material. In order to simplify the formulations, we introduce normalized quantities by setting the materiial constants to 1. For the NP shell model, $\tilde{\tau}^{\alpha\beta}_{\mathrm{NH}}$ and $\tilde{c}^{\alpha\beta\gamma\delta}_{\mathrm{NH}}$ are defined by setting $\tilde{c}_1 = 1$ in Eqs. (6.64) and (6.65), as

$$\tilde{\tau}^{\alpha\beta}_{\mathrm{NH}} := G^{\alpha\beta} - \frac{1}{\overset{*}{J}{}^2}\, g^{\alpha\beta} \;, \tag{6.72}$$

$$\tilde{c}^{\alpha\beta\gamma\delta}_{\mathrm{NH}} := 2\,\frac{\partial \tilde{\tau}^{\alpha\beta}_{\mathrm{NH}}}{\partial g_{\gamma\delta}} = \frac{2}{\overset{*}{J}{}^2}\,\left(g^{\alpha\beta}\, g^{\gamma\delta} - g^{\alpha\beta\gamma\delta}\right) \;. \tag{6.73}$$

For the membrane model and the DD shell model, the normalized $\tau^{\alpha\beta}_{\mathrm{NH}}$ and $c^{\alpha\beta\gamma\delta}_{\mathrm{NH}}$ are derived by setting $c_1 = 1$ in Eqs. (6.54) and (6.55), which yields

$$\tau^{\alpha\beta}_{\mathrm{NH}} := A^{\alpha\beta} - \frac{1}{J^2}\, a^{\alpha\beta} \tag{6.74}$$

and

$$c^{\alpha\beta\gamma\delta}_{\mathrm{NH}} := 2\,\frac{\partial \tau^{\alpha\beta}_{\mathrm{NH}}}{\partial a_{\gamma\delta}} = \frac{2}{J^2}\,\left(a^{\alpha\beta}\, a^{\gamma\delta} - a^{\alpha\beta\gamma\delta}\right) \;. \tag{6.75}$$

Accordingly, in the reference configuration,

$$c^{\alpha\beta\gamma\delta}_{\mathrm{NH0}} := \left(c^{\alpha\beta\gamma\delta}_{\mathrm{NH}}\right)_{\mathcal{S}_0} = 2\, A^{\alpha\beta}\, A^{\gamma\delta} + A^{\alpha\gamma}\, A^{\beta\delta} + A^{\alpha\delta}\, A^{\beta\gamma} \tag{6.76}$$

and trivially $\tau^{\alpha\beta}_{\mathrm{NH0}} := \left(\tau^{\alpha\beta}_{\mathrm{NH}}\right)_{\mathcal{S}_0} = 0$.

Similarly, the normalized stresses and tangent tensors for the AP shell model are defined according to Eqs. (6.66), (6.67) and (6.68) as

$$\begin{aligned} \hat{\tau}^{\alpha\beta}_{\mathrm{NH}} &= \tau^{\alpha\beta}_{\mathrm{NH}} \;, \\ \hat{\tau}^{\alpha\beta}_{\mathrm{NH},3} &= 2\left(B^{\alpha\beta} - \frac{1}{J^2}\left[b^{\alpha\beta} + 2\,(H - H_0)\, a^{\alpha\beta}\right]\right) \;, \end{aligned} \tag{6.77}$$

$$\begin{aligned} \hat{c}^{\alpha\beta\gamma\delta}_{\mathrm{NH}} &= c^{\alpha\beta\gamma\delta}_{\mathrm{NH}} \;, \qquad & \hat{c}^{\alpha\beta\gamma\delta}_{\mathrm{NH},3} &= \frac{4}{J^2}\left(b^{\alpha\beta}\, a^{\gamma\delta} + a^{\alpha\beta}\, b^{\gamma\delta}\right) + 4\,(H - H_0)\, \hat{c}^{\alpha\beta\gamma\delta}_{\mathrm{NH}} \;, \\ \hat{d}^{\alpha\beta\gamma\delta}_{\mathrm{NH}} &= 0 \;, \qquad & \hat{d}^{\alpha\beta\gamma\delta}_{\mathrm{NH},3} &= -\hat{c}^{\alpha\beta\gamma\delta}_{\mathrm{NH}} \;. \end{aligned} \tag{6.78}$$

6.2.3 Incompressible Mooney–Rivlin (MR)

The Mooney–Rivlin (MR) model is one of the oldest and most accurate constitutive laws developed for large deformations of isotropic materials (Mooney, 1940 and Rivlin, 1948). It has been used widely for the modeling of many biological tissues as listed by Wex et al. (2015). Its strain energy function is a linear combination of the first and second invariants of the right Cauchy–Green deformation tensor as

$$\tilde{W}\big(\tilde{I}_1, \tilde{I}_2, \tilde{J}\big) = \frac{\tilde{c}_1}{2}(\tilde{I}_1 - 3) + \frac{\tilde{c}_2}{2}(\tilde{I}_2 - 3) \ , \tag{6.79}$$

where $\tilde{c}_1$ and $\tilde{c}_2$ are stress-like parameters that should be found from experiments.

6.2.3.1 Membrane model

For this material model, the incompressible membrane stored energy is

$$W_{\mathrm{M}}\big(\tilde{I}_1, \tilde{I}_2, \tilde{J}\big) = \frac{c_1}{2}(\tilde{I}_1 - 2) + \frac{c_2}{2}(\tilde{I}_2 - 2) + p\,\tilde{g} \ , \tag{6.80}$$

where $c_1 := T\,\tilde{c}_1$ and $c_2 := T\,\tilde{c}_2$.

Following a procedure similar to Eqs. (6.51)-(6.55), it can be shown that

$$\tau^{\alpha\beta} = c_1\,\tau^{\alpha\beta}_{\mathrm{NH}} + \frac{c_2}{J^2}\left(A^{\alpha\beta} - I_1\,a^{\alpha\beta}\right) + c_2\,J^2\,a^{\alpha\beta} \tag{6.81}$$

and

$$\begin{aligned} c^{\alpha\beta\gamma\delta} &= (c_1 + c_2\,I_1)\;c^{\alpha\beta\gamma\delta}_{\mathrm{NH}} \\ &- \frac{2\,c_2}{J^2}\left(A^{\alpha\beta}\,a^{\gamma\delta} + a^{\alpha\beta}\,A^{\gamma\delta}\right) + 2\,c_2\,J^2\left(a^{\alpha\beta\gamma\delta} + a^{\alpha\beta}\,a^{\gamma\delta}\right) \ . \end{aligned} \tag{6.82}$$

6.2.3.2 NP shell model

For a shell formulation, the incompressible 3D strain energy density function of a Mooney–Rivlin solid can be written as

$$\tilde{W}\big(\tilde{I}_1, \tilde{I}_2, \tilde{J}\big) = \frac{\tilde{c}_1}{2}(\tilde{I}_1 - 3) + \frac{\tilde{c}_2}{2}(\tilde{I}_2 - 3) + \tilde{p}\,\tilde{g} \ . \tag{6.83}$$

The components of the Kirchhoff stress tensor thus are

$$\tilde{\tau}^{\alpha\beta} = \tilde{c}_1\,\tilde{\tau}^{\alpha\beta}_{\mathrm{NH}} + \frac{\tilde{c}_2}{\overset{*}{J}{}^2}\big(G^{\alpha\beta} - \overset{*}{I}_1\,g^{\alpha\beta}\big) + \tilde{c}_2\,\overset{*}{J}{}^2\,g^{\alpha\beta} \ , \tag{6.84}$$

which gives

$$\begin{aligned} \tilde{c}^{\alpha\beta\gamma\delta} &= \big(\tilde{c}_1 + \tilde{c}_2\,\overset{*}{I}_1\big)\;\tilde{c}^{\alpha\beta\gamma\delta}_{\mathrm{NH}} \\ &- \frac{2\,\tilde{c}_2}{\overset{*}{J}{}^2}\left(G^{\alpha\beta}\,g^{\gamma\delta} + g^{\alpha\beta}\,G^{\gamma\delta}\right) + 2\,\tilde{c}_2\,\overset{*}{J}{}^2\left(g^{\alpha\beta\gamma\delta} + g^{\alpha\beta}\,g^{\gamma\delta}\right) \ . \end{aligned} \tag{6.85}$$

6.2.3.3 AP shell model

Following Eq. (6.84),

$$\begin{aligned} \hat{\tau}^{\alpha\beta} &= \tilde{c}_1\, \tau^{\alpha\beta}_{\mathrm{NH}} + \frac{\tilde{c}_2}{J^2}\, (A^{\alpha\beta} - I_1\, a^{\alpha\beta}) + \tilde{c}_2\, J^2\, a^{\alpha\beta} \ , \\ \hat{\tau}^{\alpha\beta}_{,3} &= \tilde{c}_1\, \hat{\tau}^{\alpha\beta}_{\mathrm{NH},3} + \tilde{c}_2 \left(\hat{\tau}^{\alpha\beta}_{\mathrm{I}} + \hat{\tau}^{\alpha\beta}_{\mathrm{II}} \right) \ , \end{aligned} \tag{6.86}$$

where

$$\begin{aligned} \hat{\tau}^{\alpha\beta}_{\mathrm{I}} &= \frac{1}{J^2} \left[4\,(H - H_0)\,(A^{\alpha\beta} - I_1\, a^{\alpha\beta}) + 2\,(B^{\alpha\beta} - I_1\, b^{\alpha\beta}) - \hat{I}_{1,3}\, a^{\alpha\beta} \right] \ , \\ \hat{\tau}^{\alpha\beta}_{\mathrm{II}} &= 2\, J^2 \left[b^{\alpha\beta} - 2\,(H - H_0)\, a^{\alpha\beta} \right] \ . \end{aligned} \tag{6.87}$$

Thus, the tangent tensors are $\hat{d}^{\alpha\beta\gamma\delta} = 0$,

$$\begin{aligned} \hat{c}^{\alpha\beta\gamma\delta} &= (\tilde{c}_1 + \tilde{c}_2\, I_1)\, c^{\alpha\beta\gamma\delta}_{\mathrm{NH}} \\ &\quad - 2\, \frac{\tilde{c}_2}{J^2}\, (A^{\alpha\beta}\, a^{\gamma\delta} + a^{\alpha\beta}\, A^{\gamma\delta}) + 2\, \tilde{c}_2\, J^2\, (a^{\alpha\beta}\, a^{\gamma\delta} + a^{\alpha\beta\gamma\delta}) \ , \end{aligned} \tag{6.88}$$

$$\begin{aligned} \hat{c}^{\alpha\beta\gamma\delta}_{,3} &= \tilde{c}_1\, \hat{c}^{\alpha\beta\gamma\delta}_{\mathrm{NH},3} \\ &\quad + 2\, \tilde{c}_2 \left(\hat{\tau}^{\alpha\beta}_{\mathrm{II}} - \hat{\tau}^{\alpha\beta}_{\mathrm{I}} \right) a^{\gamma\delta} + 4\, \tilde{c}_2\, J^2 \left[b^{\alpha\beta\gamma\delta} + a^{\alpha\beta}\, b^{\gamma\delta} - 2\,(H - H_0)\, a^{\alpha\beta\gamma\delta} \right] \\ &\quad + 4\, \frac{\tilde{c}_2}{J^2} \left(I_1\, a^{\alpha\beta}\, b^{\gamma\delta} - A^{\alpha\beta}\, b^{\gamma\delta} - a^{\alpha\beta}\, B^{\gamma\delta} - \left[2\,(H - H_0)\, a^{\alpha\beta} + b^{\alpha\beta} \right] A^{\gamma\delta} \right) \\ &\quad - 4\, \frac{\tilde{c}_2}{J^2}\, I_1\, b^{\alpha\beta\gamma\delta} - 2\, \frac{\tilde{c}_2}{J^2} \left[4\,(H - H_0)\, I_1 + \hat{I}_{1,3} \right] a^{\alpha\beta\gamma\delta} \end{aligned} \tag{6.89}$$

and

$$\begin{aligned} \hat{d}^{\alpha\beta\gamma\delta}_{,3} &= \tilde{c}_1\, \hat{d}^{\alpha\beta\gamma\delta}_{\mathrm{NH},3} - \tilde{c}_2\, I_1\, c^{\alpha\beta\gamma\delta}_{\mathrm{NH}} + 2\, \frac{\tilde{c}_2}{J^2} \left(A^{\alpha\beta}\, a^{\gamma\delta} + a^{\alpha\beta}\, A^{\gamma\delta} \right) \\ &\quad - 2\, \tilde{c}_2\, J^2 \left(a^{\alpha\beta}\, a^{\gamma\delta} + a^{\alpha\beta\gamma\delta} \right) \ . \end{aligned} \tag{6.90}$$

6.2.3.4 DD shell model

In the reference configuration, $I_1 = 2$, $J = 1$ and $a^{\alpha\beta} = A^{\alpha\beta}$, thus the elasticity tensor (6.82) before deformation becomes

$$c^{\alpha\beta\gamma\delta}_{0} = \left(c_1 + c_2 \right) c^{\alpha\beta\gamma\delta}_{\mathrm{NH0}} \ . \tag{6.91}$$

The moment tensor $M^{\alpha\beta}$ and its tangent $f^{\alpha\beta\gamma\delta}$ are then derived from Eqs. (4.100) and (4.101), respectively.

6.2.4 Incompressbile Fung

This model has been proposed first by Fung (1967) and was then further investigated by Demiray (1972)[8]. Later, Humphrey and Yin (1987) extended the formulation by including an anisotropic contribution of fibers to model passive cardiac tissue. Further, it is successfully employed for the FE analysis of spleen (e.g. Carter et al., 2001 and Davies et al., 2002), liver (e.g. Chui et al., 2004 and Roan and Vemaganti, 2007) and brain (e.g. Rashid et al., 2013 and Rashid et al., 2014) tissues. The strain energy function of this model has an exponential form in terms of the first invariant of the Cauchy–Green deformation tensor as

$$\tilde{W}(\tilde{I}_1) = \frac{\tilde{c}_1}{2\,c_2}\left\{\exp\left[c_2\,(\tilde{I}_1 - 3)\right] - 1\right\}\ , \tag{6.92}$$

where $\tilde{c}_1$ is a stress-like parameter and c_2 is a dimensionless constant.

6.2.4.1 Membrane model

The corresponding membrane strain energy function is

$$W_{\mathrm{M}}(\tilde{I}_1, \tilde{J}) = \frac{c_1}{2\,c_2}\left\{\exp\left[c_2\,(\tilde{I}_1 - 3)\right] - 1\right\} + p\,\tilde{g}\ , \tag{6.93}$$

where $c_1 = T\,\tilde{c}_1$. In the same fashion as the other models, we get

$$\tau^{\alpha\beta} = D_1\,\tau^{\alpha\beta}_{\mathrm{NH}} \tag{6.94}$$

and

$$c^{\alpha\beta\gamma\delta} = D_1\left(c^{\alpha\beta\gamma\delta}_{\mathrm{NH}} + 2\,c_2\,\tau^{\alpha\beta}_{\mathrm{NH}}\,\tau^{\gamma\delta}_{\mathrm{NH}}\right)\ , \tag{6.95}$$

where

$$D_1 := \frac{\partial W_{\mathrm{M}}}{\partial \tilde{I}_1} = c_1\,\exp\left[c_2\,(\tilde{I}_1 - 3)\right]\ . \tag{6.96}$$

6.2.4.2 NP shell model

Similar to the membrane formulation, for the NP shell model, the incompressible version of the Fung model (6.92) is

$$\tilde{W}(\tilde{I}_1, \tilde{J}) = \frac{\tilde{c}_1}{2\,c_2}\left\{\exp\left[c_2\,(\tilde{I}_1 - 3)\right] - 1\right\} + \tilde{p}\,\tilde{g}\ , \tag{6.97}$$

---

[8] In literature, this model is usually called as “Fung” model while it is also named “Fung–Demiray” (e.g. by Wex et al., 2015) or “Demiray” model (e.g. by Gasser et al., 2006).

which gives

$$\tilde{\tau}^{\alpha\beta} = \tilde{D}_1\,\tilde{\tau}^{\alpha\beta}_{\mathrm{NH}}\ , \tag{6.98}$$

$$\tilde{c}^{\alpha\beta\gamma\delta} = \tilde{D}_1\left(\tilde{c}^{\alpha\beta\gamma\delta}_{\mathrm{NH}} + 2\,c_2\,\tilde{\tau}^{\alpha\beta}_{\mathrm{NH}}\,\tilde{\tau}^{\gamma\delta}_{\mathrm{NH}}\right)\ , \tag{6.99}$$

with

$$\tilde{D}_1 := \frac{\partial\tilde{W}}{\partial\tilde{I}_1} = \tilde{c}_1\,\exp\left[c_2\,(\tilde{I}_1 - 3)\right]\ . \tag{6.100}$$

6.2.4.3 AP shell model

Plugging Eq. (6.98) into Eq. (4.71), we have

$$\begin{aligned}\hat{\tau}^{\alpha\beta}\ &= \hat{D}_1\,\tau^{\alpha\beta}_{\mathrm{NH}}\ ,\\ \hat{\tau}^{\alpha\beta}_{,3}\ &= \hat{D}_1\left(\tau^{\alpha\beta}_{\mathrm{NH},3} + c_2\left[\hat{I}_{1,3} + \frac{4}{J^2}\,(H - H_0)\right]\tau^{\alpha\beta}_{\mathrm{NH}}\right)\ ,\end{aligned} \tag{6.101}$$

where $\hat{I}_{1,3}$ is given by Eq. (A.23) (see Appendix A.3) and

$$\hat{D}_1 := \tilde{c}_1\,\exp\left[c_2\left(I_1 + \frac{1}{J^2} - 3\right)\right]\ . \tag{6.102}$$

The corresponding material tangents are $\hat{d}^{\alpha\beta\gamma\delta} = 0$ and

$$\begin{aligned}\hat{c}^{\alpha\beta\gamma\delta}\ &= \hat{D}_1\left(c^{\alpha\beta\gamma\delta}_{\mathrm{NH}} + 2\,c_2\,\tau^{\alpha\beta}_{\mathrm{NH}}\,\tau^{\gamma\delta}_{\mathrm{NH}}\right)\ ,\\ \hat{c}^{\alpha\beta\gamma\delta}_{,3}\ &= \hat{D}_1\left(\hat{c}^{\alpha\beta\gamma\delta}_{\mathrm{NH},3} + c_2\left[\hat{I}_{1,3} + \frac{4}{J^2}(H - H_0)\right]c^{\alpha\beta\gamma\delta}_{\mathrm{NH}}\right) + 2\,c_2\,\hat{\tau}^{\alpha\beta}_{,3}\,\tau^{\gamma\delta}_{\mathrm{NH}}\\ &\quad + 4\,c_2\,\hat{D}_1\,\tau^{\alpha\beta}_{\mathrm{NH}}\left(B^{\gamma\delta} - \frac{1}{J^2}\left[2\,(H - H_0)\,a^{\gamma\delta} + b^{\gamma\delta}\right]\right)\ ,\\ \hat{d}^{\alpha\beta\gamma\delta}_{,3}\ &= \hat{D}_1\,\hat{d}^{\alpha\beta\gamma\delta}_{\mathrm{NH},3} - 2\,c_2\,\hat{D}_1\,\tau^{\alpha\beta}_{\mathrm{NH}}\,\tau^{\gamma\delta}_{\mathrm{NH}}\ .\end{aligned} \tag{6.103}$$

6.2.4.4 DD shell model

The membrane stress $\tau^{\alpha\beta}$ and its tangent $c^{\alpha\beta\gamma\delta}$ are given by Eqs. (6.94) and (6.95), respectively. For the moment tensor $M^{\alpha\beta}$ and its tangent $f^{\alpha\beta\gamma\delta}$, one need to find the corresponding $c_0^{\alpha\beta\gamma\delta}$. In the reference configuration, $D_1 = c_1$ and $\tau^{\alpha\beta}_{\mathrm{NH0}} = 0$. Thus, from Eq. (6.95), the elasticity tensor before deformation is then

$$c_0^{\alpha\beta\gamma\delta} := c_1\,c^{\alpha\beta\gamma\delta}_{\mathrm{NH0}}\ . \tag{6.104}$$

6.3 Anisotropic models

The fibrous structure of soft tissues adds anisotropic features to their mechanical behavior. In order to capture those, different anisotropic hyperelastic models are introduced (Chagnon et al., 2015). In general, the are two approaches to describe the anisotropy of soft tissues. On one hand, the Green–Lagrange components can be used and on the other hand one can use the strain invariants. Here, the material models of the latter approach are studied. For isotropic materials (see Sec. 6.2), the deformation can be described by three strain invariants, which are the invariants of the Cauchy–Green deformation tensor $\tilde{I}_1$, $\tilde{I}_2$ and $\tilde{I}_3 := \tilde{J}$. Similarly, the deformation of anisotropic materials can be described by the strain invariants that are related to the principal direction of the fibers. Considering the principal direction of the i^{th} family of fibers is $\tilde{\boldsymbol{L}}_i$ in the reference configuration, the structural tensor $\tilde{\boldsymbol{M}}_i$ can be expressed according to the kinematics of Kirchhoff–Love shells as

$$\tilde{\boldsymbol{M}}_i := \tilde{\boldsymbol{L}}_i \otimes \tilde{\boldsymbol{L}}_i = \overset{*}{\boldsymbol{M}}_i + \overset{*}{L}{}_i^{33}\, \boldsymbol{N} \otimes \boldsymbol{N} \ . \tag{6.105}$$

The in-plane component of structural tensor is

$$\overset{*}{\boldsymbol{M}}_i := \overset{*}{\boldsymbol{L}}_i \otimes \overset{*}{\boldsymbol{L}}_i = \overset{*}{L}{}_i^{\alpha\beta}\, \boldsymbol{G}_\alpha \otimes \boldsymbol{G}_\beta \ , \tag{6.106}$$

where

$$\overset{*}{\boldsymbol{L}}_i := \overset{*}{L}{}_i^{\alpha}\, \boldsymbol{G}_\alpha \ , \quad \overset{*}{L}{}_i^{\alpha\beta} := \overset{*}{L}{}_i^{\alpha}\, \overset{*}{L}{}_i^{\beta} \ , \quad \overset{*}{L}{}_i^{\alpha} := \tilde{\boldsymbol{L}}_i \cdot \boldsymbol{G}^\alpha \ . \tag{6.107}$$

The out-of-plane component of structural tensor is then

$$\overset{*}{L}{}_i^{33} := \left(\tilde{\boldsymbol{L}}_i \cdot \boldsymbol{N}\right)^2 \ . \tag{6.108}$$

The first invariant of the structural tensor, which is used for most anisotropic models, is[9]

$$\tilde{I}_4^i := \operatorname{tr}\left(\tilde{\boldsymbol{C}}\, \tilde{\boldsymbol{M}}_i\right) = \tilde{\boldsymbol{L}}_i \cdot \tilde{\boldsymbol{C}} \tilde{\boldsymbol{L}}_i = \overset{*}{I}{}_4^i + \overset{*}{\lambda}{}_3^2\, \overset{*}{L}{}_i^{33} \ ; \tag{6.109}$$

however, other invariants can also be used (Chagnon et al., 2015). Likewise, the in-plane invariant is defined as

$$\overset{*}{I}{}_4^i := \operatorname{tr}\left(\overset{*}{\boldsymbol{C}}\, \overset{*}{\boldsymbol{M}}_i\right) = \overset{*}{\boldsymbol{L}}_i \cdot \overset{*}{\boldsymbol{C}} \overset{*}{\boldsymbol{L}}_i = g_{\alpha\beta}\, \overset{*}{L}{}_i^{\alpha\beta} \ . \tag{6.110}$$

In the same fashion, for the membrane formulation, the corresponding quantities are defined on the shell mid-surface as

$$\tilde{\boldsymbol{M}}_i = \boldsymbol{M}_i + L_i^{33}\, \boldsymbol{N} \otimes \boldsymbol{N} \ , \tag{6.111}$$

---

[9] Some scholars (e.g. Gasser et al., 2006) use $\tilde{I}_4$ and $\tilde{I}_6$ for $\tilde{I}_4^1$ and $\tilde{I}_4^2$ if two family of fibers are considered. Here, we use $\tilde{I}_4$ if only one family of fibers is included and $\tilde{I}_4^i$ for more families of fibers.

where

$$\boldsymbol{M}_i := \boldsymbol{L}_i \otimes \boldsymbol{L}_i = L_i^{\alpha\beta}\, \boldsymbol{A}_\alpha \otimes \boldsymbol{A}_\beta \ , \tag{6.112}$$

$$\boldsymbol{L}_i := L_i^{\alpha}\, \boldsymbol{A}_\alpha \ , \quad L_i^{\alpha\beta} := L_i^{\alpha}\, L_i^{\beta} \ , \quad L_i^{\alpha} = \boldsymbol{L}_i \cdot \boldsymbol{A}^\alpha \tag{6.113}$$

and $L_i^{33} := \big(\tilde{\boldsymbol{L}}_i \cdot \boldsymbol{N}\big)^2$. Thus, the invariants are reformulated as

$$\tilde{I}_4^i = I_4^i + \lambda_3^2\, L_i^{33} \ , \tag{6.114}$$

with

$$I_4^i := \operatorname{tr}\big(\boldsymbol{C}\,\boldsymbol{M}_i\big) = \boldsymbol{L}_i \cdot \boldsymbol{C}\boldsymbol{L}_i = a_{\alpha\beta}\, L_i^{\alpha\beta} \ . \tag{6.115}$$

Remark 6.5. Based on the Kirchhoff–Love hypothesis, $\overset{*}{L}{}_i^{33} = L_i^{33}$ is constant through the thickness. For thin membrane and shells, it is more realistic to assume that fibers are distributed layer-wise, i.e. $\overset{*}{L}{}_i^{33} = L_i^{33} = 0$. This implies that $\tilde{I}_4^i = \overset{*}{I}{}_4^i$ on $\overset{*}{\mathcal{S}}$ through the thickness and $\tilde{I}_4^i = I_4^i$ on $\mathcal{S}$. For the examples investigated in this thesis, it is assumed that $\overset{*}{L}{}_i^{33} = L_i^{33} = 0$.

Fiber-reinforced models have become popular for approximating the mechanical behavior of soft tissues. For instance, in arterial wall mechanics fiber-reinforced models, where the collagen fibers are embedded in an isotropic groundmatrix, have been used successfully (see e.g. Holzapfel et al., 2000 and Gasser et al., 2006). In general, anisotropic hyperelastic material models developed for soft tissues are based on the assumption that the material is constructed from an *isotropic* matrix reinforced with several fibers that have given principal orientations, which induce *anisotropy*. Hence, the strain energy function $\tilde{W}$ is composed of an isotropic part $\tilde{W}_\mathrm{m}$ and an anisotropic part $\tilde{W}_\mathrm{f}$ as

$$\tilde{W} = \tilde{W}_\mathrm{m}\big(\tilde{I}_1, \tilde{I}_2, \tilde{J}\big) + \sum_{i=1}^{n_\mathrm{f}} \tilde{W}_\mathrm{f}\big(\tilde{I}_1, \tilde{I}_2, \cdots, \tilde{I}_4^i, \tilde{I}_5^i, \cdots\big) \ , \tag{6.116}$$

where n_f is the number of fiber families. The anisotropic part may only include the invariants of the structural tensors, like in the anisotropic Mooney–Rivlin model (Sec. 6.3.1), or it may combine them with the invariants of the right Cauchy–Green deformation tensor, like in the Gasser–Ogden–Holzapfel model (Sec. 6.3.2). A detailed survey of anisotropic models for biological tissues can be found in Chagnon et al. (2015).

6.3.1 Anisotropic Mooney–Rivlin (AMR)

Here, the anisotropic Mooney–Rivlin (AMR) material model is obtained by generalizing the formulation of Rivlin and Saunders (1951) in terms of the invariants of the structural tensor as (Kaliske, 2000)

$$\tilde{W}_{\mathrm{f}}\big(\tilde{I}_4^i\big) = \sum_{j\geq 2} \tilde{c}_j \big(\tilde{I}_4^i - 1\big)^j \ , \qquad (i = 1,\ ...,n_{\mathrm{f}}) \ . \tag{6.117}$$

For the isotropic part, an incompressible Mooney–Rivlin constitution is considered (see Sec. 6.2.3). For the anisotropic part, n_{f} families of fibers with a quadratic potential are included. The incompressibility constrained is enforced through the Lagrange multiplier method. Thus, the total strain energy of the 3D continuum is expressed as

$$\begin{aligned} \tilde{W} &= \tilde{W}_{\mathrm{m}}\big(\tilde{I}_1, \tilde{I}_2, \tilde{J}\big) + \tilde{W}_{\mathrm{f}}\big(\tilde{I}_4^1, \tilde{I}_4^2, ..., \tilde{I}_4^{n_{\mathrm{f}}}\big) \\ &= \frac{\tilde{c}_1}{2}(\tilde{I}_1 - 3) + \frac{\tilde{c}_2}{2}(\tilde{I}_2 - 3) + \sum_{i=1}^{n_{\mathrm{f}}} \tilde{c}_{3i}\big(\tilde{I}_4^i - 1\big)^2 + \tilde{p}\,\tilde{g} \ . \end{aligned} \tag{6.118}$$

6.3.1.1 Membrane model

The corresponding membrane strain energy of Eq. (6.118) is

$$\begin{aligned} W_{\mathrm{M}} &= W_{\mathrm{m}}\big(\tilde{I}_1, \tilde{I}_2, \tilde{J}\big) + W_{\mathrm{f}}\big(\tilde{I}_4^1, \tilde{I}_4^2, ..., \tilde{I}_4^{n_{\mathrm{f}}}\big) \\ &= \frac{c_1}{2}(\tilde{I}_1 - 3) + \frac{c_2}{2}(\tilde{I}_2 - 3) + \sum_{i=1}^{n_{\mathrm{f}}} c_{3i}\big(\tilde{I}_4^i - 1\big)^2 + p\,\tilde{g} \ , \end{aligned} \tag{6.119}$$

where $c_1 = T\,\tilde{c}_1$, $c_2 = T\,\tilde{c}_2$ and $c_{3i} = T\,\tilde{c}_{3i}$. Assuming that $L_i^{33} = 0$, the anisotropic part of W_{M} do not contribute to the Lagrange multiplier p, which is obtained from $\tau^{33} = 0$. Thus, p is the same as for an isotropic Mooney–Rivlin solid (see Sec. 6.2.3). The total stress on $\mathcal{S}$ is then

$$\tau^{\alpha\beta} = \tau_{\mathrm{m}}^{\alpha\beta} + \tau_{\mathrm{f}}^{\alpha\beta} \ , \tag{6.120}$$

where the matrix contribution $\tau_{\mathrm{m}}^{\alpha\beta}$ is given by Eq. (6.81) and the fiber contribution is

$$\tau_{\mathrm{f}}^{\alpha\beta} = 2\sum_{i=1}^{n_{\mathrm{f}}} c_{3i}\big(\tilde{I}_4^i - 1\big)\, L_i^{\alpha\beta} \ . \tag{6.121}$$

The corresponding tangent tensor on $\mathcal{S}$ is split as

$$c^{\alpha\beta\gamma\delta} = c_{\mathrm{m}}^{\alpha\beta\gamma\delta} + c_{\mathrm{f}}^{\alpha\beta\gamma\delta} \ . \tag{6.122}$$

The isotropic part $c_{\mathrm{m}}^{\alpha\beta\gamma\delta}$ is defined by Eq. (6.82) and the anisotropic part is

$$c_{\mathrm{f}}^{\alpha\beta\gamma\delta} = 4\sum_{i=1}^{n_{\mathrm{f}}} c_{3i}\, L_i^{\alpha\beta}\, L_i^{\gamma\delta} \ , \tag{6.123}$$

6.3.1.2 NP shell model

Considering that $\overset{*}{L}{}_i^{33} = 0$, from Eq. (6.118), the total Kirchhoff stress on $\overset{*}{\mathcal{S}}$ is

$$\tilde{\tau}^{\alpha\beta} = \tilde{\tau}_{\mathrm{m}}^{\alpha\beta} + \tilde{\tau}_{\mathrm{f}}^{\alpha\beta} \ , \tag{6.124}$$

where

$$\tilde{\tau}_{\mathrm{f}}^{\alpha\beta} := 2\,\frac{\partial \tilde{W}_{\mathrm{f}}}{\partial g_{\alpha\beta}} = 2\sum_{i=1}^{n_{\mathrm{f}}} \tilde{c}_{3i}\big(\tilde{I}_4^i - 1\big)\,\overset{*}{L}{}_i^{\alpha\beta} \tag{6.125}$$

according to Eq. (6.118) and $\tilde{\tau}_{\mathrm{m}}^{\alpha\beta}$ is given by Eq. (6.84). The total elasticity tensor on $\overset{*}{\mathcal{S}}$ is then $\tilde{c}^{\alpha\beta\gamma\delta} = \tilde{c}_{\mathrm{m}}^{\alpha\beta\gamma\delta} + \tilde{c}_{\mathrm{f}}^{\alpha\beta\gamma\delta}$, where $\tilde{c}_{\mathrm{m}}^{\alpha\beta\gamma\delta}$ is given by Eq. (6.85) and

$$\tilde{c}_{\mathrm{f}}^{\alpha\beta\gamma\delta} = 4\sum_{i=1}^{n_{\mathrm{f}}} \tilde{c}_{3i}\,\overset{*}{L}{}_i^{\alpha\beta}\,\overset{*}{L}{}_i^{\gamma\delta} \ . \tag{6.126}$$

6.3.1.3 AP shell model

Likewise to Eq. (6.124), the total stress is split into the isotropic and anisotropic contributions as

$$\hat{\tau}^{\alpha\beta} = \hat{\tau}_{\mathrm{m}}^{\alpha\beta} + \hat{\tau}_{\mathrm{f}}^{\alpha\beta} \ , \tag{6.127}$$

where $\hat{\tau}_{\mathrm{m}}^{\alpha\beta}$ is given by Eq. (6.86.1) and

$$\hat{\tau}_{\mathrm{f}}^{\alpha\beta} = 2\sum_{i=1}^{n_{\mathrm{f}}} \tilde{c}_{3i}\big(I_4^i - 1\big)\,L_i^{\alpha\beta} \ . \tag{6.128}$$

Similarly, the first-order approximated terms are

$$\hat{\tau}_{,3}^{\alpha\beta} = \hat{\tau}_{\mathrm{m},3}^{\alpha\beta} + \hat{\tau}_{\mathrm{f},3}^{\alpha\beta} \ , \tag{6.129}$$

where $\hat{\tau}_{\mathrm{m},3}^{\alpha\beta}$ follows from Eq. (6.86.2) and

$$\hat{\tau}_{\mathrm{f},3}^{\alpha\beta} = 2\sum_{i=1}^{n_{\mathrm{f}}} \tilde{c}_{3i}\left[\hat{I}_{4,3}^i\,L_i^{\alpha\beta} + \big(I_4^i - 1\big)\,\hat{L}_{i,3}^{\alpha\beta}\right] \ . \tag{6.130}$$

Here, $\hat{L}^{\alpha\beta}_{i,3}$ and $\hat{I}^{i}_{4,3}$ are given by Eqs. (A.29) and (A.30), respectively. In the same fashion, the fibers and the matrix contribute to the corresponding tangents, i.e.

$$\begin{aligned}\hat{c}^{\alpha\beta\gamma\delta} &= \hat{c}^{\alpha\beta\gamma\delta}_{\mathrm{m}} + \hat{c}^{\alpha\beta\gamma\delta}_{\mathrm{f}} \ , \\ \hat{d}^{\alpha\beta\gamma\delta} &= \hat{d}^{\alpha\beta\gamma\delta}_{\mathrm{m}} + \hat{d}^{\alpha\beta\gamma\delta}_{\mathrm{f}} \ , \\ \hat{e}^{\alpha\beta\gamma\delta} &= \hat{e}^{\alpha\beta\gamma\delta}_{\mathrm{m}} + \hat{e}^{\alpha\beta\gamma\delta}_{\mathrm{f}} \ , \\ \hat{f}^{\alpha\beta\gamma\delta} &= \hat{f}^{\alpha\beta\gamma\delta}_{\mathrm{m}} + \hat{f}^{\alpha\beta\gamma\delta}_{\mathrm{f}} \ ,\end{aligned} \tag{6.131}$$

where the isotropic tensors $\hat{c}^{\alpha\beta\gamma\delta}_{\mathrm{m}}$, $\hat{c}^{\alpha\beta\gamma\delta}_{\mathrm{m},3}$ and $\hat{d}^{\alpha\beta\gamma\delta}_{\mathrm{m},3}$ are given by Eqs. (6.88-6.90) and $\hat{d}^{\alpha\beta\gamma\delta}_{\mathrm{m}} = 0$.

The anisotropic tangents are then

$$\begin{aligned}\hat{c}^{\alpha\beta\gamma\delta}_{\mathrm{f}} &= 4 \sum_{i=1}^{n_{\mathrm{f}}} \tilde{c}_{3i}\, L^{\alpha\beta}_{i}\, L^{\gamma\delta}_{i} \ , \\ \hat{d}^{\alpha\beta\gamma\delta}_{\mathrm{f}} &= 0 \ , \\ \hat{c}^{\alpha\beta\gamma\delta}_{\mathrm{f},3} &= 4 \sum_{i=1}^{n_{\mathrm{f}}} \tilde{c}_{3i} \left(L^{\alpha\beta}_{i}\, \hat{L}^{\gamma\delta}_{i,3} + \hat{L}^{\alpha\beta}_{i,3}\, L^{\gamma\delta}_{i} \right) \ , \\ \hat{d}^{\alpha\beta\gamma\delta}_{\mathrm{f},3} &= -4 \sum_{i=1}^{n_{\mathrm{f}}} \tilde{c}_{3i}\, L^{\alpha\beta}_{i}\, L^{\gamma\delta}_{i} \ .\end{aligned} \tag{6.132}$$

6.3.1.4 DD shell model

From Eqs. (6.82) and (6.123), the elasticty tensor (6.122) before deformation becomes

$$c^{\alpha\beta\gamma\delta}_{0} = \big(c_1 + c_2\big)\, c^{\alpha\beta\gamma\delta}_{\mathrm{NH0}} + 4 \sum_{i=1}^{n_{\mathrm{f}}} c_{3i}\, L^{\alpha\beta}_{i}\, L^{\gamma\delta}_{i} \ . \tag{6.133}$$

Similar to the isotropic models, for an anisotropic Mooney–Rivlin solid, the moment tensor $M^{\alpha\beta}_{0}$ and its tangent $f^{\alpha\beta\gamma\delta}$ are obtained by plugging $c^{\alpha\beta\gamma\delta}_{0}$ (6.133) into Eqs. (4.100) and (4.101).

6.3.2 Gasser–Ogden–Holzapfel (GOH - 3D GST)

The Gasser–Ogden–Holzapfel (GOH) material model is an anisotropic hyperelastic material model, which is used to model soft tissues with distributed collagen fibers, and is mainly developed for the modeling of cardiovascular arteries (Gasser et al., 2006). This model is constructed of an isotropic part, which represents the elastin matrix of soft tissue and is modeled by the incompressible Neo-Hookean material model, and an anisotropic part due the collagen network, which is based on the structural tensors of two families of fibers. Compared to the fiber reinforced models of Holzapfel et al. (2000) and Holzapfel et al. (2002a), Gasser et al. (2006) consider that orientations of the collagen fibers are dispersed. In many soft tissues, fibers might not be completely aligned and might have some dispersion. In general, there are two approaches to include the dispersion of fibers in the constitution: (1) The *angular integration* (AI) approach, which uses a probability density function to directly incorporated the dispersion effect in a given strain energy function and (2) using the *generalized structure tensor* (GST) (Skacel and Bursa, 2014 and Holzapfel et al., 2015). Here, we adopt the concept of the generalized structural tensor to model dispersion of fibers following Gasser et al. (2006). For a given family of fibers with the principal orientation $\tilde{\boldsymbol{L}}^i$, fibers are distributed with rotational symmetry about $\tilde{\boldsymbol{L}}^i$ so that the each family introduces a transversely isotropic response. In this section, a 3D generalized structural tensor (3D GST) is considered; however, for thin structures, 2D generalized structural tensors (2D GST) can also be used (Tonge et al., 2013), as discussed in Sec. 6.3.3. Following the Lagrange multiplier method to enforce the incompressibility, the strain energy density function suggested by Gasser et al. (2006) is expressed as

$$\tilde{W}(\tilde{I}_1, \tilde{J}_4^1, \tilde{J}_4^2, \tilde{J}) = \tilde{W}_{\mathrm{m}}(\tilde{I}_1) + \tilde{W}_{\mathrm{f}}(\tilde{J}_4^1, \tilde{J}_4^2) + \tilde{p}\,\tilde{g} \ , \tag{6.134}$$

where the isotropic contribution of matrix is

$$\tilde{W}_{\mathrm{m}} = \frac{\tilde{\mu}}{2}(\tilde{I}_1 - 3) \ , \tag{6.135}$$

with $\tilde{\mu}$ to be the shear modulus. The anisotropic contribution of fibers is

$$\tilde{W}_{\mathrm{f}} = \sum_{i=1}^{2} \frac{\tilde{k}_{1i}}{2\,k_{2i}} \left\{ \exp\left[k_{2i}\,(\tilde{J}_4^i - 1)^2\right] - 1 \right\} \ , \tag{6.136}$$

where $k_{2i} > 0$ is a dimensionless parameter and $\tilde{k}_{1i} > 0$ is a stress-like parameter to be determined from mechanical tests of the tissue. Further, $\tilde{J}_4^i$ are the invariants of the 3D generalized structural tensor $\tilde{\boldsymbol{H}}_i$. In the following sections, first we introduce the generalized structural tensor following the Kirchhoff–Love kinematics and then the membrane and shell models are derived.

6.3.2.1 3D generalized structural tensor (3D GST)

The 3D generalized structural tensor $\tilde{\boldsymbol{H}}_i$ is a linear combination of the *anisotropic* structural tensor $\tilde{\boldsymbol{M}}_i$ (6.105) and the isotropic identity tensor $\boldsymbol{1} \in \mathbb{R}^3$ as

$$\tilde{\boldsymbol{H}}_i := \kappa_i\,\boldsymbol{1} + (1 - 3\,\kappa_i)\,\tilde{\boldsymbol{M}}_i \ , \qquad (i = 1, 2) \ , \tag{6.137}$$

where $\kappa_i \in [0,\ 1/3]$ is the parameter determining the degree of dispersion (Gasser et al., 2006). Following the kinematics of a Kirchhoff–Love shell (see Sec. 4.1.1), the layer-wise 3D generalized structural tensor on $\overset{*}{\mathcal{S}}$ becomes

$$\tilde{\boldsymbol{H}}_i = \kappa_i\, \boldsymbol{1} + (1 - 3\,\kappa_i)\left(\overset{*}{L}{}_i^{\alpha\beta}\, \boldsymbol{G}_\alpha \otimes \boldsymbol{G}_\beta + \overset{*}{L}{}_i^{33}\, \boldsymbol{N} \otimes \boldsymbol{N}\right)\,, \quad (i = 1, 2)\;. \tag{6.138}$$

The first invariants of the 3D generalized structural tensor $\tilde{\boldsymbol{H}}_i$ are then

$$\tilde{J}_4^i := \tilde{\boldsymbol{C}} : \tilde{\boldsymbol{H}}_i = \kappa_i\big(\overset{*}{I}_1 + \overset{*}{\lambda}{}_3^2\big) + (1 - 3\,\kappa_i)\,\big(\overset{*}{I}{}_4^i + \overset{*}{\lambda}{}_3^2\, \overset{*}{L}{}_i^{33}\big)\,, \quad (i = 1, 2)\,, \tag{6.139}$$

where $\overset{*}{I}_1$, $\overset{*}{I}{}_4^i$ and $\overset{*}{L}{}_i^{33}$ are given by Eqs. (4.52), (6.110) and (6.108), respectively. Similarly, for a membrane formulation, the 3D generalized structural tensor on $\mathcal{S}$ becomes

$$\tilde{\boldsymbol{H}}_i = \kappa_i\, \boldsymbol{1} + (1 - 3\,\kappa_i)\left(L_i^{\alpha\beta}\, \boldsymbol{A}_\alpha \otimes \boldsymbol{A}_\beta + L_i^{33}\, \boldsymbol{N} \otimes \boldsymbol{N}\right)\,, \quad (i = 1, 2)\,, \tag{6.140}$$

which gives

$$\tilde{J}_4^i := \tilde{\boldsymbol{C}} : \tilde{\boldsymbol{H}}_i = \kappa_i\big(I_1 + \lambda_3^2\big) + (1 - 3\,\kappa_i)\,\big(I_4^i + \lambda_3^2\, L_i^{33}\big)\,, \quad (i = 1, 2)\,, \tag{6.141}$$

where I_1 and I_4^i are given by Eqs. (4.32) and (6.115), respectively.

6.3.2.2 Membrane model

The corresponding membrane strain energy of Eq. (6.134) is (Roohbakhshan et al., 2016)

$$W(\tilde{I}_1, \tilde{J}_4^1, \tilde{J}_4^2, \tilde{J}) = W_{\mathrm{m}}(\tilde{I}_1) + W_{\mathrm{f}}(\tilde{J}_4^1, \tilde{J}_4^2) + \tilde{p}\,\tilde{g}\;, \tag{6.142}$$

where

$$W_{\mathrm{m}} = \frac{\mu}{2}(\tilde{I}_1 - 3)\;, \tag{6.143}$$

$$W_{\mathrm{f}} = \sum_{i=1}^{2} \frac{k_{1i}}{2\,k_{2i}} \left\{\exp\left[k_{2i}\,(\tilde{J}_4^i - 1)^2\right] - 1\right\}\;, \tag{6.144}$$

where $\mu = T\,\tilde{\mu}$ and $k_{1i} = T\,\tilde{k}_{1i}$. Here, $\tilde{I}_1$ and $\tilde{J}_4^i$ are defined by Eqs. (4.31) and (6.141), respectively.

The components of the Kirchhoff stress on $\mathcal{S}$ are

$$\begin{aligned} \tau^{\alpha\beta} &= 2\,\frac{\partial W}{\partial a_{\alpha\beta}} &&= \mu\, A^{\alpha\beta} + 2\sum_{i=1}^{2} E_i\left[\kappa_i\, A^{\alpha\beta} + (1 - 3\,\kappa_i)\, L_i^{\alpha\beta}\right] + p\, a^{\alpha\beta}\;, \\ \tau^{33} &= \frac{1}{\lambda_3}\,\frac{\partial W}{\partial \lambda_3} &&= \mu + 2\sum_{i=1}^{2} E_i\left[\kappa_i + (1 - 3\,\kappa_i)\, L_i^{33}\right] + p\, J^2\;, \end{aligned} \tag{6.145}$$

where $\tilde{J} = 1$ is plugged in after taking the partial derivatives of W. Here, we have defined

$$E_i := \frac{\partial W_{\mathrm{f}}}{\partial \tilde{J}_4^i} = k_{1i}\left(\tilde{J}_4^i - 1\right)\,\exp\left[k_{2i}\,(\tilde{J}_4^i - 1)^2\right]\,, \qquad (i = 1, 2) \tag{6.146}$$

and $\tilde{J}_4^i$ is defined by Eq. (6.141).

From the plane-stress condition, $\tau^{33} = 0$, the Lagrange multiplier can be found as

$$p = -\frac{1}{J^2}\left\{\mu + 2\sum_{i=1}^{2} E_i\left[\kappa_i + (1 - 3\,\kappa_i)\,L_i^{33}\right]\right\}\,. \tag{6.147}$$

Plugging p into Eq. (6.145), the total in-plane Kirchhoff stress can be split as

$$\tau^{\alpha\beta} = \tau_{\mathrm{m}}^{\alpha\beta} + \tau_{\mathrm{f}}^{\alpha\beta}\,, \tag{6.148}$$

where

$$\tau_{\mathrm{m}}^{\alpha\beta} = \mu\,\tau_{\mathrm{NH}}^{\alpha\beta} \tag{6.149}$$

and

$$\tau_{\mathrm{f}}^{\alpha\beta} = 2\sum_{i=1}^{2} E_i\,R_i^{\alpha\beta}\,, \qquad (i = 1, 2)\,. \tag{6.150}$$

Here,

$$R_i^{\alpha\beta} := \kappa_i\,\tau_{\mathrm{NH}}^{\alpha\beta} + (1 - 3\,\kappa_i)\left(L_i^{\alpha\beta} - L_i^{33}\frac{1}{J^2}\,a^{\alpha\beta}\right)\,. \tag{6.151}$$

The total elasticity tensor is then

$$c^{\alpha\beta\gamma\delta} := 2\,\frac{\partial\tau^{\alpha\beta}}{\partial a_{\gamma\delta}} = c_{\mathrm{m}}^{\alpha\beta\gamma\delta} + c_{\mathrm{f}}^{\alpha\beta\gamma\delta}\,, \tag{6.152}$$

where

$$c_{\mathrm{m}}^{\alpha\beta\gamma\delta} := 2\,\frac{\partial\tau_{\mathrm{m}}^{\alpha\beta}}{\partial a_{\gamma\delta}} = \mu\,c_{\mathrm{NH}}^{\alpha\beta\gamma\delta} \tag{6.153}$$

and

$$\begin{aligned} c_{\mathrm{f}}^{\alpha\beta\gamma\delta} := 2\,\frac{\partial\tau_{\mathrm{f}}^{\alpha\beta}}{\partial a_{\gamma\delta}} &= 2\sum_{i=1}^{2}\left[\kappa_i\,E_i + (1 - 3\,\kappa_i)\,L_i^{33}\right]c_{\mathrm{NH}}^{\alpha\beta\gamma\delta} \\ &\quad + 4\sum_{i=1}^{2} D_i\,R_i^{\alpha\beta}\,R_i^{\gamma\delta}\,. \end{aligned} \tag{6.154}$$

Here, we have defined

$$D_i := \frac{\partial E_i}{\partial \tilde{J}_4^i} = k_{1i}\left[1 + 2\,k_{2i}\,(\tilde{J}_4^i - 1)^2\right]\,\exp\left[k_{2i}\,(\tilde{J}_4^i - 1)^2\right]\,, \quad (i = 1, 2)\,. \tag{6.155}$$

6.3.2.3 NP shell model

The strain-energy density function is given by Eqs. (6.134), (6.135) and (6.136). For the NP shell model, $\tilde{\boldsymbol{H}}_i$ and $\tilde{J}_4^i$ are defined by Eqs. (6.138) and (6.139), respectively. Similar to the membrane formulation, the stress tensor has two parts as

$$\tilde{\tau}^{\alpha\beta} = \tilde{\tau}_{\mathrm{m}}^{\alpha\beta} + \tilde{\tau}_{\mathrm{f}}^{\alpha\beta} \ , \tag{6.156}$$

where

$$\tilde{\tau}_{\mathrm{m}}^{\alpha\beta} = \tilde{\mu}\, \tilde{\tau}_{\mathrm{NH}}^{\alpha\beta} \tag{6.157}$$

is the isotropic contribution. The anisotropic contribution of the fibers is then

$$\tilde{\tau}_{\mathrm{f}}^{\alpha\beta} = 2 \sum_{i=1}^{2} \tilde{E}_i\, \tilde{R}_i^{\alpha\beta} \ , \tag{6.158}$$

where we have defined

$$\tilde{R}_i^{\alpha\beta} := \frac{\partial \tilde{J}_4^i}{\partial g_{\gamma\delta}} = \kappa_i\, \tilde{\tau}_{\mathrm{NH}}^{\alpha\beta} + (1 - 3\,\kappa_i) \left(\overset{*}{L}{}_i^{\alpha\beta} - \overset{*}{L}{}_i^{33} \frac{1}{\overset{*}{J}{}^2}\, g^{\alpha\beta} \right) , \qquad (i = 1, 2) \tag{6.159}$$

and

$$\tilde{E}_i := \frac{\partial \tilde{W}_{\mathrm{f}}}{\partial \tilde{J}_4^i} = \tilde{k}_{1i} \left(\tilde{J}_4^i - 1 \right) \exp\left[k_{2i} \, (\tilde{J}_4^i - 1)^2 \right] , \qquad (i = 1, 2) \ . \tag{6.160}$$

From Eqs. (6.157) and (6.158), the symmetric elasticity tensor on $\overset{*}{\mathcal{S}}$ is

$$\tilde{c}^{\alpha\beta\gamma\delta} := 2\, \frac{\partial \tilde{\tau}^{\alpha\beta}}{\partial g_{\gamma\delta}} = \tilde{c}_{\mathrm{m}}^{\alpha\beta\gamma\delta} + \tilde{c}_{\mathrm{f}}^{\alpha\beta\gamma\delta} \ , \tag{6.161}$$

with

$$\tilde{c}_{\mathrm{m}}^{\alpha\beta\gamma\delta} := 2\, \frac{\partial \tilde{\tau}_{\mathrm{m}}^{\alpha\beta}}{\partial g_{\gamma\delta}} = \tilde{\mu}\, \tilde{c}_{\mathrm{NH}}^{\alpha\beta\gamma\delta} \ , \tag{6.162}$$

$$\begin{aligned} \tilde{c}_{\mathrm{f}}^{\alpha\beta\gamma\delta} := 2\, \frac{\partial \tilde{\tau}_{\mathrm{f}}^{\alpha\beta}}{\partial g_{\gamma\delta}} &= 2 \sum_{i=1}^{2} \left[\kappa_i\, \tilde{E}_i + (1 - 3\,\kappa_i)\, \overset{*}{L}{}_i^{33} \right] \tilde{c}_{\mathrm{NH}}^{\alpha\beta\gamma\delta} \\ &\quad + 4 \sum_{i=1}^{2} \tilde{D}_i\, \tilde{R}_i^{\alpha\beta}\, \tilde{R}_i^{\gamma\delta} \end{aligned} \tag{6.163}$$

and

$$\tilde{D}_i := \frac{\partial \tilde{E}_i}{\partial \tilde{J}_4^i} = \tilde{k}_{1i} \left[1 + 2\, k_{2i} \left(\tilde{J}_4^i - 1 \right)^2 \right] \exp\left[k_{2i} \left(\tilde{J}_4^i - 1 \right)^2 \right] \ , \ (i = 1, 2) \ . \tag{6.164}$$

6.3.2.4 AP shell model

On the shell mid-surface $\mathcal{S}$, $\hat{\tau}^{\alpha\beta} = \hat{\tau}^{\alpha\beta}_{\mathrm{m}} + \hat{\tau}^{\alpha\beta}_{\mathrm{f}}$, where

$$\hat{\tau}^{\alpha\beta}_{\mathrm{m}} = \tilde{\mu}\,\tau^{\alpha\beta}_{\mathrm{NH}}\,, \qquad \hat{\tau}^{\alpha\beta}_{\mathrm{f}} = 2\sum_{i=1}^{2}\hat{E}_i\,R^{\alpha\beta}_i\,. \tag{6.165}$$

Here, $R^{\alpha\beta}_i$ is given by Eq. (6.151) and we have defined

$$\hat{E}_i = \tilde{k}_{1i}\left(\hat{J}^i_4 - 1\right)\,\exp\left[k_{2i}\,(\hat{J}^i_4 - 1)^2\right] \tag{6.166}$$

and

$$\hat{J}^i_4 = \kappa_i\,(I_1 + J^{-2}) + (1 - 3\,\kappa_i)\,I^i_4\,, \qquad (i = 1, 2)\,, \tag{6.167}$$

which depend only on the mid-surface parameters. The first-order terms are then

$$\hat{\tau}^{\alpha\beta}_{\mathrm{m},3} = \tilde{\mu}\,\hat{\tau}^{\alpha\beta}_{\mathrm{NH},3}\,, \qquad \hat{\tau}^{\alpha\beta}_{\mathrm{f},3} = 2\sum_{i=1}^{2}\left(\hat{E}_i\,R^{\alpha\beta}_{i,3} + \hat{D}_i\,\hat{J}^i_{4,3}\,R^{\alpha\beta}_i\right)\,, \tag{6.168}$$

where we have defined

$$\hat{J}^i_{4,3} = \kappa_i\,(\hat{I}_{1,3} + 4\,H\,J^{-2}) + (1 - 3\,\kappa_i)\,\hat{I}^i_{4,3}\,, \tag{6.169}$$

$$\hat{R}^{\alpha\beta}_{i,3} := \kappa_i\,\hat{\tau}^{\alpha\beta}_{\mathrm{NH},3} + (1 - 3\,\kappa_i)\left[\,\hat{L}^{\alpha\beta}_{i,3} + L^{33}_i\left(\hat{\tau}^{\alpha\beta}_{\mathrm{NH},3} - 2\,B^{\alpha\beta}\right)\right] \tag{6.170}$$

and

$$\hat{D}_i := \frac{\partial \hat{E}_i}{\partial \hat{J}^i_4} = \tilde{k}_{1i}\left[1 + 2\,k_{2i}\left(\hat{J}^i_4 - 1\right)^2\right]\,\exp\left[k_{2i}\left(\hat{J}^i_4 - 1\right)^2\right]\,,\ (i = 1, 2)\,, \tag{6.171}$$

on $\mathcal{S}$. Further, $\hat{I}_{1,3}$, $\hat{L}^{\alpha\beta}_{i,3}$ and $\hat{I}^i_{4,3}$ are given by Eqs. (A.23), (A.29) and (A.30), respectively (See Appendices A.3 and A.4).

Following Eq. (6.131), the isotropic tangent tensors are

$$\hat{c}^{\alpha\beta\gamma\delta}_{\mathrm{m}} = \tilde{\mu}\,c^{\alpha\beta\gamma\delta}_{\mathrm{NH}}\,, \quad \hat{d}^{\alpha\beta\gamma\delta}_{\mathrm{m}} = 0\,, \quad \hat{c}^{\alpha\beta\gamma\delta}_{\mathrm{m},3} = \tilde{\mu}\,c^{\alpha\beta\gamma\delta}_{\mathrm{NH},3}\,, \quad \hat{d}^{\alpha\beta\gamma\delta}_{\mathrm{m},3} = \tilde{\mu}\,d^{\alpha\beta\gamma\delta}_{\mathrm{NH},3}\,. \tag{6.172}$$

The components of the anisotropic tangent tensors are $\hat{d}_{\mathrm{f}}^{\alpha\beta\gamma\delta} = 0$ and

$$\begin{aligned}
\hat{c}_{\mathrm{f}}^{\alpha\beta\gamma\delta} &= 2\sum_{i=1}^{2} \kappa_i\, \hat{E}_i\, c_{\mathrm{NH}}^{\alpha\beta\gamma\delta} + 4\sum_{i=1}^{2} \hat{D}_i\, R_i^{\alpha\beta}\, R_i^{\gamma\delta}\ , \\
\hat{c}_{\mathrm{f},3}^{\alpha\beta\gamma\delta} &= 4\sum_{i=1}^{2} \Big(\hat{D}_i\, \hat{R}_{i,3}^{\alpha\beta}\, R_i^{\gamma\delta} + \hat{F}_i\, \hat{J}_{4,3}^{i}\, R_i^{\alpha\beta}\, R_i^{\gamma\delta} + \hat{D}_i\, R_i^{\alpha\beta}\, J_{ai}^{\gamma\delta}\Big) \\
&\quad + 2\sum_{i=1}^{2} \kappa_i \Big(\hat{E}_i\, \hat{c}_{\mathrm{NH},3}^{\alpha\beta\gamma\delta} + \hat{D}_i\, \hat{J}_{4,3}^{i}\, c_{\mathrm{NH}}^{\alpha\beta\gamma\delta}\Big) + 2\sum_{i=1}^{2} (1-3\,\kappa_i)\, L_i^{33}\, c_{\mathrm{NH},3}^{\alpha\beta\gamma\delta}\ , \\
\hat{d}_{\mathrm{f},3}^{\alpha\beta\gamma\delta} &= 2\sum_{i=1}^{2} \Big(\hat{D}_i\, R_i^{\alpha\beta}\, J_{bi}^{\gamma\delta} + \kappa_i\, \hat{E}_i\, \hat{d}_{\mathrm{NH},3}^{\alpha\beta\gamma\delta}\Big) + 2\sum_{i=1}^{2} (1-3\,\kappa_i)\, L_i^{33}\, d_{\mathrm{NH},3}^{\alpha\beta\gamma\delta}\ .
\end{aligned} \tag{6.173}$$

Here, we have defined

$$\hat{F}_i := \frac{\partial \hat{D}_i}{\partial \hat{J}_4^i} = 2\,\tilde{k}_{1i}\, k_{2i}\, \big(\hat{J}_4^i - 1\big)\ \Big[3 + 2\,k_{2i}\, \big(\hat{J}_4^i - 1\big)^2\Big]\ \exp\Big[k_{2i}\, \big(\hat{J}_4^i - 1\big)^2\Big] \tag{6.174}$$

and

$$\begin{aligned}
J_{ai}^{\gamma\delta} &:= \frac{\partial \hat{J}_{4,3}^{i}}{\partial a_{\gamma\delta}} = 2\,\kappa_i \left[B^{\alpha\beta} - \frac{1}{J^2}\big(b^{\alpha\beta} + 2\,H\,a^{\alpha\beta}\big)\right] + (1-3\,\kappa_i)\ \hat{L}_{i,3}^{\alpha\beta}\ , \\
J_{bi}^{\gamma\delta} &:= \frac{\partial \hat{J}_{4,3}^{i}}{\partial b_{\gamma\delta}} = -2\,\kappa_i\, \hat{\tau}_{\mathrm{NH}}^{\alpha\beta} - 2\,(1-3\,\kappa_i)\, L_i^{\alpha\beta}\ .
\end{aligned} \tag{6.175}$$

6.3.2.5 DD shell model

For the membrane part, one can used the membrane formulation of Sec. 6.3.2.2. Having the membrane elasticity tensor $c^{\alpha\beta\gamma\delta}$ from Eq. (6.152), bending part can be derived by Eqs. (4.100) and (4.101). Before deformation, $I_4^i = 1$, which gives $D_i = k_{1i}$, and $R^{\alpha\beta} = (1-3\,\kappa_i)\, L_i^{\alpha\beta}$. Further, $\tilde{J}_4^i = 1$, which results in $E_i = 0$. Hence, plugging Eq. (6.152) into Eq. (4.97), we get

$$\begin{aligned}
c_0^{\alpha\beta\gamma\delta} &:= \Big[\mu + 2\sum_{i=1}^{2} (1-3\,\kappa_i)\, L_i^{33}\Big]\, c_{\mathrm{NH0}}^{\alpha\beta\gamma\delta} \\
&\quad +\ 4\sum_{i=1}^{2} k_{1i}\, (1-3\,\kappa_i)^2\, L_i^{\alpha\beta}\, L_i^{\gamma\delta}\ .
\end{aligned} \tag{6.176}$$

6.3.3 Gasser–Ogden–Holzapfel (GOH - 2D GST)

For a thin soft tissue, one may assume that the fibers are oriented in-plane; thus, a 2D dispersion model would be sufficient. Ogden (2009), Holzapfel and Ogden (2010) and Tonge et al. (2013) have studied 2D models of distribute fibers. For the modeling of non-symmetric collagen fiber dispersion, Holzapfel et al. (2015) have recently introduced a new structural tensor that is decomposed into in-plane and out-of-plane parts. The model is motivated by the new experiments on the dispersion of collagen fibers in human arterial layers, which have revealed that the dispersion in the tangential plane is more significant than that out-of-plane. Thus, a rotationally symmetric dispersion model (see Gasser et al., 2006) cannot perfectly capture this distinction. In this section, we adopt the 2D generalized structural tensor used by Ogden (2009), Holzapfel and Ogden (2010) and Tonge et al. (2013) for the modeling the in-plane dispersion of collagen fibers distributed over the surface of a thin membrane or shell.

6.3.3.1 2D generalized structural tensor (2D GST)

On a shell layer $\overset{*}{\mathcal{S}}$, a 2D generalized structural tensor can b e constructed as

$$\overset{*}{\boldsymbol{H}}_i := \kappa_i \, \overset{*}{\boldsymbol{I}} + (1 - 2\,\kappa_i)\, \overset{*}{\boldsymbol{M}}_i \ , \qquad (i = 1, 2) \ , \tag{6.177}$$

where $\kappa_i \in [0,\ 1/2]$ measures the in-plane dispersion of fibers (Tonge et al., 2013). The first invariants of $\overset{*}{\boldsymbol{H}}_i$ are then

$$\overset{*}{J}{}_4^i := \overset{*}{\boldsymbol{C}} : \overset{*}{\boldsymbol{H}}_i = \kappa_i \, \overset{*}{I}_1 + (1 - 2\,\kappa_i)\, \overset{*}{I}{}_4^i \ , \quad (i = 1, 2) \ , \tag{6.178}$$

where $\overset{*}{I}_1$ and $\overset{*}{I}{}_4^i$ are given by Eqs. (4.52) and (6.110). Similarly, for a membrane formulation, the 2D generalized structural tensor on $\mathcal{S}$ becomes

$$\boldsymbol{H}_i := \kappa_i \, \boldsymbol{I} + (1 - 2\,\kappa_i)\, \boldsymbol{M}_i \ , \qquad (i = 1, 2) \ , \tag{6.179}$$

which gives

$$J_4^i := \boldsymbol{C} : \boldsymbol{H}_i = \kappa_i \, I_1 + (1 - 2\,\kappa_i)\, I_4^i \ , \quad (i = 1, 2) \ , \tag{6.180}$$

where I_1 and I_4^i are given by Eqs. (4.32) and (6.115), respectively.

6.3.3.2 Membrane model

The membrane strain energy is similar to Eq. (6.142) with an anisotropic contribution expressed as

$$W_{\mathrm{f}} = \sum_{i=1}^{2} \frac{k_{1i}}{2\,k_{2i}} \left\{ \exp\left[k_{2i}\,(J_4^i - 1)^2\right] - 1 \right\} \ , \tag{6.181}$$

where J_4^i is given by Eq. (6.180). As W_{f} does not depend on λ_3, the anisotropic strain energy does not influence the Lagrange multiplier p. Thus, we have

$$\tau_{\mathrm{m}}^{\alpha\beta} = \mu \, \tau_{\mathrm{NH}}^{\alpha\beta} \tag{6.182}$$

and

$$\tau_{\mathrm{f}}^{\alpha\beta} = 2\sum_{i=1}^{2} E_i\, R_i^{\alpha\beta} \;, \qquad (i=1,2) \;, \tag{6.183}$$

where here

$$R_i^{\alpha\beta} := \frac{\partial J_4^i}{\partial a_{\alpha\beta}} = \kappa_i\, A^{\alpha\beta} + (1-2\,\kappa_i)\, L_i^{\alpha\beta} \tag{6.184}$$

and likewise to Eq. (6.146),

$$E_i := \frac{\partial W_{\mathrm{f}}}{\partial J_4^i} = k_{1i}\left(J_4^i - 1\right)\, \exp\left[k_{2i}\,(J_4^i-1)^2\right] \;, \qquad (i=1,2) \;. \tag{6.185}$$

Following Eq. (6.182), the total elasticity tensor is

$$c^{\alpha\beta\gamma\delta} := 2\,\frac{\partial \tau^{\alpha\beta}}{\partial a_{\gamma\delta}} = c_{\mathrm{m}}^{\alpha\beta\gamma\delta} + c_{\mathrm{f}}^{\alpha\beta\gamma\delta} \;, \tag{6.186}$$

where $c_{\mathrm{m}}^{\alpha\beta\gamma\delta}$ is given by Eq. (6.152) and

$$c_{\mathrm{f}}^{\alpha\beta\gamma\delta} := 2\,\frac{\partial \tau_{\mathrm{f}}^{\alpha\beta}}{\partial a_{\gamma\delta}} = 4\sum_{i=1}^{2} D_i\, R_i^{\alpha\beta}\, R_i^{\gamma\delta} \;, \tag{6.187}$$

with

$$D_i := \frac{\partial E_i}{\partial J_4^i} = k_{1i}\,\left[1 + 2\,k_{2i}\,(J_4^i-1)^2\right]\, \exp\left[k_{2i}\,(J_4^i-1)^2\right] \;, \quad (i=1,2) \;. \tag{6.188}$$

6.3.3.3 NP shell model

For the NP shell model, we adopt the 3D strain energy (6.134) with the following anisotropic contribution

$$\tilde{W}_{\mathrm{f}} = \sum_{i=1}^{2} \frac{\tilde{k}_{1i}}{2\,k_{2i}} \left\{ \exp\left[k_{2i}\,(\overset{*}{J}{}_4^i - 1)^2\right] - 1 \right\} \;, \tag{6.189}$$

where $\overset{*}{J}{}_4^i$ is given by Eq. (6.178). Likewise to the membrane formulation, here the Lagrange multiplier $\tilde{p}$ is not influenced by $\overset{*}{\lambda}_3$; therefore,

$$\tilde{\tau}_{\mathrm{m}}^{\alpha\beta} = \tilde{\mu}\, \tilde{\tau}_{\mathrm{NH}}^{\alpha\beta} \tag{6.190}$$

and

$$\tilde{\tau}_{\mathrm{f}}^{\alpha\beta} = 2\sum_{i=1}^{2} \overset{*}{E}_i\, \overset{*}{R}{}_i^{\alpha\beta} \;, \qquad (i=1,2) \;, \tag{6.191}$$

where here

$$\overset{*}{R}{}^{\alpha\beta}_i := \kappa_i\, G^{\alpha\beta} + (1 - 2\,\kappa_i)\, \overset{*}{L}{}^{\alpha\beta}_i \tag{6.192}$$

and

$$\overset{*}{E}_i := \frac{\partial \tilde{W}_\mathrm{f}}{\partial \overset{*}{J}{}^i_4} = \tilde{k}_{1i}\left(\overset{*}{J}{}^i_4 - 1\right)\,\exp\left[k_{2i}\,(\overset{*}{J}{}^i_4 - 1)^2\right]\,, \qquad (i = 1, 2)\;. \tag{6.193}$$

On $\overset{*}{\mathcal{S}}$, the total and isotropic elasticity tensors are given by Eqs. (6.161) and (6.162), respectively. The anisotropic elasticity tensor is then

$$\tilde{c}_\mathrm{f}^{\alpha\beta\gamma\delta} := 2\,\frac{\partial \tilde{\tau}_\mathrm{f}^{\alpha\beta}}{\partial g_{\gamma\delta}} = 4\sum_{i=1}^{2} \overset{*}{D}_i\, \overset{*}{R}{}^{\alpha\beta}_i\, \overset{*}{R}{}^{\gamma\delta}_i\;, \tag{6.194}$$

where

$$\overset{*}{D}_i := \frac{\partial \overset{*}{E}_i}{\partial \overset{*}{J}{}^i_4} = \tilde{k}_{1i}\,\left[1 + 2\,k_{2i}\left(\overset{*}{J}{}^i_4 - 1\right)^2\right]\,\exp\left[k_{2i}\left(\overset{*}{J}{}^i_4 - 1\right)^2\right]\;,\;(i = 1, 2)\;. \tag{6.195}$$

6.3.3.4 AP shell model

As before, the isotropic stress $\hat{\tau}_\mathrm{m}^{\alpha\beta}$ and through-the-thickness linearized tensor $\hat{\tau}_{\mathrm{m},3}^{\alpha\beta}$ are given by Eqs. (6.165.1) and (6.168.1). From Eq. (6.191), the anisotropic counterparts are

$$\hat{\tau}_\mathrm{f}^{\alpha\beta} = 2\sum_{i=1}^{2} \hat{E}_i\, R_i^{\alpha\beta} \tag{6.196}$$

and

$$\hat{\tau}_{\mathrm{f},3}^{\alpha\beta} = 2\sum_{i=1}^{2}\left(\hat{E}_i\, R_{i,3}^{\alpha\beta} + \hat{D}_i\, \hat{J}^i_{4,3}\, R_i^{\alpha\beta}\right) \tag{6.197}$$

where $R_i^{\alpha\beta}$ is given by Eq. (6.184) and here

$$\hat{E}_i = \tilde{k}_{1i}\left(J^i_4 - 1\right)\,\exp\left[k_{2i}\,(J^i_4 - 1)^2\right] \tag{6.198}$$

and J^i_4 follows from Eq. (6.180). Further,

$$\hat{R}_{i,3}^{\alpha\beta} := 2\,\kappa_i\, B^{\alpha\beta} + (1 - 2\,\kappa_i)\,\hat{L}_{i,3}^{\alpha\beta}\;, \tag{6.199}$$

$$\hat{D}_i := \frac{\partial \hat{E}_i}{\partial J^i_4} = \tilde{k}_{1i}\,\left[1 + 2\,k_{2i}\left(J^i_4 - 1\right)^2\right]\,\exp\left[k_{2i}\left(J^i_4 - 1\right)^2\right] \tag{6.200}$$

and here

$$\hat{J}^i_{4,3} = \kappa_i\,\hat{I}_{1,3} + (1 - 2\,\kappa_i)\,\hat{I}^i_{4,3}\;. \tag{6.201}$$

Following Eq. (6.131), the isotropic tangent tensors can be found from Eq. (6.172). The corresponding anisotropic tangents are then $\hat{d}_{\mathrm{f}}^{\alpha\beta\gamma\delta} = 0$ and

$$\begin{aligned} \hat{c}_{\mathrm{f}}^{\alpha\beta\gamma\delta} &= 4 \sum_{i=1}^{2} \hat{D}_i \, R_i^{\alpha\beta} \, R_i^{\gamma\delta} \; , \\ \hat{c}_{\mathrm{f},3}^{\alpha\beta\gamma\delta} &= 4 \sum_{i=1}^{2} \left(\hat{D}_i \, \hat{R}_{i,3}^{\alpha\beta} \, R_i^{\gamma\delta} + \hat{F}_i \, \hat{J}_{4,3}^{i} \, R_i^{\alpha\beta} \, R_i^{\gamma\delta} + \hat{D}_i \, R_i^{\alpha\beta} \, J_{ai}^{\gamma\delta} \right) \; , \\ \hat{d}_{\mathrm{f},3}^{\alpha\beta\gamma\delta} &= 2 \sum_{i=1}^{2} \hat{D}_i \, R_i^{\alpha\beta} \, J_{bi}^{\gamma\delta} \; , \end{aligned} \tag{6.202}$$

where here

$$\begin{aligned} J_{ai}^{\gamma\delta} &:= \frac{\partial \hat{J}_{4,3}^{i}}{\partial a_{\gamma\delta}} = 2\,\kappa_i \, B^{\alpha\beta} + (1 - 2\,\kappa_i) \; \hat{L}_{i,3}^{\alpha\beta} \; , \\ J_{bi}^{\gamma\delta} &:= \frac{\partial \hat{J}_{4,3}^{i}}{\partial b_{\gamma\delta}} = -2\,\kappa_i \, A^{\alpha\beta} - 2\,(1 - 2\,\kappa_i) \, L_i^{\alpha\beta} \; . \end{aligned} \tag{6.203}$$

6.3.3.5 DD shell model

The membrane stress tensor $\tau^{\alpha\beta}$ and the membrane elasticity tensor $c^{\alpha\beta\gamma\delta}$ are derived in Sec. 6.3.3.2. In the reference configuration, $J_4^i = 1$, which gives $D_i = k_{1i}$. Thus, likewise to the model with the 3D generalized structural tensor, we get

$$c_0^{\alpha\beta\gamma\delta} = 4 \sum_{i=1}^{2} k_{1i} \, R_i^{\alpha\beta} \, R_i^{\gamma\delta} \tag{6.204}$$

and

$$f^{\alpha\beta\gamma\delta} = \frac{T^2}{12} \, c_0^{\alpha\beta\gamma\delta} = \frac{T^2}{3} \sum_{i=1}^{2} k_{1i} \, R_i^{\alpha\beta} \, R_i^{\gamma\delta} \; . \tag{6.205}$$

6.3.4 GOH model with compression/tension switch

The strain energy density function in the form of Eq. (6.136) is polyconvex if $\tilde{I}_4^i > 1$ (Balzani et al., 2006 and Prot et al., 2007). This issue is also addressed in the model of Gasser et al. (2006), where $\tilde{I}_4^i < 1$ is avoided due to non-physical response. Physically, this restriction can be interpreted as fibers bear no compressive force and they contribute to the mechanical response only if being elongated due to tensional forces. To computationally model this behavior, such models should be equipped with a compression/tension switch to exclude the compressed fibers. The switch can be implemented as a Heaviside function (see e.g. Ateshian et al., 2007; Ateshian et al., 2009; Federico and Gasser, 2010 and Melnik et al., 2015). Hence, the GOH model can be modified as

$$\tilde{W}_{\mathrm{f}} = \sum_{i=1}^{2} \overset{*}{H}_i \, \frac{\tilde{k}_{1i}}{2\,k_{2i}} \left\{ \exp\left[k_{2i}\,(\tilde{J}_4^i - 1)^2\right] - 1 \right\} , \tag{6.206}$$

where on the shell layer $\overset{*}{\mathcal{S}}$, the compression/tension switch $\overset{*}{H}_i$ is formulated by the Heaviside step function

$$H(x) := \begin{cases} 1 \, , & x > 0 \, , \\ 0 \, , & x \leq 0 \end{cases} \tag{6.207}$$

as

$$\overset{*}{H}_i = \overset{*}{H}_i(g_{\alpha\beta}) = H\big(\overset{*}{I}{}_4^i - 1\big) \, . \tag{6.208}$$

In the same fashion, for the membrane constitution, we have

$$W_{\mathrm{f}} = \sum_{i=1}^{2} H_i \, \frac{k_{1i}}{2\,k_{2i}} \left\{ \exp\left[k_{2i}\,(\tilde{J}_4^i - 1)^2\right] - 1 \right\} , \tag{6.209}$$

in which, the compression/tension switch H_i is defined on the shell mid-surface as

$$H_i = H_i(a_{\alpha\beta}) = H\big(I_4^i - 1\big) \, . \tag{6.210}$$

Remark 6.6. As discussed by Holzapfel and Ogden (2015), in literature and FEA programs (see e.g. Abaqus, 2013), the compression/tension switch has also been implemented according to $\tilde{I}_4^i > 1$ instead of $\overset{*}{I}{}_4^i > 1$ or $I_4^i > 1$, which may give erroneous results.

Recently, Holzapfel and Ogden (2015) and Li et al. (2016) proposed modified fiber dispersion models based on the AI approach, which do not need a Heaviside function. However, it has not been applied to the GST approach yet. The focus of this thesis is on the GST approach and AI approach is not studied here. In the following, we show how the compression/tension switch can be implemented for the introduced membrane and shell models. The switch is applied to the GOH material model with both 3D and 2D GST. As the switch affects the contribution of fibers, only the anisotropic part is reported here.

6.3.4.1 Membrane model

For a membrane, the switch is defined on $\mathcal{S}$ following Eq. (6.210). Incorporating the switch in the anisotropic membrane strain energy (6.209), the membrane stress tensor and the elasticity tensor would be

$$\tau_{\mathrm{f}}^{\alpha\beta} = 2\sum_{i=1}^{2} H_i\, E_i\, R_i^{\alpha\beta} \tag{6.211}$$

and

$$c_{\mathrm{f}}^{\alpha\beta\gamma\delta} := 2\frac{\partial \tau_{\mathrm{f}}^{\alpha\beta}}{\partial a_{\gamma\delta}} = 2\sum_{i=1}^{2} \kappa_i\, H_i\, E_i\, c_{\mathrm{NH}}^{\alpha\beta\gamma\delta} + 4\sum_{i=1}^{2} H_i\, D_i\, R_i^{\alpha\beta}\, R_i^{\gamma\delta}\ . \tag{6.212}$$

For the 3D GST, $\tilde{J}_4^i$, E_i and $R_i^{\alpha\beta}$ are defined following Eqs. (6.141), (6.146) and (6.151), respectively. For the 2D GST, J_4^i, E_i and $R_i^{\alpha\beta}$ are given by Eqs. (6.180), (6.185) and (6.184), respectively, and the front term of Eq. (6.212) will vanish.

6.3.4.2 NP shell model

If the 3D GST is used, one can directly plug the switch definition (6.208) into the strain energy density function (6.206). Accordingly, the in-plane stress and elasticity tensors should be augmented with the compression/tension switch as

$$\tilde{\tau}_{\mathrm{f}}^{\alpha\beta} = 2\sum_{i=1}^{2} \overset{*}{H}_i\, \tilde{E}_i\, \tilde{R}_i^{\alpha\beta} \tag{6.213}$$

and

$$\tilde{c}_{\mathrm{f}}^{\alpha\beta\gamma\delta} := 2\frac{\partial \tilde{\tau}_{\mathrm{f}}^{\alpha\beta}}{\partial g_{\gamma\delta}} = 2\sum_{i=1}^{2} \kappa_i\, \overset{*}{H}_i\, \tilde{E}_i\, \tilde{c}_{\mathrm{NH}}^{\alpha\beta\gamma\delta} + 4\sum_{i=1}^{2} \overset{*}{H}_i\, \tilde{D}_i\, \tilde{R}_i^{\alpha\beta}\, \tilde{R}_i^{\gamma\delta}\ . \tag{6.214}$$

Similarly for the 2D GST, the compression/tension switch (6.208) can be inserted into Eq. (6.189), which leads to

$$\tilde{\tau}_{\mathrm{f}}^{\alpha\beta} = 2\sum_{i=1}^{2} \overset{*}{H}_i\, \overset{*}{E}_i\, \overset{*}{R}_i^{\alpha\beta} \tag{6.215}$$

and

$$\tilde{c}_{\mathrm{f}}^{\alpha\beta\gamma\delta} := 2\frac{\partial \tilde{\tau}_{\mathrm{f}}^{\alpha\beta}}{\partial g_{\gamma\delta}} = 4\sum_{i=1}^{2} \overset{*}{H}_i\, \overset{*}{D}_i\, \overset{*}{R}_i^{\alpha\beta}\, \overset{*}{R}_i^{\gamma\delta}\ . \tag{6.216}$$

Note that once the switch is included, the anisotropic stress $\tilde{\tau}_{\mathrm{f}}^{\alpha\beta}$ would be discontinuous through the shell thickness. Thus, the numerical integration should be performed so that there are enough number of Gaussian quadrature points in the portion(s) of the shell thickness, where the fibers are extended and the switch is active.

6.3.4.3 AP shell model

For the isotropic contribution of matrix, the cross section would be fully-stressed (see Fig. 4.3.a); thus, one can use the formulation introduced in Sec. 4.3.2.2.1 with the corresponding stress and tangent tensors given in Sec. 6.3.2.4. However, the anisotropic part, being influenced by the switch, has a partially-stressed cross section (see Fig. 4.3.b). For the anisotropic part, the formulation of Sec. 4.3.2.2.2 is adopted. Hence, the stress and moment tensors due to the fibers are

$$\begin{aligned} \tau_{\mathrm{f}}^{\alpha\beta} &= \sum_{i=1}^{2} \left\{ \left(T_2^i - T_1^i \right) \hat{\tau}_{\mathrm{f}i}^{\alpha\beta} + \frac{1}{2} \Big[\left(T_2^i\right)^2 - \left(T_1^i\right)^2 \Big] \hat{\tau}_{\mathrm{f}i,3}^{\alpha\beta} \right\} \ , \\ M_{\mathrm{f}0}^{\alpha\beta} &= \sum_{i=1}^{2} \left\{ \frac{1}{2} \Big[\left(T_2^i\right)^2 - \left(T_1^i\right)^2 \Big] \hat{\tau}_{\mathrm{f}i}^{\alpha\beta} + \frac{1}{3} \Big[\left(T_2^i\right)^3 - \left(T_1^i\right)^3 \Big] \hat{\tau}_{\mathrm{f}i,3}^{\alpha\beta} \right\} \ , \end{aligned} \tag{6.217}$$

where we have defined

$$\hat{\tau}_{\mathrm{f}i}^{\alpha\beta} := 2\,\hat{E}_i\,R_i^{\alpha\beta} \ , \qquad \hat{\tau}_{\mathrm{f}i,3}^{\alpha\beta} := 2\,\left(\hat{E}_i\,R_{i,3}^{\alpha\beta} + \hat{D}_i\,\hat{J}_{4,3}^i\,R_i^{\alpha\beta} \right) \ , \qquad i = 1, 2 \ , \tag{6.218}$$

according to Eqs. (6.165.2) and (6.168.2). As the anisotropic part is partially-stressed, one needs to find the thickness interval $[T_1^i, T_2^i] \in [-T/2, T/2]$, where $\tilde{I}_4^i > 1$. The algorithm to find T_1^i and T_2^i is given in Appendix A.4. Likewise to the stress and moment tensors, the material tangents are also derived following the formulation of Sec. 4.3.2.2.2. For instance,

$$\begin{aligned} c_{\mathrm{f}}^{\alpha\beta\gamma\delta} &= \sum_{i=1}^{2} \left\{ \left(T_2^i - T_1^i \right) \hat{c}_{\mathrm{f}i}^{\alpha\beta\gamma\delta} + \frac{1}{2} \Big[\left(T_2^i\right)^2 - \left(T_1^i\right)^2 \Big] \hat{c}_{\mathrm{f}i,3}^{\alpha\beta\gamma\delta} \right\} \\ &\quad + 2 \sum_{i=1}^{2} \left(\tilde{\tau}_{2i}^{\alpha\beta}\,U_{2i}^{\gamma\delta} - \tilde{\tau}_{1i}^{\alpha\beta}\,U_{1i}^{\gamma\delta} \right) \ , \end{aligned} \tag{6.219}$$

where $\hat{c}_{\mathrm{f}i}^{\alpha\beta\gamma\delta}$ and $\hat{c}_{\mathrm{f}i,3}^{\alpha\beta\gamma\delta}$ are given by Eq. (6.173); $\tilde{\tau}_{1i}^{\alpha\beta}$ and $\tilde{\tau}_{2i}^{\alpha\beta}$ are defined according to Eq. (4.85) and $U_{1i}^{\alpha\beta}$ and $U_{2i}^{\alpha\beta}$ can be found in Appendix A.4. The other material tangent tensors can be derived similarly.

6.3.4.4 DD shell model

The compression/tension swith is not fully consistent with the DD shell model since the assumptions made to derive Eqs. (4.89) and (4.99) are not necessarily valid if the switch is applied. As the switch has an unsymmetric structure, the material model is no longer symmetric w.r.t. the shell mid-surface. Thus, the expressions with mixed term, i.e. $E_{\alpha\beta}\,K_{\gamma\delta}$ in Eq. (4.91), do not vanish. Hence, the membrane and bending strains cannot be fully decoupled. Nonetheless, if the directly-decoupled approach is followed, in the reference configuration, $I_4^i = 1$, which implies that $H_i = 0$. Thus, the anisotropic part do not contribute to the bending energy and this reduces Eqs. (6.176) to a purely isotropic formulation, i.e.

$$c_0^{\alpha\beta\gamma\delta} = \mu\, c_{\mathrm{NH0}}^{\alpha\beta\gamma\delta}\ . \tag{6.220}$$

The directly-decoupled approach cannot capture the effects of the compression/tension switch if the bending moments are dominant or the anisotropic forces are much stronger than the isotropic ones. However, it is accurate if only the membrane forces are influential (Roohbakhshan et al., 2016).

Chapter 7

Interfacial Mechanics[10]

In human body, there are biological fluids such as serum, urine, gastric juice, amniotic fluid, digestive, urinary and reproductive tracts, endocrine glands, middle ear, cerebrospinal and alveolar lining liquid, which contain numerous surface active agents (*surfactants*), proteins, and lipids (Fathi-Azarbayjani and Jouyban, 2015). These fluids have essential contributions to the proper function of various tissues and different organs within the human body. Surface tension, which is caused due to the attraction of particles at a liquid interface by the bulk of the liquid, tries to minimize the liquid surface area. However, if surfactants are added for example to a water-air interface, the surface tension can be drastically reduced. Surfactants, which are amphiphilic compounds, have a hydrophobic tail, which is oil-soluble and allow them to stay on the surface, and a hydrophilic head, which is water-soluble and is able to bond with water molecules to prevent them from binding tightly. This behavior of surfactants is particularly crucial for the lung biomechanics as pulmonary surfactants facilitate the breathing and reduce the possibility of airways blocking by lowering the value of surface tension while the lung volume is decreased (Goerke, 1998 and Veldhuizen and Haagsman, 2000).

With respect to the material behavior, surfactants dynamically change the surface tension that results in hysteresis if a biological membrane or shell is cyclically loaded (see e.g. Kojić et al., 2006 and Kojić et al., 2009). Hence the visco-elastic behavior of many biological materials can be explained by considering a dynamic concentration-dependent surface tension at the interfaces of fluids covering soft tissues and biological organs. Thus, it is important to study how the interfacial characteristics, particularly the surface tension, of such fluids affect the mechanical response of soft tissues. Here, an efficient and simple approach is introduced to model dynamic surface tension within the framework of the membrane theory presented in Sec. 3.2. For the liquid constitution, two material models, developed for dynamic surface tension of

---

[10] This chapter is based on Roohbakhshan and Sauer (2018a).

pulmonary surfactant, are discussed; however, the presented approach can be applied to any biological liquid with dynamic or constant surface tension.

In this chapter, first the liquid membrane theory is reviewed and, then, two dynamic surface tension models for pulmonary surfactants are adopted for the liquid constitution. The corresponding numerical examples can be found in Sec. 9.5.

7.1 Liquid membrane theory

The liquid membrane formulation is followed from Sauer et al. (2014) and Sauer (2014). In fact, the membrane and shell formulation of Secs. 3.1 and 3.2 can be used to model liquid shells (Sauer et al., 2017) and liquid membranes (Sauer et al., 2014 and Sauer, 2014), respectively. This section reviews highlights of the liquid membrane theory and readers are recommended to refer to the mentioned references for more details. Similar to a solid membrane, the kinematics of a liquid membrane is derived from the differential geometry of surfaces (see Sec. 2.1.1).

The stress state in liquid membranes has a hydrostatic component that is governed by the surface tension γ (Sauer, 2014) and a viscous component that is assumed here to follow a simple linear (i.e. Newtonian) viscosity model (Sahu et al., 2017 and Sauer, 2018). In this case, the surface stress tensor can be written as

$$\boldsymbol{\sigma} = \sigma^{\alpha\beta}\, \boldsymbol{a}_\alpha \otimes \boldsymbol{a}_\beta \ , \tag{7.1}$$

where

$$\sigma^{\alpha\beta} = \gamma\, a^{\alpha\beta} - \eta_{\mathrm{s}}\, \dot{a}^{\alpha\beta} \tag{7.2}$$

with η_{s} to be the coefficient of the kinematic surface viscosity. For most of liquids, γ is constant but for interfaces with concentration-dependent surface tension, such as the pulmonary surfactant, γ evolves with time as a function of both the surface stretch and the interfacial concentration. In this case, γ is solved by an ordinary differential equation (ODE), which defines the evolution of surface tension. In Sec. 7.2, the evolution laws for two specific model that describe the dynamic surface tension of pulmonary surfactants. Then, according to Eq. (2.83), the components of Kirchhoff stress tensor are

$$\tau^{\alpha\beta} = \gamma\, J\, a^{\alpha\beta} - \eta_{\mathrm{s}}\, J\, \dot{a}^{\alpha\beta} \ . \tag{7.3}$$

The weak form is then derived similarly as discussed in Sec. 3.2.3. The corresponding FE force vectors and tangent matrices are given in Appendix B.

7.2 Dynamics models for surface tension

In this section, the existing theories, which explain concentration-dependent dynamics of surface tension, are briefly reviewed. The adsorption-limited (AL) model of Otis et al. (1994) and the compression-relaxation (CL) model of Saad et al. (2010) are discussed with more details as they are in good agreement with experimental results and can be efficiently implemented following a membrane formulation. In the literature, there are few theoretical models to explain the diffusion-adsorption process (e.g. Horn and Davis, 1975; Otis et al., 1994; Morris et al., 2001; Krueger and Gaver, 2000 and Saad et al., 2010), through which the surfactant molecules are transferred to the interface from the bulk of fluid and accordingly the surface tension of interface is reduced. All these models assume that the surface tension is determined only by the amount of surfactant at the interface. In general, the surfactants are transfered to the interface in two phases: First, surfactants are conveyed from the bulk of fluid to the regions close to the interface through a diffusion process. Second, the surfactants are adsorbed from the lower layers to the interface. As diffusion and adsorption occur at different rates, most of existing models consider either diffusion or adsorption. Accordingly, the model may account only for diffusion (e.g. Loglio et al., 1991) or it can assume that the adsorption and desorption processes are more dominant (e.g. Otis et al., 1994; Saad et al., 2010). Here, two models of the latter approach are adopted. More details of the available dynamic models can be found e.g. in Saad et al. (2010).

7.2.1 Compression-relaxation (CR) model

Saad et al. (2010) propose a model based on four main processes that affect the dynamic response of surface tension: 1) Adsorption or spreading, 2) desorption or relaxation, 3) elasticity during compression and 4) elasticity during expansion. Further, they include a minimum surface tension γ_{min}, which is the limit that surfactant layers collapse, therefore, the surface tension cannot be further decreased by more compression. Besides, Saad et al. (2010) assume that adsorption/desorption and elasticity processes can happen at the same time. Thus, they postulate a unified formulation that combines all the cases. Here, within the framework of continuum mechanics, the model of Saad et al. (2010) is described in terms of the local surface stretch J as

$$\frac{\mathrm{d}\gamma}{\mathrm{d}t} = \begin{cases} k\,(\gamma_{\text{eq}} - \gamma) + \epsilon\,\dfrac{1}{J}\,\dfrac{\mathrm{d}J}{\mathrm{d}t} & \text{if} \quad \gamma \geq \gamma_{\text{min}} \\ 0 & \text{if} \quad \gamma < \gamma_{\text{min}} \end{cases}\,, \tag{7.4}$$

with

$$k = \begin{cases} k_{\text{a}} & \text{if} \quad \gamma \geq \gamma_{\text{eq}} \\ k_{\text{r}} & \text{if} \quad \gamma < \gamma_{\text{eq}} \end{cases}\,, \tag{7.5}$$

$$\epsilon = \begin{cases} \epsilon_{\mathrm{e}} & \text{if} \quad \mathrm{d}J/\mathrm{d}t \geq 0 \\ \epsilon_{\mathrm{c}} & \text{if} \quad \mathrm{d}J/\mathrm{d}t < 0 \end{cases} , \tag{7.6}$$

where γ_{eq} is the surface tension at the equilibrium. Adsorption and relaxation rates are denoted by k_{a} and k_{r}, respectively. Further, surface tension variation is related to area changes through elasticity coefficients ϵ_{c} and ϵ_{e} during compression and expansion of surface area, respectively. Thus, the CR model requires six different parameters to be determined, namely k_{a}, k_{r}, ϵ_{c}, ϵ_{e}, $\gamma_{\min}$ and γ_{eq}. The first four parameters should be set by fitting the model to the experimental results and the last two parameters are directly measured during cyclic measurements.

7.2.2 Adsorption-limited (AL) model

Otis et al. (1994) introduce a dynamic model for *surfactant TA*®[11] based on an experiment with a pulsating bubble surfactometer (PBS). For the adsorption/desorption processes, it is assumed that the behavior of surfactant concentration Γ at the liquid-gas interface can be described in three different regimes. These regimes are distinguished by two specific concentration values: The maximum equilibrium concentration Γ^* and the maximum surfactant concentration $\Gamma_{\max}$. Otis et al. (1994) assume that the surfactant concentration cannot be increased more than $\Gamma_{\max}$ if surface area is decreased too much, since surfactant molecules are squeezed out of interface, which keeps the concentration of surfactant at $\Gamma_{\max}$. Furthermore, for the concentration values between Γ^* and $\Gamma_{\max}$, it is assumed that there is neither adsorption nor desorption, putting differently, the surfactant is frozen at the interface. For the regime below Γ^*, adsorption and desorption processes are governed by the Langmuir kinetics. Therefore, Otis et al. (1994) postulate three governing equations for the dynamics of surface concentration as

$$\frac{\mathrm{d}(\phi\, J)}{\mathrm{d}t} = \begin{cases} J\,\left[K_1\left(1-\phi\right) - k_2\,\phi\right] & \text{if} \quad \phi \leq 1 \\ 0 & \text{if} \quad 1 < \Gamma < \phi_{\max} \\ -\phi_{\max}\,\dfrac{\mathrm{d}J}{\mathrm{d}t} & \text{if} \quad \phi = \phi_{\max} \end{cases} , \tag{7.7}$$

where $K_1 := k_1\,C$ and k_1 and k_2 are the coefficients of adsorption onto and desorption from the surface, respectively. The bulk concentration C is assumed to be constant as diffusion effects, which occur at different rates, are neglected w.r.t. the adsorption/desorption process. Thus, k_1 and C are merged into one parameter K_1. Here, for the sake of simplicity, normalized concentration $\phi = \Gamma/\Gamma^*$ and normalized maximum concentration $\phi_{\max} = \Gamma_{\max}/\Gamma^*$ are used.

---

[11] Surfactant TA® is an artificial surfactant, produced by the Tokyo Tanabe company, which was widely used for clinical treatment of respiratory distress syndrome (RDS).

Remark 7.1. Morris et al. (2001) extend the formulation of Otis et al. (1994) by including the diffusion effects. In this sense, C varies by time and by position within bulk. For thin liquid membranes, which are the focus of this work, such sophisticated formulations are not efficient.

From Eq. (7.7), one can derive the surface tension according to an equation of state, which relates the surfactant concentration Γ to the surface tension γ. For this purpose, Otis et al. (1994) suggest two straight lines that meet at $\Gamma = \Gamma^*$, which gives

$$\gamma = \begin{cases} \gamma_0 - m_1\,\phi & \text{if} \quad \phi \leq 1 \\ \\ \gamma^* - m_2\,(\phi - 1) & \text{if} \quad 1 < \phi \leq \phi_{\max} \end{cases} , \tag{7.8}$$

where γ_0 is the temperature-dependent surface tension of water, e.g. ≈ 70 mN/m at 25° C, and γ^* is the minimum equilibrium surface tension, corresponding to the maximum equilibrium surfactant concentration Γ^*. The parameters K_1, k_2 and m_2 are determined through a parameter identification process; m_1 can be as

$$m_1 = \gamma_0 - \gamma^* \ . \tag{7.9}$$

and

$$\phi_{\max} = 1 + \frac{\gamma^* - \gamma_{\min}}{m_2} \ . \tag{7.10}$$

Thus, the AL model needs six independent parameters to be determined, i.e. K_1, k_2, m_2, γ_0, γ^*, and $\gamma_{\min}$. The first three ones are found by fitting the model and the last three are directly measured during repeated experiments.

7.2.3 Time integration

In a dynamic formulation, one need to distinguish between the variables at the current time step t_n and the previous time step t_{n-1}. Thus, at the time step t_n, Eq. (7.3) is rewritten as

$$\tau_n^{\alpha\beta} = \gamma_n\, J_n\, a_n^{\alpha\beta} - \eta_{\mathrm{s}}\, J_n\, \dot{a}_n^{\alpha\beta} \ . \tag{7.11}$$

where both γ_n and $\dot{a}_n^{\alpha\beta}$ depend on the history of deformation.

Note 7.2. Here, for the sake of simplicity, temporal indices in the current time step t_n may be removed, e.g. $J_n := J$, unless they are required to be distinguished from the quantities of the previous time step t_{n-1}.

Here, time-dependent quantities $\dot{\gamma}$ and $\dot{a}^{\alpha\beta}$ are discretized by the backward Euler scheme, which gives

$$\frac{\mathrm{d}\gamma}{\mathrm{d}t} \approx \frac{\Delta\gamma}{\Delta t_n} = \frac{\gamma_n - \gamma_{n-1}}{\Delta t} = \dot{\gamma}_n \ , \tag{7.12}$$

and

$$\dot{a}_n^{\alpha\beta} \approx \frac{1}{\Delta t_n}\left(a_n^{\alpha\beta} - a_{n-1}^{\alpha\beta}\right) , \tag{7.13}$$

where $\Delta t_n = t_n - t_{n-1}$ is the time step. The approximated equation (7.12) is implicit and requires solving an algebraic equation in terms of unknown γ_n, which is solved iteratively by the Newton–Raphson method introduced in Sec. 8.1.4. For the cases investigated in the next sections, γ_n has spatial variations since it explicitly depends on the current surface stretch J_n. Thus, the spatial variation of γ_n adds extra terms to the internal stiffness tangent matrix of the liquid membrane.

Remark 7.3. In general, there are three approaches to computationally model the surface tension:

1) Point-wise, where the surface tension varies locally, where $\gamma = \gamma(\boldsymbol{x}, t)$, as it is used here;
2) Element-wise, where the surface tension is assumed to be uniform over each finite element Ω^e, where $\gamma = \gamma(\Omega^e, t)$ (e.g. Wiechert et al., 2009 and Wiechert, 2011), or
3) Globally, where the surface tension is considered uniform over the whole membrane surface, i.e. $\gamma = \gamma(t)$.

If the surface deformation is homogeneous, all the approaches predict similar surface tension; however, if the strain field is not uniform, the former may result in surface tension gradient, which in turn induces interfacial flow known as *Marangoni flow* (Velarde et al., 2002). If the bulk viscosity is effective, the Marangoni flow causes internal flow inside the bulk of fluid through viscous forces. In the presented work, the bulk flows are neglected. As the dynamic surface tension models, introduced in Sec. 7.2, depend explicitly or implicitly on the surfactant concentration, Marangoni effect might be expected for some applications if the point-wise approach is followed. As shown by Roohbakhshan and Sauer (2018a), even though presented finite element formulation is described in a Lagrangian framework, it allows for such flows as long as they are small. For large flows, within an arbitrary Lagrangian–Eulerian (ALE) approach, a convection-diffusion equation should be considered, which explains how the surfactant particles are transfered as the fluid interface deforms (Sahu et al., 2017 and Stone, 1990). This is left for future work.

7.2.3.1 CR model

Plugging Eq. (7.4) into Eq. (7.12), the time-discretized version of CR model is obtained as

$$\gamma_n = \frac{1}{1 + k\,\Delta t}\left[\gamma_{n-1} + k\,\gamma_{\mathrm{eq}}\,\Delta t + \epsilon\left(1 - \frac{J_{n-1}}{J_n}\right)\right] \tag{7.14}$$

where

$$k = \begin{cases} k_{\mathrm{a}} & \text{if} \quad \gamma_n \geq \gamma_{\mathrm{eq}} \\ k_{\mathrm{r}} & \text{if} \quad \gamma_n < \gamma_{\mathrm{eq}} \end{cases} , \tag{7.15}$$

$$\epsilon = \begin{cases} \epsilon_{\mathrm{e}} & \text{if} \quad J_n \geq J_{n-1} \\ \epsilon_{\mathrm{c}} & \text{if} \quad J_n < J_{n-1} \end{cases} . \tag{7.16}$$

The spatial variation of γ is

$$\Delta_{\mathrm{x}} \gamma = \frac{\partial \gamma}{\partial J} \, \Delta_{\mathrm{x}} J \ , \tag{7.17}$$

where

$$\frac{\partial \gamma}{\partial J} = \frac{\epsilon}{1 + k \, \Delta t} \, \frac{J_{n-1}}{\left(J_n\right)^2} \ . \tag{7.18}$$

7.2.3.2 AL model

In the same fashion as the CR model, plugging Eq. (7.7) into Eq. (7.12), a discretized evolution equation for the concentration Γ_n is obtained as

$$\frac{\Delta (J \, \phi)}{\Delta t} = \frac{J_n \, \phi_n - J_{n-1} \, \phi_{n-1}}{\Delta t} = \begin{cases} J_n \, \big[K_1 \left(1 - \phi_n\right) - k_2 \, \phi_n \big] & \text{if} \quad \phi_n \leq 1 \\ 0 & \text{if} \quad 1 < \phi_n < \phi_{\max} \\ -\phi_{\max} \, \dfrac{J_n - J_{n-1}}{\Delta t} & \text{if} \quad \phi_n = \phi_{\max} \end{cases} , \tag{7.19}$$

which gives the discretized version of CR model is obtained as

$$\phi_n = \begin{cases} \left[1 + \Delta t \left(K_1 + k_2\right)\right]^{-1} \left(\Delta t \, K_1 + \dfrac{J_{n-1}}{J_n} \phi_{n-1} \right) & \text{if} \quad \phi_n \leq 1 \\ \dfrac{J_{n-1}}{J_n} \phi_{n-1} & \text{if} \quad 1 < \phi_n < \phi_{\max} \\ \dfrac{J_{n-1}}{J_n} \left(\phi_{n-1} + \phi_{\max}\right) - \phi_{\max} & \text{if} \quad \phi_n = \phi_{\max} \end{cases} . \tag{7.20}$$

Then, the surface tension is updated according to the equation of state Eq. (7.8), which gives

$$\gamma_n = \begin{cases} \gamma_0 - m_1 \, \phi_n & \text{if} \quad \phi_n \leq 1 \\ \gamma^* - m_2 \left(\phi_n - 1\right) & \text{if} \quad 1 < \phi_n \leq \phi_{\max} \end{cases} . \tag{7.21}$$

The spatial variation of γ_n is also given by Eq. (7.17). From Eq. (7.21), one can obtain

$$\frac{\partial \gamma}{\partial J} = -k_{\mathrm{s}}\, k_{\mathrm{c}}\, \frac{1}{J^2} \tag{7.22}$$

with

$$k_{\mathrm{c}} := \frac{\partial \phi_n}{\partial (1/J_n)} = \begin{cases} \left[1 + \Delta t\,(K_1 + k_2)\right]^{-1}\, \phi_{n-1}\, J_{n-1} & \text{if} \quad \phi_{n-1} \leq 1 \\ \phi_{n-1}\, J_{n-1} & \text{if} \quad 1 < \phi_{n-1} \leq \phi_{\max} \\ \left(\phi_{n-1} + \phi_{\max}\right)\, J_{n-1} & \text{if} \quad \phi_{n-1} = \phi_{\max} \end{cases} \tag{7.23}$$

and

$$k_{\mathrm{s}} = \frac{\partial \gamma}{\partial \phi} = \begin{cases} -m_1 & \text{if} \quad \phi_n \leq 1 \\ -m_2 & \text{if} \quad 1 < \phi_n \leq \phi_{\max} \end{cases} . \tag{7.24}$$

7.2.4 Linearization

Plugging Eq. (7.13) into Eq. (7.11), the time-discretized Kirchhoff stress is

$$\tau_n^{\alpha\beta} = \gamma_n\, J_n\, a_n^{\alpha\beta} - \frac{\eta_{\mathrm{s}}}{\Delta t_n}\, J_n \left(a_n^{\alpha\beta} - a_{n-1}^{\alpha\beta}\right), \tag{7.25}$$

where γ_n depends on the constitution is derived above for two particular material model.

From Eq. (7.25), the components of the tangent stiffness tensor can be derived as

$$\begin{aligned} c^{\alpha\beta\gamma\delta} := 2\,\frac{\partial \tau^{\alpha\beta}}{\partial a_{\gamma\delta}} &= 2\,\gamma\, J\, a^{\alpha\beta\gamma\delta} + \left(\gamma + J\,\frac{\partial \gamma}{\partial J}\right) J\, a^{\alpha\beta}\, a^{\gamma\delta} \\ &- \eta_{\mathrm{s}}\, J \left(\dot{a}^{\alpha\beta}\, a^{\gamma\delta} + \frac{2}{\Delta t}\, a^{\alpha\beta\gamma\delta}\right), \end{aligned} \tag{7.26}$$

where $\dfrac{\partial \gamma}{\partial J}$ is derived for two specific dynamic surface tension models in Sec. 7.2.3.

Chapter 8

Finite Element Solution[12]

The weak form of the BVP (3.23) is solved by the nonlinear finite element method (FEM). The finite element solution is based on the IGA concept (Hughes et al., 2005), which uses non-uniform rational B-spline (NURBS) shape functions for both the geometrical representation and discretization of the weak form (3.23). The main advantage of NURBS-based finite elements is the high smoothness in the representation of geometry and solution, which satisfies the C^1-continuity required for the modeling of thin rotation-free shells based on the Kirchhoff–Love hypothesis (Kiendl et al., 2009). Furthermore, quadratic and higher order NURBS-based FE discretizations help to remove membrane locking. This chapter has two sections. The first one summarizes the main steps of the FE solution. The second reviews the isogeomtric analysis (IGA) and how it is implemented within the framework of finite element method.

8.1 FEM procedure

Here, the requisites of the finite element method, i.e. spacial discretization; FE approximation of field variables and surface objects and discretization of the weak form and its linearization, are discussed. Further details of the finite element method and solution procedure can be found in Zienkiewicz and Taylor (2005) and Wriggers (2008). Here, specifically the FE formulation and implementation approach of Sauer et al. (2014) and Duong et al. (2017) are followed.

8.1.1 Surface discretization

The membrane and shell models presented in Chaps. 3 and 4 are formulated on the mid-surface $\mathcal{S}$ of a thin-walled structure. They are rotation-free displacement-based

---

[12] This chapter is based on Roohbakhshan and Sauer (2016).

formulations that require only three degrees of freedom per each node (=control point). Thus, we discretize the (mid-)surface $\mathcal{S}_0$ in the reference configuration as

$$\mathcal{S}_0 \approx S_0 = \bigcup_{e=1}^{n_{\mathrm{el}}} \Omega_0^e \ , \tag{8.1}$$

where $\mathcal{S}_0$ is the exact surface, S_0 is the discretized surface, n_{el} is the total number of elements and Ω_0^e is a discretized element over the reference surface. Within the framework of finite element method, any point $\boldsymbol{X}$ on $\mathcal{S}_0$ is approximated using the finite element interpolation functions, also called shape functions, as

$$\boldsymbol{X}\big(\xi^\alpha\big) \approx \mathbf{X}\big(\xi^\alpha\big) = \sum_{A=1}^{n_{\mathrm{ne}}} N_A\big(\xi^\alpha\big)\, \mathbf{X}_A^e \ , \quad \forall\, \mathbf{X} \in \Omega_0^e \ , \tag{8.2}$$

where $N_A = N_A\big(\xi^\alpha\big)$ and $\mathbf{X}_A^e$ are the shape function and the position of A^{th} node of the element Ω_0^e, respectively, and n_{ne} is the number of nodes per each element. In matrix notation, Eq. (8.2) can be rewritten as

$$\boldsymbol{X} \approx \mathbf{X} = \mathbf{N}\, \mathbf{X}^e \ , \quad \forall\, \mathbf{X} \in \Omega_0^e \ , \tag{8.3}$$

where the nodal positions are stacked in array

$$\mathbf{X}^e := \big[\mathbf{X}_1^e,\, \mathbf{X}_2^e,\, ...,\, \mathbf{X}_{n_{\mathrm{ne}}}^e\big]^{\mathrm{T}} \ ; \tag{8.4}$$

their associated shape functions are

$$\mathbf{N}\big(\xi^\alpha\big) := \big[N_1\, \mathbf{1},\, N_2\, \mathbf{1},\, ...,\, N_{n_{\mathrm{ne}}}\, \mathbf{1}\big] \ . \tag{8.5}$$

Here, $\mathbf{1}$ is the full identity tensor expressed as a 3×3 matrix. Accordingly, $\mathbf{N}$ and $\mathbf{X}^e$ are $3 \times 3\, n_{\mathrm{ne}}$ and $3\, n_{\mathrm{ne}} \times 1$ arrays, respectively.

Note 8.1. The discretized quantities are denoted as non-italic henceforth.

Following the isoparametric mapping, the field variables are interpolated with the same shape functions as geometry and all the elements are interpolated with a single set of shape functions. Thus, in the current configuration we have

$$\mathcal{S} \approx S = \bigcup_{e=1}^{n_{\mathrm{el}}} \Omega^e \ , \tag{8.6}$$

$$\boldsymbol{x}\big(\xi^\alpha\big) \approx \mathbf{x}\big(\xi^\alpha\big) = \sum_{A=1}^{n_{\mathrm{ne}}} N_A\big(\xi^\alpha\big)\, \mathbf{x}_A^e \ , \quad \forall\, \mathbf{x} \in \Omega^e \ , \tag{8.7}$$

$$\boldsymbol{x} \approx \mathbf{x} = \mathbf{N}\, \mathbf{x}^e \ , \quad \forall\, \mathbf{x} \in \Omega^e \ , \tag{8.8}$$

where Ω^e is the deformed element on $\mathcal{S}$ and we have introduced

$$\mathbf{x}^e := \left[\mathbf{x}^e_1,\, \mathbf{x}^e_2,\, ...,\, \mathbf{x}^e_{n_{\text{ne}}}\right]^{\text{T}} . \tag{8.9}$$

Considering a Bubnov–Galerkin formulation, both the deformation and the variation $\delta\boldsymbol{x}$ are approximated by the same interpolation functions, giving

$$\delta\boldsymbol{x} \approx \delta\mathbf{x} = \sum_{A=1}^{n_{\text{ne}}} N_A\, \delta\mathbf{x}^e_A = \mathbf{N}\, \delta\mathbf{x}^e \tag{8.10}$$

for any admissible $\delta\boldsymbol{x} \in \mathcal{V}$, with

$$\delta\mathbf{x}^e := \left[\delta\mathbf{x}^e_1,\, \delta\mathbf{x}^e_2,\, ...,\, \delta\mathbf{x}^e_{n_{\text{ne}}}\right]^{\text{T}} . \tag{8.11}$$

8.1.2 FE approximation of surface objects

Having discretized the surface $\mathcal{S}$, the other objects associated with the surface can be approximated as

$$\begin{aligned} \boldsymbol{a}_\alpha &\approx \mathbf{N}_{,\alpha}\, \mathbf{x}_e \ , \\ \delta\boldsymbol{a}_\alpha &\approx \mathbf{N}_{,\alpha}\, \delta\mathbf{x}_e \ , \\ \boldsymbol{a}_{\alpha,\beta} &\approx \mathbf{N}_{,\alpha\beta}\, \mathbf{x}_e \ , \\ \boldsymbol{a}_{\alpha;\beta} &\approx \mathbf{N}_{;\alpha\beta}\, \mathbf{x}_e \ , \end{aligned} \tag{8.12}$$

where

$$\mathbf{N}_{,\alpha}(\xi^\alpha) := \left[N_{1,\alpha}\mathbf{1},\, N_{2,\alpha}\mathbf{1},\, ...,\, N_{n_{\text{ne}},\alpha}\mathbf{1}\right] , \tag{8.13}$$

$$\mathbf{N}_{,\alpha\beta}(\xi^\alpha) := \left[N_{1,\alpha\beta}\mathbf{1},\, N_{2,\alpha\beta}\mathbf{1},\, ...,\, N_{n_{\text{ne}},\alpha\beta}\mathbf{1}\right] \tag{8.14}$$

and from Eq. (2.18)

$$\mathbf{N}_{;\alpha\beta} := \mathbf{N}_{,\alpha\beta} - \Gamma^\gamma_{\alpha\beta}\, \mathbf{N}_{,\gamma} \ . \tag{8.15}$$

Here,

$$\begin{aligned} N_{A,\alpha} &:= \frac{\partial N_A}{\partial \xi^\alpha} \ , \\ N_{A,\alpha\beta} &:= \frac{\partial^2 N_A}{\partial \xi^\alpha\, \partial \xi^\beta} \ , \end{aligned} \tag{8.16}$$

with $A = 1,\, ...,\, n_{\text{ne}}$. Further, for the internal virtual work (3.25), $\delta a_{\alpha\beta}$ and $\delta b_{\alpha\beta}$ need to be discretized as (Duong et al., 2017)

$$\delta a_{\alpha\beta} \approx \delta\mathbf{x}^{\text{T}}_e \left(\mathbf{N}^{\text{T}}_{,\alpha}\, \mathbf{N}_{,\beta} + \mathbf{N}^{\text{T}}_{,\beta}\, \mathbf{N}_{,\alpha}\right) \mathbf{x}_e \tag{8.17}$$

and

$$\delta b_{\alpha\beta} \approx \delta\mathbf{x}^{\text{T}}_e\, \mathbf{N}^{\text{T}}_{;\alpha\beta}\, \boldsymbol{n} \ . \tag{8.18}$$

8.1.3 Discretized weak form

Based on the introduced FE setting, the weak form (3.23) can be discretized. In order to discretize the weak form, the surface integration, e.g. Eq. (3.25), is carried out over the element domains Ω^e and then summed over all the finite elements as

$$\sum_{e=1}^{n_{\mathrm{el}}} \left(G^e_{\mathrm{in}} + G^e_{\mathrm{int}} - G^e_{\mathrm{ext}}\right) = 0 \quad \forall\, \delta\mathbf{x}_e \in \mathcal{V} \ , \tag{8.19}$$

where

$$\begin{aligned} G^e_{\mathrm{in}} &= \delta\mathbf{x}_e^{\mathrm{T}}\, \mathbf{f}^e_{\mathrm{in}} \ , \\ G^e_{\mathrm{int}} &= \delta\mathbf{x}_e^{\mathrm{T}}\, \mathbf{f}^e_{\mathrm{int}} \ , \\ G^e_{\mathrm{ext}} &= \delta\mathbf{x}_e^{\mathrm{T}}\, \mathbf{f}^e_{\mathrm{ext}} \end{aligned} \tag{8.20}$$

are inertial, internal and external element force vectors, respectively (Duong et al., 2017), which are given in Appendix B. The positions of all nodes in the Cartesian coordinate system and the corresponding kinematically admissible set of all nodal variations are stacked in $\mathbf{x}$ and $\mathbf{w}$, respectively, which are global $3\,n_{\mathrm{no}} \times 1$ arrays. Here, n_{no} is the total number of nodes on discretized $\mathcal{S}$. Thus, Eqs. (8.19) and (8.20) can be written as

$$\mathbf{w}^{\mathrm{T}}\, \mathbf{f}(\mathbf{x}) = 0 \ , \tag{8.21}$$

where

$$\mathbf{f} := \left(\mathbf{f}_{\mathrm{in}} + \mathbf{f}_{\mathrm{int}} - \mathbf{f}_{\mathrm{ext}}\right) \ , \tag{8.22}$$

is the global residual force vector, which is a $3\,n_{\mathrm{no}} \times 1$ array. Here, $\mathbf{f}_{\mathrm{in}}$, $\mathbf{f}_{\mathrm{int}}$ and $\mathbf{f}_{\mathrm{ext}}$ are global inertial, internal and external force vectors constructed by the assembly of the element force vectors, $\mathbf{f}^e_{\mathrm{in}}$, $\mathbf{f}^e_{\mathrm{int}}$ and $\mathbf{f}^e_{\mathrm{ext}}$, respectively, which are given in Appendix B. The corresponding entries of $\mathbf{w}$ for nodes on Dirichlet boundary $\partial_u\mathcal{S}$ are zero. Thus, for the free degrees of freedom, Eq. (8.21) reduces to the nonlinear system of equations

$$\mathbf{f}\big(\mathbf{x}\big) = \mathbf{0} \ . \tag{8.23}$$

8.1.4 Newton–Raphson iteration

As $\mathbf{f} = \mathbf{f}\big(\mathbf{x}\big)$ is highly nonlinear, it is linearized and then solved iteratively by the Newton–Raphson method. At iteration k, using a first order Taylor expansion, $\mathbf{f}$ is linearized as

$$\mathbf{f}\big(\mathbf{x}_{k+1}\big) = \mathbf{f}\big(\mathbf{x}_k\big) + \Delta\mathbf{f} = \mathbf{f}\big(\mathbf{x}_k\big) + \mathbf{k}\,\Delta\mathbf{x}_k \approx \mathbf{0} \ , \tag{8.24}$$

which gives

$$\Delta\mathbf{x}_k = -\mathbf{k}^{-1}\,\mathbf{f}\big(\mathbf{x}_k\big) \ . \tag{8.25}$$

Here,

$$\mathbf{k}\big(\mathbf{x}_k\big) := \frac{\partial \mathbf{f}\big(\mathbf{x}_k\big)}{\partial \mathbf{x}_k} \tag{8.26}$$

is the global stiffness tangent built as

$$\mathbf{k} := \mathop{\mathsf{A}}\limits_{e=1}^{n_{\text{el}}} \left(\mathbf{k}^e_{\text{in}} + \mathbf{k}^e_{\text{int}} - \mathbf{k}^e_{\text{ext}}\right) \tag{8.27}$$

by the assembly of element stiffness matrices (Duong et al., 2017)

$$\mathbf{k}^e_{\text{in}} := \frac{\partial \mathbf{f}^e_{\text{in}}}{\partial \mathbf{x}_e}\,, \quad \mathbf{k}^e_{\text{int}} := \frac{\partial \mathbf{f}^e_{\text{int}}}{\partial \mathbf{x}_e}\,, \quad \mathbf{k}^e_{\text{ext}} := \frac{\partial \mathbf{f}^e_{\text{ext}}}{\partial \mathbf{x}_e}\,, \tag{8.28}$$

which can be found in Appendix B. The solution is updated iteratively as

$$\mathbf{x}_{k+1} = \mathbf{x}_k + \Delta\mathbf{x}_k \tag{8.29}$$

until a converged solution is found i.e. $\|\Delta\mathbf{x}_k\| \to 0$ or alternatively $\|\Delta\mathbf{f}\| \to 0$. Tab. 8.1 summarizes the main steps of the solution algorithm for a nonlinear FEM procedure.

1) Update the current load step t_n
2) Fetch relevant data from the load step t_{n-1}
3) Set an initial guess for the Newton–Raphson iteration
4) Newton–Raphson iteration ($k = 1, \ \ldots, n_k$):
    i) Compute the residual force vector $\mathbf{f}\big(\mathbf{x}_k\big)$ (8.22).
    ii) Update tangent matrices $\mathbf{k}\big(\mathbf{x}_k\big)$ (8.27).
    iii) Solve Eq. (8.25) for unknown $\Delta\mathbf{x}_k$.
    iv) Check for convergence.
    v) Update $\mathbf{x}$.
5) Go to the next load step t_{n+1}.

TABLE 8.1: Solution algorithm for the nonlinear FEM

8.1.5 Numerical integration

$\xi^\alpha \in [-1,1],\ \alpha = 1,2,$ The evaluation of the discretized weak form (8.19) requires numerical integration, which is performed with standard Gaussian quadrature over a master domain like in the classic finite element method. For the presented formulation, three kinds of numerical integration are needed: 1) Surface integrals on the shell mid-surface or membrane surface, 2) in-plane line integrals along a boundary or edges on the membrane or shell surface and 3) out-of-plane line integrals across the shell thickness.

The first kind of integration is performed for example to evaluate the contribution of the membrane stress $\tau^{\alpha\beta}$ (B.2) to the discretized weak form (8.19) as

$$\begin{aligned} \mathbf{f}^e_{\mathrm{int}\tau} := \int_{\Omega^e_0} \tau^{\alpha\beta}\, \mathbf{N}^{\mathrm{T}}_{,\alpha}\, \boldsymbol{a}_\beta \, \mathrm{d}A \ &= \int_{\Omega_\Box} \tau^{\alpha\beta}\, \mathbf{N}^{\mathrm{T}}_{,\alpha}\, \boldsymbol{a}_\beta \ J_A \mathrm{d}\Box \\ &\approx \sum_{p=1}^{n_{\mathrm{gp}}} \tau^{\alpha\beta}\big(\boldsymbol{\xi}_p\big)\, \mathbf{N}^{\mathrm{T}}_{,\alpha}\big(\boldsymbol{\xi}_p\big)\, \boldsymbol{a}_\beta\big(\boldsymbol{\xi}_p\big)\, J_A\big(\boldsymbol{\xi}_p\big)\, w_p \ , \end{aligned} \tag{8.30}$$

where n_{gp} is the number of Gaussian quadrature points; $\boldsymbol{\xi}_p$ is the coordinate of the p^{th} quadrature point in the 2D master element $\Omega_\Box$ and w_p is its corresponding weight (Wriggers, 2001).

The second type of numerical integration is used for example to evaluate the contribution of constraints used to enforce patch-coupling or other edged conditions (see Sec. 8.2.2).

The third type of numerical integration is used for the numerically-projected shell model of Sec. 5.2.1, where the stress and bending moment resultants and their corresponding tangents, i.e. Eqs. (5.1) and (5.3), are evaluated by numerical integration. Similarly, the integration is carried out over a 1D master domain $\eta \in [-1,1]$. For instance, the resultant stress tensor (4.65) can be expressed as

$$\tau^{\alpha\beta}(\boldsymbol{x}) = \int_{-\frac{T}{2}}^{\frac{T}{2}} \tilde{\tau}^{\alpha\beta}\big(\boldsymbol{x},\xi\big)\, \mu_0 \, \mathrm{d}\xi \approx \frac{T}{2} \sum_{p=1}^{n_{\mathrm{gp}}} \tilde{\tau}^{\alpha\beta}\big(\boldsymbol{x},\eta_p\big)\, \mu_0\big(\eta_p\big)\, w_p. \tag{8.31}$$

Here, $\eta_p \in [-1,1]$ are the position of quadrature points in the 1D master element. For laminated composite shells, the change of integration interval needs to be taken into account. For instance, the stress resultant is numerically approximated as

$$\begin{aligned} \tau^{\alpha\beta}\big(\boldsymbol{x}\big) \ &= \sum_{i=1}^{n_{\mathrm{l}}} \int_{T_{i-1}}^{T_i} \tilde{\tau}^{\alpha\beta}_i\big(\boldsymbol{x},\xi\big)\, \mathrm{d}\xi \\ &\approx \sum_{i=1}^{n_{\mathrm{l}}} \frac{1}{2}\big(T_i - T_{i-1}\big) \sum_{p=1}^{n_{\mathrm{gp}}} \tilde{\tau}^{\alpha\beta}_i\big(\boldsymbol{x},\zeta_p\big)\, w_p \ , \end{aligned} \tag{8.32}$$

where

$$\zeta_p := \frac{T_i + T_{i-1}}{2} + \frac{T_i - T_{i-1}}{2}\,\eta_p\ . \tag{8.33}$$

8.1.6 Implementation of the contact constraint

To implement the contact constraint, introduced in Secs. 2.3 and 3.1.3, in the procedure of the finite element solution efficiently, one need to consider different numerical issues. First, to reduce the computational cost and secure the quadratic convergency of the Newton–Raphson method, an active set strategy can be followed (Sauer and De Lorenzis, 2013, 2015), where the FE force vector and tangent matrix associated to the contact force are only evaluated at those Gaussian quadrature points that are active. Second, if two bodies in contact are deformable, the weak form (3.20) should be satisfied for each body separately. Correspondingly, the contribution of the traction force $\boldsymbol{f}_{\mathrm{c}}$, which has the same magnitude but opposite sign for each body, should be added to each weak form. Thus, to be unbiased, the so called two-half-pass algorithm (Sauer and De Lorenzis, 2013, 2015) is used to evaluate the contact contribution.

8.2 Isogeometric descretization

In this section, the isogeometric analysis techniques are employed for the surface representation and the discretization of the weak form. Isogeoemtric analysis is aimed for creating a single platform for computer aided design (CAD) and finite element analysis (FEA) to reduce the overall time in the process from design to analysis (Cottrell et al., 2009). Non-uniform rational B-splines (NURBS) are widely used in isogeometric analysis as they can provide arbitrary continuity and high smoothness in representation. A comprehensive description of NURBS and B-splines is outside the scope of this paper and further conceptual, theoretical and mathematical details can be found in the classical references for IGA (e.g. Hughes et al., 2005 and Cottrell et al., 2009).

8.2.1 NURBS-based finite element

In general, a NURBS-based surface, which is an extension of a B-spline surface, is described by a mapping from a two dimensional parametric domain. The mapping is determined by the desired polynomial order p and q for each dimension, a set of control points $\mathbf{P} = \{\mathbf{P}_A\}_{A=1}^{n_{\mathrm{cp}}}$ that define the shape, and two knot vectors $\Xi = \{\xi_1, \xi_2, \cdots, \xi_{n+p+1}\}$ and $\mathcal{H} = \{\eta_1, \eta_2, \cdots, \eta_{m+q+1}\}$. Here, $n_{\mathrm{cp}} = n \times m$ is the total number of control points of the patch with m and n to be the number of control points in the directions ξ and η, respectively. Besides, for the numbering of control points, we need to define a mapping $A = A(i, j)$ based on the grid of control points, where $i = 1, \cdots, n$ and $j = 1, \cdots, m$. The NURBS surface is constructed from the rational basis functions

$$R_A^{p,q}(\xi, \eta) = \frac{w_A\, \hat{N}_i^p(\xi)\, \hat{N}_j^q(\eta)}{W(\xi, \eta)}, \tag{8.34}$$

where w_A are the weights associated to the control points and $\hat{N}_i^p(\xi)$ and $\hat{N}_j^q(\eta)$ are the B-spline basis functions in each dimension and the weighting function is

$$W(\xi, \eta) = \sum_{k=1}^{n} \sum_{l=1}^{m} w_B\, \hat{N}_k^p(\xi)\, \hat{N}_l^q(\eta) \ , \tag{8.35}$$

with $B = A(k, l)$. In matrix form, Eq. (8.34) can be written as

$$\mathbf{R}(\xi, \eta) = \frac{\mathbf{W}\, \hat{\mathbf{N}}(\xi, \eta)}{W(\xi, \eta)} \ , \tag{8.36}$$

where $\mathbf{R}(\xi, \eta) := \{R_A^{p,q}(\xi, \eta)\}_{A=1}^{n_{\text{cp}}}$, $\hat{\mathbf{N}}(\xi, \eta) := \{\hat{N}_i^p(\xi)\, \hat{N}_j^q(\eta)\}_{A=1}^{n_{\text{cp}}}$ and $\mathbf{W}$ is a diagonal matrix containing the weights of the control points. Then, the shell mid-surface is discretized by NURBS as

$$\boldsymbol{x}(\xi, \eta) = \sum_{i=1}^{n_{\text{cp}}} R_A^{p,q}(\xi, \eta)\, \mathbf{P}_A = \mathbf{P}^{\mathrm{T}}\, \mathbf{R}(\xi, \eta) \ , \quad \xi \in [\xi_1, \xi_{n+p+1}] \ , \ \eta \in [\eta_1, \eta_{m+q+1}] \ , \tag{8.37}$$

where $\mathbf{P} := \{P_A\}_{A=1}^{n_{\text{cp}}}$.

Furthermore, with the help of the Bézier extraction operator (Borden et al., 2011), the global parametric domains Ξ and $\mathcal{H}$ are changed to the domain of the Bézier elements. Then the shape functions are implemented as a classical FEM. Thus, the rational shape function of an element Ω^e is defined as

$$\mathbf{R}^e(\xi, \eta) = \frac{\mathbf{W}^e\, \mathbf{C}^e\, \mathbf{B}^e}{W(\xi, \eta)} \ , \quad \xi, \eta \in [-1,\ 1] \ , \tag{8.38}$$

where $\mathbf{R}^e(\xi, \eta) = \{R_A^e(\xi, \eta)\}_{A=1}^{n_{\text{cp}}^e}$ is the set of the rational shape functions, n_{cp}^e is the number of control points per element, $\mathbf{W}^e$ is the corresponding diagonal matrix of the element, $\mathbf{B}^e$ collects the Bernstein polynomials of the element and $\mathbf{C}^e = \mathbf{C}_\xi^e \otimes \mathbf{C}_\eta^e$ is the localized Bézier extraction operator. To construct the classic finite element setup, for the A^{th} control point (=node), the corresponding shape function in element Ω^e is set to $N_A(\xi, \eta) = R_A^e(\xi, \eta)$, where R_A^e is given by Eq. (8.38). For example, Fig. 8.1.a shows a surface discretized by quadratic NURBS-based shape functions, i.e. $p = q = 2$. Here, $\Xi = \mathcal{H} = [0\ 0\ 0\ 0.5\ 1\ 1\ 1]$, which correspond to a 2×2 mesh. The grid of control points is shown by the blue lines and the element edges are denoted by black lines. In Fig. 8.1.b, the shape functions of the control points of the first element (colored darker in Fig. 8.1.a) are shown at $\eta = -0.5$.

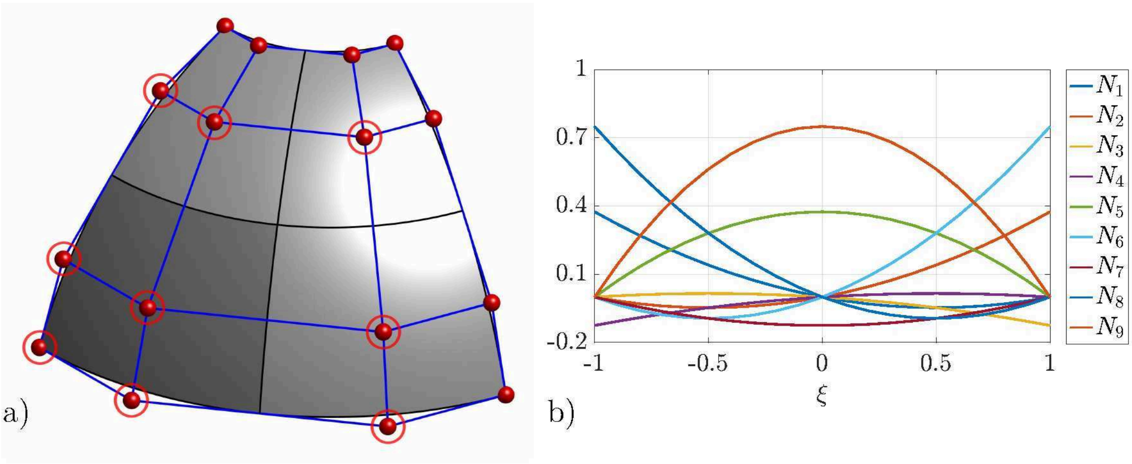

FIGURE 8.1: A NURBS-based discretized surface: a) Finite elements and the associated control points. b) The shape functions of the first element at $\eta = -0.5$ (corresponding to the control points denoted by red rings in a).

8.2.2 Patch coupling

The big challenge in using NURBS-based meshes in FE analysis of Kirchhoff–Love shells is the coupling of patches. Although within each patch the shape functions have C^1-continuity, on the boundaries they are C^0-continuous. Thus, if a mesh is constructed form multiple patches, as it is common for complicated geometries created by CAD tools, one need to enforce the continuity constraint at the patch interfaces to be able to use a Kirchhoff–Love shell formulation. In literature, there are various methods to enforce the continuity between patches. In the bending strip method of (Kiendl et al., 2010), strips of fictitious material with unidirectional bending stiffness and zero membrane stiffness are added at patch interfaces Schmidt et al. (2012) present an approach for isogeometric analysis of trimmed NURBS geometries including Kirchhoff–Love shells. The method is applied to single-patch and multi-patch meshes. Nguyen et al. (2013) use a Nitsche method to couple different mechanical models. They include coupling of a solid and a beam and of a solid and a plate. Both conforming and non-conforming formulations are presented. Similarly, Nguyen et al. (2014) apply Nitsches method for two and three dimensional NURBS patch coupling and in particular for plates. Guo and Ruess (2015b) propose a Nitsche's method for weak coupling of thin Kirchhoff–Love NURBS shell patches and a blended coupling of solid-like patches and Kirchhoff–Love shell patches. In Guo and Ruess (2015c), a Nitsche-based extension of the Kirchhoff–Love theory is investigated to enforce weakly essential boundary conditions of the shell. The method is applied to trimmed and untrimmed NURBS structures. Lei et al. (2015b) introduce a penalty and a static condensation method to enforce the C^0/G^1-continuity for NURBS-based meshes with multiple patches. Coox et al. (2017) have developed a new patch coupling method for NURBS-based conforming and non-conforming multi-patch surfaces. The coupling relationships only depend on the mesh itself and not on any problem-dependent parameters, allowing them to be generated in a pre-processing step. Their method is capable of enforcing C^0/C^1-continuity. In Goyal and Simeon (2016) an alternative formulation for the bending strip method of Kiendl et al. (2009) is proposed that improves the condition number of the system and removes the penalty parameter dependence. The non-symmetric Nitsche approach is employed by Guo et al. (2016) for isogeometric thin shell analysis and particularly for enforcing interface conditions along trimming curves.

Here, we adopt the approach of Duong et al. (2017) to enforce the G^1-continuity across the patches. The formulation of Duong et al. (2017) can also be used to describe other edge conditions such as symmetry and clamping constraints and rotational Dirichlet boundary conditions. In addition to wide applicability, the formulation of Duong et al. (2017) is favored as it is independent of constitutive equations in contrast to Nitsche's method (e.g. (Guo and Ruess, 2015b)). Further, it seems to be computationally less expensive than the bending strip method of (Kiendl et al., 2010) as it only requires line integration instead of surface integration. The formulation of Duong et al. (2017) is proposed for enforcing the G^1-continuity across conforming patches. Here, we present a simplified version of their formulation, which is suitable for patches with smooth interfaces. For fixed surface folds (e.g. V-shape and L-shape), the general formulation of Duong et al. (2017) can be used. Further, a similar formulation is proposed to enforce the C^1-continuity across patches and it is shown how this approach can be applied to patches with nonconforming meshes using a C^0-continuity constraint.

Coupling of NURBS-based patches involves two main steps: First, imposing C^0-continuity, which is the prerequisite of C^1- and G^1-continuity and second, enforcing the C^1- or G^1-continuity constraint depending on the method. In the following, a separate formulation is proposed for enforcing each constraint

8.2.2.1 C^0-continuity constraint

When two patches are attached together, as shown in Fig. 8.2, those pairs of control points on the interface of patches that coincide are merged into one control point. For the case of patches with conforming meshes, all the control points on the interface can be paired. However, for the case of nonconforming patches, only some of control points may be paired. Thus, for conforming patches, merging of control points simply guarantees the C^0-continuity at the whole interface; however, this does not hold for nonconforming patches. Therefore, for nonconforming patches, C^0-continuity must be separately enforced along the interface, which is discussed in the following. For nonconforming patches, one can introduce a C^0-continuity constraint as

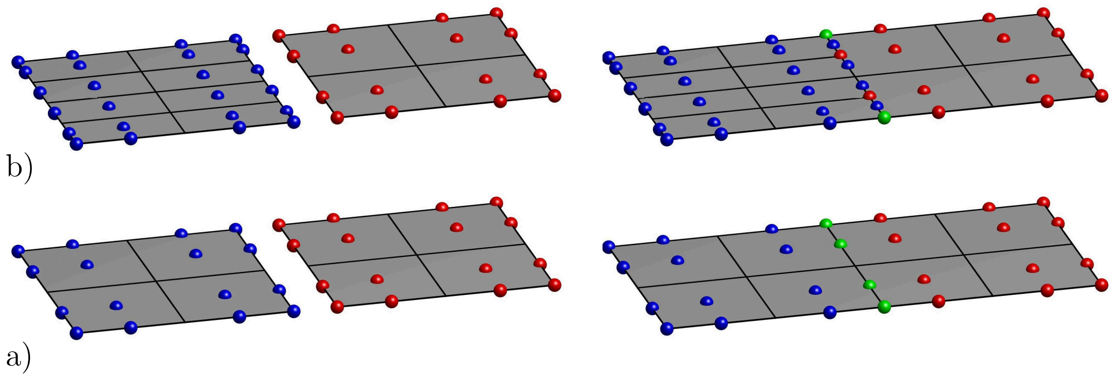

FIGURE 8.2: Merging of two NURBS-based patches: a) conforming patches and b) nonconforming patches. The red and blue spheres denote the control points of two different patches and the green ones denote those control points that are paired on the interface of patches.

$$\boldsymbol{g}_x := \big(\boldsymbol{x} - \bar{\boldsymbol{x}}\big) = \boldsymbol{0} \tag{8.39}$$

where $\boldsymbol{x}$ and $\bar{\boldsymbol{x}}$ are the position of two associated points on the interface of two adjacent patches. The constraint (8.39), can be enforced by the penalty method as

$$\Pi_x = \int_{\mathcal{L}_0} \frac{\epsilon_x}{2}\, \boldsymbol{g}_x^2 \, \mathrm{d}S \ , \tag{8.40}$$

where ϵ_n is the penalty parameter. The contribution of Eq. (8.40) to the weak form, introduced in Chap. 3, is

$$\delta\Pi_x = \int_{\mathcal{L}_0} \epsilon_n\, \boldsymbol{g}_x \cdot \big(\delta\boldsymbol{x} - \delta\bar{\boldsymbol{x}}\big)\, \mathrm{d}S \ . \tag{8.41}$$

8.2.2.2 G^1-continuity constraint

To enforce G^1-continuity between two patches, the constraint equation

$$\boldsymbol{g}_n := \big(\boldsymbol{n} - \bar{\boldsymbol{n}}\big) = \boldsymbol{0} \tag{8.42}$$

can be used on the patch interface $\mathcal{L}$, where $\boldsymbol{n}$ is the surface normal of a patch and $\bar{\boldsymbol{n}}$ is that of the adjacent patch (see Fig. 8.3). The constraint (8.42) can be enforced by the penalty method as

$$\Pi_n = \int_{\mathcal{L}_0} \frac{\epsilon_n}{2}\, \boldsymbol{g}_n^2 \,\mathrm{d}S = \int_{\mathcal{L}_0} \epsilon_n \left(1 - \boldsymbol{n}\cdot\bar{\boldsymbol{n}}\right) \mathrm{d}S \;, \tag{8.43}$$

where ϵ_n is the penalty parameter and the potential is defined over the corresponding edge $\mathcal{L}_0$ on the reference configuration.

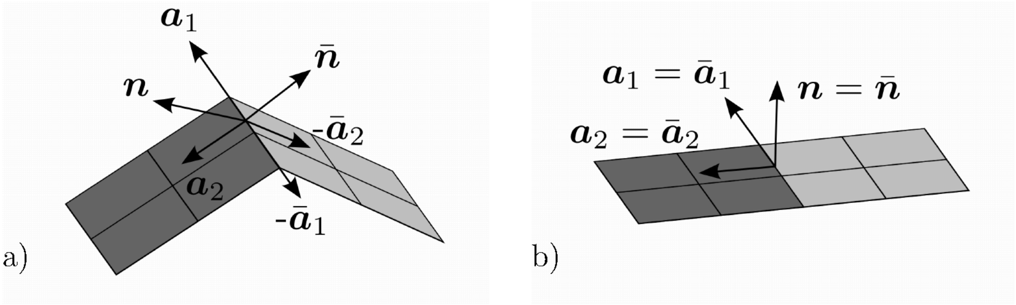

FIGURE 8.3: Schematic illustration of C^1-continuity constraint: Patches a) before and b) after imposing the constraint.

The same constraint is used in Chap. 9 to impose clamping and symmetry constraints by setting $\bar{\boldsymbol{n}} := \boldsymbol{N}$, where $\boldsymbol{N}$ is the corresponding surface normal on $\mathcal{L}_0$. If a rotational Dirichlet boundary condition is applied, $\bar{\boldsymbol{n}}$ is given at each load step. Taking the variation of Eq. (8.43), the contribution of the constraint potential to the weak form is

$$\delta\Pi_n = \int_{\mathcal{L}_0} \epsilon_n \, \boldsymbol{g}_n \cdot \left(\delta\boldsymbol{n} - \delta\bar{\boldsymbol{n}}\right) \mathrm{d}S \;. \tag{8.44}$$

Similarly, the constraint can be imposed by the Lagrange multiplier method as (Duong et al., 2017)

$$\Pi_n = \int_{\mathcal{L}_0} \lambda\, \boldsymbol{g}_n \,\mathrm{d}S = \int_{\mathcal{L}_0} \lambda \left(\boldsymbol{n} - \bar{\boldsymbol{n}}\right) \mathrm{d}S \;, \tag{8.45}$$

where λ is the Lagrange multiplier associated with the edge constraint (8.42). Eq. (8.45) gives

$$\delta\Pi_n = \int_{\mathcal{L}_0} \delta\lambda\, \boldsymbol{g}_{\mathcal{L}} \,\mathrm{d}S + \int_{\mathcal{L}_0} \lambda \left(\delta\boldsymbol{n} - \delta\bar{\boldsymbol{n}}\right) \mathrm{d}S \;. \tag{8.46}$$

The method of the Lagrange multiplier is not studied here. The associated FE force vectors and tangent matrices can be found in Duong et al. (2017). It should be noted that for the clamping and symmetry constraints and rotational Dirichlet boundary conditions, $\delta\bar{\boldsymbol{n}} = 0$, which simplifies the equations considerably.

8.2.2.3 C^1-continuity constraint

C^1-continuity between two patches, can be imposed by using two constraints

$$\begin{aligned} \boldsymbol{g}_{a_1} &:= \left(\frac{\boldsymbol{a}_1}{\boldsymbol{A}_1} - \frac{\bar{\boldsymbol{a}}_1}{\bar{\boldsymbol{A}}_1}\right) = \boldsymbol{0} \ , \\ \boldsymbol{g}_{a_2} &:= \left(\frac{\boldsymbol{a}_2}{\boldsymbol{A}_2} - \frac{\bar{\boldsymbol{a}}_2}{\bar{\boldsymbol{A}}_2}\right) = \boldsymbol{0} \ . \end{aligned} \tag{8.47}$$

Here $\{\boldsymbol{a}_1 \ , \ \boldsymbol{a}_2\}$ and $\{\bar{\boldsymbol{a}}_1 \ , \ \bar{\boldsymbol{a}}_2\}$ are sets of tangent vectors on the coupling interface of each patch (see Fig. 8.3). Further, $\{\boldsymbol{A}_1 \ , \ \boldsymbol{A}_2\}$ and $\{\bar{\boldsymbol{A}}_1 \ , \ \bar{\boldsymbol{A}}_2\}$ are the corresponding vectors in the reference configuration, which are used to normalize the tangent vectors if the patches are nonconforming. Here, it is assumed that the patches are oriented so that $\boldsymbol{a}_1$ can be paired with $\boldsymbol{a}_2$ and similarly for $\bar{\boldsymbol{a}}_1$ and $\bar{\boldsymbol{a}}_2$; however, this does not influence the generality of the formulation. Similar to the previous constraints, here the penalty method is also utilized as

$$\begin{aligned} \Pi_{a_1} &= \int_{\mathcal{L}_0} \frac{\epsilon_a}{2}\, \boldsymbol{g}_{a_1}^2 \, \mathrm{d}S \ , \\ \Pi_{a_2} &= \int_{\mathcal{L}_0} \frac{\epsilon_a}{2}\, \boldsymbol{g}_{a_2}^2 \, \mathrm{d}S \ , \end{aligned} \tag{8.48}$$

where ϵ_a is the corresponding penalty parameter. Eq. (8.48) yields

$$\begin{aligned} \delta\Pi_{a_1} &= \int_{\mathcal{L}_0} \epsilon_a \, \boldsymbol{g}_{a_1} \cdot \big(\delta\boldsymbol{a}_1 - \delta\bar{\boldsymbol{a}}_1\big) \, \mathrm{d}S \ , \\ \delta\Pi_{a_2} &= \int_{\mathcal{L}_0} \epsilon_a \, \boldsymbol{g}_{a_1} \cdot \big(\delta\boldsymbol{a}_2 - \delta\bar{\boldsymbol{a}}_2\big) \, \mathrm{d}S \ . \end{aligned} \tag{8.49}$$

Chapter 9

Numerical Examples

In this chapter the capabilities of the presented membrane and shell formulations are demonstrated through different numerical examples. First, in Sec. 9.1 linear and nonlinear benchmark tests are performed to show the accuracy of the shell formulation. Here, the results of the finite shell element simulations are compared with the available analytical or computational reference solutions. Then, in Sec. 9.2, the constitutive projection approaches for the membrane and Kirchhoff–Love shell models of Chap. 4 are compared. For this purpose, different material models of Chap. 6 are taken into account. In Sec. 9.3, similar numerical experiments are investigated for the laminated composite shell models of Chap. 5. The capability of the presented formulation for contact simulation is demonstrated in Sec. 9.4. Last, the dynamic surface tension model, introduced in Chap. 7, is examined.

9.1 Shell benchmark tests

For the linear and nonlinear problems discussed below, the St. Venant–Kirchhoff material model (see Sec. 6.2.1) is used. As the results of the NP, AP and DD shell models are identical, only the result of DD shell model is reported. Later, in Sec. 9.2, these shell models are compared in detail. For the St. Venant–Kirchhoff material model, the Lamé's constants

$$\tilde{\Lambda} = \frac{E\,\nu}{(1+\nu)(1-2\,\nu)}\ , \quad \tilde{\mu} = \frac{E}{2\,(1+\nu)} \tag{9.1}$$

are needed, where E and ν are the Young's modulus and Poisson's ratio, respectively.

9.1.1 Linear problems[13]

In this section, only two problems from linear elasticity are studied as the focus of this thesis is nonlinear deformations. Further examples can be found in Duong et al. (2017). The selected examples are classically used to benchmark shell formulations (see e.g. Hughes et al., 2005 and Kiendl et al., 2009).

9.1.1.1 Simply supported plate

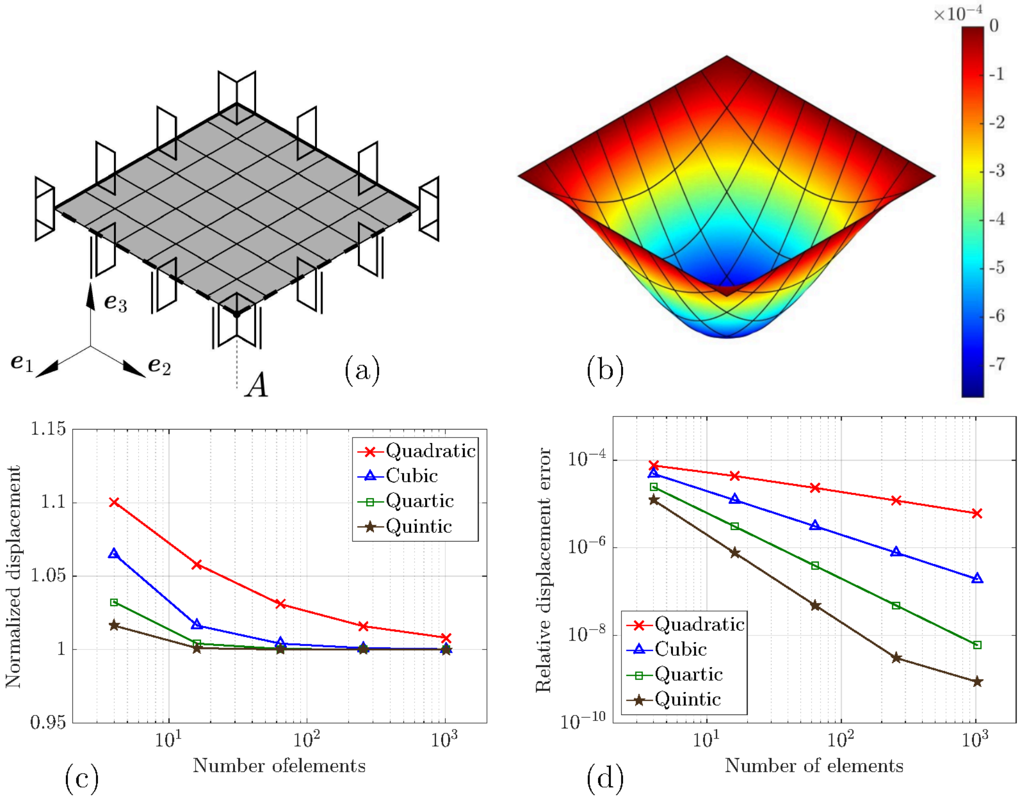

FIGURE 9.1: Simply supported plate under sinusoidal pressure: (a) Initial configuration with boundary conditions (quarter system), (b) deformed configuration (full system scaled 10^4 times) colored by the vertical displacement, (c) displacement of point A normalized w.r.t. the analytical solution and (d) relative error of the displacement.

As the second example, we analyze a plate with dimension $L \times L \times T = 12 \times 12 \times 0.375\,[\mathrm{m}^3]$, Young's modulus $E = 4.8 \times 10^5$, Poisson's ratio $\nu = 0.38$, subjected to sinusoidal pressure $p(x, y) = p_0 \sin(\pi\, x/L) \sin(\pi\, y/L)$. According to *Navier*'s solution

---

[13] The examples of this section are taken from Duong et al. (2017) with slight modification.

(Ugural, 2009), the maximum deflection is at the middle point and given by

$$w_{\max} = \frac{p_0\, L^2}{4\, \pi^4\, D} \,, \tag{9.2}$$

where $D := E\, T^3/12\,(1-\nu^2)$ is the flexural rigidity of the plate. The setup of the computational model is shown in Fig 9.1a. Only 1/4 of the plate is modeled using symmetry boundary conditions enforced by the penalty method of Duong et al. (2017) with the penalty parameter $\epsilon = 0.01\, E\; n^{p-1}$, where p is the NURBS order and n is the number of elements in each direction. Fig. 9.1.b illustrates the deformed plate and Fig. 9.1.c shows the convergence of the computational solution to the analytical one as the mesh is refined. For the comparison, the vertical displacement at the center of the plate is normalized by the analytical solution given in Eq. (9.2). The corresponding relative error is shown in Fig. 9.1.d. As expected, more accuracy is gained by increasing the NURBS order.

9.1.1.2 Pinching of a cylinder

Next, we the pinched cylinder test with rigid diaphragms at its ends is examined. It is designed to examine the performance of shell elements in inextensional bending modes and complex membrane states (Belytschko et al., 1985). The analytical solution for this problem was introduced by Flügge (1962) based on a double Fourier series and can be found in Duong et al. (2017).

The parameters are adopted from Belytschko et al. (1985) as $E = 3 \times 10^6$, $\nu = 0.3$, $R \times L \times T = 300 \times 600 \times 3\,[\mathrm{m}^3]$. For the FE computation, 1/8 of the cylinder is modeled due to its symmetry as is shown in Fig. 9.2.a. The symmetry boundary conditions are enforced by the penalty method discussed in Sec. 8.2.2. The penalty parameters used are $\epsilon = 2 \times 10^2\, n_l^{p-1}\, E$ for the axial symmetry, and $\epsilon = 2 \times 10^2\, n_t^{p-1}\, E$ for the circumferential symmetry. Here, n_t and n_l are the number of elements in circumferential and axial directions, respectively.

Two opposing pinching forces $F = 1[\mathrm{N}]$ are applied at the middle of cylinder. For the symmetric model, a quarter of the force is applied. The deflection due to the loads is measured for comparison with the reference solution. For 80×80 Fourier terms, the deflection under the point load is 1.82488×10^{-5}, which is the reference value commonly used in the literature. However, for 8192×8192 Fourier terms the converged solution is $1.82715781 \times 10^{-5}$ and for $2^{14} \times 2^{14}$ Fourier terms, a solution of $1.82715797 \times 10^{-5}$ is obtained (Duong et al., 2017).

Fig. 9.2.c shows the convergence behavior of the computed displacement at the loading point w.r.t. the analytical solution as the mesh is refined. From Fig. 9.2.d, we observe that the relative error only converges up to a certain point. As discussed by Duong

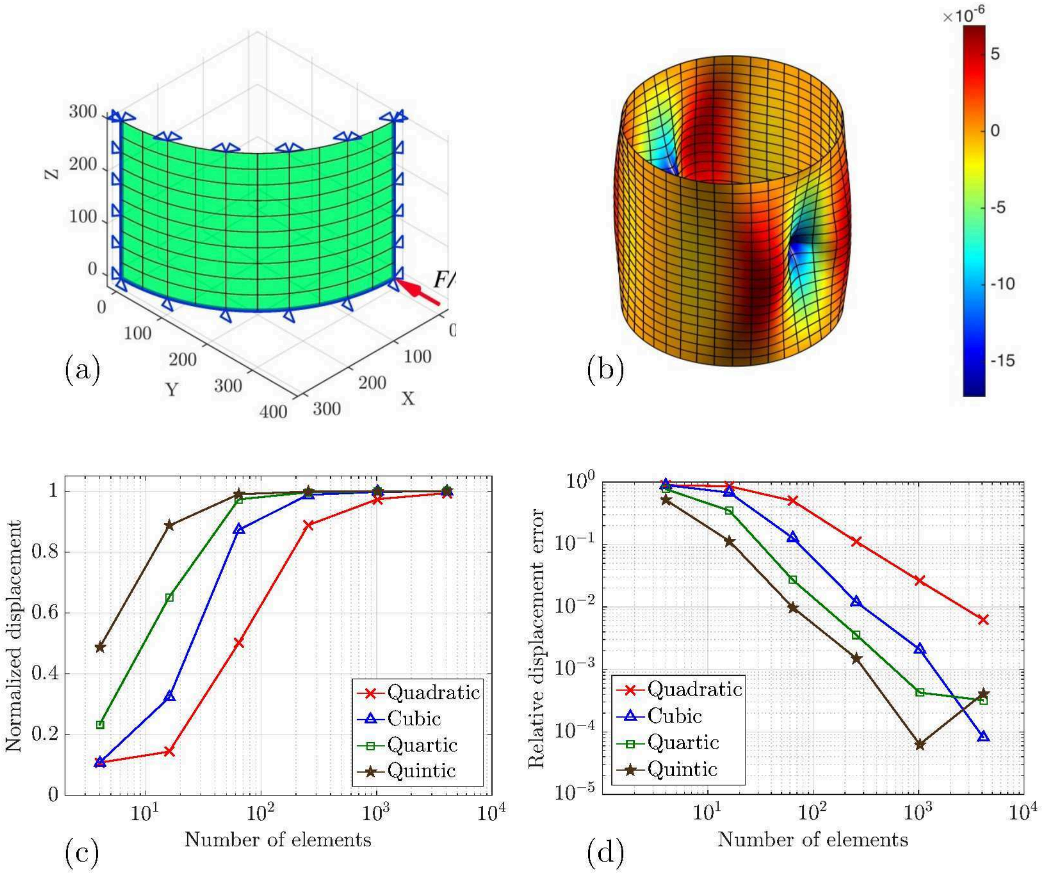

FIGURE 9.2: Pinching of the cylinder with rigid end diaphragms: (a) Setup of the computation model, (b) deformed shell (scaled 10^6 times) colored by the radial displacement, (c) normalized radial displacement at the point load and (d) error w.r.t. the reference solution as the mesh is refined.

et al. (2017), this can be due to several numerical and theoretical reasons: Under the point load, two symmetry constraint are applied, which can make the problem over-constrained. Further, although the NURBS order can be increased for the areas inside patches, the patch boundaries are only G^1-continuous according to Eq. (8.43). This affects higher order NURBS, especially at the boundaries around the singular point load. Finally, the analytical solution is based on the Fourier representation of a concentrated load (see Appendix E of Duong et al., 2017), which cannot be exact.

9.1.2 Nonlinear problems[14]

In the following, several nonlinear test cases are presented to illustrate the robustness and accuracy of the proposed shell formulation.

---

[14] The examples of this section, except the one in Sec. 9.1.2.5, are taken from Duong et al. (2017) with slight modification.

9.1.2.1 Cantilever subjected to end shear forces

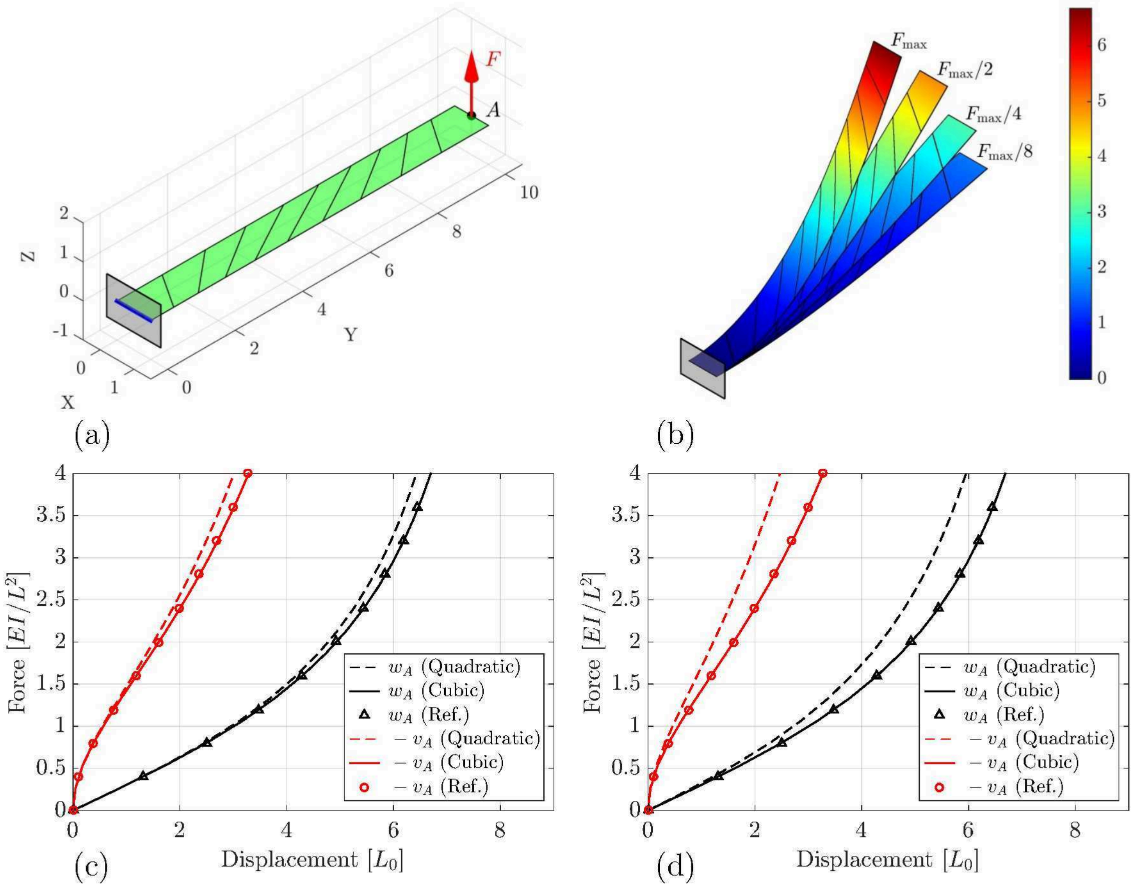

FIGURE 9.3: Cantilever subjected to end shear force: (a) Undeformed configuration, (b) deformed configuration colored by the vertical displacement. Horizontal ($-v_A$) and vertical (w_A) displacement at tip A for (c) a regular mesh with uniform element length and (d) a skew mesh as shown in (b). The results are compared with Sze et al. (2004).

The large deflection of a cantilever beam, with dimensions $L \times W \times T = 10 \times 1 \times 0.1$ [m^3], due to shear traction $\bar{\boldsymbol{t}} = \boldsymbol{F}/W$ applied to its free end is computed. The forces at the nodes located on the free end are derived from Eq. (B.5.3). The fixed end is clamped by the penalty method (see Sec. 8.2.2) with $\epsilon = 10^3$. The material parameters are $E = 1.2 \times 10^6$ and $\nu = 0.0$ (Sze et al., 2004). The beam is modeled is discretized by 1×10 NURBS elements, considering both a regular mesh and a skew mesh. The applied maximum shear force is $F_{\max} = 4\,F_0$ with $F_0 = EI/L^2$ and $I = 1/12\,W\,T^3$. As shown in Fig. 9.3, considering 10 elements, cubic NURBS give very good results for both regular and skew meshes.

9.1.2.2 Pinching of a hemisphere with a hole

In this example, we compute the large deformation of a hemisphere with a hole at the top, under two pairs of equally large but opposing forces that are applied on the equator of the hemisphere as shown in Fig. 9.4. The parameters are extracted from

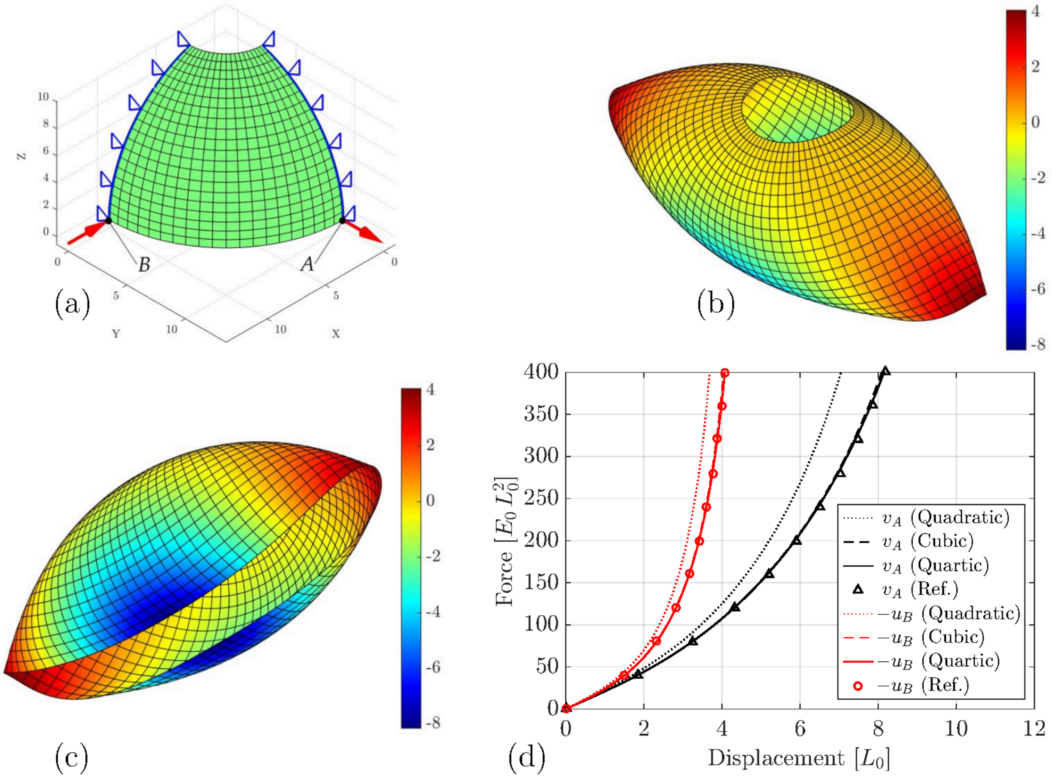

FIGURE 9.4: Pinching of a hemisphere with a hole at 18°: (a) Undeformed configuration with boundary conditions, (b-c) deformed configuration colored by the radial displacement and (d) the force vs. displacement of points A and B compared with the reference solution of Sze et al. (2004).

Sze et al. (2004) as $R \times T = 10 \times 0.04\,[\mathrm{m}^2]$, $E = 6.825 \times 10^7$, $\nu = 0.3$ and the point load $F_{\max} = 400\,[\mathrm{N}]$. The symmetry of the hemisphere is modeled by the penalty method with $\epsilon = 6 \times 10^3\, E$ (see Fig. 9.4.a). The surface is meshed with 20×20 quadratic, cubic and quartic NURBS based finite elements. As observed in Fig. 9.4.d, the computed results approach the reference solution as the NURBS order is increased.

9.1.2.3 Pinching of a cylinder with end rigid diaphragms

Here, the pinched cylinder test of Sec. 9.1.1.2 is reconsidered with large deformations as shown in Fig. 9.5. The dimensions of cylinder are $L \times R \times T = 200 \times 100 \times 1.0\,[\mathrm{m}^3]$. Here, $E = 30 \times 10^3\, E_0$ and $\nu = 0.3$. The point load $F_{\max} = 12 \times 10^3\,[\mathrm{N}]$ is applied. Due to the symmetry, only 1/8 of the cylinder is modeled. The symmetry boundary conditions are enforced by the Lagrange multiplier method (8.45). The cylinder is discretized by 50×50 quadratic NURBS finite elements. Fig. 9.5.f shows good agreement with the reference result of Sze et al. (2004).

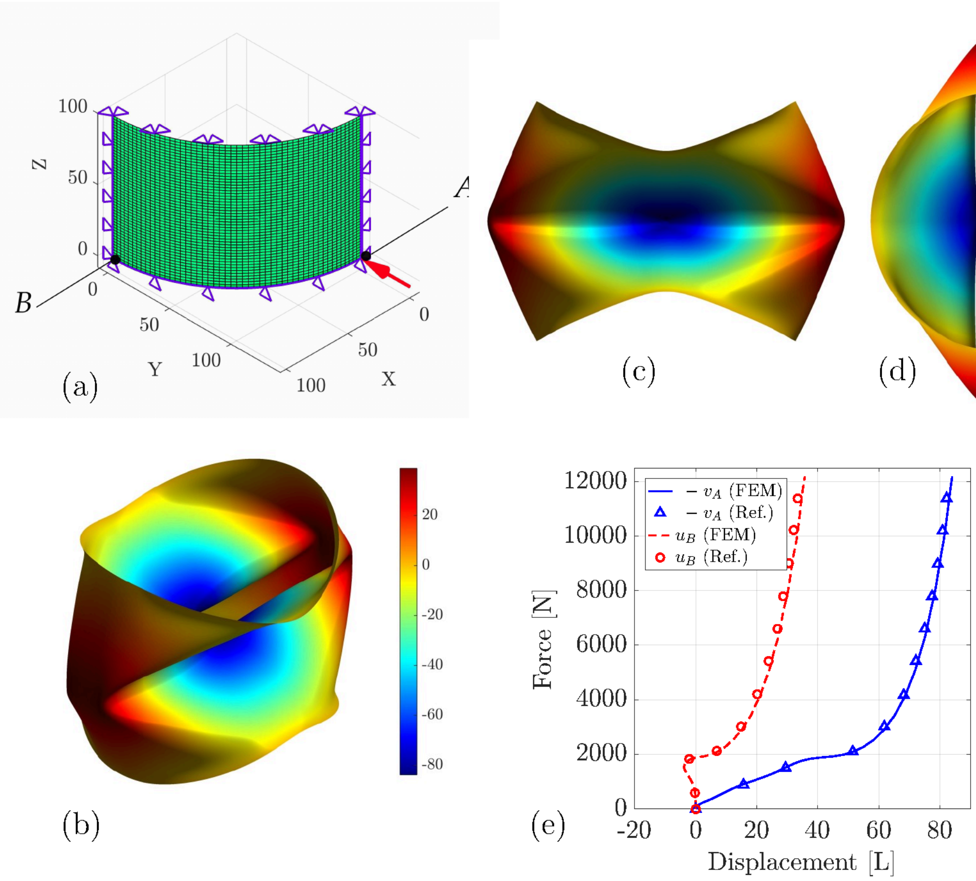

FIGURE 9.5: Nonlinear pinching of a cylinder with rigid end diaphragm: (a) Undeformed configuration with boundary conditions. Deformed configurations in (b) 3D view, (c) y-axis view, (d) z-axis view. The color here denotes the radial displacement. (f) Force vs. displacement at points A and B compared to the results of Sze et al. (2004).

9.1.2.4 Spreading of a cylinder with free ends

In this test, a cylinder, with dimensions $L \times R \times T = 10.35 \times 4.953 \times 0.094\,[\mathrm{m}^3]$, with open ends is pulled apart by a pair of opposite forces up to $F_{\max} = 40 \times 10^3$ [N], which are applied at the middle of the cylinder (see Fig. 9.6). The Young's modulus and the Poisson's ratio are $E = 10.5 \times 10^6$ and $\nu = 0.3125$, respectively. Here, the results of Sze et al. (2004) are used as a reference for comparison. Due to the symmetry, only 1/8 of the cylinder is modeled as shown in Fig. 9.6a. The cylinder is discretized by

20×20 NURBS finite elements. The symmetry boundary conditions are enforced by the penalty method (see Sec. 8.2.2). A good agreement with the reference results is also observed in Fig. 9.6.c.

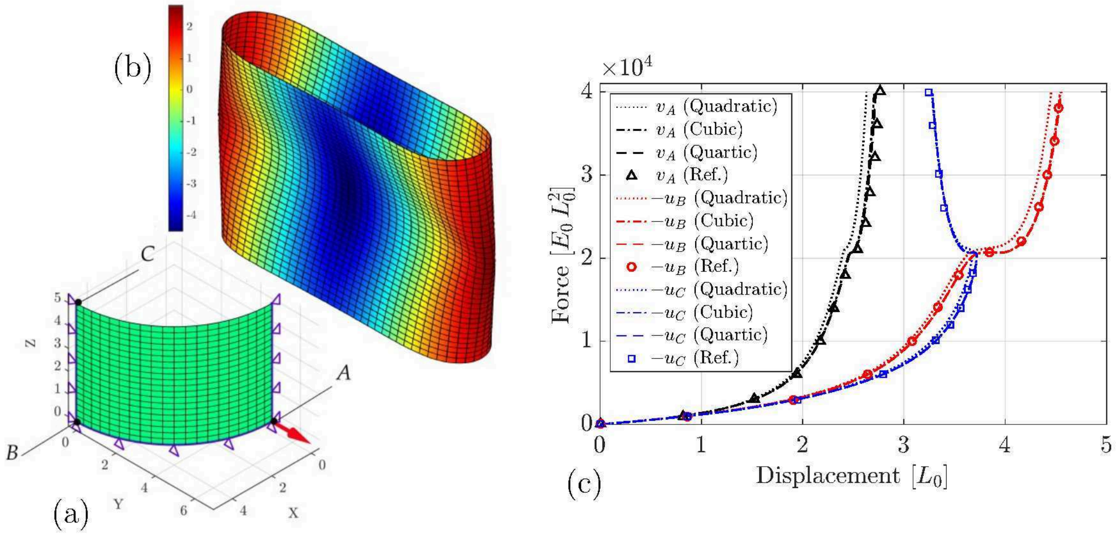

FIGURE 9.6: Spreading of a cylinder with free ends: (a) Undeformed configuration with boundary conditions, (b) deformed configuration colored with radial displacement, (c) force vs. displacement of points A, B and C compared to the results of Sze et al. (2004).

9.1.2.5 Multi-patch cantilever subjected to end shear forces

In Sec. 8.2.2, two penalty formulations for the coupling of two NURBS-based patches with conforming and nonconforming meshes are introduced. In this example, the performance of these formulations are investigated for the case of a cantilever subjected to end shear forces. As shown in Fig. 9.7.a-b, two cases are considered: 1) A cantilever constructed of two conforming patches with G^1-continuity constraint (denoted a 2P-G^1) and 2) a cantilever constructed of two nonconforming patches with C^0/C^1-continuity constraint (denoted a 2P-C^0/C^1). Both cases are compared with a single patch cantilever, denoted as 1P. It is assumed that the cantilever is an incompressible Neo–Hookean solid and its dimensions are $L \times W = 10 \times 3\ L_0^2$, where L_0 is a length scale. For the 2P-G^1 case, each patch has a 3×3 mesh and all the control points on the shared patch boundary are paired (see Fig. 9.7.a). For the 2P-C^0/C^1 case, the mesh size of one patch is 3×3 while the other one has a 4×3 mesh and only two control point on the shared boundary are paired (see Fig. 9.7.b). In all the cases, quadratic NURBS-based elements are used. For the 2P-G^1 case, the constraint (8.42) is enforced with $\epsilon_n = 300\, W\, \tilde{\mu}$, where $\tilde{\mu}$ is the shear modulus. For the 2P-C^0/C^1 case, constraints

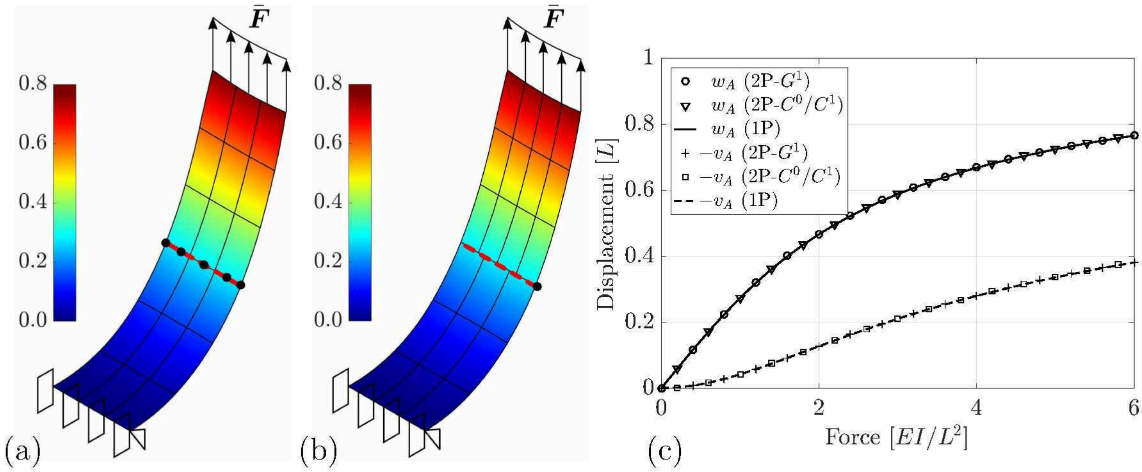

FIGURE 9.7: Multi-patch cantilever subjected to end shear forces: Deformed configuration colored by the vertical displacement normalized by L for (a) 2P-G^1 and (b) 2P-C^0/C^1 meshes. The constrained interface is denoted by the dashed red lines and the filled circles show the paired control points. (c) Displacement of a point at the middle of pulled edge vs. the applied shear force.

(8.47) and (8.39) are enforced with $\epsilon_a = 300\,W\,\tilde{\mu}$ and $\epsilon_x = 10^4\,\epsilon_a$. Fig. 9.7.c shows the displacement of a point at the middle of pulled edge vs. the applied shear force for the three cases. As expected, the presented formulations can accurately enforce the continuity constraints.

9.2 Comparison of projection methods

In this section, the constitutive projection approaches, introduced in Chap. 4, are investigated. For each material model of Sec. 6, different numerical examples are considered to study the performance of the three presented membrane and shell models. To investigate the membrane model (see Sec. 4.2), the inflation of of an artery is examined. The artery is modeled as a tube with open and closed ends constituted of Gasser–Ogden–Holzapfel (GOH - 3D GST) material model (see Sec. 6.3.2). Then, in Secs. 9.2.2-9.2.4, the numerically-projected (NP), analytically-projected (AP) and directly-decoupled (DD) shell models of Sec. 4.3.2 are evaluated. First, a uniaxial tension test is performed to compare the presented shell models if the membrane forces are dominating. Second, the pure bending of a cantilever subjected to a given rotation on its free end is considered, which shows how the models behave if the bending forces are dominant. Third, the large deformation of a square plate under pressure is studied, where the membrane and bending modes exist together.

For the NP shell model, two Gaussian quadrature points are considered for the integration through the thickness of shell unless specified otherwise. For the examples of Secs. 9.2.2-9.2.4, the material constants are set according to the Tab. 9.1. For the anisotropic material models (GOH and AMR), two families of fibers are considered, i.e. $n_\mathrm{f} = 2$. For the GOH material model, $\kappa_i \in \{0.0,\ 0.226,\ 1/3\}$ following Gasser et al. (2006).

NH	$\tilde{c}_1 = 10$ [kPa]	—	—
MR	$\tilde{c}_1 = 10$ [kPa]	$\tilde{c}_2 = 2\,\tilde{c}_1$ [kPa]	—
Fung	$\tilde{c}_1 = 10$ [kPa]	$c_2 = 10$	—
AMR	$\tilde{c}_1 = 10$ [kPa]	$\tilde{c}_2 = 2\,\tilde{c}_1$ [kPa]	$\tilde{c}_3 = 100\,\tilde{c}_1$ [kPa]
GOH	$\tilde{\mu} = 10$ [kPa]	$\tilde{k}_{1i} = 100\,\tilde{c}_1$ [kPa]	$k_{2i} = 500$

TABLE 9.1: Material constants of the considered material models for the examples of Secs. 9.2.2-9.2.4

9.2.1 Tube inflation[15]

In the first example, a thin tube with two identical families of collagen fibers is modeled. The problem geometry is shown in Fig. 9.8. The tube is inflated by applying the internal pressure p_i and the principle stresses and stretches are measured for comparison. The tube ends are set either free or pulled by an axial force. The two families of collagen fibers, with principal directions $\boldsymbol{L}_1$ and $\boldsymbol{L}_2$, have the same mechanical

---

[15] This example is taken from Roohbakhshan et al. (2016) with slight modifications.

properties and they are inclined equally from the axial direction, z. The inclination angle γ is measured from the tangential axis, θ, as shown in Fig. 9.8. Following Gasser et al. (2006), the tube dimensions are $R \times T = 4.745 \times 0.5\,[\mathrm{m}^2]$ and $L = 3\,R$. The material properties are $\tilde{\mu} = 7.64\,[\mathrm{kPa}]$, $\tilde{k}_{11} = \tilde{k}_{12} = 996.6\,[\mathrm{kPa}]$ and $k_{21} = k_{22} = 524.6$. The derivation of the analytical solution for this problem is given in Appendix A of Roohbakhshan et al. (2016).

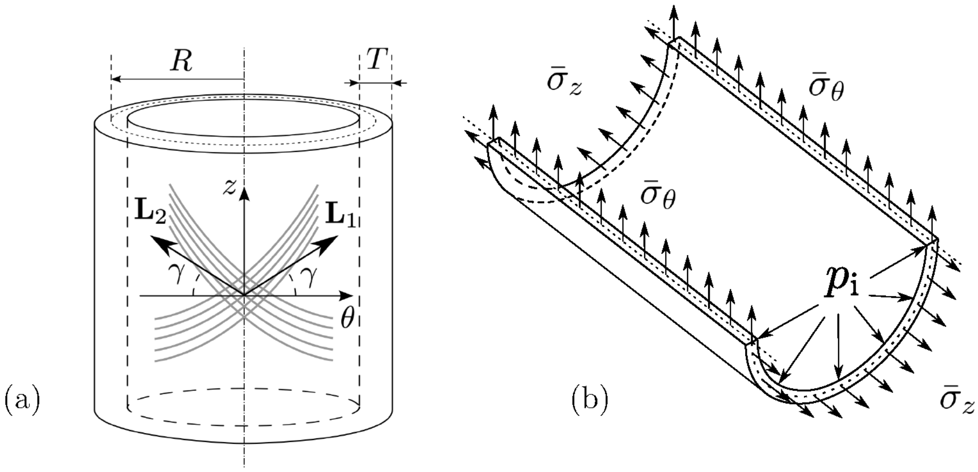

FIGURE 9.8: Inflation of a membrane tube: (a) Geometry and (b) stresses and tractions

On the tube ends, two different boundary conditions are considered, namely zero Dirichlet and zero Neumann boundary conditions. As the tube has three symmetry planes, the symmetry of the problem is used in order to model only 1/8 of the tube. Here, quadratic NURBS-based elements are used for meshing. If the traction on the tube ends is zero, i.e. $\bar{\sigma}_z = 0$, and the tube ends are free to move.

As shown in Fig. 9.9, the membrane model is able to accurately predict the stretches and stresses of the analytical solution. The results of the FE analysis (denoted by circles) are in agreement with the analytical solution (denoted by lines). Three different dispersion parameters κ are considered with $\gamma = 30$, 45 and 60 deg. As it can be expected, if the fiber distribution is isotropic, i.e. $\kappa = 1/3$, the artery response does not change as γ varies. In Fig. 9.9.d, the relative error in the radial stretch $\lambda_r = 1/(\lambda_z\,\lambda_\theta)$ is plotted against the mesh size, which shows the desired convergence to the reference solution. The same trend is also observed for the axial and tangential stretches and corresponding stresses. The relative error of λ_r defined as

$$\mathrm{err}(\lambda_r) = \frac{1}{2\,\pi\,R\,L}\int_{\mathcal{S}_0} |\lambda_r - \lambda_r^{\mathrm{a}}|\,\mathrm{d}A\;, \tag{9.3}$$

where λ_r is the computed radial stretch and λ_r^{a} is the radial stretch based on the analytical solution. As it can be observed in Fig. 9.9.d, $\mathrm{err}(\lambda_r) \sim N^{-2}$. Thus, the mesh refinement leads to quadratic convergence as it can be expected.

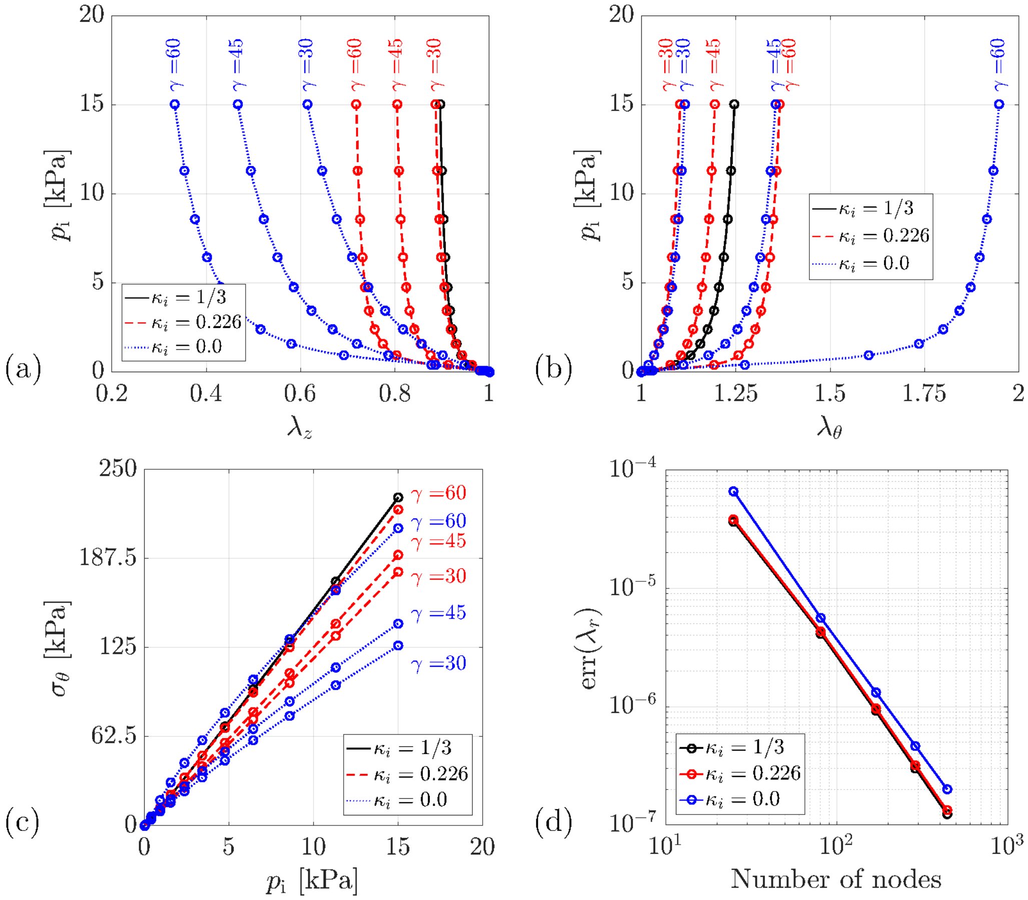

FIGURE 9.9: Tube inflation with zero Neumann BC: (a) Axial stretches, (b) circumferential stretches, (c) circumferential stresses and (d) convergence behavior of the relative error of λ_r against the number of nodes. Axial stresses are zero for both finite element and analytical approaches and are not plotted. The analytical solution is plotted with solid or dashed lines while FE results are denoted by circles (Roohbakhshan et al., 2016).

A similar experiment is performed on a tube with fixed ends, i.e. zero Dirichlet boundary condition. The material and geometrical parameters are the same as in the previous example. In this case, the tube extension in axial direction is restricted, i.e. $\lambda_z = 1$. In addition to the radial stretches, the relative error in the axial reaction force F_z exerted on the tube end supports is also defined, as

$$\mathrm{err}(F_z) = \frac{1}{2\,\pi\,R}\int_{\partial_t \mathcal{S}_0} |F_z - F_z^{\mathrm{a}}|\,\mathrm{d}S\ , \tag{9.4}$$

where F_z^S is the computed axial reaction force on $\partial_t\mathcal{S}$, F_z^{a} is the corresponding force calculated analytically (Roohbakhshan et al., 2016). As it is shown in Fig. 9.10, similar to the tube with Neumann boundary condition, the desired convergence is also observed here.

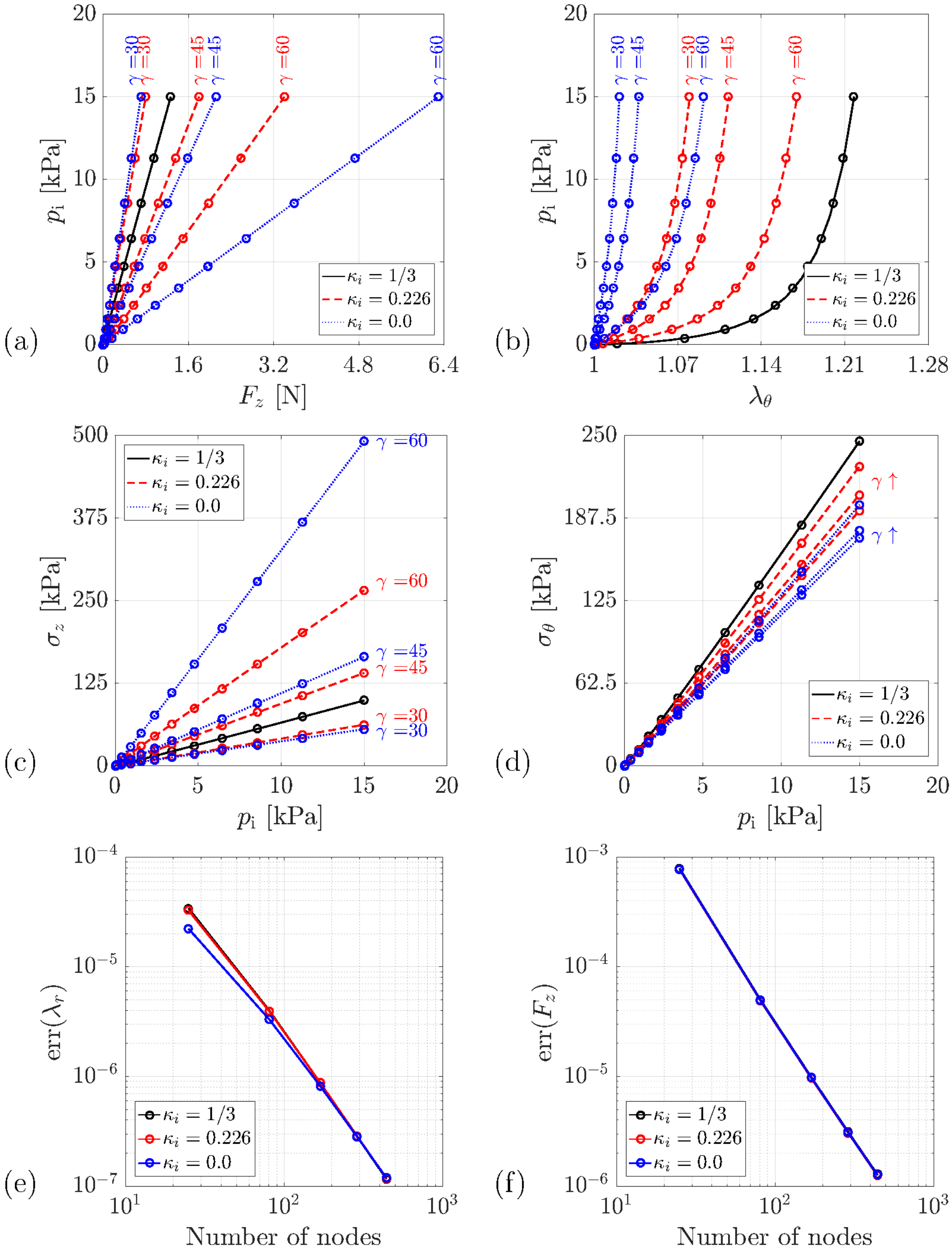

FIGURE 9.10: Tube inflation with zero Dirichlet BC: (a) Axial reaction force, (b) circumferential stretches, (c) axial stresses, (d) circumferential stresses, (e) convergence behavior of the relative error of λ_r against the number of nodes and (f) the relative error of axial reaction force. The analytical solution is plotted with solid or dashed lines while FE results are denoted by circles (Roohbakhshan et al., 2016).

9.2.2 Uniaxial tension test[16]

To examine the presented shell models for the case that membrane forces are dominating, a rectangular strip of $T \times W \times L = 0.3 \times 3 \times 9$ [mm^3] is pulled as shown in Fig. 9.11.a. On the pulled edged, the displacements in $\boldsymbol{e}_2$ direction are enforced to be equal. The pulling force F is applied at the corner of the same edge. The strip is meshed by 6×18 quadratic NURBS elements (see Fig. 9.11.a).

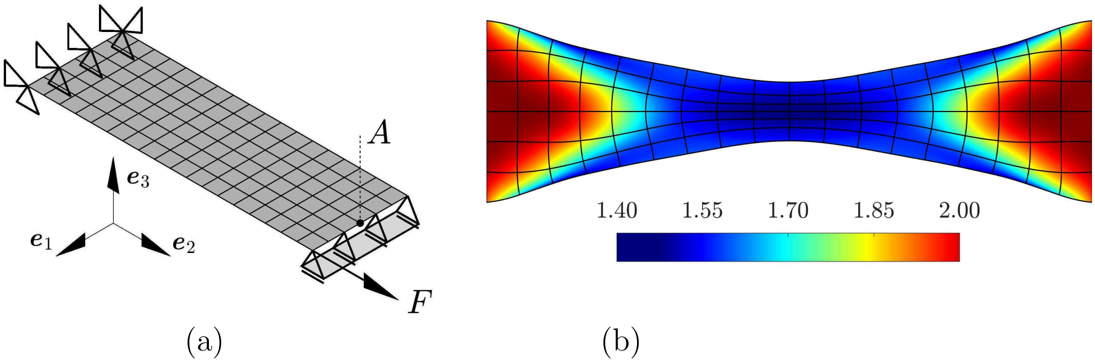

(a) (b)

FIGURE 9.11: Uniaxial tension test: (a) Reference configuration with boundary conditions and (b) deformed configuration for the GOH model (with $\kappa_i = 0$) colored by $I_1 := \operatorname{tr} \boldsymbol{C}$.

For the anisotropic materials, the principal directions of fibers are defined as

$$\tilde{\boldsymbol{L}}_i = \sin\theta_i\, \boldsymbol{e}_1 + \cos\theta_i\, \boldsymbol{e}_2, \quad (i = 1, 2)\ , \tag{9.5}$$

where $\boldsymbol{e}_1$ and $\boldsymbol{e}_2$ are the unit vectors of the Cartesian coordinate system (shown in Fig. 9.11.a). For this example, $\theta_1, \theta_2 = \pm 45°$ for the AMR model and $\theta_1, \theta_2 = \pm 30°$ for GOH model. As already mentioned, here it is assumed that $\overset{*}{L}{}_i^{33} = L_i^{33} = 0$. Henceforth, the displacements in $\boldsymbol{e}_1$, $\boldsymbol{e}_2$ and $\boldsymbol{e}_3$ directions are denoted by u, v and w, respectively.

Fig. 9.12 shows the displacement of point A (shown in Fig. 9.11.a) versus the applied total force. The applied force is normalized by EA, where $E = 3\,\tilde{c}_1$ corresponds to an infinitesimal Young's modulus and $A = W\,T$ is the cross section area. As expected, for all the isotropic and anisotropic materials, the AP and DD shell models give exactly the same results as the NP shell model.

---

[16] This example is taken from Roohbakhshan and Sauer (2017) with slight modification.

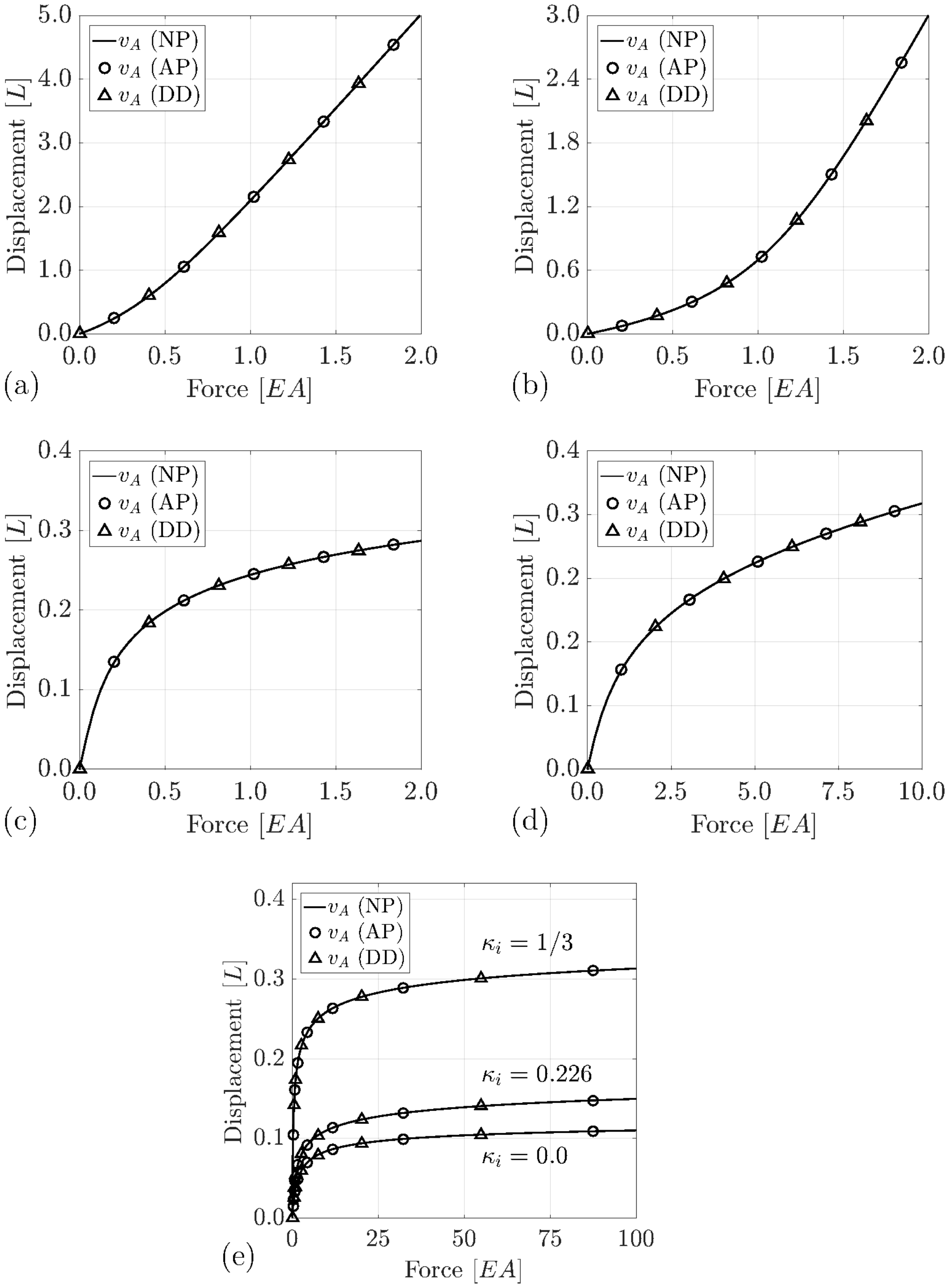

FIGURE 9.12: Uniaxial tension test – the displacement of the tip vs. the applied force: (a) NH, (b) MR, (c) Fung, (d) AMR and (e) GOH material model for the three constitutive approaches (NP, AP and DD) presented in Sec. 4.3.2.

9.2.3 Cantilever bending[17]

The cantilever has the same geometry and mesh properties as the strip of Sec. 9.2.2 although here $T = W/20$. On the clamped edge (see Fig. 9.13.a), the rotations are restricted following the penalty formulation of Duong et al. (2017). On the free end, the surface normal $\boldsymbol{n}$ is constrained to be equal to the given normal $\bar{\boldsymbol{n}}$ using the constraint of Duong et al. (2017). Here, $\bar{\boldsymbol{n}} = \cos\alpha\,\boldsymbol{e}_3 - \sin\alpha\,\boldsymbol{e}_2$, where α is the angle of rotation around $\boldsymbol{e}_1$. In the reference configuration, $\bar{\boldsymbol{n}} = \boldsymbol{N}$ and $\alpha = 0$ (see Fig. 9.13.a). Here, the maximum rotation is set to $\alpha = 90°$ (see Fig. 9.13.b).

The total bending moment corresponding to this rotation is determined following the formulation of Duong et al. (2017). The corresponding bending moment is normalized by $E\,I/L$, where $I = W\,T^3/12$ is the second moment of area of the cross section. The orientation of the fibers is defined based on Eq. (9.5). Here, $\theta_1, \theta_2 = \pm 45°$ for the AMR model and $\theta_1, \theta_2 = \pm 30°$ for the GOH model.

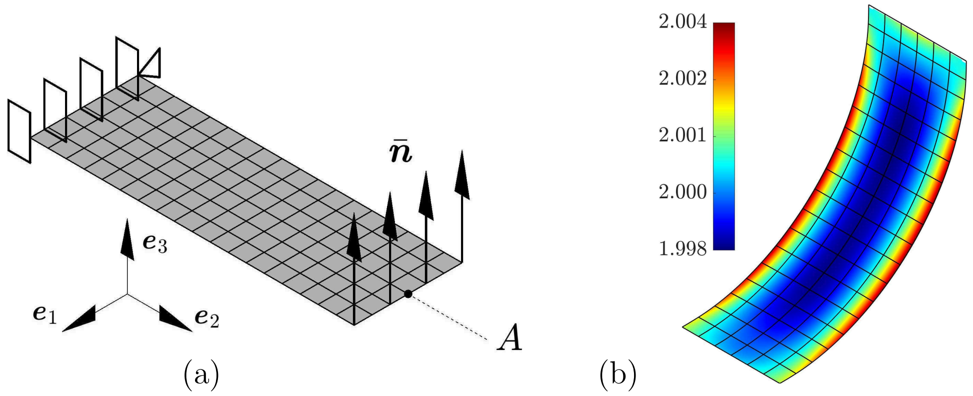

(a) (b)

FIGURE 9.13: Cantilever bending test: (a) Reference configuration with boundary conditions and (b) deformed configuration for the GOH model (with $\kappa_i = 0.226$ and the compression/tension switch) colored by $I_1 := \mathrm{tr}\,\boldsymbol{C}$.

In Figs. 9.14 and 9.15, the corresponding bending moment is plotted against the applied rotation. Similar to the previous example, for the Neo–Hookean, Mooney–Rivlin and Fung material models, which are isotropic, as well as for the anisotropic Mooney–Rivlin material model, the AP and DD shell models are as accurate as the NP shell model (see Fig. 9.14).

Fig. 9.15 shows the results for the Gasser–Ogden–Holzapfel material model. If the compression/tension switch is excluded (see Figs. 9.15.a-9.15.c), all the three introduced shell models behave very similarly. In this case, for the NP shell model, 2 Gaussian quadrature points are sufficient to evaluate the integration through the shell

---

[17] This example is taken from Roohbakhshan and Sauer (2017) with slight modification.

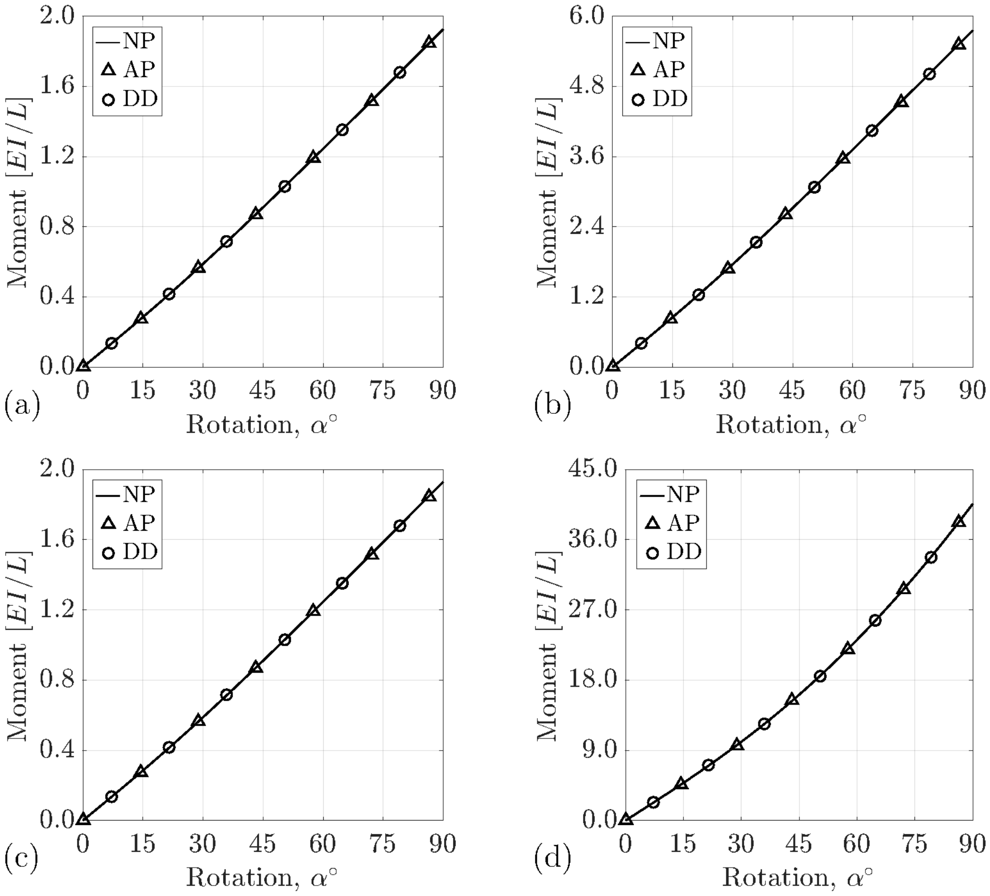

FIGURE 9.14: Cantilever bending test – the corresponding bending moment vs. the applied rotation: (a) NH, (b) MR, (c) Fung and (d) AMR material model for the three constitutive approaches (NP, AP and DD) presented in Sec. 4.3.2.

thickness. However, if the compression/tension switch is included (see Figs. 9.15.d-9.15.f), the DD shell model cannot capture the switch effect since the material model is no longer symmetric w.r.t. the shell mid-surface. Although if the material model is completely isotropic (i.e. setting $\kappa_i = 1/3$), the fibers are excluded and trivially the switch has no effect on the constitutive equations (see Fig. 9.15.f). By increasing the anisotropy (i.e. $\kappa_i \to 0$), the AP and NP shell models behave very similarly although the DD shell model deviates from the correct solution (see Figs. 9.15.d-9.15.e).

If the compression/tension switch is included, more Gaussian quadrature points are needed to capture the discontinuity of switch through the shell thickness. For the results shown in Figs. 9.15.d-9.15.f, 5 quadrature points are used, which is computationally more expensive compared to the cases that no switch is considered. This issue is further investigated in Fig. 9.16, which shows how the NP shell model approaches the AP shell model by increasing the number of Gaussian quadrature points.

Furthermore, as the shell thickness decreases, the AP shell model becomes more accurate. Fig. 9.17.a shows the displacement of the tip versus the applied rotation for different thickness-to-width (T/W) ratios. Fig.9.17.c shows how the corresponding bending moments change. Here, for all the cases modeled by the NP shell model, 5 Gaussian quadrature points are considered through the shell thickness. Fig. 9.17.b and 9.17.d show the corresponding relative errors evaluated w.r.t. the solution of the NP shell model. As can be observed, the AP shell model becomes inaccurate for thick shells; however, such shells are not covered by the Kirchhoff-Love hypothesis.

9.2.4 A clamped plate under pressure[18]

Large deformation of a clamped plate under live pressure is a challenging example. Such an example is used here to compare the capabilities of the three introduced shell models to capture the membrane and bending forces together. As shown in Fig. 9.18.a, a square plate, with $T \times L \times L = 0.25 \times 10 \times 10$ [mm^3], is clamped with appropriate boundary conditions. As the problem is symmetric, only 1/4 of the whole system is modeled and symmetry constraints are applied along the corresponding boundaries. On the clamped and symmetry edges, the rotations are fixed following the constraint formulation of Duong et al. (2017). The plate quarter is meshed by 6×6 quadratic NURBS-based elements. Furthermore, for both the anisotropic material models, the fibers are oriented according to Eq. (9.5) with $\theta_1, \theta_2 = \pm 45°$.

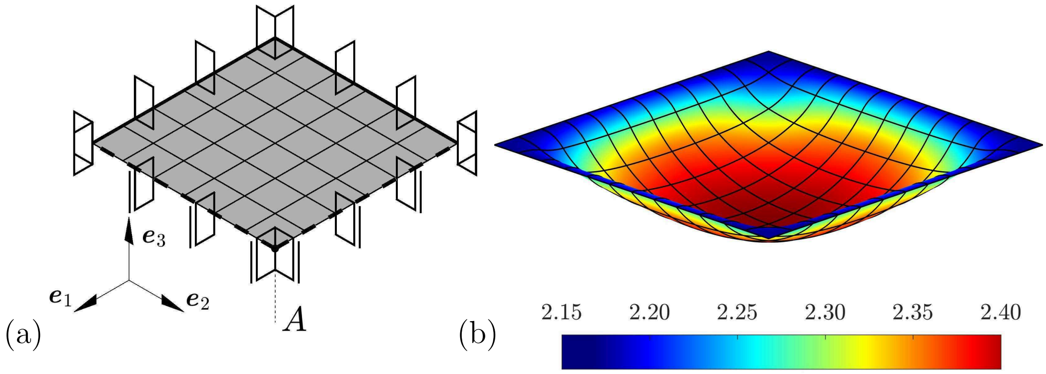

FIGURE 9.18: Clamped plate under pressure: (a) Reference configuration (1/4 system) with boundary conditions and (b) deformed configuration (full system) for the GOH model (with $\kappa = 1/3$ and the compression/tension switch) colored by $I_1 := \mathrm{tr}\,\boldsymbol{C}$.

---

[18] This example is taken from Roohbakhshan and Sauer (2017) with slight modification.

Figs. 9.19 and 9.20 represent the deflection of the mid point A (shown in Fig. 9.18.a) under the applied live pressure. As expected, all the three presented shell models predict similar displacements. Further, the results for the Gasser–Ogden–Holzapfel material model with and without the compression/tension switch are shown in Figs. 9.19.a-9.19.c and Figs. 9.19.d-9.19.f, respectively. Here, for the cases modeled by the NP shell model, 3 Gaussian quadrature points are considered across the thickness if the compression/tension switch is excluded and 5 Gaussian quadrature points are used if the switch is included.

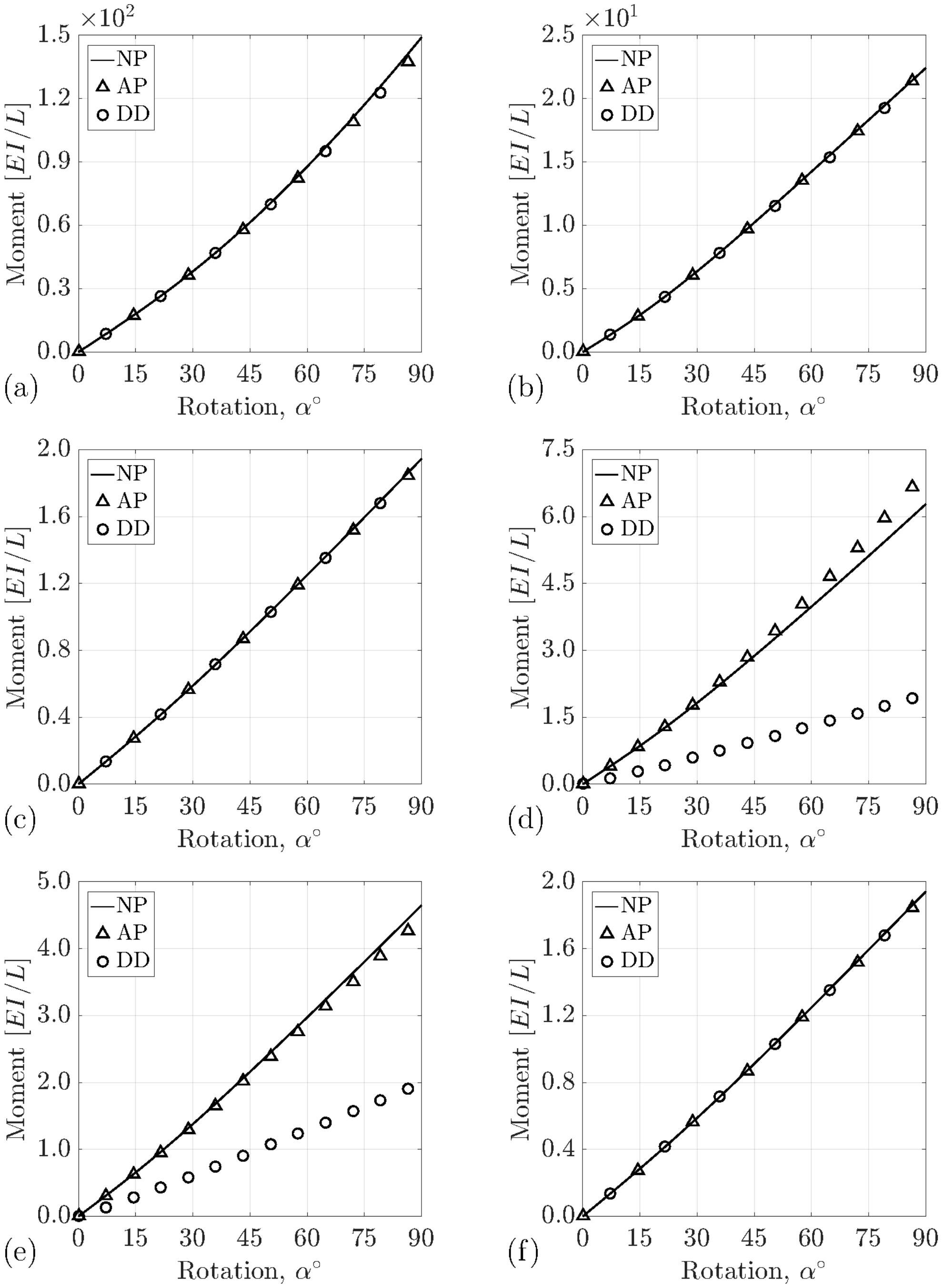

FIGURE 9.15: Cantilever bending test for the GOH material model – the corresponding bending moment vs. the applied rotation for the three constitutive approaches NP, AP and DD: (a-c) without and (d-f) with the compression/tension switch. Further, for (a) and (d) $\kappa_i = 0.0$, for (b) and (e) $\kappa_i = 0.226$ and for (c) and (f) $\kappa_i = 1/3$.

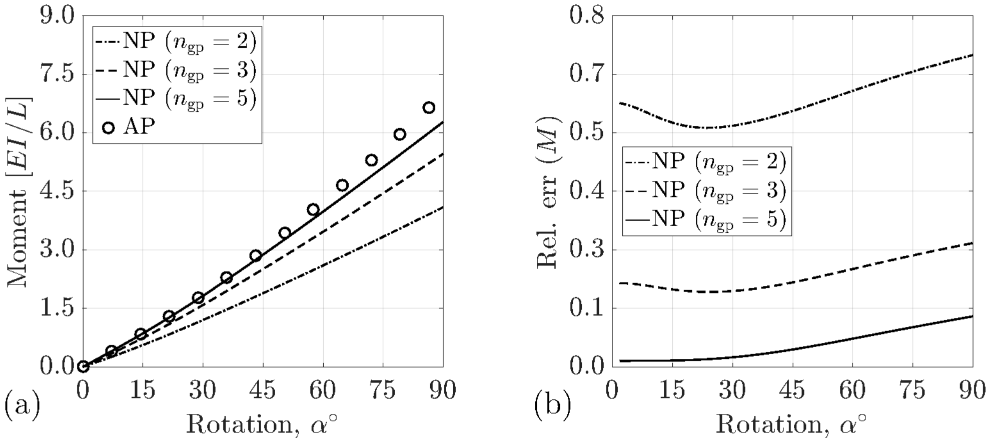

FIGURE 9.16: Cantilever bending test for the GOH material model (with $\kappa_i = 0.0$ and the compression/tension switch): The corresponding bending moment (a) and its error (b) vs. the applied rotation for the NP and AP shell model with different number of Gaussian quadrature points n_{gp} considered across the thickness.

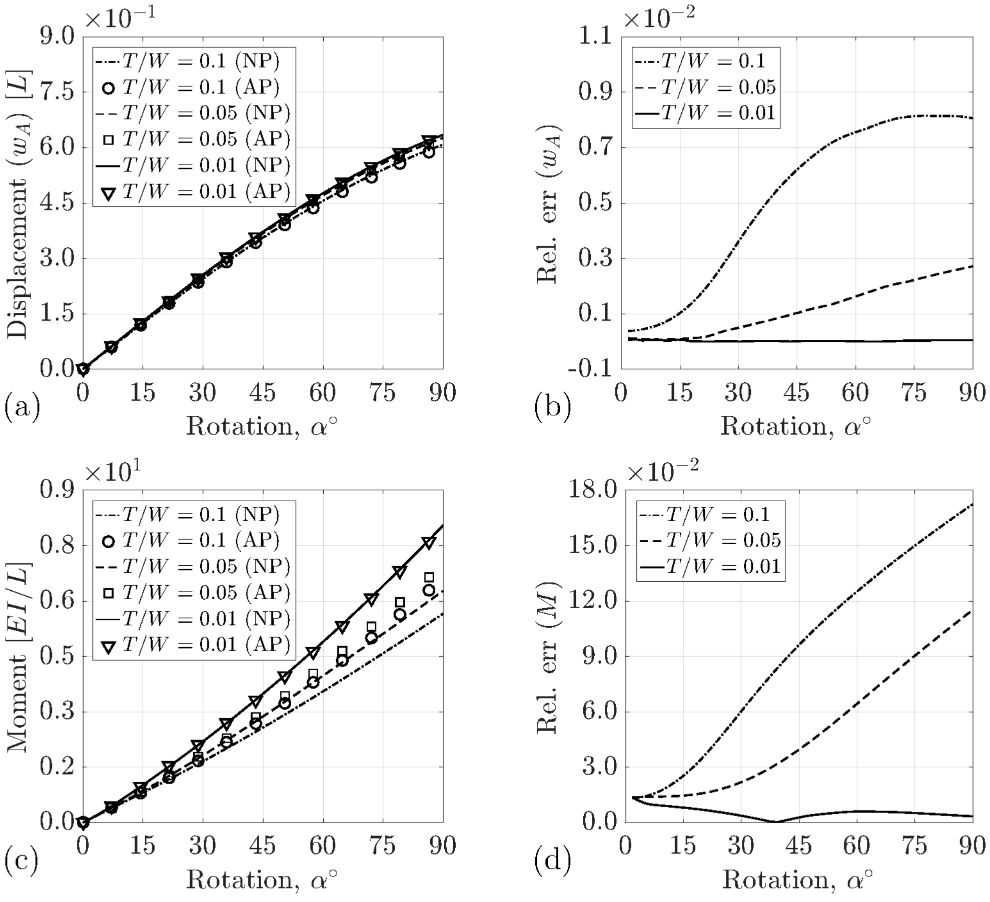

FIGURE 9.17: Cantilever bending test for the GOH material model (with $\kappa_i = 0.0$ and the compression/tension switch): Comparison of the NP and AP shell models with different thickness to width ratios (T/W).

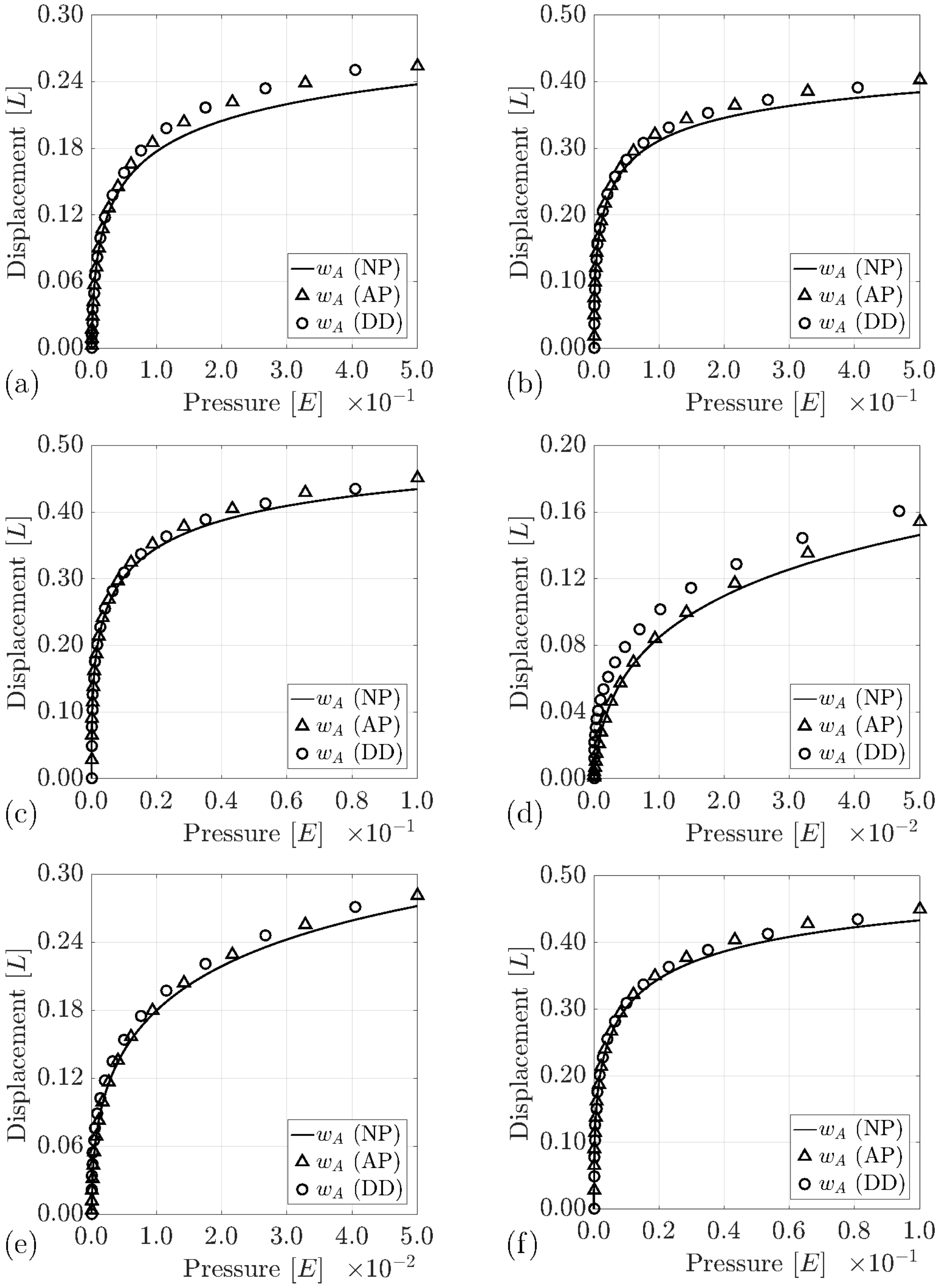

FIGURE 9.19: Clamped plate under pressure for the GOH material model – the displacement of the middle point vs. the applied pressure for the three constitutive approaches NP, AP and DD: (a-c) without and (d-f) with the compression/tension switch. Further, for (a) and (d) $\kappa_i = 0.0$, for (b) and (e) $\kappa_i = 0.226$ and for (c) and (f) $\kappa_i = 1/3$.

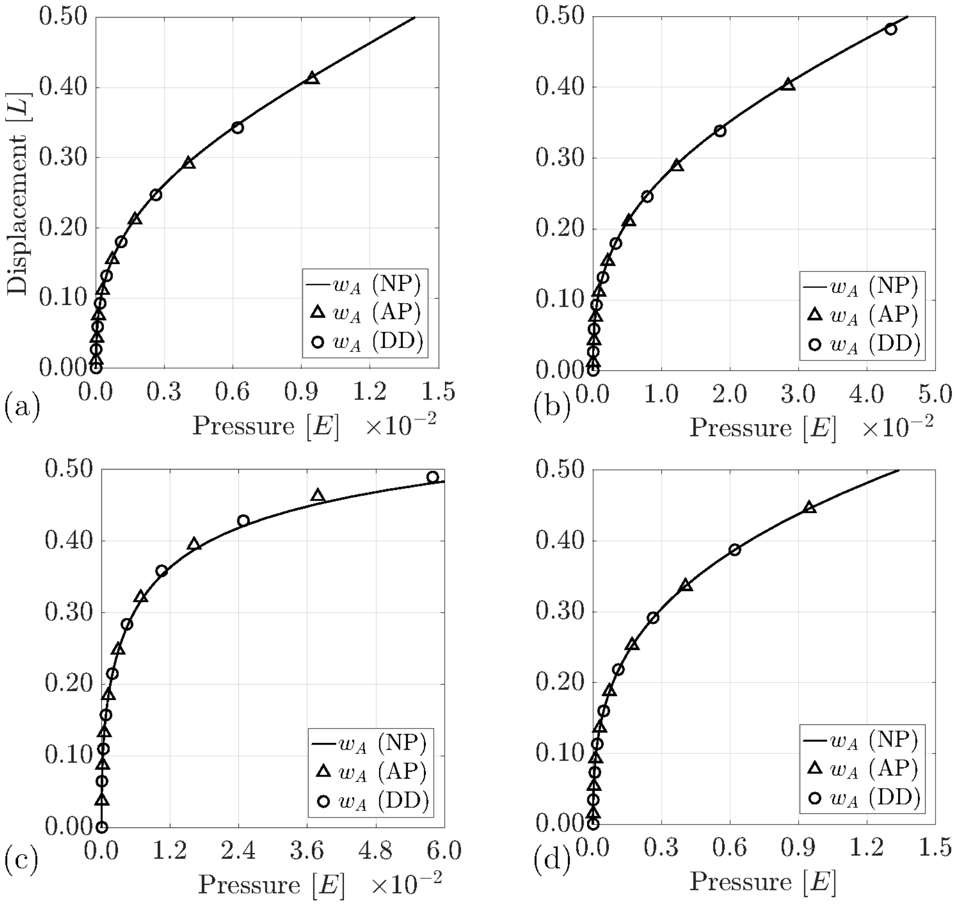

FIGURE 9.20: Clamped plate under pressure – the displacement of the middle point vs. the applied pressure: (a) NH, (b) MR, (c) Fung and (d) AMR material model for the three constitutive approaches (NP, AP and DD) presented in Sec. 4.3.2.

9.3 Thin laminated composite shell examples[19]

In this section, the examples of previous sections are examined for the laminated composite shell formulations of Chap. 5. For each laminate configuration (see Fig. 5.1), an example is presented. The first example is devoted to a symmetric laminate configuration. The second example evaluates a general laminate configuration, where the laminate layers have arbitrary geometrical and material properties. Finally, the last example simulates the pressurization of a laminated composite tube. For all the examples, an incompressible anisotropic Mooney–Rivlin material model (6.118) with two families of fibers is considered and the angle between two families of fibers is given by 2γ.

9.3.1 Cantilever bending

As shown in Fig. 9.21.a, a cantilever strip, with $L \times W \times T = 10 \times 3 \times 0.3$ [mm^3], is subjected to a distributed vertical force on its free end. The cantilever is meshed by 6×18 quadratic NURBS-based elements (see Fig. 9.21.b). It is assumed that the composite shell is composed of 5 symmetric layers laminated as shown in Fig. 5.1.b. The layers are distributed equally through the shell thickness T such that the thickness of each layer is $T/5$. The material properties vary layer-wise as listed in Table 9.2. The angle γ is measured w.r.t. the longitudinal direction.

Layer $\#i$	T_i $[T]$	$\tilde{c}_1$ [kPa]	$\tilde{c}_2$ [kPa]	$\tilde{c}_{3j}$ [kPa]	γ [deg]
1	0.1	30	120	600	±60
2	0.3	20	60	1000	±45
3	0.5	10	20	1000	±30

Table 9.2: Material properties of the laminated composite cantilever.

Fig. 9.21.b shows the deformed configuration colored by $I_1 := \operatorname{tr}\boldsymbol{C}$. As can be observed, I_1 slightly deviates from 2, which is the expected value for the case of pure bending. Further, there is transverse bending in the strip (like a saddle) due to the incompressibility of material. As shown in Fig. 9.21.c, both DD and NP shell models predict the same deflection for the cantilever tip. The total force applied on the cantilever tip is normalized by $E\,I/L^2$, where $E = 3\,\tilde{c}_1$ and $I = T\,W^3/12$ is the second moment of area of the cross section. For the numerically-projected shell model, 2 Gaussian quadrature points are used for each laminate. As compared in Fig. 9.21.d

---

[19] The examples of this section are taken from Roohbakhshan and Sauer (2016) with slight modification.

for different mesh sizes, the directly-decoupled shell model is numerically less expensive and more efficient than the numerically-projected shell model; nevertheless, it is restricted to symmetric layers.

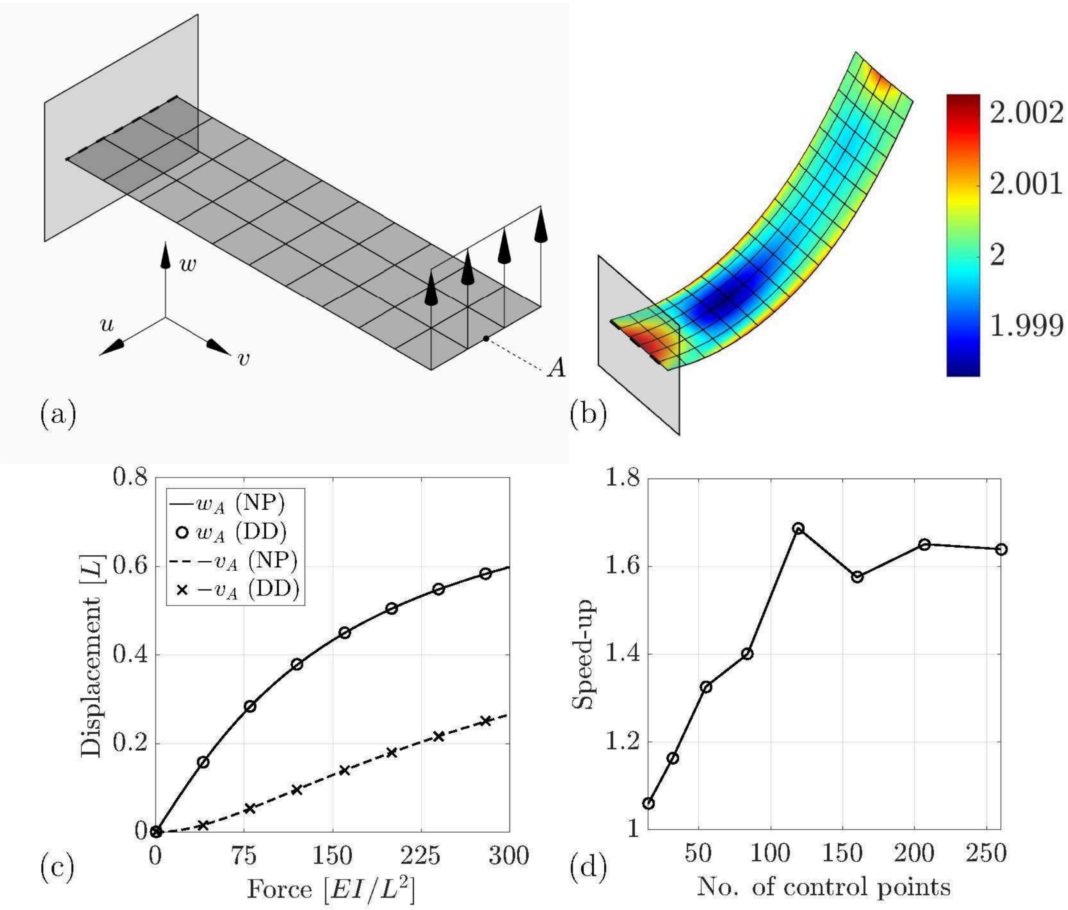

FIGURE 9.21: The bending of a laminated composite cantilever constructed from an *anisotropic* Mooney–Rivlin solid: (a) Undeformed configuration. (b) Deformed configuration colored by $I_1 := \operatorname{tr} \boldsymbol{C}$. (c) Displacement of the tip vs. the total applied force. (d) Speed-up of the DD shell model w.r.t. the NP shell model.

Further, the same experiment is performed with a cantilever constructed from an isotropic Mooney–Rivlin solid. Fig. 9.22 shows the bending of the same cantilever of Fig. 9.21.a for this case. The corresponding material parameters are extracted from Table 9.2, setting $\tilde{c}_{3j} = 0$. Like the anisotropic example, the directly-decoupled shell model is as accurate as the numerically-projected shell model.

9.3.2 Clamped plate

This example is designed to investigate the cases that both bending and membrane forces are dominant. Accordingly, a completely clamped square plate, with $L \times L \times T =$

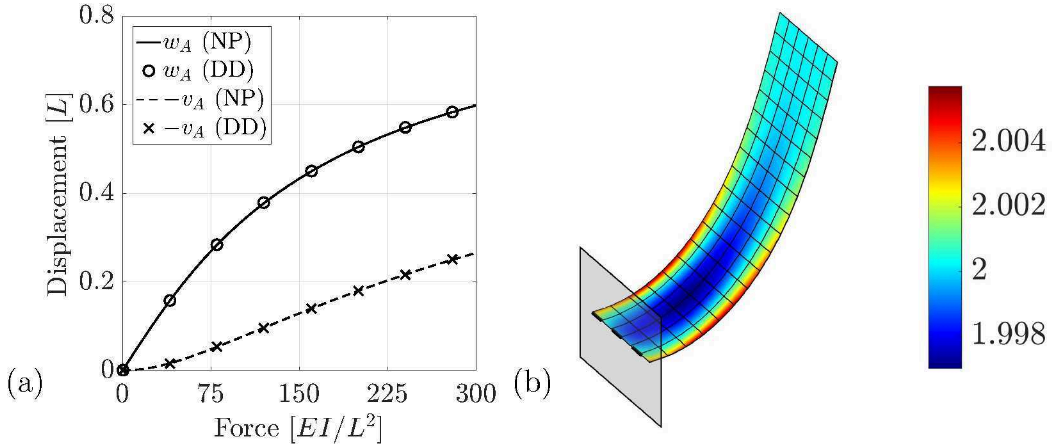

FIGURE 9.22: The bending of a laminated composite cantilever constructed from an *isotropic* Mooney–Rivlin solid: (a) Displacement of the tip vs. the total applied force. (b) Deformed configuration colored by $I_1 := \operatorname{tr} \boldsymbol{C}$.

$10 \times 10 \times 0.1$ [mm^3], is loaded by an external live pressure. The problem boundary conditions are similar to Fig. 9.20.a; therefore, only a quarter of plate is modeled due to the symmetry of the problem. The rotation is fixed along the symmetry and clamped boundaries according to the penalty formulation of Duong et al. (2017). The plate is meshed by 4×4 quadratic NURBS-based elements as shown in Fig. 9.23.a. The plate constitution is modeled by the incompressible anisotropic Mooney–Rivlin material model of Eq. (6.118). Now, the laminates are not symmetric w.r.t. the shell mid-surface (see Table 9.3). The orientation of fibers is defined by the angle γ measured w.r.t. the right symmetry edge (see Fig. 9.23.a). Here, the analytical and numerical projection approaches are compared. For the NP shell model, 2 Gaussian quadrature points are considered for each laminate layer. As shown in Figs. 9.23.c and 9.23.d, the results of AP and NP shell models are in excellent agreement.

Layer #i	T_i [T]	$\tilde{c}_1$ [kPa]	$\tilde{c}_2$ [kPa]	$\tilde{c}_{3j}$ [kPa]	γ [deg]
1	-0.35	20	60	200	±15
2	0.10	15	30	75	±30
3	0.20	30	30	60	±45
4	0.40	25	50	125	±60
5	0.50	10	20	100	±75

TABLE 9.3: Material properties of the laminated composite plate.

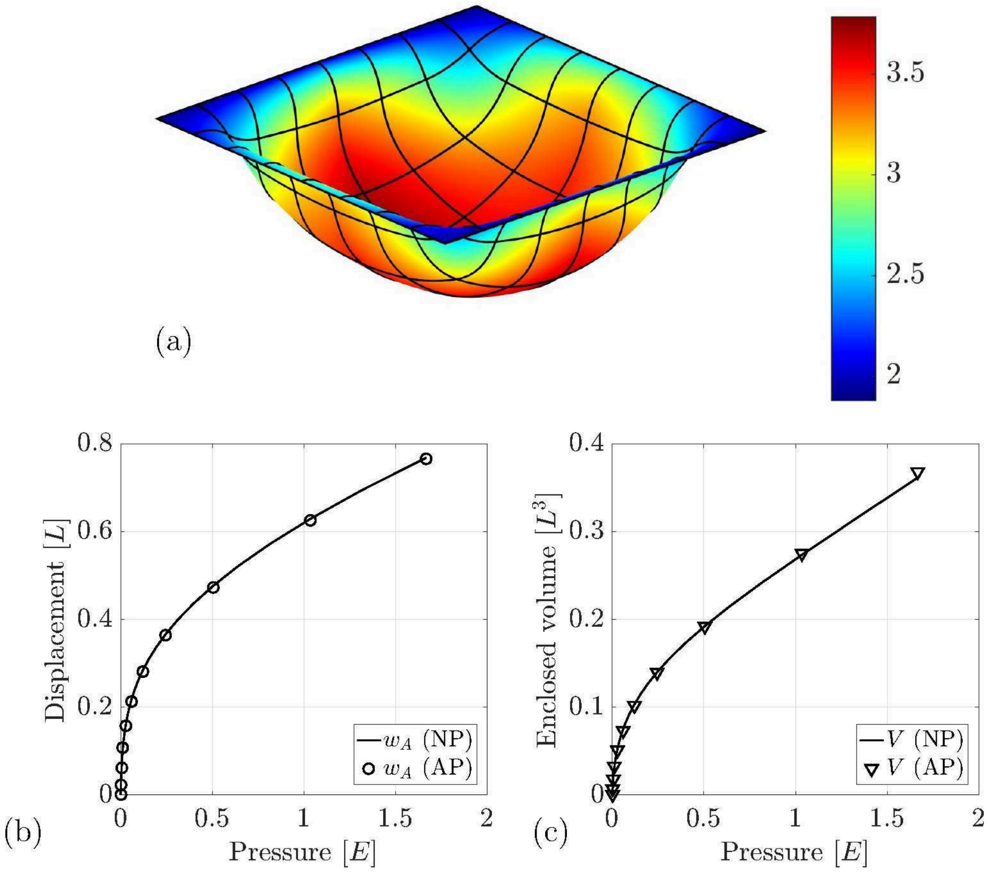

FIGURE 9.23: Pressurization of a laminated composite plate: (a) Deformed configuration colored by $I_1 := \operatorname{tr}\boldsymbol{C}$. (b) Displacement of the center point vs. the applied pressure. (c) Enclosed volume of plate vs. the applied pressure.

9.3.3 Inflation of a composite tube

As shown in Fig. 9.24, a laminated composite tube, with $L \times R \times T = 20 \times 5 \times 0.25$ [mm^3], is pressurized by the live pressure p_{ext}. It is assumed that the tube is constructed from 5 layers as listed in Table 9.3; however, here the fiber directions are measured w.r.t. the axial direction. As the problem is symmetric, only 1/8 of tube is modeled (see Fig. 9.24.a) and the symmetry boundary conditions are applied accordingly using the constraint of Duong et al. (2017). On the tube end, three different boundary conditions are considered: (1) Free end, (2) closed end, where the tensile traction $p_{\text{ext}}\,R/2\,T$ is applied along the axial direction, and (3) fixed end, where all the displacements are restricted. Furthermore, for the first two cases, the rotations on the tube end are fixed by the constraint of Duong et al. (2017).

As shown in Figs. 9.24.b-d, the circumferential stretch λ_θ and axial stretch λ_z of the tube are predicted identically by both the NP and AP shell models. The stretches

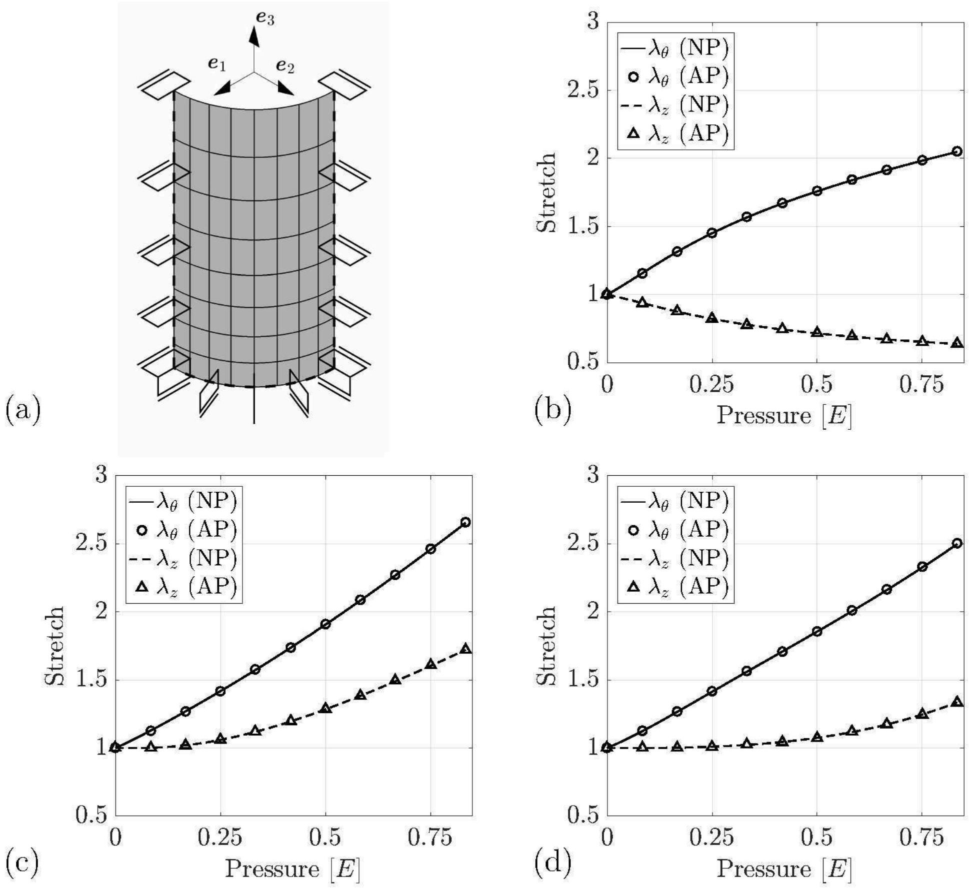

FIGURE 9.24: Inflation of a composite tube: (a) Undeformed configuration (quarter system). The symmetric boundaries are denoted by thick dashed lines. Circumferential stretch λ_θ and axial stretch λ_z of the tube with (b) free end, (c) traction on the end and (d) fixed end.

$\lambda_\bullet$ are calculated at the middle point A shown in Fig. 9.24.a. The applied pressure is normalized by $E = 3\,\tilde{c}_1$.

9.4 Contact problems

In this section two numerical experiments are performed to demonstrate how the presented formulation can simulate contact problems: Inflation of a tissue sheet, which involve contact between a rigid indenter and a deformable sheet, and the angioplasty example which includes contact between two deformable bodies. For both of the examples, the contact computations is based on an unbiased penalty formulation of Sauer and De Lorenzis (2015) and the contact constraint is enforced at the quadrature points of the isogeometric finite elements.

9.4.1 Indentation of a sheet[20]

In vitro and in silico indentation tests are widely used to empirically and numerically determine the mechanical characteristics of soft tissues (Zhang et al., 1997; Liu et al., 2004; Choi and Zheng, 2005; McKee et al., 2011; Lu et al., 2012). For instance, puncture testing has been applied frequently for the mechanical characterization of the human fetal membrane tissue (Bürzle et al., 2014).

Here, the indentation of a square sheet is simulated. The sheet has the same dimensions and material properties as the plate of Sec. 9.2.4. As shown in Figs. 9.25.a and 9.25.b, two types of boundary conditions are considered, i.e. the outer edges are either fixed or clamped. The sheet is pressed by an indenter with a rigid spherical cap (see Figs. 9.25.c and 9.25.d). The indenter radius is $R = L/6$, where L is the width of sheet. Here, the sheet is meshed by 6×6 quadratic NURBS-based elements. In the contact area, the mesh is finer. The size of the finest element is 1/4 of the coarsest one. The sheet constited of the GOH material model with the constants given in Tab. 9.1. Following Sauer and De Lorenzis (2015), the penalty parameter is set to $\epsilon = 10^8\,E\,T$, where $E = 3\,\tilde{\mu}$. Figs. 9.26 shows the sequence of simulation with different indentation depth.

In Fig. 9.27, the vertical component of the total contact force is plotted against the indentation depth for different indenter radius R. As expected, both the AP and NP shell models perform similarly.

---

[20] This example is taken from Roohbakhshan and Sauer (2017) with slight modification.

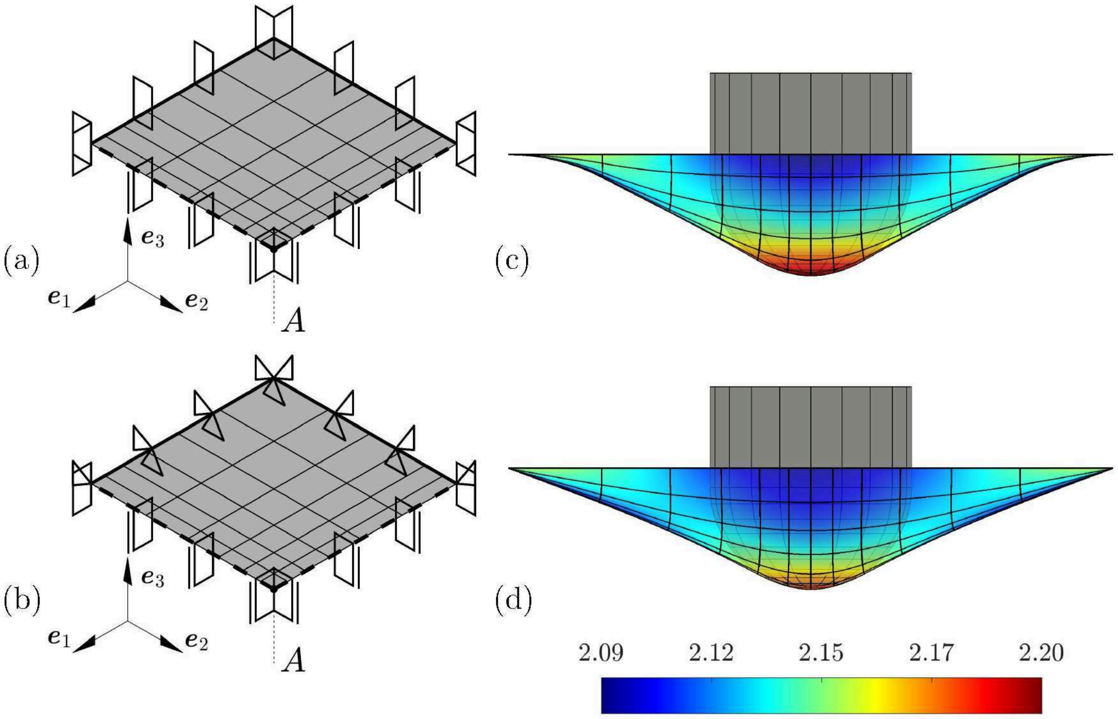

FIGURE 9.25: Indentation test: Reference configuration (quarter system) with (a) clamped and (b) fixed outer edges. Deformed configuration (full system) with (c) clamped and (d) fixed outer edges for the GOH model (with the compression/tension switch and $\kappa_i = 0.226$) colored by $I_1 := \operatorname{tr} \boldsymbol{C}$.

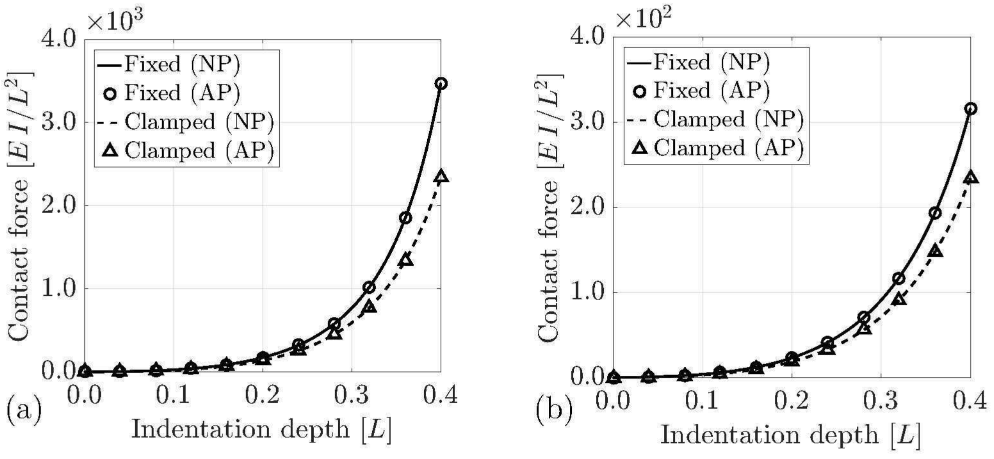

FIGURE 9.27: Indentation test – contact force vs. the indentation depth: GOH model with the compression/tension switch and (a) $\kappa_i = 0.226$ and (b) $\kappa_i = 1/3$.

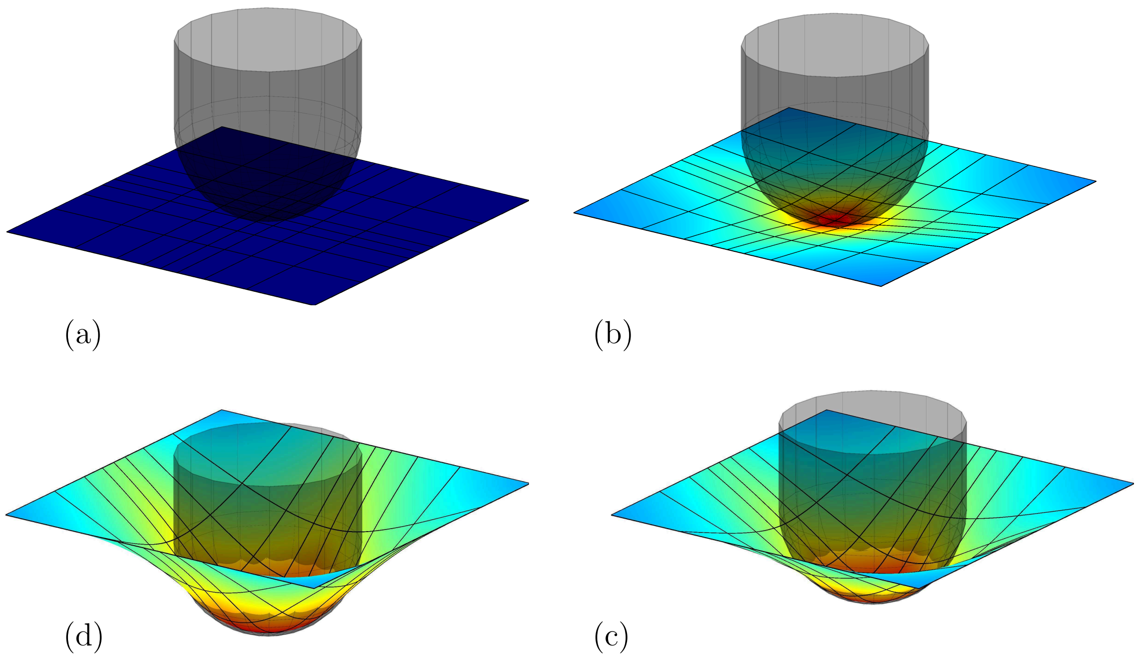

(a) (b)

(d) (c)

FIGURE 9.26: Indentation test – the sequence of the indentation process with indentation depth (a) 0, (b) $0.1\,L$, (c) $0.6\,L$ and (d) L.

9.4.2 Angioplasty[21]

Balloon angioplasty is the typical treatment to widen obstructed arteries or veins (Humphrey, 2013). This procedure has been studied computationally by many scholars (e.g. Holzapfel et al., 1996b; Rogers et al., 1999; Holzapfel et al., 2002b; Gasser and Holzapfel, 2007; Gervaso et al., 2008; Pant et al., 2012) in order to optimize the internal pressure, mechanical properties and location of the balloon. Here, the angioplasty is simulated as the contact between a deformable initially-spherical balloon, modeled by finite membrane elements, and a deformable artery, modeled as a tube discretized by finite shell elements. Both bodies are discretized by quadratic NURBS-based elements. To run the simulation, the volume of balloon is controlled. As shown in Fig. 9.28, it is assumed that an artery is constructed from three layers: Intima, media and adventitia. Further, for each of the three layers, the same material model of Sec. 6.3.2 is considered as the constitution with the parameters given in Tab. 9.4 (Schriefl et al., 2011). For all the artery examples, the compression/tension switch is included.

To simulate the angioplasty procedure, a portion of an artery with the dimensions $T_\mathrm{a}\times R_\mathrm{a}\times L = 1.35\times 5\times 30$ [mm^3] is inflated by a balloon with initial radius $R_\mathrm{b} = 0.9\,R_\mathrm{a}$ and thickness $T_\mathrm{b} = 0.1\,R_\mathrm{b}$. The balloon is initially pre-stretched by $\lambda_\mathrm{p} = 1.1$. Two

---

[21] The examples of this section are taken from Roohbakhshan and Sauer (2017), Roohbakhshan et al. (2017) and Roohbakhshan and Sauer (2018b) with slight modification.

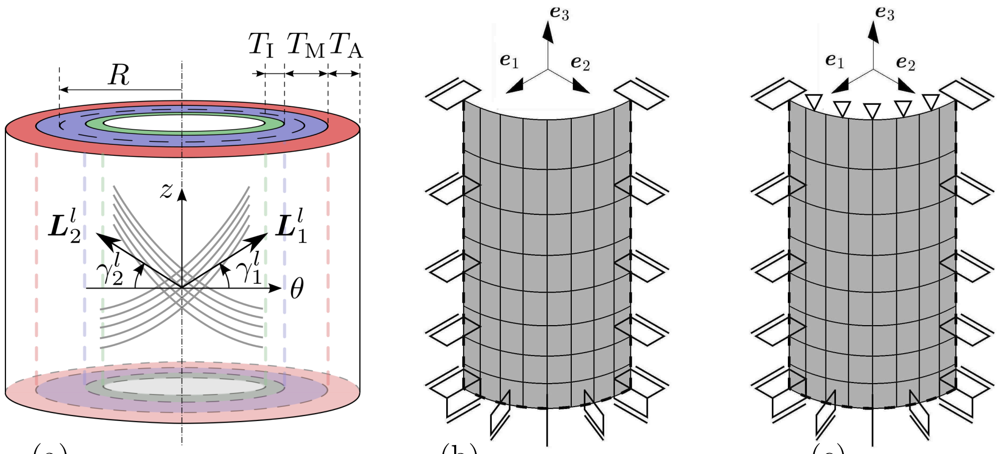

(a) (b) (c)

FIGURE 9.28: Artery model for angioplasty: a) Three layers of an artery: Intima, media and adventitia. Reference configuration (1/8 system) with boundary conditions for b) free end and c) axially restricted end.

Layer	T_i^l $[T]$	$\tilde{\mu}_l$ [kPa]	$\tilde{k}_{1i}^l$ [kPa]	k_{2i}^l	γ_i^l [deg]	κ_i^l
Intima	0.1	28	2×10^3	1000	±40	0.052
Media	0.57	1.3	0.5×10^3	50	±30	0.046
Adventitia	0.43	7.5	1×10^3	500	±50	0.055

TABLE 9.4: Material properties of the three-layer artery

families of fibers are considered with

$$\tilde{\boldsymbol{L}}_i^l = \cos\gamma_i^l \, \sin\psi \, \boldsymbol{e}_1 + \cos\gamma_i^l \, \cos\psi \, \boldsymbol{e}_2 + \sin\gamma_i^l \, \boldsymbol{e}_3, \quad (i = 1, 2) \ , \tag{9.6}$$

where γ_i^l are the corresponding angles for the two families of fibers on each layer (see Fig. 9.28.a). As the problem is symmetric, only 1/8 of the artery is modeled and the symmetry boundary conditions are applied to the corresponding edges. On the artery end, two different boundary conditions are considered for the examples considered here: Free ends and axially restricted end.

Now, the laminated composite shell formulation of Chap. 5 is used to model a three-layer artery consisting of intima, media and adventitia layers. First the artery with free end and then the artery with axially restricted end are investigated. Fig. 9.29 shows the deformed artery colored by the surface tension $\gamma := \frac{1}{2}\,\sigma^\alpha_\alpha$. On the left side, the surface stress of ground matrix, which is isotropic, is plotted. On the right side, the tension of the fibers is shown. As it can be observed, among the three layers, adventitia has the most contribution to the mechanical response.

Furthermore, the results of the laminated composite shell model are compared to the corresponding results of 3D solid elements in Fig. 9.30. Figs. 9.31-9.32 compare the stress field and strains predicted by the solid model (with 1252 degrees of freedom)

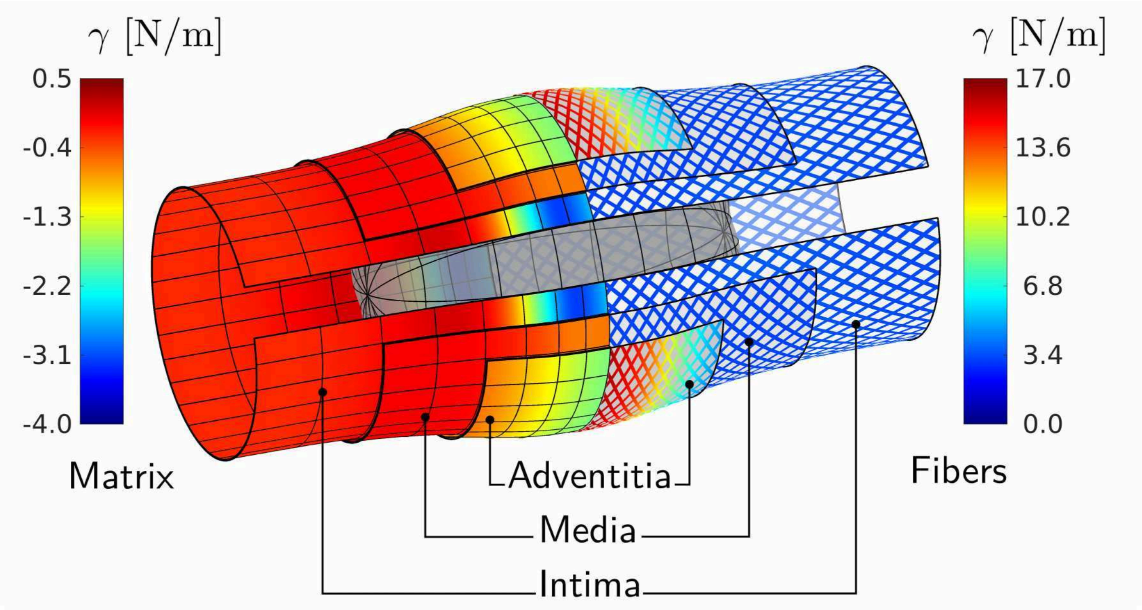

FIGURE 9.29: Balloon angioplasty for three-layer artery (Roohbakhshan et al., 2017).

and the shell model (with 409 degrees of freedom). The solid model is discretized fully isogeometric with quadratic B-splines (Corbett and Sauer, 2015; Corbett, 2016). Although the artery is relatively thick, the results of the presented shell formulation are close to 3D solid model.

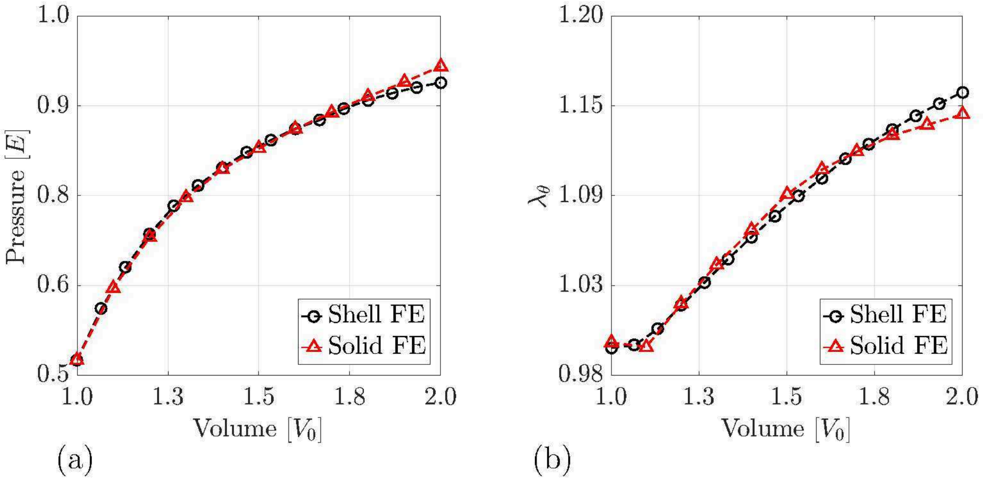

(a) (b)

FIGURE 9.30: Balloon angioplasty for three-layer artery – comparison with solid elements: (a) The internal pressure and (b) the average circumferential stretch, λ_θ, in the middle of the artery vs. the volume of the inflated balloon.

As shown before, among the three layers, adventitia has the most contribution to the mechanical behavior of the artery. Therefore, one can model an artery with a single adventitia layer and neglect the other layers (Gasser et al., 2006). Here the artery

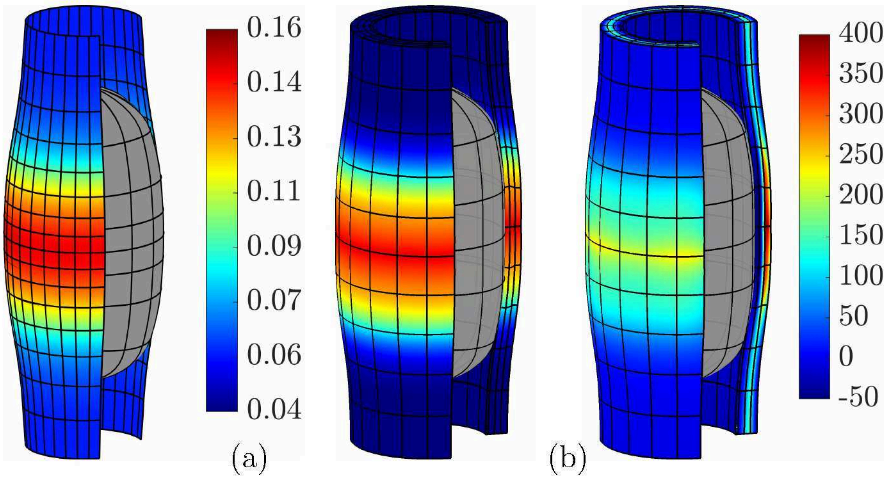

(a) (b)

FIGURE 9.31: Balloon angioplasty for three-layer artery – comparison of solid and shell elements: a) Deformed artery, modeled by the finite shell (left) and solid (right) elements, colored by the first invariant of the 2D projected stress tensor $I_\sigma = \text{tr}\,\boldsymbol{\sigma}$ [kPa]. b) Deformed artery, modeled by the finite solid elements, colored by the first invariant of the 3D stress tensor $I_{\tilde{\sigma}} = \text{tr}\,\tilde{\boldsymbol{\sigma}}$ [kPa] (Roohbakhshan and Sauer, 2018b).

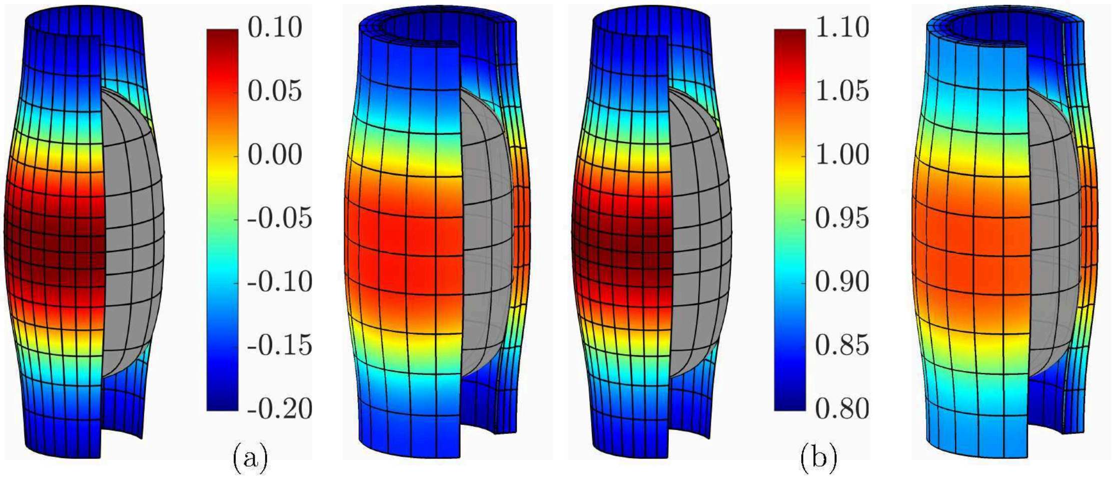

(a) (b)

FIGURE 9.32: Balloon angioplasty for three-layer artery – comparison of solid and shell elements: Deformed artery, modeled by the finite shell (left) and solid (right) elements, colored by the a) radial displacement (normalized by R) and b) circumferential stretch (Roohbakhshan and Sauer, 2018b).

dimensions are $T_\text{a} \times R_\text{a} \times L = 0.5 \times 5 \times 30$ [mm^3] and the artery is modeled by the GOH material model with $\kappa_i = 0$. The other material constants are taken from Tab. 9.1, which is similar to the properties of the adventitia of an artery (Gasser et al., 2006). For the adventitia, two families of fibers are considered with $\gamma_i \pm 45°$. The AP shell model is also used for the artery. Now, it is assumed that the artery ends are free following Fig. 9.28.b.

In Fig. 9.34.a the internal pressure of the balloon is plotted against its volume for

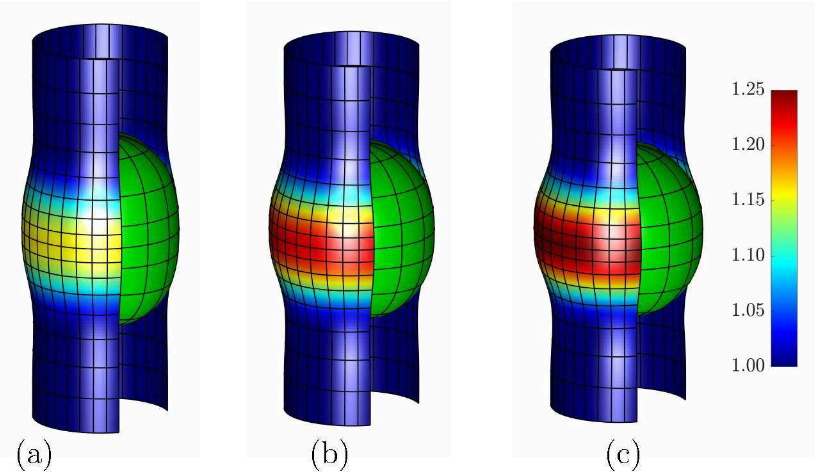

FIGURE 9.33: Balloon angioplasty for single layer artery: Deformed configuration colored by the circumferential stretch λ_θ for (a) $\tilde{\mu}_\mathrm{b} = 2\,\tilde{\mu}_\mathrm{a}$, (b) $\tilde{\mu}_\mathrm{b} = 10\,\tilde{\mu}_\mathrm{a}$ and (c) $\tilde{\mu}_\mathrm{b} = 20\,\tilde{\mu}_\mathrm{a}$ (Roohbakhshan and Sauer, 2017).

different values of $\tilde{\mu}_\mathrm{b}$. Fig. 9.34.b shows the average circumferential stretch, λ_θ, computed in the middle of the artery (see the circumferential dashed line in Fig. 9.33.a) against the volume of the inflated balloon. As expected, the results of the AP and NP shell models are very close even though the single-layer artery is also quite thick ($T/R = 0.1$).

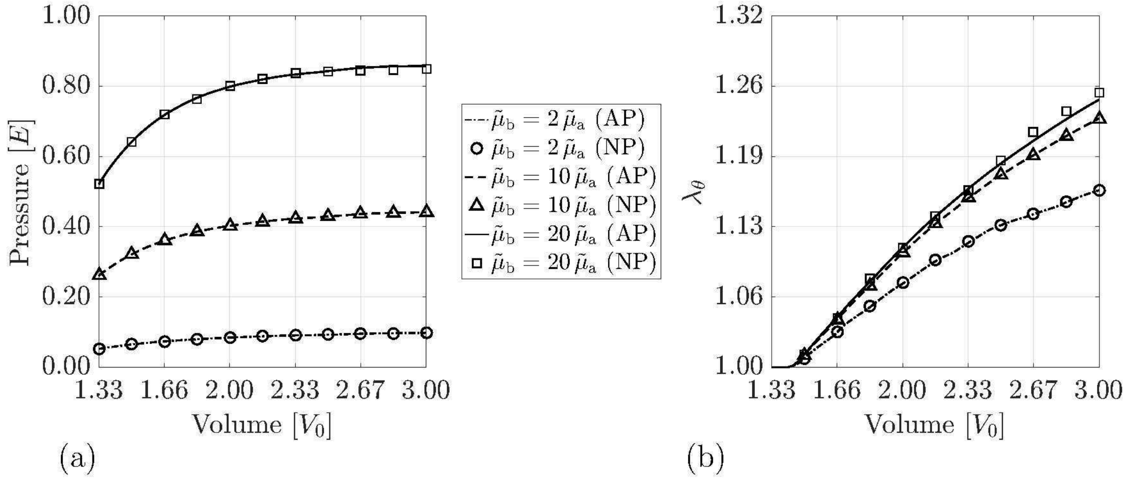

FIGURE 9.34: Balloon angioplasty for single layer artery: (a) The internal pressure and (b) the average circumferential stretch, λ_θ, in the middle of the artery vs. the volume of the inflated balloon.

9.5 Dynamic surface tesnion of the pulmonary surfactant

In this section, dynamic surface tension of the pulmonary surfactant is investigated following the dynamic models introduced in Chap. 7. First the expansion and compression of a liquid film is studied to investigate the behavior of the CR and AL models introduced in Secs. 7.2.1-7.2.2. Then, the application of the presented membrane formulation to the simulation of the alveolar tissue is shown, which is a very first step towards building a comprehensive model of lung parenchyma.

9.5.1 Liquid film expansion/compression[22]

In the *Langmuir–Wilhelmy balance*, a movable barrier controls the total area available for a thin film of interfacial molecules, and the surface tension is measured from the wetting force acting over the Wilhelmy plate. Similarly, here a thin liquid film is modeled by a $2\,L_0 \times L_0$ rectangular membrane, where L_0 is a length scale. The bulk effects are not considered and only the free surface is modeled. As shown in Fig. 9.35, three edges of the membrane are fixed as zero-displacement Dirichlet boundaries and the forth edge is controlled by a prescribed Dirichlet boundary condition $\bar{\boldsymbol{u}} = [\bar{u}_x,\ 0,\ 0]^{\mathrm{T}}$ that changes with time as

$$\bar{u}_x(t) = \Delta L\,\sin\big(2\,\pi\,t/T\big)\ , \tag{9.7}$$

where here $T = 3$ s and the loading amplitude is $\Delta L = 0.33\,L_0$.

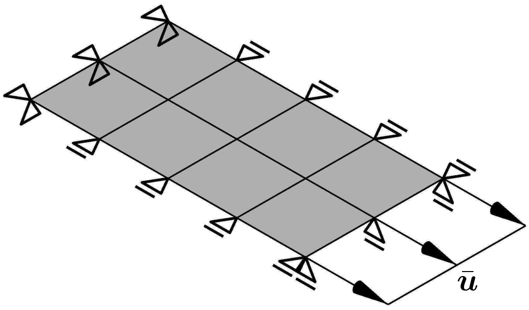

FIGURE 9.35: Liquid film expansion/compression: Computational model with boundary conditions. The thin film is a free surface without bulk.

In this example, the behavior of the surfactants monolayer is described by the CR model (see Sec. 7.2.1) and the AL model (see Sec. 7.2.2). The material constants are

---

[22] This example is taken from Roohbakhshan and Sauer (2018a) with slight modification.

set as listed in Tab. 9.6 following Wiechert (2011). For the CR model, following (Saad et al., 2010), two different concentrations of BLES in humid and dry conditions are considered. As already mentioned, the CR model requires elasticity of compression ϵ_c, elasticity of expansion ϵ_e, relaxation coefficient k_r, adsorption coefficient k_a, equilibrium surface tension γ_eq, which are adopted from Saad et al. (2010) as listed in Tab. 9.5. Further the minimum surface tension is set as $\gamma_\mathrm{min} = 2$[mN/m]. For the AL model, the material parameters are adopted from (Wiechert, 2011) as

	Content	Humidity	ϵ_c [mN/m]	ϵ_e [mN/m]	k_r [s^{-1}]	k_a [s^{-1}]	$\gamma_\mathrm{eq}{}^\star$ [mN/m]
1)	BLES 0.5 mg/ml	Humid	125.1	157.8	0.547	2.474	24
2)	BLES 0.5 mg/ml	Dry	112.7	120.0	0.001	2.783	22
3)	BLES 2.0 mg/ml	Humid	126.3	136.0	3.751	4.991	23
4)	BLES 2.0 mg/ml	Dry	123.1	129.9	0.006	0.712	23

* The values are estimated by the authors.

TABLE 9.5: Parameters of the CR model (Saad et al., 2010)

K_1 [s^{-1}]	k_2 [s^{-1}]	m_1 [mN/m]	m_2 [mN/m]	γ_min [mN/m]	γ_0 [mN/m]
1	0.016	48	140	10	70

TABLE 9.6: Parameters of the AL model (Wiechert, 2011)

Fig. 9.36 shows changes of the surface tension γ vs. the surface area change J.

In Fig. 9.37, the changes of surface tension γ and the normalized interfacial surfactants concentration of surfactants ϕ are plotted against the surface area change J with different values for the model parameters. As is expected, the presented finite element results are in agreement with the finite element results of Wiechert (2011).

It should be noted that a detailed comparison of two models is only possible when the parameters of each model is identified for the same experiment with the same type of surfactants, which is not considered in thus work. Here, the parameters are adopted from two different resources. Nevertheless, Saad et al. (2010) and Saad (2011) used both the AL and CR models to fit the experimental results of different BLES preparation evaluated in humid and dry air. The AL model can predict similar to experimental results for some of the cases. This drawback can be explained by the strict assumption of the AL model, where the surfactant cannot be adsorbed nor desorbed below the maximum equilibrium interfacial surfactant concentration Γ^*.

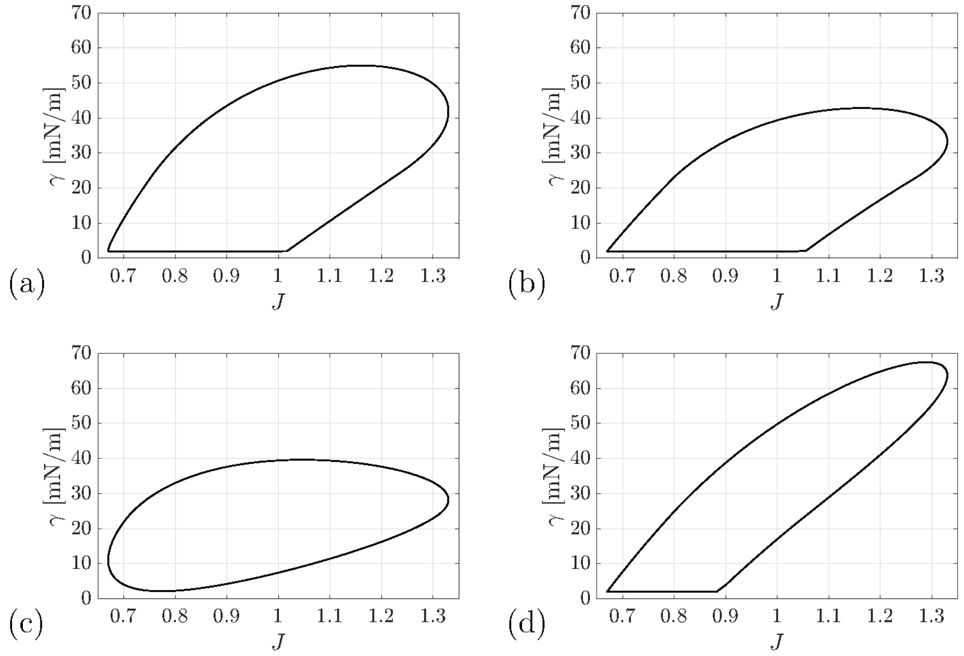

FIGURE 9.36: Liquid film expansion/compression (CR model): Change of the surface tension γ vs. the surface area change J. Figs. a-d correspond to the cases 1-4 in Tab. 9.5, respectively. The loop orientation is clockwise.

9.5.2 Alveolar tissue simulation

It is well know that the alveolar wall is covered with a liquid layer consisting of the pulmonary surfactants mainly (Goerke, 1998). Different approaches are proposed for the computational analysis of the alveolar tissue considering the interfacial effects (see e.g. Immel, 2016, for a concise review of the current approaches). Here, we approximate a single alveolus by a truncated octahedron, whose walls are modeled by composite membranes. The composite is constructed from a solid layer and a liquid layer following the formulation of Sec. 5.2.4. For the solid wall, the material model of Sec. 6.3.2 is used and the surfactant layer is modeled with the CR model of Sec. 7.2.1.

Truncated octahedron has been used for a long time, as a space-filling geometry to represent alveolar models. For instance, Karakaplan et al. (1980) propose an alveolar model discretized by triangular planar finite elements that combines the elastic properties of the alveolar wall and the surface tension of the pulmonary surfactants. In the same fashion, Kowe et al. (1986) add the triangular planar surface tension elements to the earlier model of Dale et al. (1980) who use elastic pin-joined bar elements to build a 3D alveolus model approximated by a truncated octahedron consisting of fibers only. The single alveolus model of Kowe et al. (1986) is extended by Denny and Schroter (1995, 1997) to an alveolar model constructed by an assembly of 36 truncated octahedra. Denny and Schroter (2000, 2006) modify the earlier work of Denny and Schroter

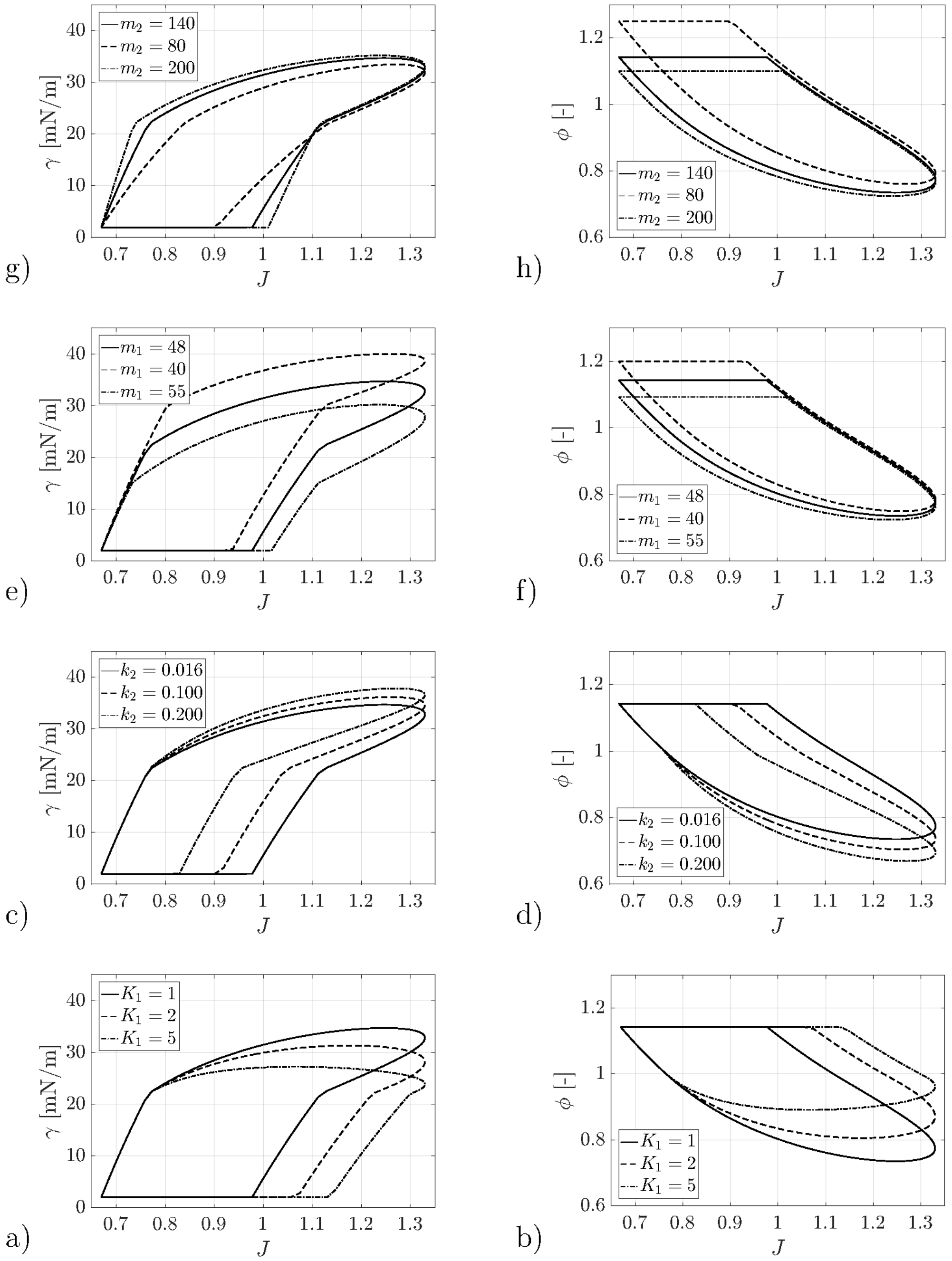

FIGURE 9.37: Liquid film expansion/compression (AL model): Influence of a-b) K_1, c-d) k_2, e-f) m_1 and g-h) m_2. Left: Surface tension γ vs. surface area change J and right: Normalized interfacial surfactants concentration ϕ vs. surface area change J. The loop orientation is clockwise.

(1995, 1997) by using the dynamic surface tension model of Otis et al. (1994) instead of the quasi-static exponential model of surface tension. Wiechert et al. (2009) and Wiechert (2011) also use the dynamic model of Otis et al. (1994) to add the interfacial energy of the surfactants layer to the surface of the alveolar wall modeled by finite solid elements.

Figs. 9.38.a-c shows the inflated alveoli at $V = 1.15\,V_0$. The hexagonal and square faces of each alveolus are meshed by 2 and 1 quadratic NURBS-based elements, respectively. The maximum distance between two opposite faces of the reference truncated octahedron is 60 μm. The thickness of the alveolar wall is assumed to be 8 μm. For the surfactant layer, the material parameters are set according to the case 1 in Tab. 9.5. As discussed by Alonso et al. (2004) and Hermans et al. (2015), in addition to the adsorption/desorption mechanisms, surface viscosity also contributes to the interfacial behavior of pulmonary surfactants. Thus, here the surface viscosity is taken as $\eta = 1$ mNs/m. For the solid membrane wall, the material constants are $\tilde{\mu} = 1$ kPa, $\tilde{k}_1 = 13.5$ kPa, $\tilde{k}_2 = 76.5$ and $\kappa = 1/3$ implies that the fiber distribution is isotropic. Further, the volume constraint formulation of Sauer et al. (2014) is used to control the volume, which is cyclically changed as

$$V(t) = V_0 + \Delta V_{\max} \sin\big(2\,\pi\,t/T\big)\ , \tag{9.8}$$

where $T = 1$ s and $V_{\max} = 0.15\,V_0$ here. Fig. 9.38.d shows the volume-pressure loop

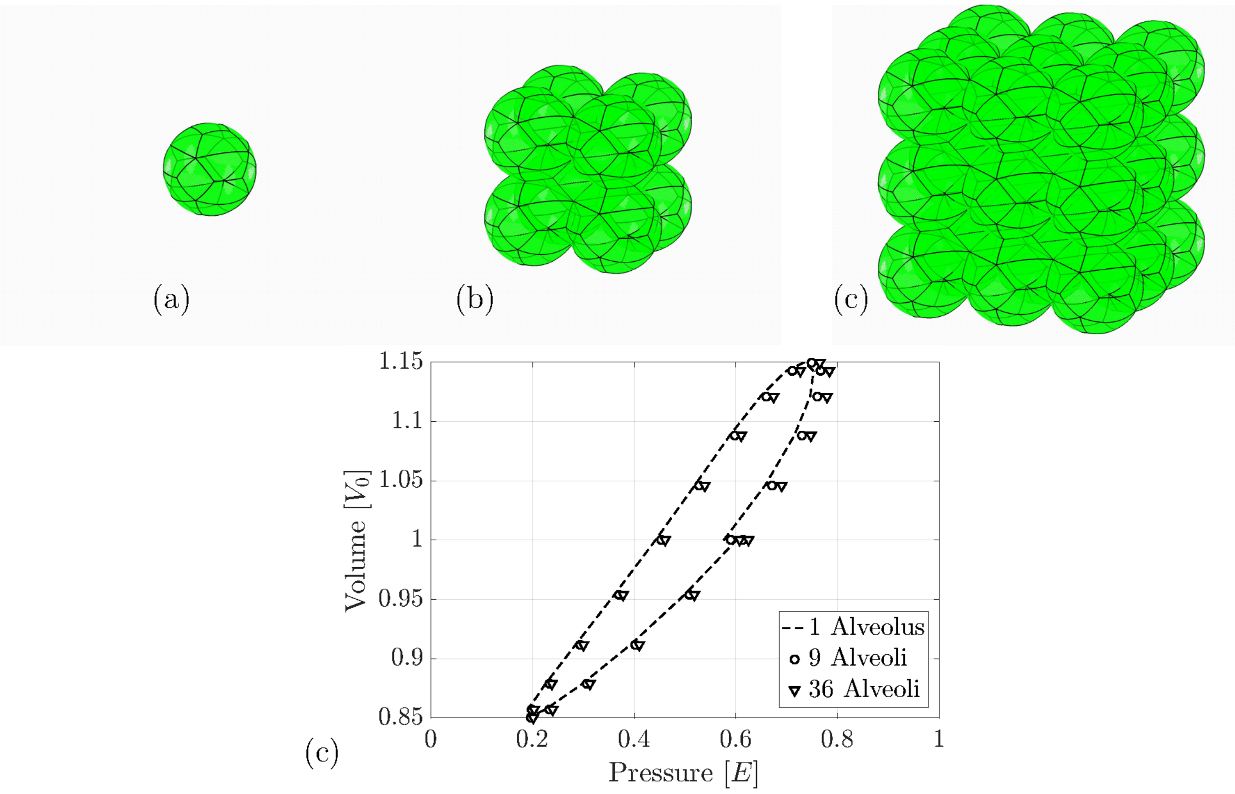
(a)
(b)
(c)
(c)

FIGURE 9.38: Alveolar tissue simulation: The inflated configurations for a) 1 alveolus, b) 9 alveoli and c) 35 alveoli. d) The corresponding volume-pressure curves. The loop orientation is counter-clockwise.

after 4 cycles. The pressure is normalized by a Young modulus defined as $E = 3\,\tilde{\mu}$. As expected, a hysteresis effect is observed due to the interracial properties of the surfactant layer. Being in agreement with the experiments, at a given volume, the required pressure for inflation is bigger than the corresponding one in deflation.

Chapter 10

Conclusion

This works presents different membrane and rotation-free shell formulations to model thin structures composed of soft biological materials. The formulation is designed for large deformations and allows for geometrical and material nonlinearities, which makes it very suitable for the modeling of soft tissues. The formulation is based on the Kirchhoff–Love hypothesis; thus, it needs only displacement degrees of freedom. This is the main benefit of the presented model as it considerably reduces the number of degrees of freedom compared to the usual 3D solid finite element discretization. As it is illustrated by various numerical examples, the membrane and shell models can accurately predict the material response with a much lower computational cost compared to the existing models. Following an isogeometric approach, NURBS-based finite elements are used for the FE discretization and the FE solution, which satisfies the necessary C^1-continuity of solution for rotation-free shells. However, for a membrane, where C^0-continuity is sufficient, Lagrange finite elements can also be used (Sauer et al., 2014 and Roohbakhshan et al., 2016).

Different approaches for constitutive projection of the existing 3D material models onto the surface of membranes and thin shells are presented. In addition to the membrane model, three different approaches to model thin shells are introduced: The *numerically-projected* (NP) shell model is the most general formulation, which allows any material nonlinearities. However, it is computationally more expensive since it uses numerical integration through the shell thickness. Furthermore, the *analytically-projected* (AP) and *directly-decoupled* (DD) shell models are developed, which do not need any numerical through-the-thickness integration. For anisotropic constitutive laws like the Gasser–Ogden–Holzapfel material model (Gasser et al., 2006), the NP shell model can be very expensive as one may need many quadrature points across the shell thickness to capture discontinuities of the stress across the thickness. Alternatively, the AP shell model, which is computationally more feasible, can be used. If the shell thickness is considerably smaller than the in-plane dimensions or the radii of curvature, for an initially-planar or an initially-curved shell, receptively, the NP and

AP shell models perform similarly. Furthermore, the DD shell model is presented, which is directly defined on a 2D manifold. This formulation assumes that the material properties and the constitutive law are symmetric w.r.t. the shell mid-surface. Apart from this restriction, the DD shell model is the most efficient approach.

It is generally assumed that collagen fibers bear no compressive force and they only contribute to tension. Therefore, they should be exclude from the mechanical response if being compressed. Accordingly, the exclusion of compressed fibers is considered for the presented membrane and shell models. As shown by different examples, the introduced compression/tension switch works very well for both the NP and AP shell models. The DD shell model, however, cannot capture the effect of the switch if the bending forces are dominant.

Moreover, the models are extended to the laminated composite shells following the equivalent single layer (ESL) theory. Beside the Kirchhoff–Love assumptions, it is assumed that: (1) the layers are perfectly bonded together, (2) each layer is of uniform thickness, (3) the material can have any desired nonlinear isotropic or anisotropic constitution and (4) the strains and deformations can be arbitrarily large. The presented shell models can be used to analyze any composite arrangement and material behavior of the layers,

The introduced membrane and shell models are specifically derived for different isotropic and anisotropic material models, which are commonly used for soft biological materials. For both the isotropic and anisotropic models, two types of strain energy density function are examined: Polynomial forms (i.e. Neo–Hooke, Mooney–Rivlin, and anisotropic Mooney–Rivlin material models) and exponential forms (i.e. Fung and Gasser–Ogden–Holzapfel material models). The procedure can be easily applied to other material models, which are not discussed here.

The robustness and accuracy of the presented shell models is demonstrated by different examples. Many benchmark tests for shell formulations are conducted. The membrane model is even compared successfully with the analytical solution. Further, different numerical examples are performed, which examine pure membrane, pure bending and mixed modes of the shell deformation. In particular, the formulation is applied to contact problems, i.e. the indentation of a sheet under a rigid spherical indenter and an angioplasty example that involves contact between two deformable bodies. The formulation is also used for the modeling of arteries, which are constructed from different layers and the liquid layer lining the lung alveolar tissue, where the interfacial forces are important.

Altogether, the presented formulations can be characterized by increased computational efficiency and algorithmic complexity. Accordingly, an appropriate formulation should be chosen specifically by a trade-off between efficiency and complexity depending on the application, structure and constituent.

The presented formulation can be improved in different aspects. For instance, many soft tissues have viscoelastic characteristics (Holzapfel et al., 2002a), which can be easily incorporated in the current formulation. Biological membranes are able to grow and adapt to the mechanical changes in the environment (Rausch and Kuhl, 2014). Therefore, the presented formulation can be modified to allow for the growth and remodeling of soft tissues. Further, residual stresses have a very important role in the mechanical response of many tissues, in particular, arterial wall mechanics (Ogden, 2003). Similar to Rausch and Kuhl (2013), the residual stresses and strains can also be included in our shell and membrane models. The current formulation assumes that the laminated layers are perfectly bonded. In the future, one can also account for delamination and inter-layer contact. Further, the model can be modified according to layer-wise and higher order shear deformation theories to analyze thicker shells or plates.

Appendix A

Variation and Linearization of Kinematical Variables

This appendix summarizes the variation of surface objects, such as metric and curvature tensor, and kinematical variables of a shell defined from a 3D perspective. Further, the 3D kinematical variables are linearized w.r.t. the through-the-thickness coordinate ξ as it is required for the AP shell model.

A.1 Variation of surface objects

Here, the variation of main surface variables are listed. For more details on derivation, see Sauer et al. (2014) and Sauer and Duong (2017). From Eq. (2.2), $\delta\boldsymbol{a}_\alpha = \delta\boldsymbol{x}_{,\alpha}$, which gives

$$\delta a_{\alpha\beta} = \delta\boldsymbol{a}_\alpha \cdot \boldsymbol{a}_\beta + \boldsymbol{a}_\alpha \cdot \delta\boldsymbol{a}_\beta \; . \tag{A.1}$$

The variation of the surface normal and curvature tensor are, respectively

$$\delta\boldsymbol{n} = -\big(\boldsymbol{a}^\alpha \otimes \boldsymbol{n}\big)\, \delta\boldsymbol{a}_\alpha \; , \tag{A.2}$$

$$\delta b_{\alpha\beta} = \big(\delta\boldsymbol{a}_{\alpha,\beta} - \Gamma^\gamma_{\alpha\beta}\delta\boldsymbol{a}_\gamma\big) \cdot \boldsymbol{n} \; , \tag{A.3}$$

where $\delta\boldsymbol{a}_{\alpha,\beta} = \delta\boldsymbol{x}_{,\alpha\beta}$.

As shown by Sauer et al. (2014) and Sauer and Duong (2017), $\delta a^{\alpha\beta} = a^{\alpha\beta\gamma\delta}\,\delta a_{\gamma\delta}$, where

$$a^{\alpha\beta\gamma\delta} := \frac{\partial a^{\alpha\beta}}{\partial a_{\gamma\delta}} = -\frac{1}{2}\left(a^{\alpha\gamma}a^{\beta\delta} + a^{\alpha\delta}a^{\beta\gamma}\right) \tag{A.4}$$

and $\delta b^{\alpha\beta} = b^{\alpha\beta\gamma\delta}\,\delta a_{\gamma\delta} - a^{\alpha\beta\gamma\delta}\,\delta b_{\gamma\delta}$, where

$$b^{\alpha\beta\gamma\delta} := \frac{\partial b^{\alpha\beta}}{\partial a_{\gamma\delta}} = 2H\left(a^{\alpha\beta}a^{\gamma\delta} + a^{\alpha\beta\gamma\delta}\right) - \left(a^{\alpha\beta}b^{\gamma\delta} + b^{\alpha\beta}a^{\gamma\delta}\right)\ . \tag{A.5}$$

Besides, $\delta a = a\, a^{\alpha\beta}\,\delta a_{\alpha\beta}$, which gives (Sauer et al., 2014)

$$\delta J = \frac{J}{2}\, a^{\alpha\beta}\,\delta a_{\alpha\beta}\ . \tag{A.6}$$

Further, the variation of the mean and Gaussian curvatures are

$$\begin{aligned} \delta H &= \frac{\partial H}{\partial a_{\alpha\beta}}\,\delta a_{\alpha\beta} + \frac{\partial H}{\partial b_{\alpha\beta}}\,\delta b_{\alpha\beta}\ , \\ \delta K &= \frac{\partial K}{\partial a_{\alpha\beta}}\,\delta a_{\alpha\beta} + \frac{\partial K}{\partial b_{\alpha\beta}}\,\delta b_{\alpha\beta}\ , \end{aligned} \tag{A.7}$$

with

$$\begin{aligned} \frac{\partial H}{\partial a_{\alpha\beta}} &= -\frac{1}{2}\, b^{\alpha\beta}\ , & \frac{\partial H}{\partial b_{\alpha\beta}} &= \frac{1}{2}\, a^{\alpha\beta}\ , \\ \frac{\partial K}{\partial a_{\alpha\beta}} &= -K\, b^{\alpha\beta}\ , & \frac{\partial K}{\partial b_{\alpha\beta}} &= \bar{b}^{\alpha\beta}\ . \end{aligned} \tag{A.8}$$

Here, the co-factor of curvature is defined as

$$\bar{b}^{\alpha\beta} := 2\, H\, a^{\alpha\beta} - b^{\alpha\beta}\ . \tag{A.9}$$

A.2 Variation of kinematic variables

Following the approach of Sauer and Duong (2017), Duong et al. (2017) and Roohbakhshan and Sauer (2017), the variation of 3D kinematic variables on $\overset{*}{\mathcal{S}}$ are expressed in terms of $\delta a_{\alpha\beta}$, which captures the stretching deformations, and $\delta b_{\alpha\beta}$, which captures the bending deformations. These variations are used in Chap. 4 to derive the stress and tangent tensors.

From Eq. (4.6), the variation of $g_{\alpha\beta}$ is

$$\delta g_{\alpha\beta} = \delta a_{\alpha\beta} - 2\,\xi\,\delta b_{\alpha\beta} \tag{A.10}$$

and since $[g^{\alpha\beta}] = [g_{\alpha\beta}]^{-1}$,

$$\delta g^{\alpha\beta} = g^{\alpha\beta\gamma\delta}\,\delta g_{\gamma\delta}\ , \tag{A.11}$$

with

$$g^{\alpha\beta\gamma\delta} := \frac{\partial g^{\alpha\beta}}{\partial g_{\gamma\delta}} = -\frac{1}{2}\left(g^{\alpha\gamma}g^{\beta\delta} + g^{\alpha\delta}g^{\beta\gamma}\right)\ . \tag{A.12}$$

Similar to the surface counterpart, it can be proven that

$$\delta \overset{*}{J} = \frac{\overset{*}{J}}{2}\, g^{\alpha\beta}\, \delta g_{\alpha\beta} \ . \tag{A.13}$$

The variation of the first invariant of the right Cauchy–Green tensor is

$$\delta \tilde{I}_1 = \delta I_1 + 2\,\lambda_3\,\delta\lambda_3 = \delta \overset{*}{I}_1 + 2\,\overset{*}{\lambda}_3\,\delta\overset{*}{\lambda}_3 \ , \tag{A.14}$$

where the in-plane components are

$$\begin{aligned} \delta I_1 &= A^{\alpha\beta}\,\delta a_{\alpha\beta} \ , \\ \delta \overset{*}{I}_1 &= G^{\alpha\beta}\,\delta g_{\alpha\beta} \ . \end{aligned} \tag{A.15}$$

Similarly, the variation of the other invariants can be found as

$$\begin{aligned} \delta \tilde{I}_2 &= \lambda_3^2\,\delta I_1 + 2J\,\delta J + 2\,I_1\,\lambda_3\,\delta\lambda_3 \ , \\ &= \overset{*}{\lambda}{}_3^2\,\delta\overset{*}{I}_1 + 2\overset{*}{J}\,\delta\overset{*}{J} + 2\,\overset{*}{I}_1\,\overset{*}{\lambda}_3\,\delta\overset{*}{\lambda}_3 \end{aligned} \tag{A.16}$$

and

$$\begin{aligned} \delta \tilde{I}_3 &= 2\,\lambda_3^2\,J\,\delta J + 2\,J^2\lambda_3\,\delta\lambda_3 \ , \\ &= 2\,\overset{*}{\lambda}{}_3^2\,\overset{*}{J}\,\delta\overset{*}{J} + 2\,\overset{*}{J}{}^2\,\overset{*}{\lambda}_3\,\delta\overset{*}{\lambda}_3 \ . \end{aligned} \tag{A.17}$$

A.3 Out-of-plane linearization of kinematic variables

In this section, on the shell mid-surface, the kinematical variables are linearized w.r.t. ξ. From Eq. (4.6), we have

$$g_{\alpha\beta,3} := \frac{\partial g_{\alpha\beta}}{\partial \xi} = -2\,b_{\alpha\beta} \ . \tag{A.18}$$

Combining Eqs. (A.11) and (A.18) gives

$$g^{\alpha\beta}_{,3} := \frac{\partial g^{\alpha\beta}}{\partial \xi} = -2\,g^{\alpha\beta\gamma\delta}\,b_{\gamma\delta} \ . \tag{A.19}$$

It can be shown that $g^{\alpha\beta\gamma\delta}\,b_{\gamma\delta} = -b^{\alpha\beta}$ if $\xi = 0$. Thus, on the shell mid-surface,

$$\hat{g}^{\alpha\beta}_{,3} := \left(g^{\alpha\beta}_{,3}\right)_{\xi=0} = 2\,b^{\alpha\beta} \ . \tag{A.20}$$

Similar quantities can be derived for $G_{\alpha\beta}$ and $G^{\alpha\beta}$ in the reference configuration. Plugging Eq. (A.18) into Eq. (A.13), we have

$$\overset{*}{J}_{,3} := \frac{\partial \overset{*}{J}}{\partial \xi} = \overset{*}{J} \left(G^{\alpha\beta}\, B_{\alpha\beta} - g^{\alpha\beta}\, b_{\alpha\beta} \right) \ , \tag{A.21}$$

which gives

$$\hat{J}_{,3} := \left(\overset{*}{J}_{,3} \right)_{\xi=0} = 2\, J \, (H_0 - H) \tag{A.22}$$

on the shell mid-surface. In a similar fashion, the first invariant of the right Cauchy–Green tensor is linearized as

$$\hat{I}_{1,3} := \left(\frac{\partial \overset{*}{I}_1}{\partial \xi} \right)_{\xi=0} = 2 \left(a_{\alpha\beta}\, B^{\alpha\beta} - b_{\alpha\beta}\, A^{\alpha\beta} \right) \ . \tag{A.23}$$

The Green–Lagrange strain tensor can also be linearized across the shell thickness. From Eq. (4.58)

$$\overset{*}{E}_{\alpha\beta,3} = \frac{1}{2} \left(g_{\alpha\beta,3} - G_{\alpha\beta,3} \right) \ ; \tag{A.24}$$

therefore,

$$\hat{E}_{\alpha\beta} := \left(\overset{*}{E}_{\alpha\beta,3} \right)_{\xi=0} = B_{\alpha\beta} - b_{\alpha\beta} = -K_{\alpha\beta} \ . \tag{A.25}$$

Further, from Eq. (6.33),

$$\overset{*}{E}{}^{\alpha\beta}_{,3} = \overset{*}{E}_{\gamma\delta,3}\, G^{\alpha\gamma}\, G^{\beta\delta} + \overset{*}{E}_{\gamma\delta}\, G^{\alpha\gamma}_{,3}\, G^{\beta\delta} + \overset{*}{E}_{\gamma\delta}\, G^{\alpha\gamma}\, G^{\beta\delta}_{,3} \ . \tag{A.26}$$

Thus, plugging Eqs. (A.25) and (A.20) into Eq. (A.26), at $\xi = 0$ we get

$$\begin{aligned} \hat{E}^{\alpha\beta}_{,3} := \left(\overset{*}{E}{}^{\alpha\beta}_{,3} \right)_{\xi=0} &= \hat{E}_{\gamma\delta,3}\, A^{\alpha\gamma}\, A^{\beta\delta} + 2\, E_{\gamma\delta}\, B^{\alpha\gamma}\, A^{\beta\delta} + 2\, E_{\gamma\delta}\, A^{\alpha\gamma}\, B^{\beta\delta} \\ &= -K^{\alpha\beta} + 2\, E_{\gamma\delta} \Big(B^{\alpha\gamma}\, A^{\beta\delta} + A^{\alpha\gamma}\, B^{\beta\delta} \Big) \ . \end{aligned} \tag{A.27}$$

From Eq. (6.30), one can obtain

$$\left(\frac{\partial \mathrm{tr}\, \overset{*}{\boldsymbol{E}}}{\partial \xi} \right)_{\xi=0} = 2\, B^{\alpha\beta}\, E_{\alpha\beta} - A^{\alpha\beta}\, K_{\alpha\beta} = -\mathrm{tr}\, \boldsymbol{K} + 2\, B^{\alpha\beta}\, E_{\alpha\beta} \ . \tag{A.28}$$

A.4 First-order compression/tension switch for fibers

For the principal directions of anisotropic materials, it can be shown that

$$\hat{L}^{\alpha\beta}_{i,3} := \left(\frac{\partial \overset{*}{L}{}^{\alpha\beta}_{i}}{\partial \xi} \right)_{\xi=0} = 2\, L^{\alpha}_{i}\, L^{\beta}_{i,3} \ , \tag{A.29}$$

where $L^{\alpha}_{i,3} := B^{\alpha\beta}\, L^{i}_{\beta}$ and $L^{i}_{\alpha} := \boldsymbol{L}_i \cdot \boldsymbol{A}_{\alpha}$. Thus, on the mid-surface, we have

$$\hat{I}^{i}_{4,3} := \Big(\frac{\partial \overset{*}{I}{}^{i}_{4}}{\partial \xi}\Big)_{\xi=0} = -2\, b_{\alpha\beta}\, L^{\alpha\beta}_{i} + a_{\alpha\beta}\, \hat{L}^{\alpha\beta}_{i,3}\ . \tag{A.30}$$

Using a first order Taylor expansion, on a shell layer at ξ, $\overset{*}{I}{}^{i}_{4}$ can be related to the similar quantity I^{i}_{4} on the mid-surface as

$$\overset{*}{I}{}^{i}_{4} = I^{i}_{4} + \xi\, \hat{I}^{i}_{4,3}\ , \tag{A.31}$$

which gives $\xi^{i}_{0} = \xi^{i}_{0}(\boldsymbol{x})$, where $\tilde{I}^{i}_{4} = \overset{*}{I}{}^{i}_{4} = 1$[23], as

$$\xi^{i}_{0} := \frac{1 - I^{i}_{4}}{\hat{I}^{i}_{4,3}}\ . \tag{A.32}$$

Then, T^{i}_{1} and T^{i}_{2} are defined according to the algorithm shown in Tab. A.1.

	$\xi_0 < -\dfrac{T}{2}$	$-\dfrac{T}{2} \le \xi_0 \le \dfrac{T}{2}$	$\dfrac{T}{2} < \xi_0$
$\hat{I}^{i}_{4,3} > 0$	$T^{i}_{1} = -\dfrac{T}{2},\ T^{i}_{2} = \dfrac{T}{2}$	$T^{i}_{1} = \xi^{i}_{0},\ T^{i}_{2} = \dfrac{T}{2}$	N.A.
$\hat{I}^{i}_{4,3} < 0$	N.A.	$T^{i}_{1} = -\dfrac{T}{2},\ T^{i}_{2} = \xi^{i}_{0}$	$T^{i}_{1} = -\dfrac{T}{2},\ T^{i}_{2} = \dfrac{T}{2}$

	$I^{i}_{4} > 1$	$I^{i}_{4} \le 1$
$\hat{I}^{i}_{4,3} = 0$	$T^{i}_{1} = -\dfrac{T}{2},\ T^{i}_{2} = \dfrac{T}{2}$	N.A.

TABLE A.1: Algorithm to find $[T^{i}_{1}, T^{i}_{2}]$, where $\tilde{I}^{i}_{4} > 1$.

Furthermore, for the material tangents of Sec. 4.3.2.2.2, one needs to linearize T^{i}_{1} and T^{i}_{2} as

$$\begin{aligned} U^{\alpha\beta}_{1i} &:= \frac{\partial T^{i}_{1}}{\partial a_{\alpha\beta}}\ , \qquad & U^{\alpha\beta}_{2i} &:= \frac{\partial T^{i}_{2}}{\partial a_{\alpha\beta}}\ , \\ V^{\alpha\beta}_{1i} &:= \frac{\partial T^{i}_{1}}{\partial b_{\alpha\beta}}\ , \qquad & V^{\alpha\beta}_{2i} &:= \frac{\partial T^{i}_{2}}{\partial b_{\alpha\beta}}\ , \end{aligned} \tag{A.33}$$

---

[23] Here, it is assumed that $\overset{*}{L}{}^{33}_{i} = L^{33}_{i} = 0$ (see Remark 6.5)

which depend on

$$
\begin{aligned}
Y_i^{\alpha\beta} &:= \frac{\partial \xi_0^i}{\partial a_{\alpha\beta}} = -\left(\hat{I}_{4,3}^i\right)^{-2} \left[\hat{I}_{4,3}^i \, L_i^{\alpha\beta} + (1 - I_4^i) \, \hat{L}_{i,3}^{\alpha\beta}\right] \, , \\
Z_i^{\alpha\beta} &:= \frac{\partial \xi_0^i}{\partial b_{\alpha\beta}} = 2 \left(\hat{I}_{4,3}^i\right)^{-2} (1 - I_4^i) \, L_i^{\alpha\beta}
\end{aligned}
\tag{A.34}
$$

as shown in Tab. A.2.

	$\xi_0 < -\frac{T}{2}$	$-\frac{T}{2} \leq \xi_0 \leq \frac{T}{2}$	$\frac{T}{2} < \xi_0$
$\hat{I}_{4,3}^i > 0$	$U_{1i}^{\alpha\beta} = V_{1i}^{\alpha\beta} = 0$ $U_{2i}^{\alpha\beta} = V_{2i}^{\alpha\beta} = 0$	$U_{1i}^{\alpha\beta} = Y_i^{\alpha\beta}$, $V_{1i}^{\alpha\beta} = Z_i^{\alpha\beta}$ $U_{2i}^{\alpha\beta} = V_{2i}^{\alpha\beta} = 0$	N.A.
$\hat{I}_{4,3}^i < 0$	N.A.	$U_{1i}^{\alpha\beta} = V_{1i}^{\alpha\beta} = 0$ $U_{2i}^{\alpha\beta} = Y_i^{\alpha\beta}$, $V_{2i}^{\alpha\beta} = Z_i^{\alpha\beta}$	$U_{1i} = V_{1i} = 0$ $U_{2i}^{\alpha\beta} = V_{2i}^{\alpha\beta} = 0$

	$I_4^i > 1$	$I_4^i \leq 1$
$\hat{I}_{4,3}^i = 0$	$U_{1i}^{\alpha\beta} = V_{1i}^{\alpha\beta} = U_{2i}^{\alpha\beta} = V_{2i}^{\alpha\beta} = 0$	N.A.

Table A.2: Algorithm to linearize T_1^i and T_2^i.

Appendix B

FE Force Vectors and Tangents

Here, the FE force vector and tangent matrices are summarized. For more details on derivation and efficient implementation see Sauer et al. (2014) and Duong et al. (2017).

B.1 FE force vectors

Plugging Eqs. (8.17) and (8.18) into Eq. (8.20), we get

$$\mathbf{f}^e_{\mathrm{int}} = \mathbf{f}^e_{\mathrm{int}\tau} + \mathbf{f}^e_{\mathrm{int}M} \ , \tag{B.1}$$

where the contribution of the membrane stress $\tau^{\alpha\beta}$ and the bending moment $M_0^{\alpha\beta}$ are, respectively

$$\mathbf{f}^e_{\mathrm{int}\tau} := \int_{\Omega_0^e} \tau^{\alpha\beta}\, \mathbf{N}^{\mathrm{T}}_{,\alpha}\, \boldsymbol{a}_\beta \, \mathrm{d}A \tag{B.2}$$

and

$$\mathbf{f}^e_{\mathrm{int}M} := \int_{\Omega_0^e} M_0^{\alpha\beta}\, \mathbf{N}^{\mathrm{T}}_{;\alpha\beta}\, \boldsymbol{n} \, \mathrm{d}A \ . \tag{B.3}$$

Here the symmetry of $\tau^{\alpha\beta}$ has been exploited.

Considering a dead loading of $\boldsymbol{f}$, i.e. $\boldsymbol{f} = \boldsymbol{f}_0/J + p\mathrm{ext}\,\boldsymbol{n}$, the external virtual work follows as (Sauer et al., 2014; Sauer and Duong, 2017)

$$G^e_{\mathrm{ext}} = \delta\mathbf{x}^{\mathrm{T}}_e \left(\mathbf{f}^e_{\mathrm{ext}0} + \mathbf{f}^e_{\mathrm{ext}p} + \mathbf{f}^e_{\mathrm{ext}t} + \mathbf{f}^e_{\mathrm{ext}m} \right) \ , \tag{B.4}$$

where the external FE force vectors are

$$\begin{aligned} \mathbf{f}^e_{\mathrm{ext}0} &:= \int_{\Omega^e_0} \mathbf{N}^{\mathrm{T}}\, \boldsymbol{f}_0 \, \mathrm{d}A \ , \\ \mathbf{f}^e_{\mathrm{ext}p} &:= \int_{\Omega^e} \mathbf{N}^{\mathrm{T}}\, p\, \boldsymbol{n} \, \mathrm{d}a \ , \\ \mathbf{f}^e_{\mathrm{ext}t} &:= \int_{\partial_t \Omega^e} \mathbf{N}^{\mathrm{T}}\, \boldsymbol{t} \, \mathrm{d}s \ , \\ \mathbf{f}^e_{\mathrm{ext}m} &:= -\int_{\partial_m \Omega^e} \mathbf{N}^{\mathrm{T}}_{,\alpha}\, \nu^\alpha\, m_\tau\, \boldsymbol{n} \, \mathrm{d}s \ . \end{aligned} \tag{B.5}$$

B.2 FE tangent matrices

The linearization of G^e_{int} yields (Duong et al., 2017)

$$\Delta G^e_{\mathrm{int}} = \delta \mathbf{x}^{\mathrm{T}}_e \left(\mathbf{k}^e_{\tau\tau} + \mathbf{k}^e_{\tau M} + \mathbf{k}^e_{M\tau} + \mathbf{k}^e_{MM} + \mathbf{k}^e_{\tau} + \mathbf{k}^e_{M} \right) \Delta \mathbf{x}_e \ , \tag{B.6}$$

with the material stiffness matrices

$$\begin{aligned} \mathbf{k}^e_{\tau\tau} &:= \int_{\Omega^e_0} c^{\alpha\beta\gamma\delta}\, \mathbf{N}^{\mathrm{T}}_{,\alpha} \left(\boldsymbol{a}_\beta \otimes \boldsymbol{a}_\gamma \right) \mathbf{N}_{,\delta} \, \mathrm{d}A \ , \\ \mathbf{k}^e_{\tau M} &:= \int_{\Omega^e_0} d^{\alpha\beta\gamma\delta}\, \mathbf{N}^{\mathrm{T}}_{,\alpha} \left(\boldsymbol{a}_\beta \otimes \boldsymbol{n} \right) \mathbf{N}_{;\gamma\delta} \, \mathrm{d}A \ , \\ \mathbf{k}^e_{M\tau} &:= \int_{\Omega^e_0} e^{\alpha\beta\gamma\delta}\, \mathbf{N}^{\mathrm{T}}_{;\alpha\beta} (\boldsymbol{n} \otimes \boldsymbol{a}_\gamma) \, \mathbf{N}_{,\delta} \, \mathrm{d}A \ , \\ \mathbf{k}^e_{MM} &:= \int_{\Omega^e_0} f^{\alpha\beta\gamma\delta}\, \mathbf{N}^{\mathrm{T}}_{;\alpha\beta} \left(\boldsymbol{n} \otimes \boldsymbol{n} \right) \mathbf{N}_{;\gamma\delta} \, \mathrm{d}A \end{aligned} \tag{B.7}$$

and the geometric stiffness matrices

$$\begin{aligned} \mathbf{k}^e_{\tau} &:= \int_{\Omega^e_0} \mathbf{N}^{\mathrm{T}}_{,\alpha}\, \tau^{\alpha\beta}\, \mathbf{N}_{,\beta} \, \mathrm{d}A \ , \\ \mathbf{k}^e_{M} &= \mathbf{k}^e_{M1} + \mathbf{k}^e_{M2} + (\mathbf{k}^e_{M2})^{\mathrm{T}} \ , \end{aligned} \tag{B.8}$$

with

$$\begin{aligned} \mathbf{k}^e_{M1} &:= -\int_{\Omega^e_0} b_{\alpha\beta}\, M_0^{\alpha\beta}\, a^{\gamma\delta}\, \mathbf{N}^{\mathrm{T}}_{,\gamma} \left(\boldsymbol{n} \otimes \boldsymbol{n} \right) \mathbf{N}_{,\delta} \, \mathrm{d}A \ , \\ \mathbf{k}^e_{M2} &:= -\int_{\Omega^e_0} M_0^{\alpha\beta}\, \mathbf{N}^{\mathrm{T}}_{,\gamma} \left(\boldsymbol{n} \otimes \boldsymbol{a}^\gamma \right) \mathbf{N}_{;\alpha\beta} \, \mathrm{d}A \ . \end{aligned} \tag{B.9}$$

The tangent matrices associated with the external force vectors can be found in Sauer et al. (2014) and Duong et al. (2017).

Appendix C

Nomenclature

$\mathbf{1}$	identity tensor in $\mathbb{R}^3$
a	determinant of matrix $[a_{\alpha\beta}]$
A	determinant of matrix $[A_{\alpha\beta}]$
$\boldsymbol{a}_\alpha$	co-variant tangent vectors of surface $\mathcal{S}$ at point $\boldsymbol{x}$; $\alpha = 1, 2$
$\boldsymbol{A}_\alpha$	co-variant tangent vectors of surface $\mathcal{S}_0$ at point $\boldsymbol{X}$; $\alpha = 1, 2$
$\boldsymbol{a}_{\alpha,\beta}$	parametric derivative of $\boldsymbol{a}_\alpha$ w.r.t. ξ^β
$\boldsymbol{a}_{\alpha;\beta}$	co-variant derivative of $\boldsymbol{a}_\alpha$ w.r.t. ξ^β
$a_{\alpha\beta}$	co-variant metric tensor components of surface $\mathcal{S}$ at point $\boldsymbol{x}$
$A_{\alpha\beta}$	co-variant metric tensor components of surface $\mathcal{S}_0$ at point $\boldsymbol{X}$
$a^{\alpha\beta\gamma\delta}$	contra-variant components of the derivative of $a^{\alpha\beta}$ w.r.t. $a_{\gamma\delta}$
b	determinant of matrix $[b_{\alpha\beta}]$
B	determinant of matrix $[B_{\alpha\beta}]$
$\boldsymbol{b}$	curvature tensor of surface $\mathcal{S}$ at point $\boldsymbol{x}$
$\boldsymbol{b}_0$	curvature tensor of surface $\mathcal{S}_0$ at point $\boldsymbol{X}$
$\boldsymbol{B}$	left Cauchy-Green tensor of the shell mid-surface
$b_{\alpha\beta}$	co-variant curvature tensor components of surface $\mathcal{S}$ at point $\boldsymbol{x}$
$B_{\alpha\beta}$	co-variant curvature tensor components of surface $\mathcal{S}_0$ at point $\boldsymbol{X}$
$\mathbf{B}$	matrix of the coefficients of the Bernstein polynomials for element Ω^e
γ	surface tension
c	bending stiffness
$c^{\alpha\beta\gamma\delta}$	contra-variant components of the derivative of $\tau^{\alpha\beta}$ w.r.t. $a_{\gamma\delta}$
$\boldsymbol{C}$	right Cauchy-Green tensor of the shell mid-surface
$\tilde{\boldsymbol{C}}$	right Cauchy-Green tensor of a 3D continuum
$\overset{*}{\boldsymbol{C}}$	right Cauchy-Green tensor of a shell layer
$\mathbf{C}^e$	Bézier extraction operator for finite element Ω^e
$\boldsymbol{d}$	shell director vector
$d^{\alpha\beta\gamma\delta}$	contra-variant components of the derivative of $\tau^{\alpha\beta}$ w.r.t. $b_{\gamma\delta}$
δ...	variation of ...

ϵ	penalty parameter
η_{s}	kinematic surface viscosity
$\boldsymbol{E}$	Green-Lagrange strain tensor of the shell mid-surface
$e^{\alpha\beta\gamma\delta}$	contra-variant components of the derivative of $M_0^{\alpha\beta}$ w.r.t. $a_{\gamma\delta}$
$\boldsymbol{f}$	prescribed surface loads
f^α	in-plane components of $\boldsymbol{f}$
$f^{\alpha\beta\gamma\delta}$	contra-variant components of the derivative of $M_0^{\alpha\beta}$ w.r.t. $b_{\gamma\delta}$
$\mathbf{f}^e_\bullet$	discretized finite element force vector
$\boldsymbol{F}$	deformation gradient of the shell mid-surface
$\tilde{\boldsymbol{F}}$	deformation gradient of a 3D continuum
g	determinant of matrix $[g_{\alpha\beta}]$
G	determinant of matrix $[G_{\alpha\beta}]$
$\boldsymbol{g}_\alpha$, $\boldsymbol{g}_3$	current tangent and normal vectors of a shell layer; $\alpha = 1, 2$
$\boldsymbol{G}_\alpha$, $\boldsymbol{G}_3$	reference tangent vectors and normal of a shell layer; $\alpha = 1, 2$
g_{c}	G^1-continuity and symmetry constraints
$g_{\alpha\beta}$	co-variant components of the metric tensor of $\mathcal{S}^*$
$G_{\alpha\beta}$	co-variant components of the metric tensor of $\mathcal{S}_0^*$
G_{ext}	external virtual work
G_{int}	internal virtual work
$\Gamma^\gamma_{\alpha\beta}$	Christoffel symbols of the second kind
H	mean curvature of surface $\mathcal{S}$ at $\boldsymbol{x}$
H_0	mean curvature of surface $\mathcal{S}_0$ at $\boldsymbol{X}$
$\boldsymbol{i}$	identity tensor in $\mathcal{S}$
$\boldsymbol{I}$	identity tensor in $\mathcal{S}_0$
I_1	first invariant of $\boldsymbol{C}$
$\tilde{I}_1$	first invariant of $\tilde{\boldsymbol{C}}$
J	surface area change
$\tilde{J}$	volume change of a 3D continuum
J_a	Jacobian of the mapping $\mathcal{P} \to \mathcal{S}$
J_A	Jacobian of the mapping $\mathcal{P} \to \mathcal{S}_0$
$\mathbf{k}^e_\bullet$	finite element tangent matrices
κ	Gaussian curvature of surface $\mathcal{S}$ at $\boldsymbol{x}$
$\boldsymbol{\kappa}$	pull-back of the curvature tensor $\boldsymbol{b}$
$\boldsymbol{K}$	relative curvature tensor
$\tilde{K}$	bulk modulus of 3D continua
$\boldsymbol{\mathcal{L}}$	patch boundary on which edge rotation conditions are prescribed
λ	Lagrange multiplier for the continuity constraint
λ_i	principal stretches of surface $\mathcal{S}$ at $\boldsymbol{x}$
μ	surface shear modulus
$\tilde{\mu}$	shear modulus of 3D continua
$\boldsymbol{\mu}_0$	moment tensor in the reference configuration
$\boldsymbol{\mu}$	moment tensor in the current configuration

$M^{\alpha\beta}$, $M_0^{\alpha\beta}$	contra-variant bending moment components
$\boldsymbol{n}$, $\tilde{\boldsymbol{n}}$	surface normals of $\mathcal{S}$ at $\boldsymbol{x}$
$\boldsymbol{N}$, $\tilde{\boldsymbol{N}}$	surface normals of $\mathcal{S}_0$ at $\boldsymbol{X}$
$\mathbf{N}$	array of NURBS-based shape functions
$\hat{\mathbf{N}}^e$	array of B-spline basis functions in terms of the Bernstein polynomials
$\hat{N}_A^e$	B-spline basis function of the A^{th} control point; $A = 1, \ ..., \ n$
$N^{\alpha\beta}$	total, contra-variant components of $\boldsymbol{\sigma}$
$\boldsymbol{\nu}$	unit normal on $\partial\mathcal{S}$
ξ	out-of-plane coordinate
ξ^α	in-plane coordinates; $\alpha = 1, 2$
p_{ext}	external pressure
$\mathcal{P}$	parametric domain spanned by ξ^1 and ξ^2
P	shell material point
$\Pi_{\mathcal{L}}$	potential of the constraint used to enforce edge rotation conditions
$\boldsymbol{\varphi}$	deformation map of surface $\mathcal{S}$
ρ	areal density of surface $\mathcal{S}$
$\mathcal{S}$	current configuration of the shell surface
$\mathcal{S}_0$	reference configuration of the shell surface
$\overset{*}{\mathcal{S}}$	current configuration of a shell layer
$\overset{*}{\mathcal{S}}_0$	reference configuration of a shell layer
$\partial\mathcal{S}$	boundary of $\mathcal{S}$
$\boldsymbol{S}$	second Piola-Kirchhoff stress tensor of the shell
$\tilde{\boldsymbol{S}}$	second Piola-Kirchhoff stress tensor of a 3D continuum
S^α	contra-variant, out-of-plane shear stress components
$\boldsymbol{\sigma}$	Cauchy stress tensor of the shell
$\tilde{\boldsymbol{\sigma}}$	Cauchy stress tensor of a 3D continuum
$\sigma^{\alpha\beta}$	stretch related, contra-variant components of $\boldsymbol{\sigma}$
t	current shell thickness
T	reference shell thickness
$\boldsymbol{T}$	traction acting on a cut $\partial\mathcal{S}$ normal to $\boldsymbol{\nu}$
$\boldsymbol{T}^\alpha$	traction acting on a cut $\partial\mathcal{S}$ normal to $\boldsymbol{a}^\alpha$
$\boldsymbol{\tau}$	unit direction along a surface boundary
$\tilde{\boldsymbol{\tau}}$	Kirchhoff stress tensor of a 3D continuum
$\tau^{\alpha\beta}$	contra-variant components of the Kirchhoff stress tensor of the shell
$\tilde{\tau}^{\alpha\beta}$	in-plane components of $\tilde{\boldsymbol{\tau}}$
$\boldsymbol{v}$	velocity, i.e. the material time derivative of $\boldsymbol{x}$
$\mathcal{V}$	space for admissible variations $\delta\boldsymbol{x}$
w_A	NURBS weight of the A^{th} control point ($\hat{=}$ FE node); $A = 1, \ ..., \ n$
W	strain energy density function per reference area
$\tilde{W}$	strain energy density function per reference volume
$\boldsymbol{x}$	current position of a surface point on $\mathcal{S}$
$\boldsymbol{X}$	initial position of $\boldsymbol{x}$ on the reference surface $\mathcal{S}_0$

$\tilde{\boldsymbol{x}}$	current position of a material point of a 3D continuum
$\tilde{\boldsymbol{X}}$	reference position of a material point of a 3D continuum
$\mathbf{x}_e$	array of all nodal positions for finite element Ω^e
$\mathbf{X}_e$	array of all nodal positions for finite element Ω_0^e
Ω^e	current configuration of finite element e
Ω_0^e	reference configuration of finite element e

References

Abaqus (2013). *Abaqus 6.13 Analysis Users Guide.* Dassault Systémes. Sec. 22.5.3: Anisotropic hyperelastic behavior.

Abdessalem, J., Kallel, I. K., and Fakhreddine, D. (2011). Theory and finite element implementation of orthotropic and transversely isotropic incompressible hyperelastic membrane. *Multidiscip. Model. Mater. Struct.*, **7**(4):424–439.

Adam, C., Bouabdallah, S., Zarroug, M., and Maitournam, H. (2015). Improved numerical integration for locking treatment in isogeometric structural elements. part II: Plates and shells. *Comp. Meth. Appl. Mech. Engrg.*, **284**:106–137.

Alonso, C., Alig, T., Yoon, J., Bringezu, F., Warriner, H., and Zasadzinski, J. A. (2004). More than a monolayer: Relating lung surfactant structure and mechanics to composition. *Biophysic. J.*, **87**(6):4188–4202.

Ambati, M. and De Lorenzis, L. (2016). Phase-field modeling of brittle and ductile fracture in shells with isogeometric NURBS-based solid-shell elements. *Comp. Meth. Appl. Mech. Engrg.*, **312**:351–373.

Arciniega, R. A. and Reddy, J. (2005). Consistent Third-Order Shell Theory with Application to Composite Cylindrical Cylinders. *AIAA J.*, **43**(9):2024–2038.

Arciniega, R. A. and Reddy, J. N. (2007). Tensor-based finite element formulation for geometrically nonlinear analysis of shell structures. *Comput. Methods Appl. Mech. Engrg.*, **196**(4-6):1048–1073.

Ateshian, G. A., Ellis, B. J., and Weiss, J. A. (2007). Equivalence between short-time biphasic and incompressible elastic material responses. *J. Biomech. Engrg.*, **129**(3):405–412.

Ateshian, G. A., Rajan, V., Chahine, N. O., Canal, C. E., and Hung, C. T. (2009). Modeling the matrix of articular cartilage using a continuous fiber angular distribution predicts many observed phenomena. *J. Biomech. Engrg.*, **131**(6):061003.

Babuška, I. (1973). The finite element method with Lagrangian multipliers. *Num. Math.*, **20**(3):179–192.

Balzani, D., Gruttmann, F., and Schröder, J. (2008). Analysis of thin shells using anisotropic polyconvex energy densities. *Comput. Methods Appl. Mech. Eng.*, **197**(912):1015 – 1032.

Balzani, D., Neff, P., Schröder, J., and Holzapfel, G. A. (2006). A polyconvex framework for soft biological tissues. Adjustment to experimental data. *Int. J. Solids Struct.*, 43(20):6052–6070.

Balzani, D., Schröder, J., and Gross, D. (2007). Numerical simulation of residual stresses in arterial walls. *Comput. Mater. Sci.*, **39**:117–123.

Balzani, D., Schröder, J., and Neff, P. (2010). Applications of anisotropic polyconvex energies: thin shells and biomechanics of aterial walls. In *Poly-, Quasi- and Rank-One Convexity in Applied Mechanics*, volume **516**, pages 131–176. Springer Vienna.

Basar, Y. and Ding, Y. (1996). Finite-element analysis of hyperelastic thin shells with large strains. *Comput. Mech.*, **18**(3):200–214.

Bazilevs, Y., Deng, X., Korobenko, A., di Scalea, F. L., Todd, M., and Taylor, S. (2015). Isogeometric fatigue damage prediction in large-scale composite structures driven by dynamic sensor data. *J. Appl. Mech.*, **82**(9):091008.

Bazilevs, Y., Hsu, M.-C., Kiendl, J., Wüchner, R., and Bletzinger, K.-U. (2011). 3D simulation of wind turbine rotors at full scale. Part II: Fluid–structure–interaction modeling with composite blades. *Int. J. Num. Meth. Fluids*, **65**(1-3):236–253.

Bazilevs, Y., Hsu, M.-C., and Scott, M. (2012). Isogeometric fluid–structure interaction analysis with emphasis on non-matching discretizations, and with application to wind turbines. *Comp. Meth. Appl. Mech. Engrg.*, **249**:28–41.

Becker, G., Geuzaine, C., and Noels, L. (2011). A one field full discontinuous galerkin method for Kirchhoff–Love shells applied to fracture mechanics. *Comp. Meth. Appl. Mech. Engrg.*, **200**(45–46):3223–3241.

Beirão Da Veiga, L., Hughes, T., Kiendl, J., Lovadina, C., Niiranen, J., Reali, A., and Speleers, H. (2015). A locking-free model for Reissner–Mindlin plates: Analysis and isogeometric implementation via NURBS and triangular NURPS. *Math. Mod. Meth. Appl. Sci.*, **25**(08):1519–1551.

Belytschko, T., Stolarski, H., Liu, W. K., Carpenter, N., and Ong, J. S. (1985). Stress projection for membrane and shear locking in shell finite elements. *Comp. Meth. Appl. Mech. Engrg.*, **51**(1–3):221–258.

Benson, D., Bazilevs, Y., Hsu, M., and Hughes, T. (2010). Isogeometric shell analysis: The Reissner–Mindlin shell. *Comp. Meth. Appl. Mech. Engrg.*, **199**(5–8):276–289. Computational Geometry and Analysis.

Benson, D. J., Bazilevs, Y., Hsu, M.-C., and Hughes, T. J. R. (2011). A large deformation, rotation-free, isogeometric shell. *Comp. Methods Appl. Mech. Engrg.*, **200**(13-16):1367–1378.

Benson, D. J., Hartmann, S., Bazilevs, Y., Hsu, M.-C., and Hughes, T. J. R. (2013). Blended isogeometric shells. *Comp. Methods Appl. Mech. Engrg.*, **255**:133–146.

Bischoff, M. and Ramm, E. (1997). Shear deformable shell elements for large strains and rotations. *Int. J. Numer. Meth. Engrg.*, **40**(23):4427–4449.

Bischoff, M., Wall, W. A., Bletzinger, K.-U., and Ramm, E. (2004). Models and finite elements for thin-walled structures. In Stein, E., de Borst, R., and Hughes, T. J. R., editors, *Encyclopedia of Computational Mechanics. Vol. 2: Solids and Structures. Chapter 3.* Wiley.

Bonet, J. and Wood, R. D. (1997). *Nonlinear continuum mechanics for finite element analysis.* Cambridge university press, New York.

Bonet, J., Wood, R. D., and Mahaney, J. (2000). Aspects of the analysis of membrane structures. In *Computational civil and structural engineering*, pages 105–113. Civil-Comp. Press.

Borden, M. J., Scott, M. A., Evans, J. A., and Hughes, T. J. R. (2011). Isogeometric finite element data structures based on Bezier extraction of NURBS. *Int. J. Numer. Meth. Engng.*, **87**:15–47.

Borri-Brunetto, M., Chiaia, B., and Deambrosi, M. (2009). A micromechanical model for fibrous biological membranes at finite strain. *Biomater. Tissue Eng.*, **3**:1–23.

Bouclier, R., Elguedj, T., and Combescure, A. (2013a). Efficient isogeometric NURBS–based solid–shell elements: Mixed formulation and method. *Comp. Meth. Appl. Mech. Engrg.*, **267**(0):86–110.

Bouclier, R., Elguedj, T., and Combescure, A. (2013b). On the development of NURBS-based isogeometric solid shell elements: 2D problems and preliminary extension to 3D. *Comput. Mech.*, **52**(5):1085–1112.

Bouclier, R., Elguedj, T., and Combescure, A. (2015). An isogeometric locking-free NURBS-based solid-shell element for geometrically nonlinear analysis. *Int. J. Numer. Meth. Engrg.*, **101**(10):774–808.

Breitenberger, M., Apostolatos, A., Philipp, B., Wüchner, R., and Bletzinger, K.-U. (2015). Analysis in computer aided design: Nonlinear isogeometric B-Rep analysis of shell structures. *Comp. Meth. Appl. Mech. Engrg.*, **284**:401–457.

Brezzi, F. (1974). On the existence, uniqueness and approximation of saddle-point problems arising from lagrangian multipliers. *Revue française d'automatique, informatique, recherche opérationnelle. Analyse numérique*, **8**(2):129–151.

Brunet, M. and Sabourin, F. (2006). Analysis of a rotation-free 4-node shell element. *Int. J. Numer. Meth. Engrg.*, **66**(9):1483–1510.

Bürzle, W., Mazza, E., and Moore, J. J. (2014). About puncture testing applied for mechanical characterization of fetal membranes. *J. Biomech. Engrg.*, **136**(11):111009.

Canham, P. B. (1970). The minimum energy of bending as a possible explanation of the biconcave shape of the human red blood cell. *J. Theoret. Biol.*, **26**:61–81.

Carrera, E. (2002). Theories and finite elements for multilayered, anisotropic, composite plates and shells. *Arch. Comput. Meth. Engrg.*, **9**(2):87–140.

Carrera, E. and Brischetto, S. (2009). A survey with numerical assessment of classical and refined theories for the analysis of sandwich plates. *App. Mech. Rev.*, **62**(1):010803.

Carter, F. J., Frank, T. G., Davies, P. J., McLean, D., and Cuschieri, A. (2001). Measurements and modelling of the compliance of human and porcine organs. *Med. Image Anal.*, **5**(4):231–236.

Casanova, Cesar F.; Gallego, A. (2013). NURBS-based analysis of higher-order composite shells. *Compos. Struct.*, **104**:125–133.

Caseiro, J., Valente, R., Reali, A., Kiendl, J., Auricchio, F., and De Sousa, R. A. (2014). On the Assumed Natural Strain method to alleviate locking in solid–shell NURBS–based finite elements. *Comput. Mech.*, **53**(6):1341–1353.

Caseiro, J., Valente, R., Reali, A., Kiendl, J., Auricchio, F., and de Sousa, R. A. (2015). Assumed Natural Strain NURBS–based solid-shell element for the analysis of large deformation elasto-plastic thin-shell structures. *Comp. Meth. Appl. Mech. Engrg.*, **284**:861–880.

Casquero, H., Liu, L., Zhang, Y., Reali, A., Kiendl, J., and Gomez, H. (2017). Arbitrary-degree T-splines for isogeometric analysis of fully nonlinear Kirchhoff–Love shells. *Comput. Aided Des.*, **82**:140–153.

Chagnon, G., Rebouah, M., and Favier, D. (2015). Hyperelastic energy densities for soft biological tissues: A review. *J. Elast.*, **120**(2):129–160.

Chapelle, D., Mardare, C., and Münch, A. (2004). Asymptotic considerations shedding light on incompressible shell models. *J. Elast.*, **76**(3):199–246.

Chen, L., Nguyen-Thanh, N., Nguyen-Xuan, H., Rabczuk, T., Bordas, S. P. A., and Limbert, G. (2014). Explicit finite deformation analysis of isogeometric membranes. *Comp. Meth. Appl. Mech. Engrg.*, **277**:104–130.

Choi, A. and Zheng, Y. (2005). Estimation of Young's modulus and Poisson's ratio of soft tissue from indentation using two different-sized indentors: Finite element analysis of the finite deformation effect. *Med. Biol. Engrg. Comput.*, **43**(2):258–264.

Chui, C., Kobayashi, E., Chen, X., Hisada, T., and Sakuma, I. (2004). Combined compression and elongation experiments and non-linear modelling of liver tissue for surgical simulation. *Med. Bio. Engrg. Comput.*, **42**(6):787–798.

Ciarlet, P. G. (2005). An introduction to differential geometry with applications to elasticity. *J. Elast.*, **78-79**:3–201.

Cirak, F. and Long, Q. (2010). Advances in subdivision finite elements for thin shells. In De Mattos Pimenta, P. and Wriggers, P., editors, *New Trends in Thin Structures: Formulation, Optimization and Coupled Problems*, volume **519** of *CISM International Centre for Mechanical Sciences*, pages 205–227. Springer Vienna.

Cirak, F. and Ortiz, M. (2001). Fully C^1–conforming subdivision elements for finite deformation thin-shell analysis. *Int. J. Numer. Meth. Engrg.*, **51**:813–834.

Cirak, F., Ortiz, M., and Pandolfi, A. (2005). A cohesive approach to thin-shell fracture and fragmentation. *Comp. Meth. Appl. Mech. Engrg.*, **194**(21):2604–2618.

Cirak, F., Ortiz, M., and Schröder, P. (2000). Subdivision surfaces: a new paradigm for thin-shell finite-element analysis. *Int. J. Numer. Meth. Engrg.*, **47**(12):2039–2072.

Coox, L., Greco, F., Atak, O., Vandepitte, D., and Desmet, W. (2017). A robust patch coupling method for NURBS-based isogeometric analysis of non-conforming multipatch surfaces. *Comp. Meth. Appl. Mech. Engrg.*, **316**:235–260.

Corbett, C. J. (2016). *Isogeometric Finite Element Enrichment for Problems Dominated by Surface Effects*. PhD thesis, RWTH Aachen University.

Corbett, C. J. and Sauer, R. A. (2015). Three-dimensional isogeometrically enriched finite elements for mixed-mode contact and debonding. *Comput. Methods Appl. Mech. Engrg.*, **284**:781–806.

Cottrell, J. A., Hughes, T. J. R., and Bazilevs, Y. (2009). *Isogeometric Analysis*. Wiley.

Cottrell, J. A., Reali, A., Bazilevs, Y., and Hughes, T. J. (2006). Isogeometric analysis of structural vibrations. *Comp. Meth. Appl. Mech. Engrg.*, **195**(41):5257–5296.

Dale, P. J., Matthews, F. L., and Schroter, R. C. (1980). Finite element analysis of lung alveolus. *J. Biomech.*, **13**(10):865–873.

Davies, P. J., Carter, F. J., and Cuschieri, A. (2002). Mathematical modelling for keyhole surgery simulations: A biomechanical model for spleen tissue. *IMA J. Appl. Math.*, **67**(1):41–67.

De Borst, R. (1991). The zero-normal-stress condition in plane-stress and shell elastoplasticity. *Commun. Appl. Num. Meth.*, **7**(1):29–33.

Delingette, H. and Ayache, N. (2004). Soft tissue modeling for surgery simulation. *Handbook Num. Anal.*, 12:453–550.

Demiray, H. (1972). A note on the elasticity of soft biological tissues. *J. Biomech.*, **5**(3):309–311.

Deng, X., Korobenko, A., Yan, J., and Bazilevs, Y. (2015). Isogeometric analysis of continuum damage in rotation-free composite shells. *Comp. Meth. Appl. Mech. Engrg.*, **284**:349–372. Isogeometric Analysis Special Issue.

Denny, E. and Schroter, R. (1995). The mechanical behavior of a mammalian lung alveolar duct model. *J. Biomech. Engrg.*, **117**(3):254–261.

Denny, E. and Schroter, R. (1997). Relationships between alveolar size and fibre distribution in a mammalian lung alveolar duct model. *J. Biomech. Engrg.*, **119**(3):289–297.

Denny, E. and Schroter, R. (2000). Viscoelastic Behavior of a Lung Alveolar Duct Model. *J. Biomech. Engrg.*, **122**(2):143–151.

Denny, E. and Schroter, R. (2006). A model of non-uniform lung parenchyma distortion. *J. Biomech.*, **39**(4):652–663.

Doll, S. and Schweizerhof, K. (2000). On the development of volumetric strain energy functions. *J. Appl. Mech.*, **67**(1):17–21.

Doolin, B. F. and Martin, C. F. (2013). *Introduction to differential geometry for engineers*. Courier Corporation, New York.

Dornisch, W. and Klinkel, S. (2014). Treatment of Reissner–Mindlin shells with kinks without the need for drilling rotation stabilization in an isogeometric framework. *Comp. Meth. Appl. Mech. Engrg.*, **276**:35–66.

Dornisch, W., Klinkel, S., and Simeon, B. (2013). Isogeometric Reissner–Mindlin shell analysis with exactly calculated director vectors. *Comp. Meth. Appl. Mech. Engrg.*, **253**:491–504.

Dornisch, W., Müller, R., and Klinkel, S. (2016). An efficient and robust rotational formulation for isogeometric Reissner–Mindlin shell elements. *Comp. Meth. Appl. Mech. Engrg.*, **303**:1–34.

Dornisch, W., Stöckler, J., and Müller, R. (2017). Dual and approximate dual basis functions for B-splines, and NURBS–comparison and application for an efficient coupling of patches with the isogeometric mortar method. *Comp. Meth. Appl. Mech. Engrg.*, **316**:449–496.

Dornisch, W., Vitucci, G., and Klinkel, S. (2015). The weak substitution method – An application of the mortar method for patch coupling in NURBS-based isogeometric analysis. *Int. J. Numer. Meth. Engrg.*, **103**(3):205–234.

Du, X., Zhao, G., and Wang, W. (2015). Nitsche method for isogeometric analysis of Reissner-Mindlin plate with non-conforming multi-patches. *Comp. Aid. Geom. Des.*, **35-36**:121–136. Geometric Modeling and Processing 2015.

Duong, T. X., Roohbakhshan, F., and Sauer, R. A. (2017). A new rotation-free isogeometric thin shell formulation and a corresponding C^1-constraint for patch boundaries. *Comp. Meth. Appl. Mech. Engrg.*, **316**:43–83.

Dvorkin, E. N., Pantuso, D., and Repetto, E. A. (1995). A formulation of the mitc4 shell element for finite strain elasto-plastic analysis. *Comp. Meth. Appl. Mech. Engrg.*, **125**(1):17–40.

Echter, R. (2013). *Isogeometric analysis of shells*. PhD thesis, Institut für Baustatik und Baudynamik der Universität Stuttgart.

Echter, R., Oesterle, B., and Bischoff, M. (2013). A hierarchic family of isogeometric shell finite elements. *Comp. Meth. Appl. Mech. Engrg.*, **254**:170–180.

Elguedj, T., Bazilevs, Y., Calo, V. M., and Hughes, T. J. (2008). $\bar{B}$ and $\bar{F}$ projection methods for nearly incompressible linear and non-linear elasticity and plasticity using higher-order NURBS elements. *Comput. Methods Appl. Mech. Engrg.*, **197**(33):2732–2762.

Ericksen, J. L. (1960). Tensor fields. In Flügge, S., editor, *Encyclopedia of Physics*, volume III/1, pages 794–858. Springer.

Fan, R. and Sacks, M. S. (2014). Simulation of planar soft tissues using a structural constitutive model: Finite element implementation and validation. *J. Biomech.*, **47**(9):2043–2054.

Fathi-Azarbayjani, A. and Jouyban, A. (2015). Surface tension in human pathophysiology and its application as a medical diagnostic tool. *BioImpacts: BI*, **5**(1):29.

Federico, S. and Gasser, T. C. (2010). Nonlinear elasticity of biological tissues with statistical fibre orientation. *J. Roy. Soc. Interface*, **7**(47):955–966.

Flügge, W. (1962). *Stresses in shells.* Springer-Verlag.

Flynn, D., Peura, G., Grigg, P., and Hoffman, A. (1998). A finite element based method to determine the properties of planar soft tissue. *J. Biomech. Engrg*, **120**(2):202–210.

Fried, I. (1982). Finite element computation of large rubber membrane deformations. *Int. J. Numer. Mech. Engng.*, **18**:653–660.

Fung, Y. (1967). Elasticity of soft tissues in simple elongation. *Amer. J. Physio.*, 213(6):1532–1544.

Fung, Y. C. (1993). *Biomechanics: Mechanical Properties of Living Tissues.* Springer-Verlag, New York.

Gasser, T. C. and Holzapfel, G. A. (2007). Finite element modeling of balloon angioplasty by considering overstretch of remnant non-diseased tissues in lesions. *Comput. Mech.*, **40**(1):47–60.

Gasser, T. C., Ogden, R. W., and Holzapfel, G. A. (2006). Hyperelastic modelling of arterial layers with distributed collagen fibre orientations. *J. Roy. Soc. Interface*, **3**(6):15–35.

Gervaso, F., Capelli, C., Petrini, L., Lattanzio, S., Di Virgilio, L., and Migliavacca, F. (2008). On the effects of different strategies in modelling balloon-expandable stenting by means of finite element method. *J. Biomech.*, **41**(6):1206–1212.

Goerke, J. (1998). Pulmonary surfactant: functions and molecular composition. *Biochim. Biophys. Acta Molec. Basis Dis.*, **1408**(2-3):79–89.

Goyal, A. and Simeon, B. (2016). On penalty-free formulations for multipatch isogeometric Kirchhoff–Love shells. *Math. Comput. Simulat.*, Available online, DOI:10.1016/j.matcom.2016.12.001.

Green, A. E. (1992). *Theoretical elasticity.* Dover, New York.

Green, S. and Turkiyyah, G. M. (2005). A rotation-free quadrilateral thin shell subdivision finite element. *Commun. Numer. Meth. Engrg.*, **21**(12):757–767.

Guinovart-Sanjuán, D., Rodríguez-Ramos, R., Guinovart-Díaz, R., Bravo-Castillero, J., Sabina, F., Merodio, J., Lebon, F., Dumont, S., and Conci, A. (2016). Effective properties of regular elastic laminated shell composite. *Compos. B Engrg*, **87**:12–20.

Guo, Y. (2016). *Isogeometric analysis for thin-walled composite structures.* TU Delft, Delft University of Technology, Enschede, The Netherlands.

Guo, Y., Nagy, A. P., and Gürdal, Z. (2014a). A layerwise theory for laminated composites in the framework of isogeometric analysis. *Compos. Struct.*, **107**:447–457.

Guo, Y. and Ruess, M. (2015a). A layerwise isogeometric approach for NURBS-derived laminate composite shells. *Compos. Struct.*, **124**:300–309.

Guo, Y. and Ruess, M. (2015b). Nitsches method for a coupling of isogeometric thin shells and blended shell structures. *Comp. Meth. Appl. Mech. Engrg.*, **284**:881–905. Isogeometric Analysis Special Issue.

Guo, Y. and Ruess, M. (2015c). Weak Dirichlet boundary conditions for trimmed thin isogeometric shells. *Comput. Math. Appl.*, **70**(7):1425–1440. High-Order Finite Element and Isogeometric Methods.

Guo, Y., Ruess, M., and Gürdal, Z. (2014b). A contact extended isogeometric layerwise approach for the buckling analysis of delaminated composites. *Compos. Struct.*, **116**:55–66.

Guo, Y., Ruess, M., and Schillinger, D. (2016). A parameter-free variational coupling approach for trimmed isogeometric thin shells. *Comput. Mech.*, DOI:10.1007/s00466-016-1368-x:1–23.

Haughton, D. and Ogden, R. (1978). On the incremental equations in non-linear elasticity — I. Membrane theory. *J. Mech. Phys. Solids*, **26**(2):93 – 110.

Hermans, E., Bhamla, M. S., Kao, P., Fuller, G. G., and Vermant, J. (2015). Lung surfactants and different contributions to thin film stability. *Soft Matter*, **11**(41):8048–8057.

Holzapfel, G. A. (2000). *Nonlinear Solid Mechanics: A Continuum Approach for Engineering.* Wiley.

Holzapfel, G. A. (2001). Biomechanics of soft tissue. In Lemaitre, J., editor, *The handbook of materials behavior models*, volume **3**, pages 1049–1063. Academic Press, San Diego, USA.

Holzapfel, G. A., Eberlein, R., Wriggers, P., and Weizsäcker, H. W. (1996a). Large strain analysis of soft biological membranes: Formulation and finite element analysis. *Comput. Methods Appl. Mech. Eng.*, **132**(12):45 – 61.

Holzapfel, G. A., Eberlein, R., Wriggers, P., and Weizsäcker, H. W. (1996b). Large strain analysis of soft biological membranes: Formulation and finite element analysis. *Comp. Meth. Appl. Mech. Engrg.*, **132**(1):45–61.

Holzapfel, G. A., Gasser, T. C., and Ogden, R. W. (2000). A new constitutive framework for arterial wall mechanics and a comparative study of material models. *J. Elast. Phys. Sci. Solids*, **61**(1-3):1–48.

Holzapfel, G. A., Gasser, T. C., and Stadler, M. (2002a). A structural model for the viscoelastic behavior of arterial walls: continuum formulation and finite element analysis. *Eur. J. Mech. A/Solids*, **21**(3):441–463.

Holzapfel, G. A., Niestrawska, J. A., Ogden, R. W., Reinisch, A. J., and Schriefl, A. J. (2015). Modelling non-symmetric collagen fibre dispersion in arterial walls. *J. Roy. Soc. Interface*, **12**(106):20150188.

Holzapfel, G. A. and Ogden, R. W. (2009). On planar biaxial tests for anisotropic nonlinearly elastic solids. A continuum mechanical framework. *Math. Mech. Solids*, 14(5):474–489.

Holzapfel, G. A. and Ogden, R. W. (2010). Constitutive modelling of arteries. In *Proceed. Roy. Soc. London/A Math. Phys. Engrg. Sci.*, volume **466**, pages 1551–1597.

Holzapfel, G. A. and Ogden, R. W. (2015). On the tension–compression switch in soft fibrous solids. *Eur. J. Mech. A/Solids*, **49**:561–569.

Holzapfel, G. A., Stadler, M., and Schulze-Bauer, C. A. (2002b). A layer-specific three-dimensional model for the simulation of balloon angioplasty using magnetic resonance imaging and mechanical testing. *Ann. Biomed. Engrg.*, **30**(6):753–767.

Horgan, T. and Gilchrist, M. D. (2003). The creation of three-dimensional finite element models for simulating head impact biomechanics. *Int. J. Crash.*, **8**(4):353–366.

Horn, L. W. and Davis, S. H. (1975). Apparent surface tension hysteresis of a dynamical system. *J. Colloid Interface Sci.*, **51**(3):459 – 476.

Hosseini, S., Remmers, J. J., Verhoosel, C. V., and Borst, R. (2015). Propagation of delamination in composite materials with isogeometric continuum shell elements. *Int. J. Numer. Meth. Engrg.*, **102**(3-4):159–179.

Hosseini, S., Remmers, J. J., Verhoosel, C. V., and de Borst, R. (2014). An isogeometric continuum shell element for non-linear analysis. *Comp. Meth. Appl. Mech. Engrg.*, **271**:1–22.

Hosseini, S., Remmers, J. J. C., Verhoosel, C. V., and de Borst, R. (2013). An isogeometric solid–like shell element for nonlinear analysis. *Int. J. Numer. Meth. Engrg.*, **95**(3):238–256.

Hughes, T. J. and Carnoy, E. (1983). Nonlinear finite element shell formulation accounting for large membrane strains. *Comp. Meth. Appl. Mech. Engrg.*, **39**(1):69–82.

Hughes, T. J. R., Cottrell, J. A., and Bazilevs, Y. (2005). Isogeometric analysis: CAD, finite elements, NURBS, exact geometry and mesh refinement. *Comp. Meth. Appl. Mech. Engrg.*, **194**:4135–4195.

Humphrey, J. (1998). Computer methods in membrane biomechanics. *Comput. Meth. Biomech. Biomed. Eng.*, **1**(3):171–210.

Humphrey, J., Strumpf, R., and Yin, F. (1992). A constitutive theory for biomembranes: application to epicardial mechanics. *J. Biomech. Engrg.*, **114**(4):461–466.

Humphrey, J. and Yin, F. (1987). On constitutive relations and finite deformations of passive cardiac tissue: I. A pseudostrain-energy function. *J. Biomech. Engrg.*, **109**(4):298–304.

Humphrey, J. D. (2013). *Cardiovascular solid mechanics: cells, tissues, and organs.* Springer Science & Business Media, New York.

Ibrahimbegovic, A. and Gruttmann, F. (1993). A consistent finite element formulation of nonlinear membrane shell theory with particular reference to elastic rubberlike material. *Finite Elem. Anal. Des.*, **13**(1):75–86.

Immel, K. (2016). An Introduction to Computational Modeling of Lung Failure and Current Approaches. Seminar Thesis, RWTH Aachen.

Itskov, M. (2009). *Tensor Algebra and Tensor Analysis for Engineers.* Springer-Verlag Berlin Heidelberg, 2^{nd} edition.

Ivannikov, V., Tiago, C., and Pimenta, P. (2014). Meshless implementation of the geometrically exact Kirchhoff–Love shell theory. *Int. J. Numer. Meth. Engrg.*, **100**(1):1–39.

Jacobs, N. T., Cortes, D. H., Vresilovic, E. J., and Elliott, D. M. (2013). Biaxial tension of fibrous tissue: using finite element methods to address experimental challenges arising from boundary conditions and anisotropy. *J. Biomech. Engrg.*, **135**(2):021004.

Kaliske, M. (2000). A formulation of elasticity and viscoelasticity for fibre reinforced material at small and finite strains. *Comp. Meth. Appl. Mech. Engrg.*, **185**(2):225–243.

Kang, P. and Youn, S. (2015). Isogeometric analysis of topologically complex shell structures. *Finite Elem. Anal. Des.*, **99**:68–81.

Kang, P. and Youn, S.-K. (2016a). Isogeometric shape optimization of trimmed shell structures. *Struct. Multidiscip. Optim.*, **53**(4):825–845.

Kang, P. and Youn, S.-K. (2016b). Isogeometric topology optimization of shell structures using trimmed NURBS surfaces. *Finite Elem. Anal. Des.*, **120**:18–40.

Kapoor, H. and Kapania, R. (2012). Geometrically nonlinear NURBS isogeometric finite element analysis of laminated composite plates. *Compos. Struct.*, **94**(12):3434–3447.

Karakaplan, A., Bieniek, M., and Skalak, R. (1980). A mathematical model of lung parenchyma. *J. Biomech. Engrg.*, **102**(2):124–136.

Kazakevičiūtė-Makovska, R. (2001). Non-linear response functions for transversely isotropic elastic membranes. *Statyba*, **7**(5):345–351.

Kiendl, J., Ambati, M., De Lorenzis, L., Gomez, H., and Reali, A. (2016). Phase-field description of brittle fracture in plates and shells. *Comp. Meth. Appl. Mech. Engrg.*, **312**:374–394.

Kiendl, J., Auricchio, F., da Veiga, L. B., Lovadina, C., and Reali, A. (2015a). Isogeometric collocation methods for the Reissner–Mindlin plate problem. *Comp. Meth. Appl. Mech. Engrg.*, **284**:489–507. Isogeometric Analysis Special Issue.

Kiendl, J., Bazilevs, Y., Hsu, M.-C., Wüchner, R., and Bletzinger, K.-U. (2010). The bending strip method for isogeometric analysis of Kirchhoff-Love shell structures comprised of multiple patches. *Comput. Methods Appl. Mech. Engrg.*, **199**(37-40):2403–2416.

Kiendl, J., Bletzinger, K.-U., Linhard, J., and Wüchner, R. (2009). Isogeometric shell analysis with Kirchhoff–Love elements. *Comput. Methods Appl. Mech. Engrg.*, **198**:3902–3914.

Kiendl, J., Hsu, M.-C., Wu, M. C., and Reali, A. (2015b). Isogeometric Kirchhoff–Love shell formulations for general hyperelastic materials. *Comp. Meth. Appl. Mech. Engrg.*, **291**:280–303.

Klinkel, S. and Govindjee, S. (2002). Using finite strain 3D-material models in beam and shell elements. *Engrg. Comput.*, **19**(3):254–271.

Kojić, M., Filipović, N., Stojanović, B., and Kojić, N. (2009). *Biological Soft Tissue*, chapter 11, pages 201–225. John Wiley & Sons, Chichester, England Hoboken, NJ.

Kojić, M., Vlastelica, I., Stojanović, B., Ranković, V., and Tsuda, A. (2006). Stress integration procedures for a biaxial isotropic material model of biological membranes and for hysteretic models of muscle fibres and surfactant. *Int. J. Numer. Meth. Engrg.*, **68**(8):893–909.

Kowe, R., Schroter, R., Matthews, F., and Hitchings, D. (1986). Analysis of elastic and surface tension effects in the lung alveolus using finite element methods. *J. Biomech.*, **19**(7):541–549.

Kraus, H. (1967). *Thin elastic shells: an introduction to the theoretical foundations and the analysis of their static and dynamic behavior.* Wiley, New York.

Kreja, I. (2011). A literature review on computational models for laminated composite and sandwich panels. *Open Engrg.*, **1**(1):59–80.

Kreyszig, E. (1991). *Differential Geometry.* Dover, New York.

Kroon, M. and Holzapfel, G. A. (2009). Elastic properties of anisotropic vascular membranes examined by inverse analysis. *Comput. Methods Appl. Mech. Eng.*, **198**(45–46):3622 – 3632.

Krueger, M. A. and Gaver, D. P. (2000). A theoretical model of pulmonary surfactant multilayer collapse under oscillating area conditions. *J. Colloid Interface Sci.*, **229**(2):353–364.

Kyriacou, S., Humphrey, J., and Schwab, C. (1996). Finite element analysis of nonlinear orthotropic hyperelastic membranes. *Comput. Mech.*, **18**(4):269–278.

Le-Manh, T., Huynh-Van, Q., Phan, T. D., Phan, H. D., and Nguyen-Xuan, H. (2017). Isogeometric nonlinear bending and buckling analysis of variable-thickness composite plate structures. *Compos. Struct.*, **159**:818–826.

Lei, Z., Gillot, F., and Jezequel, L. (2015a). Developments of the mixed grid isogeometric Reissner–Mindlin shell: Serendipity basis and modified reduced quadrature. *Eur. J. Mech. A:Solids*, **54**:105–119.

Lei, Z., Gillot, F., and Jezequel, L. (2015b). A multiple patches connection method in isogeometric analysis. *Appl. Math. Model.*, **39**(15):4405–4420.

Li, J., Luo, X., and Kuang, Z. (2001). A nonlinear anisotropic model for porcine aortic heart valves. *J. Biomech.*, **34**(10):1279–1289.

Li, K., Ogden, R. W., and Holzapfel, G. A. (2016). Computational method for excluding fibers under compression in modeling soft fibrous solids. *Eur. J. Mech. A/Solids*, **57**:178–193.

Li, X., Zhang, J., and Zheng, Y. (2014). Static and free vibration analysis of laminated composite plates using isogeometric approach based on the third order shear deformation theory. *Adv. Mech. Engrg*, **6**:232019.

Libai, A. (1988). *The Nonlinear Theory of Elastic Shells: One Spatial Dimension.* Academic Press, Boston.

Liu, Y., Kerdok, A. E., and Howe, R. D. (2004). A nonlinear finite element model of soft tissue indentation. In Cotin, S. and Metaxas, D., editors, *Proceed. Int. Sympos. Medical Simulation, ISMS 2004*, pages 67–76. Springer, Berlin, Heidelberg.

Loglio, G., Tesei, U., Innocenti, N., Miller, R., and Cini, R. (1991). Non-equilibrium surface thermodynamics. measurement of transient dynamic surface tension for fluid–fluid interfaces by the trapezoidal pulse technique. *Colloids and Surfaces*, **57**(2):335 – 342.

Lu, M.-H., Mao, R., Lu, Y., Liu, Z., Wang, T.-F., and Chen, S.-P. (2012). Quantitative imaging of Young's modulus of soft tissues from ultrasound water jet indentation: A finite element study. *Comput. Math. Methods Med.*, **2012**.

Luo, K., Liu, C., Tian, Q., and Hu, H. (2016). An efficient model reduction method for buckling analyses of thin shells based on iga. *Comp. Meth. Appl. Mech. Engrg.*, **309**:243–268.

Malvern, L. E. (1969). *Introduction to the Mechanics of a continuous Medium.* Prentice-Hall.

Marsden, J. E. and Hughes, T. J. R. (1994). *Mathematical Foundations of Elasticity.* Dover, Mineola.

Martins, P., Natal Jorge, R., and Ferreira, A. (2006). A comparative study of several material models for prediction of hyperelastic properties: Application to silicone-rubber and soft tissues. *Strain*, **42**(3):135–147.

Massabò, R. and Gambarotta, L. (2006). Wrinkling of plane isotropic biological membranes. *J. Appl. Mech.*, **74**(3):550–559.

McKee, C. T., Last, J. A., Russell, P., and Murphy, C. J. (2011). Indentation versus tensile measurements of Young's modulus for soft biological tissues. *Tissue Engrg. Part B Rev.*, **17**(3):155–164.

Melnik, A. V., Da Rocha, H. B., and Goriely, A. (2015). On the modeling of fiber dispersion in fiber-reinforced elastic materials. *Int. J. Nonlin. Mech.*, **75**:92–106.

Mooney, M. (1940). A theory of large elastic deformation. *J. Appl. Phys.*, **11**(9):582–592.

Morris, J., Ingenito, E., Mark, L., Kamm, R., and Johnson, M. (2001). Dynamic behavior of lung surfactant. *ASME. J Biomech. Engrg.*, **123**(1):106–113.

Munglani, G., Vetter, R., Wittel, F., and Herrmann, H. (2015). Orthotropic rotation-free thin shell elements. *Comput. Mech.*, **56**(5):785–793.

Naghdi, P. M. (1982). Finite deformation of elastic rods and shells. In Carlson, D. E. and Shields, R. T., editors, *Proceedings of the IUTAM Symposium on Finite Elasticity*, pages 47–103, The Hague. Martinus Nijhoff Publishers.

Nagy, A. P., IJsselmuiden, S. T., and Abdalla, M. M. (2013). Isogeometric design of anisotropic shells: Optimal form and material distribution. *Comp. Meth. Appl. Mech. Engrg.*, **264**:145–162.

Nguyen, V., Kerfriden, P., Brino, M., Bordas, S., and Bonisoli, E. (2014). Nitsche's method for two and three dimensional NURBS patch coupling. *Comput. Mech.*, **53**(6):1163–1182.

Nguyen, V. P., Kerfriden, P., and Bordas, S. C. S. (2013). Nitsche's method method for mixed dimensional analysis: conforming and non-conforming continuum-beam and continuum-plate coupling. *arXiv preprint*, Available online: arXiv:1308.2910.

Nguyen-Schäfer, H. and Schmidt, J.-P. (2014). *Tensor analysis and elementary differential geometry for physicists and engineers.* Springer, Heidelberg.

Nguyen-Thanh, N., Kiendl, J., Nguyen-Xuan, H., Wüchner, R., Bletzinger, K.-U., Bazilevs, Y., and Rabczuk, T. (2011). Rotation free isogeometric thin shell analysis using PHT–splines. *Comput. Methods Appl. Mech. Engrg.*, **200**(47-48):3410–3424.

Nguyen-Thanh, N., Valizadeh, N., Nguyen, M., Nguyen-Xuan, H., Zhuang, X., Areias, P., Zi, G., Bazilevs, Y., Lorenzis, L. D., and Rabczuk, T. (2015). An extended isogeometric thin shell analysis based on Kirchhoff–Love theory. *Comp. Meth. Appl. Mech. Engrg.*, **284**:265–291. Isogeometric Analysis Special Issue.

Nguyen-Thanh, N., Zhou, K., Zhuang, X., Areias, P., Nguyen-Xuan, H., Bazilevs, Y., and Rabczuk, T. (2016). Isogeometric analysis of large-deformation thin shells using RHT-splines for multiple-patch coupling. *Comp. Meth. Appl. Mech. Engrg.*, Available online, DOI:10.1016/j.cma.2016.12.002.

Noels, L. and Radovitzky, R. (2008). A new discontinuous galerkin method for Kirchhoff–Love shells. *Comp. Meth. Appl. Mech. Engrg.*, **197**(33–40):2901–2929.

Ochoa, O. O. and Reddy, J. N. (1992). *Finite element analysis of composite laminates.* Springer, Dordrecht.

Oden, J. T. (2006). *Finite Elements of Nonlinear Continua.* Dover Edition.

Oden, J. T. and Sato, T. (1967). Finite strains and displacements of elastic membranes by the finite element method. *Int. J. Solids Struct.*, **3**(4):471–488.

Oesterle, B., Ramm, E., and Bischoff, M. (2016). A shear deformable, rotation-free isogeometric shell formulation. *Comp. Meth. Appl. Mech. Engrg.*, **307**:235–255.

Ogden, R. W. (1987). *Non-Linear Elastic Deformations.* Dover, Mineola, N.Y.

Ogden, R. W. (2003). Nonlinear elasticity, anisotropy, material stability and residual stresses in soft tissue. In Holzapfel, G. A. and Ogden, R. W., editors, *Biomechanics of soft tissue in cardiovascular systems*, pages 65–108. Springer, Vienna.

Ogden, R. W. (2009). Anisotropy and nonlinear elasticity in arterial wall mechanics. In Holzapfel, G. A. and Ogden, R. W., editors, *Biomechanical modelling at the molecular, cellular and tissue levels*, pages 179–258. Springer, Vienna.

O'Hagan, J. J. and Samani, A. (2008). Measurement of the hyperelastic properties of tissue slices with tumour inclusion. *Phys. Med. Bio.*, **53**(24):7087.

Oñate, E. and Zárate, F. (2000). Rotation-free triangular plate and shell elements. *Int. J. Numer. Meth. Engrg.*, **47**(1-3):557–603.

OpenStax (2014). OpenStax, Anatomy & Physiology. `http://cnx.org/content/col11496/1.6/`. OpenStax CNX. Jul 30, 2014.

Otis, D. R., Johnson, M., and Kamm, R. D. (1994). Dynamic surface tension of surfactant TA: experiments and theory. *J. Appl. Physiol.*, **77**(6):2681–2688.

Pant, S., Bressloff, N. W., and Limbert, G. (2012). Geometry parameterization and multidisciplinary constrained optimization of coronary stents. *Biomech. Model. Mechanobiol.*, **11**(1-2):61–82.

Picinbono, G., Delingette, H., and Ayache, N. (2001). Nonlinear and anisotropic elastic soft tissue models for medical simulation. In *Proceed. 2001 ICRA. IEEE Int. Conf. Robot. Automat.*, volume **2**, pages 1370–1375.

Picinbono, G., Delingette, H., and Ayache, N. (2003). Non-linear anisotropic elasticity for real-time surgery simulation. *Graph. Models*, **65**(5):305–321.

Prot, V., Skallerud, B., and Holzapfel, G. A. (2007). Transversely isotropic membrane shells with application to mitral valve mechanics. constitutive modelling and finite element implementation. *Int. J. Numer. Methods Eng.*, **71**(8):987–1008.

Qatu, M. S., Asadi, E., and Wang, W. (2012). Review of recent literature on static analyses of composite shells: 2000–2010. *Open J. Compos. Mater.*, **2**:61–86.

Qatu, M. S., Sullivan, R. W., and Wang, W. (2010). Recent research advances on the dynamic analysis of composite shells: 2000–2009. *Compos. Struct.*, **93**(1):14 – 31.

Ramakrishna, S., Mayer, J., Wintermantel, E., and Leong, K. W. (2001). Biomedical applications of polymer-composite materials: A review. *Composites science and technology*, **61**(9):1189–1224.

Rashid, B., Destrade, M., and Gilchrist, M. D. (2013). Mechanical characterization of brain tissue in simple shear at dynamic strain rates. *J. Mech. Behav. Biomed. Mater.*, **28**:71–85.

Rashid, B., Destrade, M., and Gilchrist, M. D. (2014). Mechanical characterization of brain tissue in tension at dynamic strain rates. *J. Mech. Behav. Biomed. Mater.*, **33**:43–54.

Rausch, M. K. and Kuhl, E. (2013). On the effect of prestrain and residual stress in thin biological membranes. *J. Mech. Phys. Solids*, **61**(9):1955 – 1969.

Rausch, M. K. and Kuhl, E. (2014). On the mechanics of growing thin biological membranes. *J. Mech. Phys. Solids*, **63**:128–140.

Rausch, S., Martin, C., Bornemann, P., Uhlig, S., and Wall, W. (2011). Material model of lung parenchyma based on living precision-cut lung slice testing. *J. Mech. Behav. Biomed. Mater.*, **4**(4):583–592.

Reali, A. and Gomez, H. (2015). An isogeometric collocation approach for Bernoulli–Euler beams and Kirchhoff plates. *Comp. Meth. Appl. Mech. Engrg.*, **284**:623–636. Isogeometric Analysis Special Issue.

Reddy, J. (1989). On refined computational models of composite laminates. *Int. J. Numer. Meth. Engrg.*, **27**(2):361–382.

Reddy, J. and Robbins, D. (1994). Theories and computational models for composite laminates. *Appl. Mech. Rev.*, **47**(6):147–169.

Reddy, J. N. (2004). *Mechanics of laminated composite plates and shells: theory and analysis*. CRC press, Boca Raton, Florida.

Reese, S., Raible, T., and Wriggers, P. (2001). Finite element modelling of orthotropic material behaviour in pneumatic membranes. *Int. J. Solids Struct.*, **38**(52):9525 – 9544.

Riffnaller-Schiefer, A., Augsdörfer, U., and Fellner, D. (2016). Isogeometric shell analysis with NURBS compatible subdivision surfaces. *Appl. Math. Comput.*, **272**, Part 1:139–147. Subdivision, Geometric and Algebraic Methods, Isogeometric Analysis and Refinability.

Rivlin, R. (1948). Large elastic deformations of isotropic materials. IV. Further developments of the general theory. *Phil. Trans. Roy. Soc. Lon. A: Math. Phys. Engrg Sci.*, **241**(835):379–397.

Rivlin, R. S. and Saunders, D. (1951). Large elastic deformations of isotropic materials. VII. Experiments on the deformation of rubber. *Phil. Trans. Roy. Soc. Lon. A: Math. Phys. Engrg Sci.*, **243**(865):251–288.

Roan, E. and Vemaganti, K. (2007). The nonlinear material properties of liver tissue determined from no-slip uniaxial compression experiments. *J. Biomech. Engrg.*, **129**(3):450–456.

Rogers, C., Tseng, D. Y., Squire, J. C., and Edelman, E. R. (1999). Balloon–artery interactions during stent placement: A finite element analysis approach to pressure, compliance, and stent design as contributors to vascular injury. *Circ. Res.*, **84**(4):378–383.

Roohbakhshan, F., Duong, T. X., and Sauer, R. A. (2016). A projection method to extract biological membrane models from 3D material models. *J. Mech. Behav. Biomed. Mater.*, **58**:90–104.

Roohbakhshan, F., Duong, T. X., and Sauer, R. A. (2017). Isogeometric Kirchhoff–Love shells: Numerics, constitution and biomechanical applications. *Proc. 11th Int. Conf. SSTA*, **4**.

Roohbakhshan, F. and Sauer, R. A. (2016). Isogeometric nonlinear shell elements for thin laminated composites based on analytical thickness integration. *J. Micromech. Molec. Phys.*, **01**(03 & 04):1640010(1–24).

Roohbakhshan, F. and Sauer, R. A. (2017). Efficient isogeometric thin shell formulations for soft biological materials. *Biomech. Model. Mechanobiol.*, **16**:1569–1597.

Roohbakhshan, F. and Sauer, R. A. (2018a). A finite membrane element formulation for surfactants. Preprint available online, arXiv:1807.08693.

Roohbakhshan, F. and Sauer, R. A. (2018b). Simulation of angioplasty using isogeometric laminated composite shell elements. *Proc. Appl. Math. Mech.*, To be published.

Saad, S. M., Neumann, A., and Acosta, E. J. (2010). A dynamic compression–relaxation model for lung surfactants. *Coll. Surf. A Physicoch. Engrg. Asp.*, **354**(1-3):34–44.

Saad, S. M. I. (2011). *Axisymmetric Drop Shape Analysis (ADSA) and Lung Surfactant*. PhD thesis, University of Toronto.

Sahu, A., Sauer, R. A., and Mandadapu, K. K. (2017). Irreversible thermodynamics of curved lipid membranes. *Physic. Rev. E*, **96**(4):042409.

Sauer, R. A. (2013). Local finite element enrichment strategies for 2D contact computations and a corresponding postprocessing scheme. *Comput. Mech.*, **52**(2):301–319.

Sauer, R. A. (2014). Stabilized finite element formulations for liquid membranes and their application to droplet contact. *Int. J. Numer. Meth. Fluids*, **75**(7):519–545.

Sauer, R. A. (2018). On the computational modeling of lipid bilayers using thin-shell theory. In *The Role of Mechanics in the Study of Lipid Bilayers*, pages 221–286. Springer International Publishing, Cham.

Sauer, R. A. and De Lorenzis, L. (2013). A computational contact formulation based on surface potentials. *Comput. Methods Appl. Mech. Engrg.*, **253**:369–395.

Sauer, R. A. and De Lorenzis, L. (2015). An unbiased computational contact formulation for 3D friction. *Int. J. Numer. Meth. Engrg.*, **101**:251–280.

Sauer, R. A. and Duong, T. X. (2017). On the theoretical foundations of solid and liquid shells. *Math. Mech. Solids*, **22**(3):343–371.

Sauer, R. A., Duong, T. X., and Corbett, C. J. (2014). A computational formulation for constrained solid and liquid membranes considering isogeometric finite elements. *Comput. Methods Appl. Mech. Engrg.*, **271**:48–68.

Sauer, R. A., Duong, T. X., Mandadapu, K. K., and Steigmann, D. J. (2017). A stabilized finite element formulation for liquid shells and its application to lipid bilayers. *J. Comput. Phys.*, **330**:436–466.

Schlebusch, R. and Zastrau, B. W. (2005). On an analogy between the deformation gradient and a generalized shell shifter tensor. *Arch. Appl. Mech.*, **74**(11):853–862.

Schmidt, R., Wüchner, R., and Bletzinger, K.-U. (2012). Isogeometric analysis of trimmed NURBS geometries. *Comp. Meth. Appl. Mech. Engrg.*, **241**:93–111.

Schriefl, A. J., Zeindlinger, G., Pierce, D. M., Regitnig, P., and Holzapfel, G. A. (2011). Determination of the layer-specific distributed collagen fibre orientations in human thoracic and abdominal aortas and common iliac arteries. *J. Roy. Soc. Interface*, **0**:1275–1286.

Simo, J. C. and Fox, D. D. (1989). On a stress resultant geometrically exact shell model. Part I: Formulation and optimal parameterization. *Comput. Meth. Appl. Mech. Engrg.*, **72**:267–304.

Simo, J. C., Fox, D. D., and Rifai, M. S. (1990). On a stress resultant geometrically exact shell model. Part III: Computational aspects of the nonlinear theory. *Comput. Meth. Appl. Mech. Engrg.*, **79**:21–70.

Skacel, P. and Bursa, J. (2014). Comparison of constitutive models of arterial layers with distributed collagen fibre orientations. *Acta Bioeng. Biomech.*, **16**(3).

Sobota, P., Dornisch, W., Müller, R., and Klinkel, S. (2016). Implicit dynamic analysis using an isogeometric Reissner–Mindlin shell formulation. *Int. J. Numer. Meth. Engrg.*, available online, DOI:10.1002/nme.5429.

Sokolnikoff, I. S. (1964). *Tensor analysis: Theory and applications to geometry and mechanics of continua.* Wiley, New York.

Stanley, G. and Park, K. (1986). A curved c^0 shell element based on assumed natural-coordinate strains. *J. Appl. Mech.*, **53**:278–290.

Steigmann, D. (2009). A concise derivation of membrane theory from three-dimensional nonlinear elasticity. *J. Elast.*, **97**(1):97–101.

Steigmann, D. J. (1999). On the relationship between the Cosserat and Kirchhoff–Love theories of elastic shells. *Math. Mech. Solids*, **4**:275–288.

Steigmann, D. J. (2013). Koiters shell theory from the perspective of three-dimensional nonlinear elasticity. *J. Elast.*, **111**(1):91–107.

Stolarski, H., Gilmanov, A., and Sotiropoulos, F. (2013). Nonlinear rotation-free three-node shell finite element formulation. *Int. J. Numer. Meth. Engrg.*, **95**(9):740–770.

Stone, H. (1990). A simple derivation of the time–dependent convective–diffusion equation for surfactant transport along a deforming interface. *Phys. Fluid. A Fluid. Dyn.*, **2**(1):111–112.

Sun, W. and Sacks, M. S. (2005). Finite element implementation of a generalized fung-elastic constitutive model for planar soft tissues. *Biomech. Model. Mechanobiol.*, **4**(2-3):190–199.

Sze, K., Liu, X., and Lo, S. (2004). Popular benchmark problems for geometric nonlinear analysis of shells. *Finite Elem. Anal. Des.*, **40**(11):1551–1569.

Tepole, A. B., Kabaria, H., Bletzinger, K.-U., and Kuhl, E. (2015). Isogeometric Kirchhoff–Love shell formulations for biological membranes. *Comp. Meth. Appl. Mech. Engrg.*, **293**:328–347.

Thai, C. H., Ferreira, A., Bordas, S., Rabczuk, T., and Nguyen-Xuan, H. (2014). Isogeometric analysis of laminated composite and sandwich plates using a new inverse trigonometric shear deformation theory. *Eur. J. Mech. A-Solid*, **43**:89–108.

Thai, C. H., Ferreira, A., Carrera, E., and Nguyen-Xuan, H. (2013a). Isogeometric analysis of laminated composite and sandwich plates using a layerwise deformation theory. *Compos. Struct.*, **104**:196–214.

Thai, C. H., Nguyen-Xuan, H., Bordas, S., Nguyen-Thanh, N., and Rabczuk, T. (2015). Isogeometric analysis of laminated composite plates using the higher-order shear deformation theory. *Mech. Adv. Mater. Struct.*, **22**(6):451–469.

Thai, C. H., Nguyen-Xuan, H., Nguyen-Thanh, N., Le, T.-H., Nguyen-Thoi, T., and Rabczuk, T. (2012). Static, free vibration, and buckling analysis of laminated composite Reissner–Mindlin plates using NURBS-based isogeometric approach. *Int. J. Numer. Meth. Engrg.*, **91**(6):571–603.

Thai, C. H., Rabczuk, T., and Nguyen-Xuan, H. (2013b). A rotation-free isogeometric analysis for composite sandwich thin plates. *Int. J. Compos. Mat.*, **3**(A):10–18.

Tonge, T. K., Voo, L. M., and Nguyen, T. D. (2013). Full-field bulge test for planar anisotropic tissues: Part II – A thin shell method for determining material parameters and comparison of two distributed fiber modeling approaches. *Acta Biomater.*, **9**(4):5926–5942.

Tran, L. V., Ferreira, A., and Nguyen-Xuan, H. (2013a). Isogeometric analysis of functionally graded plates using higher-order shear deformation theory. *Compos. B Engrg*, **51**:368–383.

Tran, L. V., Thai, C. H., and Nguyen-Xuan, H. (2013b). An isogeometric finite element formulation for thermal buckling analysis of functionally graded plates. *Finite Elem. Anal. Des.*, **73**:65–76.

Truesdell, C. and Noll, W. (2004). *The Non-Linear Field Theories of Mechanics.* Springer, 3rd edition.

Ugural, A. C. (2009). *Stresses in beams, plates, and shells.* CRC Press, Boca Raton.

Uhm, T.-K. and Youn, S.-K. (2009). T-spline finite element method for the analysis of shell structures. *Int. J. Numer. Meth. Engrg.*, **80**(4):507–536.

Velarde, M. G., Zeytounian, R. K., et al. (2002). *Interfacial phenomena and the Marangoni effect.* Springer, Wien.

Veldhuizen, E. J. and Haagsman, H. P. (2000). Role of pulmonary surfactant components in surface film formation and dynamics. *Biochim. Biophys. Acta Biomembr.*, **1467**(2):255–270.

Wenk, J. F., Ratcliffe, M. B., and Guccione, J. M. (2012). Finite element modeling of mitral leaflet tissue using a layered shell approximation. *Med. Bio. Engrg. Comp.*, **50**(10):1071–1079.

Wex, C., Arndt, S., Stoll, A., Bruns, C., and Kupriyanova, Y. (2015). Isotropic incompressible hyperelastic models for modelling the mechanical behaviour of biological tissues: A review. *Biomed. Engrg./Biomed. Tech.*, **60**(6):577–592.

Wiechert, L. (2011). *Computational modeling of multi-field and multi-scale phenomena in respiratory mechanics.* PhD thesis, Technical University of Munich.

Wiechert, L., Metzke, R., and Wall, W. (2009). Modeling the mechanical behavior of lung tissue at the microlevel. *J. Engrg. Mech.*, **135**(5):434–438.

Willmore, T. J. (2013). *An introduction to differential geometry.* Courier Corporation, New York.

Wriggers, P. (2001). *Nichtlineare Finite-Element-Methoden.* Springer.

Wriggers, P. (2006). *Computational Contact Mechanics.* Springer, 2nd edition.

Wriggers, P. (2008). *Nonlinear Finite Element Methods.* Springer, Berlin.

Wriggers, P. and Taylor, R. L. (1990). A fully non-linear axisymmetrical membrane element for rubber-like materials. *Engrg. Comput.*, **7**(1):303–310.

Yang, H. T. Y., Saigal, S., Masud, A., and Kapania, R. K. (2000). A survey of recent shell finite elements. *Int. J. Numer. Meth. Engng*, **47**:101–127.

Yin, S., Yu, T., Bui, T. Q., and Nguyen, M. N. (2015). Geometrically nonlinear analysis of functionally graded plates using isogeometric analysis. *Engrg Comput.*, **32**(2):519–558.

Yu, T. T., Yin, S., Bui, T. Q., and Hirose, S. (2015). A simple FSDT-based isogeometric analysis for geometrically nonlinear analysis of functionally graded plates. *Finite Elem. Anal. Des.*, **96**:1–10.

Zárate, F. and Oñate, E. (2012). Extended rotation-free shell triangles with transverse shear deformation effects. *Comput. Mech.*, **49**(4):487–503.

Zhang, H., Wang, D., and Liu, W. (2014). Isogeometric-meshfree coupled analysis of Kirchhoff plates. *Adv. Struct. Engrg.*, **17**(8):1159–1176.

Zhang, M., Zheng, Y., and Mak, A. F. (1997). Estimating the effective Young's modulus of soft tissues from indentation tests—nonlinear finite element analysis of effects of friction and large deformation. *Med. Engrg. Phys.*, **19**(6):512–517.

Zhang, Y. and Yang, C. (2009). Recent developments in finite element analysis for laminated composite plates. *Compos. Struct.*, **88**(1):147–157.

Zienkiewicz, O. C. and Taylor, R. L. (2005). *The Finite Element Method for Solid and Structural Mechanics*. Butterworth-Heinemann, Amsterdam, 6th edition.